**Document Version**
Final published version

**Citation (APA)**
Bolognin, M. (2026). *Sand slope failures: experimental and numerical advances: From static to dynamic processes by means of Material Point Method analyses* . [Dissertation (TU Delft), Delft University of Technology].
https://doi.org/10.4233/uuid:7d4c9a11-d92d-4133-a558-51a1a2797ddc

# Sand slope failures: experimental and numerical advances

## From static to dynamic processes by means of Material Point Method analyses

Marco Bolognin

# Sand slope failures: experimental and numerical advances

## From static to dynamic processes by means of Material Point Method analyses

# Sand slope failures: experimental and numerical advances

## From static to dynamic processes by means of Material Point Method analyses

## Dissertation

for the purpose of obtaining the degree of doctor
at Delft University of Technology,
by the authority of the Rector Magnificus,
Prof. dr. ir. H. Bijl,
chair of the Board for Doctorates
to be defended publicly on
Tuesday 23rd, June 2026 at 10:00

by

**Marco BOLOGNIN**

This Dissertation has been approved by the promotors.

Composition of the Doctoral Committee:

| | |
|---|---|
| Rector Magnificus, | Chairperson |
| Prof. dr. ir. S. N. Jonkman, | Delft University of Technology, promotor |
| Prof. dr. M. A. Hicks, | Delft University of Technology, promotor |
| Prof. dr. P. J. Vardon, | Delft University of Technology, promotor |
| *Independent members:* | |
| Prof. dr. K. G. Gavin, | Delft University of Technology |
| Prof. dr. ir. W. S. J. Uijttewaal, | Delft University of Technology |
| Dr. J. T. Eggenhuisen, | Utrecht University, The Netherlands |
| Dr. ir. R. Schmitz, | Sibelco, Belgium |
| Dr. ir. R. J. Labeur, | Delft University of Technology, reserve member |

*Keywords:* Flood defences, dredging, sediment transport, flow slide, liquefaction, breaching, soil-water interaction, phase transition, material point method

*Printed by:* Proefschriftspecialist
*Cover by:* Marco Bolognin

*Front & Back:* UAV picture taken during the flowslide experiment described in Chapter 6

This study was conducted as part of the MPM-Flow project "Understanding flow slides in flood defences". This project was accomplished with financial support from the Netherlands Organization for Scientific Research (NWO) (grant number 13889). Additional support was granted by Sibelco, Deltares, Rijkwaterstaat, Van Oord, Boskalis, and FloodControl IJkdijk.

ISBN/EAN 978-94-6518-228-5

An electronic version of this dissertation is available at
http://repository.tudelft.nl/.

# Contents

# Summary

This dissertation focuses on validating the Material Point Method (MPM) for analyzing underwater flow slides and slope stability issues to enhance understanding and predictive capabilities. By addressing the complexities of multi-phase, multi-physics, and multi-scale problems, the research aims to establish a reliable numerical solution for simulating these phenomena, which are critical for flood defense systems. The research bridges gaps in knowledge by integrating experimental data, advanced numerical modeling, and validation studies.

## Background and Motivation

The research highlights the challenges of assessing slope stability and failure for complex geometries, material behaviors, and large deformations. Flow slides pose substantial risks to infrastructure such as dikes and flood defenses. Despite over a century of geotechnical advancements, a coupled framework for analyzing underwater flow slides remains underdeveloped. This study aims to address this gap through the application and validation of MPM.

## Objectives and Research Questions

The primary objective is to validate the MPM for simulating flow slides, from failure initiation to sediment deposition, offering a economical and consistent visualization of hydro-mechanical stress-displacement fields. The research is guided by key questions, such as how to simulate fluid flows and material addition/removal in MPM, how MPM can be validated for slope failure and submerged flow slide dynamics, and what experimental protocols and monitoring tools are required to validate numerical solutions. As starting point the Anura3D software is used to test the MPM implementation.

## Approach and results

This dissertation employs a stepwise approach. It begins with an extensive literature review that delves into flow slide mechanisms and numerical methods for their analysis, with a focus on identifying the strengths and limitations of MPM. Then it validates MPM solutions through benchmarks for liquid and solid phases separately, and then by coupling the two phases. Starting from single phase laboratory scale benchmarks and increasing the complexity of the problem to full-scale multiphase scenarios.

Firstly, inflow and outflow boundary conditions (BCs) are developed and applied in order to simulate single phase fluid flow problems by the MPM. This corresponds to velocity and pressure controlled BCs. Uniform open channel flow and free overfall in open channels problems are simulated. It is shown that the numerical results predict well the flow geometry including the end depth ratio, pressure distribution and accelerations, and therefore the velocities and displacements.

Following these water flow validation exercises, a fully saturated soil material is assessed against numerical benchmarks following standard methodologies for the assessment of dike safety macrostability by means of Limit Equilibrium Method (LEM) and Finite Element Method (FEM). However, these approaches do not take into account the capacity of the dike to retain water, and are only concerned with the mechanical equilibrium of the dike's initial composition. Hence the analysis of a progressive dike failure is undertaken with MPM, in order to get a better insight of the post failure behaviour, and a proposal is made to better reflect on the concept of Safety Factor (SF). Hence it is demonstrated that the MPM yield similar results to standard methodologies for the assessment of dike safety and that it can additionally compute the transient evolution and final consequences of the slope instability by taking into account large deformations.

After the above mentioned numerical benchmarks, a large-scale field experiment and MPM simulations have been undertaken to investigate the dry (i.e. above water) slope failure phenomenon and the capability of MPM to simulate accurately the full process, including the kinematics of the failure. The instrumented slope located well above the water table and in a uniform horizontal quartz sand layer. It is seen that the single phase MPM with a material model that is able to capture strain-softening behaviour during the failure process is necessary to achieve a kinematic and geometric evolution that is consistent with field measurements.

Finally a flowslide field experiment is presented with the aim of providing a dataset to validate numerical models for the simulation of slope failures in underwater sandy slopes. A monitoring setup is designed and used to record the dynamic features of the partially submerged flowslide in an artificially induced slope failure in a sand quarry. These experiments generate vital datasets for numerical validation. The proposed experimental set up proved its effectiveness in capturing the main features of the occurring flowslide and its results are used as a benchmark for the preliminary simulation of the slope failure with MPM. This includes soil parameters like deformations, accelerations and pore pressure evolution. The numerical model of the proposed experiment has been solved with a 2-phase 1-point MPM formulation, which finds reasonable agreement with field observations, such as the retrogressive failure mechanism, qualitative pore pressure fluctuations, and estimation of the retrogression length.

## Key findings

The research highlights significant advancements in the numerical modeling of flow slides. The development of inflow and outflow boundary conditions in MPM improves its ability to simulate flow-like problems, enhancing accuracy and computational efficiency. The validation efforts demonstrate that MPM can replicate complex scenarios, including dike failures and submerged flow slides, while providing insights into slope stability and the reliability of residual structural performance of flood defenses. Field experiments in sand quarries serve as a critical validation step, showcasing MPM's ability to predict failure initiation, kinematics, and post-failure morphologies. Moreover, the study introduces innovative monitoring techniques, such as Lagrangian sensors, which provide invaluable data for understanding soil-water interactions and for validating numerical models.

### Recommendations for Future Work

The dissertation concludes with recommendations for future research. It suggests how to refine MPM formulations to tackle remaining challenges in fluid-solid coupling and large deformation modeling. It provides recommendations on how to advance its validation for flood defenses applications, and on how to apply MPM successfully to real-world engineering scenarios. Finally, the study calls for additional field experiments involving diverse materials and conditions to expand the dataset available for numerical validation and to improve the robustness of the proposed methodologies.

# Acknowledgements

Completing this dissertation has been an extraordinary journey, one that would not have been possible without the unwavering support, guidance, and inspiration of many remarkable individuals and institutions.

First and foremost, I would like to express my deepest gratitude to my Promoters: S.N. Jonkman, M.A. Hicks and P.J. Vardon; whose expertise and mentorship have been invaluable throughout this research. Your trust in my work and insightful feedback have significantly shaped the outcomes of this project. I am also immensely grateful to my daily Supervisors A. Rohe and K.J. Bakker, who, although leaving their positions during the course of my research, provided me with crucial guidance and support during their tenure.

To my research group and department, thank you for fostering an environment of collaboration, intellectual growth, and innovation. Your collective knowledge and encouragement have motivated me at every step. I extend my heartfelt thanks to my research colleagues from different universities and the broader research community worldwide, whose inspiring dissemination events and shared knowledge have enriched my understanding and passion for this field.

I would also like to acknowledge Deltares for their technical support and the research industry partners for their financial support and invaluable feedback. Your contributions were pivotal in advancing this project.

I wish to formally express my appreciation for the collaboration with Sibelco, which significantly strengthened the applied dimension and operational viability of the research.

On a personal note, I want to thank my friends and family for their unwavering encouragement, patience, and belief in me during this demanding journey. A special thanks to my cat Nebula, whose playful antics provided comfort and joy during long working hours.

Finally, and most importantly, to my partner Dr. Mannat Kaur, your endless love, support, and encouragement have been the bedrock of this achievement. You pushed me beyond my limits and brought balance, happiness, and purpose to my life beyond academia. This milestone is as much yours as it is mine.

To all of you, I owe my heartfelt gratitude.

Delft, 2026

# 1

# Introduction

## 1.1. Background

Assessing the stability and failure of slopes is a challenging task, due to the often complex investigations, geometries, material behaviour and large deformations associated with this type of problem. Hence, validation and verification activities for new numerical solutions are not straightforward. When uncertainties are difficult to quantify, they are often taken into account by applying factors of safety or safety margins for which the value increases proportionally with the uncertainty. Moreover, additional factors are also often included based on the consequence of failure, i.e. the value destroyed if a failure occurs.

Geoengineering projects often require the use of severe values of factors of safety because of the uncertainties following from typical geotechnical analyses and the potentially large impact of failure. Severe values of factors of safety usually correspond to uneconomical design and consequentially larger quantities of $CO_2$ emissions. By approaching design in this way, projects typically satisfy only strength criteria in order to determine their feasibility, and deformation criteria are accounted for with large safety margins that put out of sight the cogent failure mechanism and complicates the structural behaviour analysis.

Engineering design criteria have (and should have) the common goal of ensuring a safe and functional structure. Therefore, limit state design philosophy requires structures to satisfy two principal criteria: the ultimate limit state (ULS, generally associated with strength criteria) and the serviceability limit state (SLS, generally associated with deformation criteria). This demands modern engineers to optimise their design, construction, management and maintenance of their infrastructure in order to minimise the negative environmental impact and maximise the positives. In order to deal with complex socio-technical systems, software tools have been proven to play an important integrating role. New technologies not only have allowed us to improve the quality of engineering projects but also to speed up our construction capacity.

Assuming that the design of the superstructure is well executed, foundations or substructures should guarantee that the required load bearing capacity is achieved. As the bearing capacity should prevent the soil from producing shear failure under the calculated service life loads and because we are not living in a perfectly spherical world, many infrastructure systems (e.g. dams, dikes, railways embankments, roads, offshore pipes etc.) have to deal with slopes surrounding them and therefore deal with slope stability analysis sooner or later.

Natural slopes all around the world are subjected to continuous alternation of sediment erosion and deposition processes. The most undesirable and deadly often are referred to as landslides. Flow slides are a particular class of landslide, in which the failure mechanism involves a build up of pore fluid pressure in the sediments that are moving down slope, up to partial or total liquefaction of the material [17]. Hence, the material within the failure associated with this phenomena resembles that of viscous fluids and displacements are typically very large.

A recent example of this phenomenon is the Edenville (USA) dam collapse reported in Figure 1.1: the initially rigid soil material that was withstanding the hydrostatic water load retained by the dam started sliding, building up pore water pressure while sliding, to such high values that water is released during failure, leading to a total liquefaction of the material. In underwater flow slides, as the failed soil moves through the water, it also can induce a turbulent water flow, which in turn interacts with the eroding soil surface [31]. After more than 100 years of geotechnical and hydraulic engineering experience there is not yet an established coupled framework for analysing an underwater flow slide that includes both the fluid and solid behaviour, even though there are some workable rules for expressing the behaviour of them separately [10]. Hence the understanding of the phenomenon is still relatively shallow [22].

Computational methods have, in recent years, helped tremendously in producing strength and deformation visualisations of engineering structures. This make them a very valuable asset for engineering design, which justify their rapid and widespread use since their invention. However, computational methods often have their limitations, especially when dealing with geotechnical problems.

Civil engineers typically consider a slope stable or unstable by means of slope stability analyses [6, 11, 13, 14, 28]. However, traditional engineering slope stability analysis methods, such as the limit equilibrium method (LEM) or the finite element method (FEM) with strength reduction protocol, cannot quantify the consequences of the slope failure. LEM identifies the initial slip surface, but does not consider any slope deformations. FEM allows estimations of pre-failure slope deformations, but it cannot be used to calculate large deformations occurring during or after an initial failure. This is mostly due to the FEM mesh, which distorts when solving large deformation problems, and consequently causes analyses to abort abruptly or to give misleading results.

Additionally, detecting an initial slope failure with traditional slope analysis methods is not necessarily a good indicator of the overall safety of a considered slope. For example, when we consider dikes or levees, where the main function is retaining water (for example to prevent flooding), a factor of safety smaller than one could

Figure 1.1: Example of flow slide: Edenville dam collapse, USA, May 19th, 2020. Damage included complete destruction of a number of homes, washout of numerous roads and bridges and almost 11000 people evacuated. No loss of life. Videolink: `https://youtu.be/Hc3u_CHVHJ8`

result in sliding events that involve only a fraction of the considered soil body, that quickly finds a new equilibrium configuration, leaving the water retaining capacity of the considered system practically unchanged.

Preventing, mitigating and repairing flow slides in flood defenses is an expensive but unavoidable task for asset managers and, therefore, accurate assessment methods are required; even more so in view of intensifying land use and the impact of human intervention (climate change) on low-lying coastal areas worldwide. The use of advanced computational methods for the analysis of these problems plays a key role for the design and the optimisation of many projects [22].

With the growth of available computational power, more advanced mathematical solutions were gradually developed such as mesh free methods. Several past studies [2, 8, 9, 21] proposed possible solutions to evaluate the consequences of a flow slide. However, the requirements for the solution of large deformation problems, that are typical of this discipline, are difficult to meet. Generally speaking, these studies fall short in cost-effectiveness and in modelling of boundaries [19]. Hence they must rely on empirical approaches that apply to specific circumstances only and require using considerable simplifications.

There is no prospect of an analytical solution to analyse the hydro-mechanical interaction of soil and water in large deformation problems. Due to the lack of suitable analytical solutions, physical experiments are still necessary to perform validation studies of flow slide phenomena, which is the main aim of this dissertation. However, these often involve high costs as length scale effects necessitate large test facilities and such tests often only allow predictions for specific projects. In fact, flow slides may take place on the scale of river shores to continental slopes [20].

Unlike slope failures which involve a single soil mass that moves, hind-casting of flow slides utilising only data retrieved after a failure is not possible, due to the failure features evolving in time (i.e. retrogressive failure). In addition, the time scale effects are usually expensive to investigate, difficult to quantify and poorly understood. The duration of a flow slide ranges from hours (e.g. breaching), to seconds (e.g. liquefaction). Laboratory scale experiments are considered as a good starting point to gain deeper insight into solid and fluid fundamental mechanical processes that occur at the onset of and during flow slides. However, eventually field experiments are necessary for assessing the performance of the new numerical solutions for engineering scale problems.

Recently, a numerical framework is resolving some of the aforementioned shortcomings of computational methods for large deformation geotechnical problems and appears to be able to address their analysis with an algorithm that is based and makes use of the FEM heritage: this algorithm is frequently called the Material Point Method (MPM).

MPM is an arbitrary Eulerian-Lagrangian (ALE) method which take advantage of both Eulerian and Lagrangian approaches to remove mesh distortion limitations without the drawbacks of pure Eulerian or Lagrangian methods [27]. The method has been applied to different states of matter (i.e. solid, liquid, gas), which can be coupled and analysed in the same simulation. For geotechnical problems, MPM has been implemented in the open-source software called Anura3D [12] among others, which will be used for the analyses presented in this dissertation. In other words, MPM represents an opportunity to change from qualitative estimations of landslide consequences based on expert advice (as common in engineering practice), to more rational interpretations of landslide kinematics.

At the same time experimental research has provided some additional insights into the understanding of the physical processes involved in flow slides [18], allowing a better investigation of the salient features and influence of material behaviour on flow slides. With this dissertation, the author is attempting to enhance current engineering interpretation tools (e.g. through the application and enhancement of available computational methods), with the aim to more accurately represent physcial processes and then eventually to allow reliable estimates of less severe factors of safety and hence a more efficient use of natural resources. A focus is made on uniform sandy materials and on the combination of new experimental data, numerical developments and numerical analysis/validation.

## 1.2. Knowledge gaps

The knowledge gaps in the field of MPM modelling for flow slides can be summarised as follows. Solid single-phase granular material problems currently offer only semi-analytical solutions due to their nature. Additionally they are already better investigated and documented in literature compared to fluid flows as MPM was born to study history dependent materials such as soil (i.e. [4, 5, 26, 27]).

Proper validation of Anura3D for liquid phase analyses requires enhancements because most of the analytical solutions for flow problems include steady state boundary conditions. It is not yet known until what extent and which approach (including integration schemes, coupling technique, constitutive laws, site investigation protocol, laboratory protocol) is suitable for simulating flow slides accurately [3], nor have simulations been compared with comprehensive experimental data to validate the veracity of the method. When there are no analytical solutions to solve particular engineering problems, practitioners often rely on numerical methods as first approximation of the solution, in order to hold an interpretation framework that is useful for parametric and sensitivity studies.

Several numerical method are available to tackle large deformation problems: their requirements are relatively very stringent compared to small deformation problems, but they are not as well established as the latter, nor in engineering practice nor in academic literature. Hence, there is limited literature on robustness, advantages and limitations of these methods when applied to soil and water interaction problems. The lack of well established benchmarks hinders the quantitative assessment of the numerical artifacts on the error that will inevitably be present due to the nature of numerical methods solutions. For rigorous validation, first verification activities are recommended in order to ensure that the software implementation is doing what it is intended for. Unfortunately this requires analytical solutions that are available for a very small number of problems.

Once the modeller has built confidence in his modelling strategies, he may attempt validation versus more complex experiments that, in flow-slide case studies, are challenging due to the lack of similarities among experiments. To further complicate the validation procedure, one has to account for the different scales at which the phenomena take place (time scale, geometrical scale). From a physical perspective, there is not an investigation protocol to analyse flow-slide phenomena because of the intrinsic variability of the material involved and difficulties of having accessible and reliable investigation tools. This is particularly challenging for simultaneously underground and underwater environment that characterise these phenomena.

## 1.3. Scope and objective

The main aim of this dissertation is validating numerical solutions that offer an accurate, cheap, consistent visualisation of hydro-mechanical stress-displacement fields for sand flow-slides in flood defenses, from initiation of the failure up to deposition of the sediments, within the Anura3D MPM framework. A special effort is made to highlight remaining unsolved aspects of MPM flow slide simulations. A new set of benchmark problems is provided, complementary to the already existing ones in literature (e.g. [23]) and literature elsewhere (e.g. [7, 15, 25, 30, 32]).

This dissertation contributes to knowledge development about MPM, increasing the confidence about its use for site-specific, quantitative and qualitative evaluations of the flow slide vulnerability of underwater sand slopes. Note however, that the validation remains challenging due to the abundant complexity and uniqueness of real slopes. Implementation and validation activities are necessary to make MPM useable for civil engineering applications.

In order to achieve the goals of the dissertation, the present work should be seen as part of a collaborative research project together with other partners of the NWO [1] project "MPM-Flow" (grant number 1388). Other sub-projects have addressed the mathematical aspects of MPM in modelling soil and water interaction [29], the laboratory features and relevant variables for flow slides investigation [24] and the behaviour of turbidity currents [1]. Nevertheless, this dissertation is written in order to eliminate gaps in literature about MPM independently from the results of other colleagues.

It is the author's hope that the next generation of engineers will be using this enhanced algorithm as one of the tools to analyse and improve current design standards, exploiting deeper knowledge of material behaviour (e.g. to safely decrease required values of factor of safety) so far untapped due to lack of suitable numerical analysis tools.

## 1.4. Research hypotheses

Flow slides are an unavoidable threat and their dynamics, hence their consequences, are highly uncertain due to the lack of suitable analysis tools. Therefore, designers will apply large factors of safety or safety margins in order to deem their design safe. This naturally results in less efficient designs and a waste of natural resources.

---

[1] see The Netherlands Organisation for Scientific Research (NWO), `https://www.nwo.nl/en`.

A dynamic coupled numerical framework based on continuum mechanical balance equations offers an opportunity to gain a deeper insight into the stress-strain behaviours of the different materials involved in flow slides, allowing an agile quantitative and deterministic interpretation of the natural phenomena. The validation of the method and analyses of benchmark problems of increasing complexity is aimed to help build confidence in this method and to distinguish numerical artifacts from modelling errors.

Verification of methods often use analytical solutions; however, these often involve simple boundary conditions and geometries, particularly when analysing flow problems, and therefore do not provide a comprehensive test of the model. This problem can be addressed by performing real scale experiments. Based on the findings from the literature review of the flow slide phenomena and of available engineering methods for their analysis, that are presented in Chapter 2 of this dissertation, the following research hypotheses have been formulated:

- The implementation of steady state inflow and outflow boundary conditions in Anura3D will improve efficiency and accuracy of the simulation of fluid flow problems.
- It is possible to define a numerical solution for the coupled hydro-mechanical interpretation of flow slide phenomena based on MPM.
- The relevant parameters for an accurate prediction of a flow slide are few. They can be determined by standard laboratory tests used in civil engineering practice.
- MPM is able to model large deformation problems in geo-mechanics that involve the coupling of soil with water whilst using advanced soil models.
- innovative monitoring techniques, such as the use of Lagrangian point sensors, will be needed to for the investigation of turbulent soil mass motion, which is typical of flow slide phenomena.

## 1.5. Research questions

In order to test the hypothesis formulated in Section 1.4, the following research questions (RQ) were formulated. As the main research objective focuses on the validation of MPM for flow slides in flood defenses, the proposed benchmarks will increase in complexity in order to access the performance of the method against a wide variety of geometries, materials and loading conditions.

1. **How is it possible to simulate fluid flows while adding/removing material points in/from the computational domain in the Anura3D framework?**

   The RQ.1 can be further split in the following parts:

   - What boundary conditions should be applied?
   - What integration scheme is required?

- If required, what smoothing technique improves the results?

Once the liquid phase is satisfactorily modelled, the MPM coupled hydro-mechanical formulation can be tested against literature examples. Logic would suggest starting from numerical studies as a verification test, then performing validation against laboratory experiments and later against engineering scale slopes, where scaling effects are also present. However, there is no established protocol to perform such validation, nor is it known how well MPM can capture the phenomena in analysis. Hence the following RQ is formulated:

2. **How can Anura3D be validated for slope failure analyses?**

   By performing verification studies against established numerical solutions available in literature (presented in later chapters), and by being able to simulate also the interim and morphology post-failure, the following sub questions will be answered:

   - Does Anura3D yield comparable results to traditional LEM and FEM for the safety assessment of slopes?
   - Does initial shear failure of a dike lead to the loss of the dike's capability to retain water?
   - What are the opportunities that the MPM solutions offer to better reflect on the concept of safety factor?

Once the proposed algorithm is verified, it can be tested against real slopes. Several studies have been reasonably successful in simulating the failure initiation and final deposition, although no measurements were available of the dynamic evolution of the failure. Therefore, the failure process, i.e. the kinematics and the material behaviour, could not be readily validated. This led to formulating the following RQ:

3. **How can full scale slope failures be simulated, including the forecast of its initial instability, kinematics and final geometry?**

   Trying to answer RQ.3 also requires answering:

   - What are the material model requirements for accurate displacement forecasts of slope failure consequences?

Finally, in order to access the performances of MPM for real scale flowslide problems, after identifying suitable formulations and constitutive models able to capture the interim and final morphology of the slope failure, it is possible to tackle validation studies against underwater slopes experiments. In order to do so, the following RQ is formulated:

4. **How can Anura3D be validated for submerged flowslide dynamics and morphology against full scale experiments?**

   To answer RQ.4, the following subquestions need to be addressed:

- How can underwater mining activities being monitored as experiments/case-studies to validate Anura3D for flowslides?
- What monitoring tools and experimental protocols are required to produce a useful dataset for the validation of the numerical solution?

## 1.6. Research approach and Outline

A step wise investigative approach is here proposed to validate Anura3D for flow-slide phenomena. This approach tackles one-by-one several of the key knowledge gaps, building towards a more comprehensive body of knowledge in the processes leading up to and during flow slides.

Flow-slide phenomena generally involve different materials. For simplicity, this dissertation considers only two fundamental material phases, fluid and solid. The gas phase can be disregarded as for the case of fully saturated soil it plays a minor role more often than not.

The performance of Anura3D in simulating relevant phenomena can be better assessed by starting from single-phase problems and then increasing the complexity to multi-phase coupled problems, so to allow the modeller to gain sensitivity about the influence of modelling assumptions depending on the materials in use and their state. However, field data are lacking and experiments are necessary for assessing the performance of the new numerical solutions for engineering scale problems. The validation models described in this dissertation are two-dimensional problems, preparatory for successful three-dimensional studies, and are considered complementary to those available in literature.

The stability of slopes is a topic of interest in the mining industry where the stability of slopes is strongly correlated with costs and risks in mining activities. Hence, in the early stages of this research, an agreement was reached with an industry partner, Sibelco, in order to monitor their mining activities with the aim to generate datasets useful for the validation of the proposed numerical solutions.

Sibelco periodically performs geotechnical investigation in their quarries in order to access the slope stability based on advanced analysis rather than based on experience only. Their monitoring data can be used for flow slide case studies. Additionally, it was possible to perform real scale experiments in their sandquarries for monitoring artificially triggered flow slide phenomena from initiation up to deposition of the sediments. The quarries are located on rather uniform and horizontal sand deposits. Such data sets are scarce in literature.

The step-wise investigative approach led the author to organise this dissertation into seven chapters which can be summarised as follows:

- **Chapter 2**: The literature review describes both the physical understanding of flow slides and the available computational methods for the analysis of these phenomena. This chapter includes an overview of the currently affirmed landslide classification system in order to define flow slides. Triggering mechanisms and onset processes are discussed as well as the current guidelines for flow slide susceptibility assessments. This chapter also provides background information about numerical methods in geotechnical engineering that can be used to tackle the flow slide phenomenon, with a focus on MPM. Advantages and disadvantages are highlighted as well as the governing equations and computational algorithms of the Anura3D software used in this dissertation.

- **Chapter 3**: The first application of Anura3D in this dissertation concerns fluid flow problems at laboratory scale where analytical descriptions were available in literature. This chapter answers RQ.1 and its subquestions by presenting the implementation of a steady-state in/outflow boundary condition in the MPM. To simulate a constant flow in a spatially fixed domain, material points are required to be introduced or removed from the domain. This new implementation, not only provides an opportunity to validate Anura3D for single phase fluid problems, but also allows the simulation of soil-water problems more accurately, with a vastly reduced computational time.

- **Chapter 4**: This chapter answers RQ.2 by performing a validation study of Anura3D versus an established numerical experiment of a fully saturated slope under increasing gravity. The first subquestion is answered by simulating, once again, a laboratory scale problem, but this time involving coupled interaction of solid and liquid phase, by replicating the experience of Hicks and Wong [16]. Hence a relatively larger step in this investigative approach is taken to answer the remaining subquestions by performing exploratory slope failure analyses of a typical Dutch dike profile with simple constitutive models. This provided insights into the slope failure mechanism, including the reliability of the residual structure. The opportunities to improve current guidelines are highlighted.

- **Chapter 5**: In order to answer RQ.3, this chapter validates Anura3D for full scale slope failure analysis by comparing simulation results to dataset from a real scale landslide experiment. This is undertaken in dry conditions, in order to reduce the complexity and risks involved. Different constitutive models are used to simulate the experiment with Anura3D to answer the subquestion. This case study is used to assess the reliability of the proposed experimental set up for monitoring slope failures as well as the reliability of the Lagrangian sensor technology developed for this dissertation.

- **Chapter 6**: This chapter presents results from two field experiments that have been performed of underwater flow slide events. These slopes were fully saturated in order to validated the Anura3D coupled formulation. Hence RQ.4 is answered by proposing, executing and analysing an experimental set up for recording the dynamic features of partially submerged slopes flowslide in sand quarries. Its results are considered useful for the validation of numerical solutions for flowslide analysis. Finally, simulations of the proposed experiment have been performed with Anura3D 2-phase 1-point formulation as a validation exercise.

- **Chapter 7**: The dissertation concludes by summarising the main findings from this research project and the recommendations for future research work are given.

### Contributions to Geotechnical Engineering

This dissertation makes significant contributions to geotechnical engineering. It addresses the limitations of traditional slope stability analysis methods and provides a robust tool for analyzing complex geotechnical problems involving large deformations. The research offers practical applications, enabling more precise safety assessments and reducing conservative safety margins, which results in resource-efficient and environmentally sustainable designs. Additionally, it deepens the understanding of physical processes underlying flow slides thus enhancing the predictive capabilities of geotechnical engineers.

## References

[1] S. Alhaddad. *Breaching Flow Slides and the Associated Turbidity Currents Large-Scale Experiments and 3D Numerical Modelling*. PhD thesis, Delft University of Technology. 2021.

[2] A. Azizian and R. Popescu. Finite element simulation of seismically induced retrogressive failure of submarine slopes. *Can. Geotech. J.*, 42:1532–1547, 2005.

[3] S. Bandara and K. Soga. Coupling of soil deformation and pore fluid flow using material point method. *Computers and Geotechnics*, 63:199–214, 2015.

[4] S. G. Bardenhagen. Energy conservation error in the material point method for solid mechanics. *Journal of Computational Physics*, 180:383–403, 2002.

[5] S. G. Bardenhagen, J. U. Brackbill, and D. Sulsky. The material-point method for granular materials. *Comput. Methods Appl. Mech. Engrg*, 187:529–541, 2000.

[6] A. W. Bishop. The use of the slip circle in the stability analysis of slopes. *Géotechnique*, 5:7–17, 1955.

[7] M. Bolognin, M. Martinelli, K. J. Bakker, and S. N. Jonkman. Validation of material point method for soil fluidisation analysis. *Procedia Engineering*, 175:233–241, 2017.

[8] L. Calvo, B. Haddad, M. Pastor, and D. Palacios. Runout and deposit morphology of bingham fluid as a function of initial volume: implication for debris flow modelling. *Journal of the International Society for the Prevention and Mitigation of Natural Hazards*, 75:489–513, 2014.

[9] B.-G. Chae, H.-J. Park, F. Catani, A. Simoni, and M. Berti. Landslide prediction, monitoring and early warning: a concise review of state-of-the-art. *Geosciences Journal*, 21:1033–1070, 2017.

[10] L. Cheng, S. Draper, H. An, S. Draper, and H. An. Scour and erosion. *Geotechnical Special Publication*, 2010.

[11] E. Dawson, W. Roth, and A. Drescher. Slope stability analysis by strength reduction. *Geotechnique*, 49:835–840, 1999.

[12] J. Fern, A. Rohe, K. Soga, E. Alonso, A. Rohe, K. Soga, and E. Alonso. *The Material Point Method for Geotechnical Engineering: a Practicle Guide*. CRC Press, 1st editio edition, 2019.

[13] T. D. Gast, M. A. Hicks, A. P. V. D. Eijnden, and P. J. Vardon. On the reliability assessment of a controlled dyke failure. *Géotechnique*, pages 1–46, 2020.

[14] D. V. Griffiths and P. A. Lane. Slope stability analysis by finite elements. *Géotechnique*, 49:387–403, 1999.

[15] F. Hamad, Z. Więckowski, and C. Moormann. Interaction of fluid–solid–geomembrane by the material point method. *Computers and Geotechnics*, 81:112–124, 2017.

[16] M. A. Hicks and S. W. Wong. Static liquefaction of loose slopes. *Numerical Methods in Geomechanics*, I:1361–1367, 1988.

[17] O. Hungr, S. Leroueil, and L. Picarelli. The varnes classification of landslide types, an update. *Landslides*, 11:167–194, 2014.

[18] R. R. D. Jager, A. Maghsoudloo, A. Askarinejad, and F. Molenkamp. Preliminary results of instrumented laboratory flow slides. *Procedia Engineering*, 175:212–219, 2017.

[19] S. Li and W. K. Liu. Meshfree and particle methods and their applications. *American Society of Mechanical Engineers*, 55, 2002.

[20] D. R. Mastbergen and J. H. V. D. Berg. Breaching in fine sands and the generation of sustained turbidity currents in submarine canyons. *Sedimentology*, 50:625–637, 2003.

[21] M. Pastor, A. Yague, M. M. Stickle, D. Manzanal, and P. Mira. A two-phase sph model for debris flow propagation. *International Journal for Numerical and Analytical Methods in Geomechanics*, pages 1–31, 2017.

[22] S. Pathmanandavel, . Charles, J. Macrobert, and C. J. Macrobert. Digitisation, sustainability, and disruption-promoting a more balanced debate on risk in the geotechnical community. *Georisk: Assessment and Management of Risk for Engineered Systems and Geohazards*, 2020.

[23] A. Rohe and Y. Alba. Validation manual – mpm software – anura3d, 2016.

[24] J. Silva. *The influence of underwater embankment properties on breaching failures*. PhD thesis, Utrecht University 2020.

[25] S. Sinaie, T. D. Ngo, V. P. Nguyen, and T. Rabczuk. Validation of the material point method for the simulation of thin-walled tubes under lateral compression. *Thin-Walled Structures*, 130:32–46, 2018.

[26] D. Sulsky, Z. Chen, and H. L. Schreyer. A particle method for history-dependent materials. *Computer Methods in Applied Mechanics and Engineering*, 118:179–196, 1994.

[27] D. Sulsky, S.-J. Zhou, and H. L. Schreyer. Application of a particle-in-cell method to solid mechanics. *Computer Physics Communications*, 87:236–252, 1995.

[28] K. Terzaghi. Theoretical soil mechanics. *Géotechnique*, page 510, 1943.

[29] L. Wobbes. *Algorithmic improvements of the material-point method and Taylor least-squares function reconstruction*. PhD thesis, Delft University of Technology. 2019.

[30] A. Yerro, E. Alonso, and N. Pinyol. The material point method for unsaturated soils. *Géotechnique*, 65:201–217, 2015.

[31] Y. You. *Dynamics of dilative slope failure*. PhD thesis, The University of Texas at Austin. 2013.

[32] L. Zambrano-Cruzatty and A. Yerro. Numerical simulation of a free fall penetrometer deployment using the material point method. *Soils and Foundations*, 60:668–682, 2020.

# 2

# Literature study for sand flow slides

## 2.1. Introduction

Slope erosion processes are expected to increase as we are consuming more marine sand than its natural production. The world is in fact expiring its marine sand reserves [6, 33] which is the most used raw material by human activities after water and air (even more than oil) and one of its major uses is for concrete. Sand is also used for food production, cosmetics, computer chips, glass, breast implants, paper, paint, plastic, and many more human activities. The environmental impact of sand mining includes the impact of moving large quantities of such a heavy material across the globe. Sand use and scarcity are contributing to the continuous sand mean price increases (more than 5 times in the last 40 years) and more recently, it is fostering sand mafias and sand production related crimes. Marine sand mining is also a major contributing factor for coastal erosion, which poses additional threat to flood defenses and more in general to all slopes. Finding new locations for sand mining shows in recent years increasing difficulties. Consequently, the current trend is to utilize existing sand extraction sites to their full capacity. In order to reduce the space occupied by sand extraction sites, the steepest possible slopes and deeper designs are desired. This, however, increases the susceptibility of boundary slopes to flow slide events.

In recent years, a number of unintentionally triggered flow slide events were recorded during excavation activities at different locations, sometimes with substantial damage to the environment [32]. Predicting the retrogression length of breaching events is still a challenging task for practitioners. In the first part of this chapter, flow slide phenomena are defined by means of a typological classification based on widespread definitions in geotechnical engineering by [24]. Then the possible triggering mechanisms and physical onset processes are described. Dutch and European governing codes for site investigation and the assessment of geotechnical parameters are indicated and commented on.

The second reminder of this chapter describes the literature review of the numerical method for the analysis of flow slides. The alternatives to the MPM method as well as its successful applications are listed from existing literature and the assumptions, main features and limitations are highlighted. The results from this literature review are useful to identify an MPM formulation for an accurate, cheap, consistent visualization of hydro-mechanical stress-displacement fields for sand flow slides, from initiation of the failure up to deposition of the sediments.

## 2.2. Landslide classification

### 2.2.1. General

A landslide is a movement of soil or rock, driven generally by the self-weight of the soil or rock and elevation differences, i.e. a slope. Landslides are physical systems that develop in time, starting with slope pre-failure deformations, slope failure and post-failure displacements [13, 44]. The failure usually involves the formation of a rupture surface (initial slide) and its post-failure behaviour, i.e. amount of material which moves, its velocity and secondary failures are determined by the geometry and material properties, including potential strength loss with large deformations [48]. The type of material is one of the most important parameters influencing landslide behavior, as well as the slope geometry. The evolution of a landslide can also be complicated by the interaction of adjacent sliding material in a variety of styles and distributions.

Given the uncertainties concerning failure mechanisms, classifications are commonly used in order to organise and communicate conveniently about different types of land slides. Taxonomy for these types of phenomena is difficult: hence the typological classification by Oldrich Hungr [24], based on the widespread definitions in civil engineering practice by Varnes [49] and Hutchinson [25], is here adopted, and is summarised by Table 2.1. Hungr [24] suggested the following definition for **sand flow slides**: *"Very rapid to extremely rapid flow of sorted or unsorted saturated granular material on moderate slopes, involving excess pore-pressure or liquefaction of material originating from the landslide source. [...] Usually originates as a multiple retrogressive failure. May occur subaerially, or under water."*. By definition [14], granular material **flows** are spatially continuous movements in which surfaces of shear are short lived, closely spaced and usually not preserved. The distribution of velocities in the displacing mass resembles that in a viscous liquid. Similarly, granular material **slides** are defined as down slope movements of mass occurring dominantly on the surface of rupture or on relatively thin zones of intense shear strain. A **flow slide** is a complex motion resulting from the two previously described movements (granular material flows and slides).

Flow slide phenomena often present a wide range of ground movements, such as deep failure of slopes and shallow debris flow. Their classification is not trivial because flow slides are not perfectly repeatable and usually being characterised by different triggers, movements, morphology, and involving different materials. The main difficulties in analyzing flow slide related problems are: 1) unavoidable lack of similarity in model experiments and 2) inadequate knowledge of the natural process. The current classification is based on genetic and morphological aspects (classification criteria) rather than arbitrary and subjective discriminating factors. The adopted classification criteria are: involved material (grain size, water content, etc.), movement mechanism (liquefaction, slide, etc.) and movement velocity (range of values related to the discharge).

### 2.2.2. Flowslide mechanical behaviour

Our sensorial experience says that there is no difference of mass failure type between under water and dry sand slopes, except for the occurrence of turbidity currents [27]. When focusing on coarse granular material (i.e. marine sand), we can distinguish between retrogressive breach failures (RBF) and liquefaction failures as additional dimensions in this class of phenomena. Dense sands favor RBF flow slides [7], while loose sands favor liquefaction flow slides [39, 46]. The main differences between these types of flowslide are the retrogressive pattern of propagation and the mass movement rate. The behavior of saturated sand deposits strongly depends on its initial relative density. However, the susceptibility of sand deposits to flow slides depends, not only on the initial relative density of the deposit, but also on the effective mean (confining) stress state of the soil. The confining pressure influences sand dilative behaviour to the point that even densely consolidated sand, if sheared at sufficiently high confining pressure, will behave similarly to unconsolidated loose sand [5]. Therefore, the susceptibility of a sand deposit to flow sliding cannot be expressed in terms of relative density alone; a description of stress level must also be included.

When the sand is in a loose state and it is sheared in a drained condition, it compacts, decreasing the volume of the inter granular pores (compressive behaviour). If the shearing is quick enough (undrained behaviour) the reduction of pore volume translates in excess pore water pressure. Increasing pore pressure reduces the effective stress present in the solid skeleton of the sand deposit and might lead to soil liquefaction [47]. This type of phenomenon is quick and sudden, and the sand and water mixture usually flows away in a motion that resembles velocity fields of viscous fluids (Figure 2.2-a). Moreover, the soil shear strength shows hardening behaviour up to the critical state.

In contrast, when densely packed sand is sheared, initially it has to overcome interlocking and apparent cohesion, which give to the soil an apparent higher shear resistance during monotonic loading. Dense sand drained shear test curves present softening behaviour when large deformations are considered. The peak shear strength is in an unstable condition and changes of the loading conditions (e.g. pore water pressure changes due to sedimentation) can suddenly decrease the shear strength and cause a drop to the critical state. On top of this, after a brief elastic contraction due to the application of the loading forces during a test, the soil will show a dilative behaviour due to the reconstitution of the grain skeleton up to the critical state. Because of dense sand tendency to dilate, the generated suction in undrained conditions appears as a cohesive force. This transient state increases the soil strength until consolidation dissipates the generated suction and hence al-

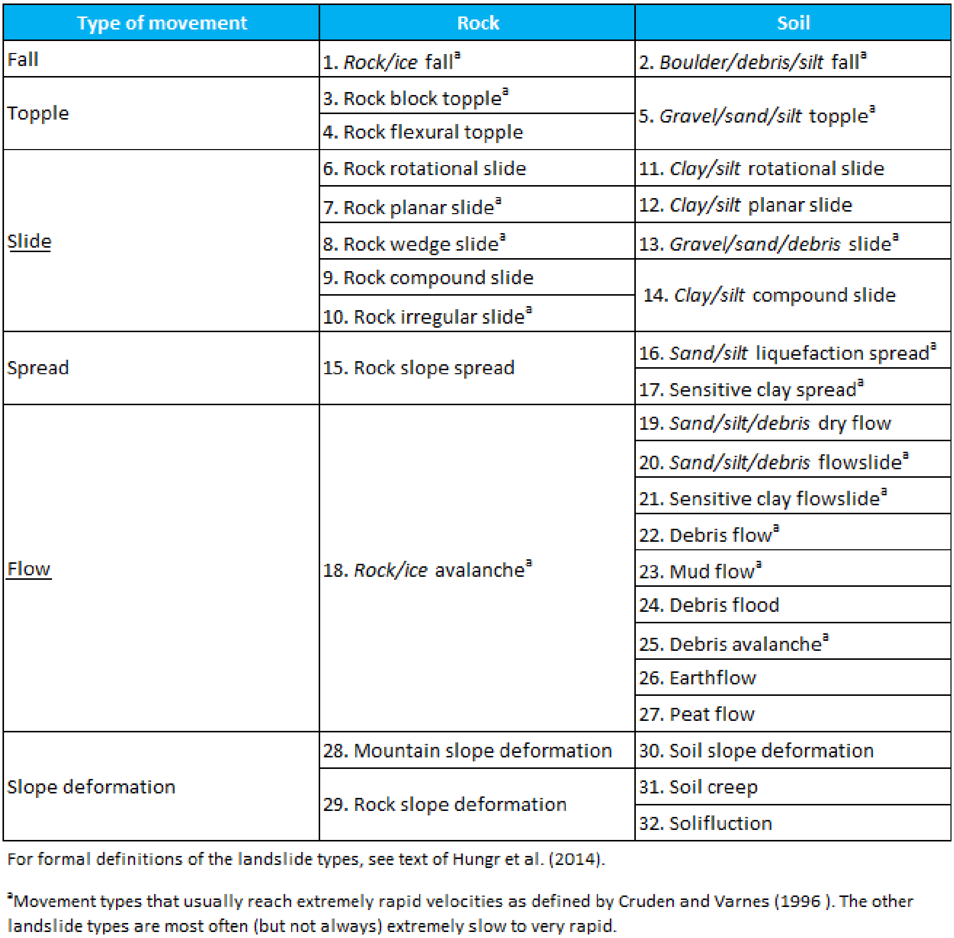

| Type of movement | Rock | Soil |
|---|---|---|
| Fall | 1. *Rock/ice* fall[a] | 2. *Boulder/debris/silt* fall[a] |
| Topple | 3. Rock block topple[a] | 5. *Gravel/sand/silt* topple[a] |
| | 4. Rock flexural topple | |
| Slide | 6. Rock rotational slide | 11. *Clay/silt* rotational slide |
| | 7. Rock planar slide[a] | 12. *Clay/silt* planar slide |
| | 8. Rock wedge slide[a] | 13. *Gravel/sand/debris* slide[a] |
| | 9. Rock compound slide | 14. *Clay/silt* compound slide |
| | 10. Rock irregular slide[a] | |
| Spread | 15. Rock slope spread | 16. *Sand/silt* liquefaction spread[a] |
| | | 17. Sensitive clay spread[a] |
| Flow | 18. *Rock/ice* avalanche[a] | 19. *Sand/silt/debris* dry flow |
| | | 20. *Sand/silt/debris* flowslide[a] |
| | | 21. Sensitive clay flowslide[a] |
| | | 22. Debris flow[a] |
| | | 23. Mud flow[a] |
| | | 24. Debris flood |
| | | 25. Debris avalanche[a] |
| | | 26. Earthflow |
| | | 27. Peat flow |
| Slope deformation | 28. Mountain slope deformation | 30. Soil slope deformation |
| | 29. Rock slope deformation | 31. Soil creep |
| | | 32. Solifluction |

For formal definitions of the landslide types, see text of Hungr et al. (2014).

[a] Movement types that usually reach extremely rapid velocities as defined by Cruden and Varnes (1996 ). The other landslide types are most often (but not always) extremely slow to very rapid.

Figure 2.1: A schematic landslide classification adopting the classification of [49] and taking into account the modifications made by [24]. The italic words are placeholders (use only one).

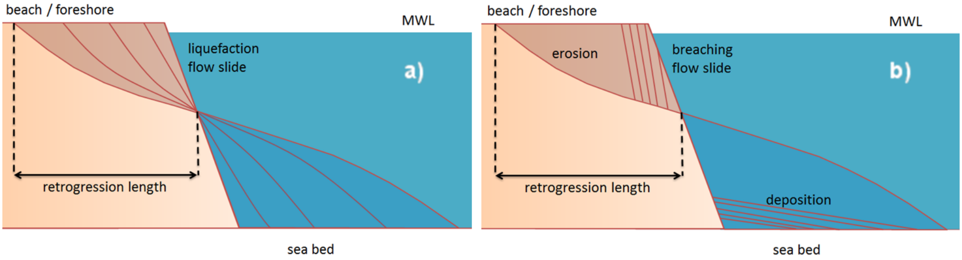

Figure 2.2: Failure mechanism and post-event morphology of a sand slopes, sketch redrawn from [31]: a) liquefaction failure and b) retrogressive breach failure.

lows for steeper slope angles than the angle of repose. As the suction pulls the otherwise cohesionless sand grains together, the erosion rate of the slope during failure is slower compared to liquefaction and takes the name of RBF (Figure 2.2-b). During RBF, turbidity currents can transport a fine suspension of sand several hundreds of meters away from the toe of the slope, depending on its momentum. Also, for quantifying the turbidity current contribution, scale effects are not negligible: as the sediment concentrated flow accelerates down slope, it includes more sediments from the bed and further contributes to the erosional process taking place (positive feedback). This feedback is typically further strengthened during the active phase by the characteristic amphitheatre shape morphology at the slope crest and including a choke in the lower part of the slope where the turbidity currents are channelled.

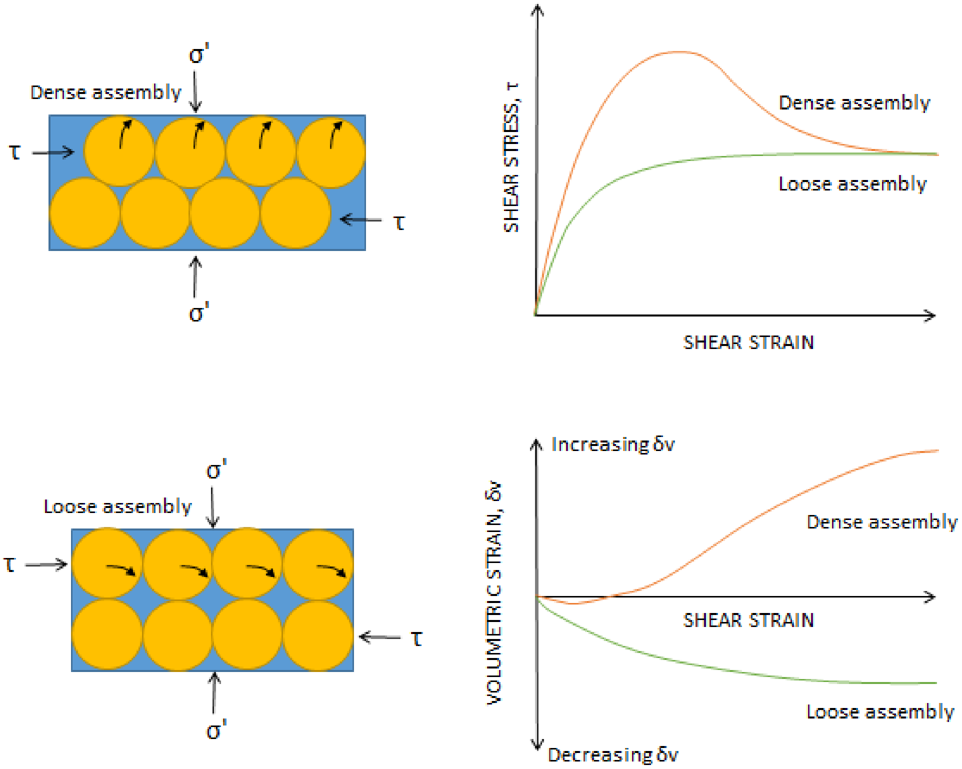

Figure 2.3: Qualitative behaviour of compressible loose assemblies and dilatant dense assemblies of sand when sheared drained.

If the active breaching wall height grows (unstable breaching [34]), pure RBF events eventually develop into 'dual mode failure' events where the failure mechanism switches between breaching and sliding [54]. This greatly increases the erosion rate and turbidity current momentum. Sandy stable (almost) vertical breaching walls have been witnessed with heights of about 5-7 meters before switching from pure breaching to sliding [29].

Eventually, the turbidity current/debris flow encounters gentler slopes and gradually loses its momentum, depositing the entrained sand in a tongue or fan shape. This will gradually decrease the slope steepness, decreasing the shearing forces due to the self weight of the soil.

Hence, the underwater sand slope's susceptibility to a flow slide is mainly dependent on three key factors:

1. relative density of the soil;
2. height and the steepness of the slope (slope geometry);
3. and triggering mechanism (by human activities or by natural processes).

In order to enable easy modelling strategies of parameters and boundary conditions, this chapter analyses flow slides triggered by industrial processes (i.e. dredging operations) rather than natural processes (where uncertainties are abundant). For industrial processes, the main triggering mechanisms are: (i) overloading due to the presence of human activities or (ii) alteration of the slope geometry during excavation.

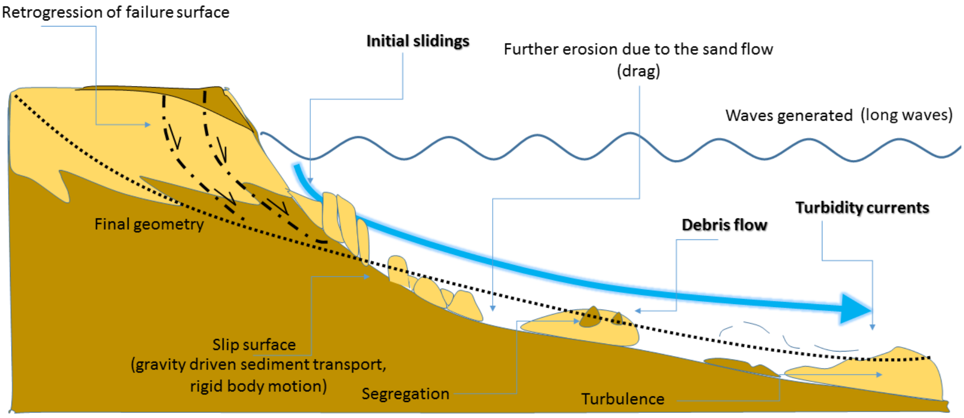

Figure 2.4: Qualitative description of a submerged flow slide.

### 2.2.3. Triggering mechanisms of submerged flow slides

Flow slides have different natural causes which relate to both the geological attributes of the sliding material and transient environmental factors affecting the submerged environment. Common natural causes of flow slides include [50]:

1. presence of weak geological layers;
2. overpressure (i.e. due to rapid accumulation of sedimentary deposits);
3. earthquakes and vibrations;

4. storm wave loading and hurricanes;
5. gas hydrate dissociation;
6. groundwater seepage;
7. pore water pressure fluctuations;
8. glacial loading;
9. volcanic island growth;
10. flora and fauna excavations;
11. over steepening (i.e. due to scour erosion).

For industrial processes, the main triggering mechanisms are:

1. overloading due to presence of human activities;
2. alteration of the slope geometry during excavation.

### 2.2.4. Onset Processes

Flow slides can occur in a wide range of environments, even on slopes as gentle as 1 degree, and may cause severe damage to both life and property. During such events, large volumes of granular material can be displaced within seconds or gradually over several hours, affecting slopes that range in scale from laboratory settings to entire continental margins. Although various types of movement take place in submerged environments, only slides, debris flows, and turbidity currents make a significant contribution to gravity-driven sediment transport [27]. The displaced sediments will predominantly travel through the water, falling, bouncing and rolling.

During the onset, there is mass and energy exchange occurring between the backscarp and the free surface water surrounding it. This exchange also occurs during the entrainment of water in the moving soil mass. In contrast to simplified models or laboratory experiments, soil state is rarely homogeneous but exhibits interlayering and inter-bedding properties. Spatial variation of soil properties in turn impacts flow slide onset. These also influence the creation of erosion channels and fluctuations of pore water pressures throughout the flow slide phenomenon. Similarly, the transport of inhomogeneous sediments must accounted for. However, turbulent flow of inhomogeneous soil lumps carried by water currents tend to remould into homogenous mixtures [18]. The expected observable physical processes that are involved during the onset of a flow slide can be listed as follows:

- erosion;
- drag;
- localization of strain (thin regions of high strain);

- seepage;
- gravity driven sediment transport;
- rigid body motion;
- segregation;
- rapid fluid flow;
- turbulence.

This list can be used to model and validate possible onset processes. For an extensive validation, not only the single process should be validated but also the interface of all possible combinations. In practice, the onset behaviour is evaluated by professionals by means of experience or existing empirical solutions that fall short in sufficiently capturing the interacting processes of the solid and liquid masses.

## 2.3. Analysis of flow slides

Flow slide studies so far mostly rely on empirical approaches that apply to specific circumstances only and use considerable simplifications. In order to investigate quantitatively the susceptibility of a sand slope to flow sliding, modelling activities are required (analytic, numerical solutions or physical modelling). Soil behaviour is classically studied by means of constitutive models that are tuned on geotechnical investigation tests. Investigation test results include quantitative estimations of geotechnical parameters (possibly affirmed in engineering practice). Desk study and site investigation activities are therefore necessary. Preliminary investigation should provide estimates for:

- the type of soils and their stratification;
- the groundwater table or pore pressure profile;
- the preliminary strength and deformation properties for soils;
- the potential occurrence of contaminated ground or groundwater.

Desk study activities are undertaken in order to collect the already available datasets for the geotechnical parameters first estimation from:

- topographical maps;
- old city maps describing the previous use of the site;
- geological maps and descriptions;
- engineering geological maps;
- hydrogeological maps and descriptions;
- geotechnical maps;

- aerial photos and previous photo interpretations;
- previous investigations at the site and in the surroundings;
- previous experiences from the area;
- local climatic conditions.

The more information that is available in an initial stage, the more accurately and easily will be predicting the geotechnical profile of the site. Additional in situ or laboratory tests on undisturbed or reconstructed samples are often necessary. Eurocode 7 [9] provides some suggestions about the type of test and spatial density of the sampling. For sands it can be very challenging and expensive to collect undisturbed samples. For example, one can use ground freezing techniques to attempt undisturbed sampling, but in practice it is more frequent to reconstruct the sample in the laboratory and trying to reproduce the in situ conditions previously investigated by CPT tests or other in situ investigation tests. Test execution and monitoring activities require special care. A detailed assessment of the geotechnical parameters helps to describe with accuracy the physical processes involved. Codes and guidelines often include standard procedures (protocols) for testing. Standard procedures increase the probability of reproducibility for the test.

The stability of a slope, also in the special case of flow slides, is often assessed by means of LEM analyses, as they represent a fast algorithm to find a solution to a problem which has no analytical solution. Alternatively, the FEM with strength reduction protocol can be used. This analysis reduces the number of assumptions to find a solution and automatically detects the path of minimal resistance, beside providing visualizations of stress-displacement fields over the whole model. Sections 2.4 and 2.7 respectively describe alternative methods for slope stability and for large deformation problems in more detail.

## 2.4. Alternative methods for slope analysis

Flow slides always originate from local instabilities of slopes. In Europe, submerged sand slope designs as well as all other geotechnical designs are ruled by the Eurocode 7 [9] by means of the limit state design philosophy. Eurocode 7 does not prescribe a specific inequality for slope stability analyses. Instead, it requires verification of the overall moment and vertical equilibrium of the sliding mass. However, it indicates that the inter-slice forces should be considered acting horizontally, if not assessed more rigorously. This implicitly rules out the use of certain slope stability analysis methods (e.g. the Method of Slices).

Classic engineering approaches include limit equilibrium methods such as Bishop, Fellenius and Spencer. Because of these relatively loose criteria, erosion and sedimentation processes are often modeled on the basis of empirical relations rather than a consistent continuum mechanical description or on the basis of rigorous mathematical descriptions (through the use of advanced numerical and complex analytical models). More detailed analyses are typical of industrial processes and are performed with advanced Computational Fluid Dynamics (CFD) methods not commonly applied in geotechnical practice (e.g. DEM, SPH, OpenFoam). More details will be given in CFD methods for submerged flow slides (Section 2.7).

The main limitation of LEM regards the definition of safety, as it strongly depends on the assumptions made for the slip surface [22, 26]. Further, failure is defined as occurring when the shear strength required to guarantee the slope equilibrium is equal to the soil shear strength. This failure criterion, however does not directly imply a loss of functionality of the structure. A detailed review of limit equilibrium methods is reported by Duncan[17].

In order to overcome some limitations of LEM, it is possible to model the slope material stress-strain behavior with numerical methods. The FEM is an advanced methodology that has significant advantages for the analysis of slope stability: the shape and location of the slip surface are not predefined, and are automatically found; the analysis provides insight into the initiation of failure and failure mechanism; it allows using complex models for the stress-strain behavior of the soil [19, 22, 26]; failure definition is not limited by the strength criteria but may include displacement criteria (or non-convergence of the solution) [22]. In FEM, slope failure and numerical non-convergence often occur simultaneously, and are accompanied by a major increase in the nodal displacements within the mesh. This leads to problems related to mesh distortion (negative determinant of Jacobian matrix for the mapping) that prevent the use of FEM for post-failure analysis of slopes. This means that, although the FEM is an appropriate tool to analyze slopes up to the moment of initial failure, the behavior following this initial failure cannot be described in the same framework.

In the attempt of overcoming the limitations of FEM, discrete and continuous mesh-free methods have been developed for addressing the problem of large deformations. However, discrete modeling methods involve numerous averaging assumptions while simulating soils because of the tens of thousands grains that constitutes the smallest sand sample for element testing [23].

In continuum frameworks, such as in the MPM, the material can be modeled using a collection of Lagrangian points (material points) interacting with an Eulerian (fixed) background mesh. These points carry all the continuum properties, including mass, stress, strain, and material parameters. The discrete equations for momentum balance are obtained and solved on the background mesh similarly to the FEM with an updated Lagrangian formulation. As a result, MPM integrates features of both Lagrangian and Eulerian formulations. This approach avoids issues of mesh distortion under large deformations and eliminates the diffusion effects typically linked to the convective terms in Eulerian methods [42, 43].

The use of Lagrangian MPs ensures mass conservation and allows the use of complex history dependent stress-strain material models. The MPM has been successfully used for geomechanics problems involving slope stability e.g. [15, 20, 40, 55]. In particular, [15] successfully simulated an experimental liquefaction flow slide with Anura3D [3]; therefore this thesis focuses on retrogressive breaching events.

To date, no coupled numerical approach has been validated for simultaneously modelling the deformation of water-saturated soil, the flow of free-surface water, and the transition between them in flow slide analyses.

## 2.5. Laboratory experience

Researchers Joana Silva and Said Alhaddad from the MPM-Flow project conducted extensive laboratory testing of sand column collapse experiments in instrumented water tanks, and among these experiments, those performed at Utrecht University [38]. These experiments indicate what parameters are important for the mechanical interpretation of the results, confirming the findings of You 2013 [54].

In particular, the experiment result shown in Figure 2.5 indicates how the dilatancy of soil strongly influences the failure mode when considering saturated sand. The sand used for this experiment is fine uniformly graded silica Geba sand BR37 with an average diameter $d_{50} = 140$ $\mu$m and a fines content well below 10% of its mass. The sand column is exactly 40 cm long and 22 cm wide, due to the tank walls dimensions; the soil column mass was estimated in advance so as to give a sand column height of about 40 cm after compaction. The sand was pluviated in wet conditions and manually compacted in layers of about 5 cm. The void ratio $e$ after compaction equals 0.785, corresponding to a 71.35% relative density and a value of porosity of 0.44.

After preparation of the experimental setup, the lateral confining wall is suddenly lifted (Figure 2.5-c), so that the sand column is suddenly loaded by its tendency to spread laterally because of its self weight. This tendency, when considering fully saturated sand, is translated in a sudden increase in suction, as visible by the pore pressure evolution in time shown in Figure 2.6. This peak in suction slowly dissipates as ambient water flows into the sand body. It's dissipation rate depends on the local porosity of the sand and pressure gradient. Because the sand particles at the interface between the compacted sand and the ambient water are unconfined on one side, these will rain down due to gravitational forces and result in an accelerating debris flow, often referred to by literature on this topic as a turbidity current. The turbidity current contributes to the erosion of the bed, increasing the overall erosion rate at the base of the slope, often resulting in undercutting geometries that favor sliding events of sand, as visible in Figure 2.5-d. As the RBF reaches the sensor location, the hydro-static pressure is re-established, as indicated by 0 kPa in Figures 2.6.

Interestingly, after about 135 seconds from the beginning of the experiment, a hydraulic jump occurs at the location of the pore pressure sensor indicated with a black square in Figure 2.5-e. The hydraulic jump arises from the super-critical flow of water and sediments mixture having an almost vertical trajectory, thereby decelerating on the developing gentler slope at the toe of the sand column. This local phenomenon leaves a unique signature on the pore pressure evolution: a slow positive pressure build up followed by dissipation with a similar rate in magnitude but opposite in sign. The incoming flow of sediments from the collapsing column gently deposits at its base. This process generates a developing slope, that slowly increases with respect to its angle and height. The local slope so formed is in a loose state compared to the sand column, and is therefore susceptible to sand liquefaction.

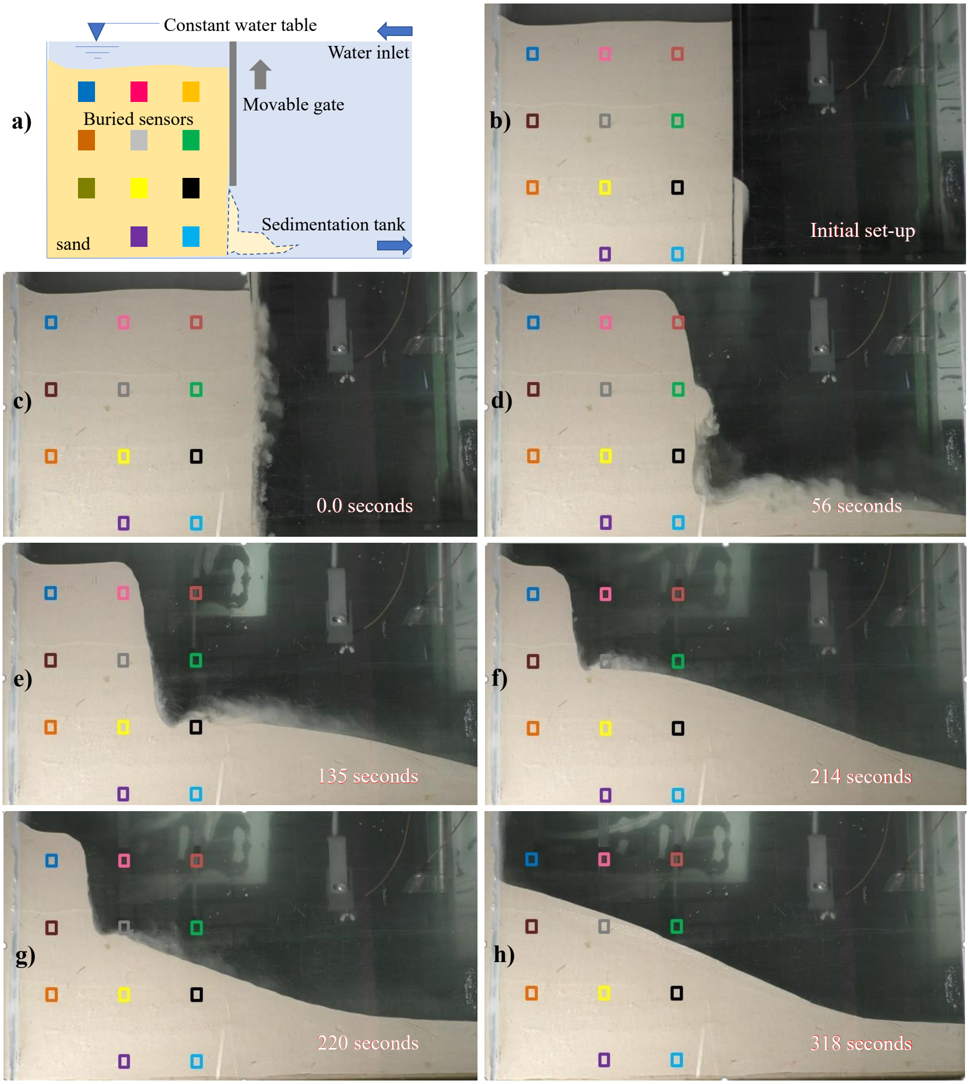

Figure 2.5: Schematic sketch of experimental setup and screenshots from sand column collapse experiment in instrumented water tanks with buried pore pressure transducer sensors from [38].

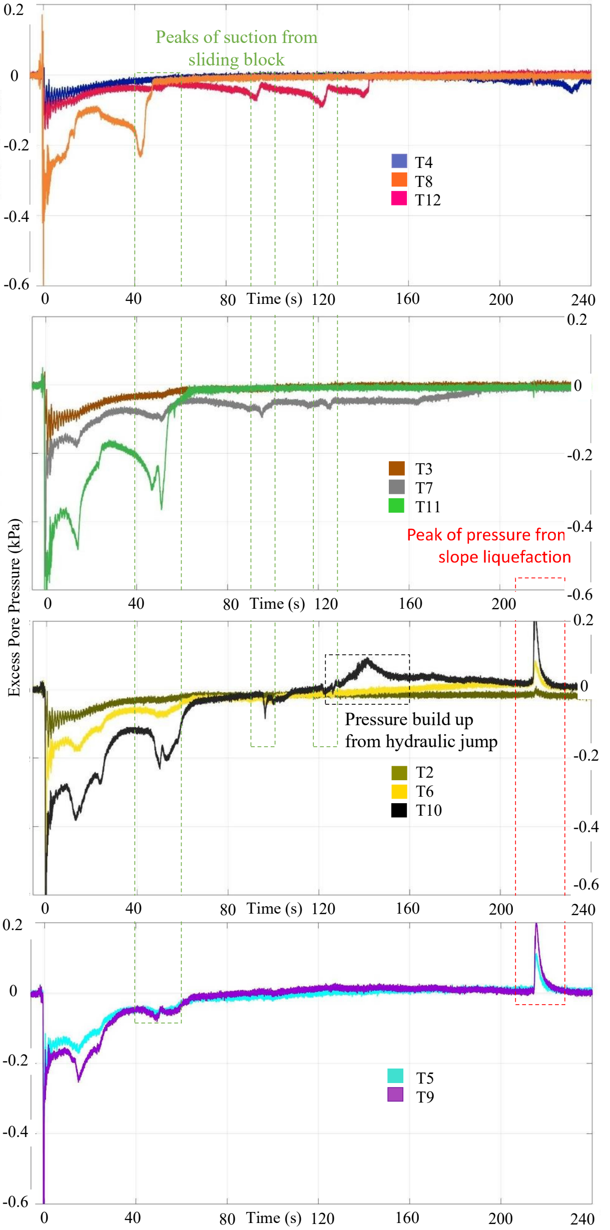

Figure 2.6: Pore pressure transducer results and interpretation of the column collapse experiment presented in Figure 2.5 from [38].

As this slope reaches a critical height/angle, it collapses in a rapid fashion, as seen by comparing the geometry and time of Figure 2.5-f and 2-g. This liquefaction flowslide occurs in just 6 seconds, mobilizing relatively large sand volumes downslope until reaching a new equilibrium configuration. The liquefaction flowslide also leaves a distinct signature on readings from the sensors buried in dense lower layers of sand. This signature is characterized by a sudden pressure increase followed by a slow dissipation. The RBF terminates once the local steepening of the sand slope evolves up to an angle of repose shallower than the friction angle of the sand.

## 2.6. Computational models in geotechnics as interpretation frameworks

A computational model can fulfill many purposes, such as testing hypotheses, uncovering new insights, enhancing understanding, guiding and interpreting experiments, performing sensitivity analyses, supporting optimization, integrating existing knowledge, and inspiring novel approaches [45]. Computational modelling of geotechnical phenomena generally follows one of two different approaches: discrete element methods and continuum mechanics. Continuum mechanics is a mathematical interpretative framework introduced in the 19th century by Augustin-Louis Cauchy for studying the transmission of forces through and deformation of all material types. It is considered advantageous to adopt this framework because it enables using the mathematical tools of continuous functions such as differentiation.

Opposite to discrete element descriptions, continuum mechanics uses representative and statistical elementary volume concepts and returns a homogeneous description of the space in analysis. Although there is no continuum material in nature from physical observations, this approximation results in accurate solutions for a wide range of problems. Since the introduction of the continuum mechanics framework, it has been wildly applied in all the fields of science due to its success. Although there are certain problems in which it is necessary to take in account of the discrete nature of the materials, the ultimate justification for using continuum mechanics is that predictions are often in agreement with observation and measurements. Its application requires mathematical descriptions (idealization) of the material response. If the formulation of the problem is well posed, it allows reliable predictions and (maybe more importantly) a clear interpretation of the results.

To thoroughly understand and quantify physical phenomena—such as structural or fluid behavior, thermal transport, wave propagation, or biological cell growth—mathematical formulations are essential. These processes are most often represented by Partial Differential Equations (PDEs). Over the past several decades, numerical methods have been developed to solve such equations, with Finite Element Analysis (FEA) emerging as one of the most prominent approaches. From a historical perspective, the roots of FEA can even be traced back to Euler's work in the 16th century. However, the earliest mathematical papers on Finite Element Analysis can be found in the works of Schellbach [37] and Courant [11]. In the last 50 years, many resources have been spent in research to develop advanced numerical methods for geo-engineering applications, although the most frequent applications include the assumptions of small deformations and simple constitutive models. Nowadays, applications concerning structural and material failures more often involve large deformations and complex constitutive models by using modern computational techniques [36]. Large deformation problems are of great interest and concern in geomechanics (i.e. landslides, scouring, liquefaction etc.), not only to analyse the structure up to the moment of failure, but also to hypothesize beyond it (i.e. what is the residual function of the structure after failure). The main challenge with large deformation problems is satisfying the requirements of the numerical methods necessary to approximate the solutions. The principal criteria here considered to appraise computational models are:

1. level of description;
2. completeness;
3. cost and ease of use;
4. range of applicability;
5. accuracy.

The level of description is an index that describes the phenomena in terms of parameter number needed in an analysis. Completeness is an index that describes how many problem dependent specifications are necessary to find a solution. A model is deemed complete when it requires no additional specifications. The suitability of a particular computational model depends upon a weighted combination of the above discussed criteria. This means that there is no "best model", but rather a set of models that can be usefully applied to a broad range of flow problems.

Discrepancies between measured and calculated properties can arise from:

1. inaccuracies of the model;
2. numerical errors;
3. measurements errors;
4. discrepancies in the boundary conditions.

When saturated soil masses are sheared, their displacement field resembles that of a viscous fluid. Hence CFD provides the fundamentals to analyse flow slide problems.

## 2.7. Large deformations methods for submerged flow slides

In the 1960s the T3 group, based in Los Alamos National Laboratory, led by Francis H. Harlow, worked on Galerkin methods implemented in calculators applied to large deformation problems and set the basis for most of the CFD methods available today. The basic governing equations of CFD methods are usually conservation equations (i.e. mass conservation, momentum conservation, etc.), frequently called Navier-Stokes equations for the special case of fluid flows. The solution of these boundary value problems allows analysing and visualizing deformation problems for a wide range of physical problems, including the mechanical interpretation of solid and fluid phase material behaviour. Traditionally, and for sake of simplicity, soil and fluid mechanics courses are separate disciplines in engineering educational programs. Additionally, a solution which is based on interfacing geo-technical engineering and the physics of fluids is not straight forward.

Geo-mechanical problems require a Lagrangian description of material deformations in order to account for the nonlinear history dependent stress-strain response of soils, and the widely used FEM is commonly used for their solution. CFD software more frequently follow an Eulerian approach by using a finite difference or finite volume scheme. These methods are typically better suited for the simulations of fluid flows, but they have shortcomings in handling deforming boundaries. Combining such differing approaches often causes numerical inaccuracies.

Assuming in advance which method is more performing (”better than others”) shows some short comings in our ability to understand the problem in analysis, especially without taking into consideration the geometrical and mathematical features and the required accuracy of the results. Nevertheless, a qualitative comparison is possible. For example, FEM often encounters problems of tangled meshes, reducing its applicability mainly to small deformation problems.

Conversely, FVM and other pure Eulerian methods handle well large deformation problems (such as flow problems), but often model saturated soils as viscous fluids and this requires strong assumptions about triggering mechanisms for slope failures and more generally about the modeling of boundary conditions. In addition, these methods are less suited to deal with sharp interfaces since being diffusive. FEM and FVM allow for unstructured meshes, which is an important requirement for high accuracy forecast and to be adaptable to complex geometries.

Alternative CFD modelling procedures allow getting rid of completely the mesh discretization from the analyses, as in the case for SPH, which is one of the earliest purely Lagrangian methods, better suited to model large deformation problems. However, SPH is known for being computationally expensive because of the neighbor particles searching algorithm and it also suffers from tensile instability [28].

In recent years, significant progress has been achieved in the numerical analysis of coupled problems involving large deformations in water-saturated soils through the use of the Material Point Method (MPM) [2, 4, 40, 51, 56]. MPM is an arbitrary Lagrangian–Eulerian technique that combines material point (MP) discretization with a standard finite element computational grid to represent dynamic, history-dependent continuum bodies. The collection of MPs represents the body under consideration, carrying all physical properties and external loads. In contrast, the finite element mesh and its Gauss points hold no permanent information; they are employed solely for computation.

At the beginning of each time step, the physical properties are transferred from the MPs to the mesh nodes, ensuring implicit conservation of mass. This mixed Lagrangian–Eulerian framework inherently accounts for material separation, gap-

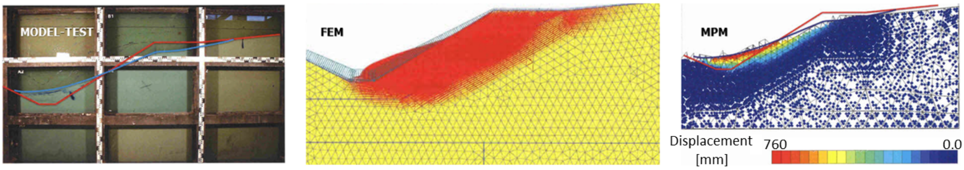

Figure 2.7: Pictures from [41]. Final geometry of a sand slope as a result of a flow slide laboratory test (on the left) and comparison with FEM (middle) and MPM (right) simulations.

ping, and erosion-like processes. It also provides a straightforward formulation for soil–structure and water–structure interactions. To achieve reliable results, the MPs must represent volumes small enough for averaged properties to approximate local variables, yet large enough to render fluctuations within those volumes negligible. The incremental solution of governing equations follows the principles of conventional Lagrangian finite element methods. After each time step, the computed solution is mapped back to update the MPs' information, and the computational mesh is reset to its original configuration [2].

These characteristics make this software a very good candidate for solving most geotechnical problems that involve large deformations and multi-phase fully coupled historical dependent materials. One should remind oneself that MPM, as with any other numerical method, is just a tool to conveniently solve PDEs: any tool is only as good as its user!

## 2.8. Anura3D formulation

As a starting point, heat effects or any source of thermal energy is disregarded and the mechanical work is the only considered source/sink of energy. The code has already implemented highly non-linear, density dependent, strain softening constitutive models (i.e. Hypoplastic, NorSand, ModCamClay, etc.), which are well suited to modelling granular materials. Anura3D, which employs an explicit time integration scheme, has been extended to perform fully coupled two-phase analyses. This approach has proven effective for simulating erosion and sediment transport problems [52], allowing soil with pore water flow, fluidized soil, and the transitions between these states to be modeled within a unified numerical framework [8]. However, calibrating and applying these features requires significant enhancement of the existing code.

The collection of applications presented in this Thesis promises a successful extension and validation of Anura3D for flow slide phenomena. Nevertheless it represents just a partial validation, since crucial aspects of flow slide phenomena have not yet been fully investigated (i.e. erosion, sedimentation, mass exchange between mixture and free water, segregation, etc.).

The MPM implementation of Anura3D is also known to be dissipative, although the energy dissipation resulting from numerical errors usually compensates for the apparent energy loss due to thermal exchange (or more in general neglected physics from the mathematical description of the problem). Although several turbulence models are already available in the literature, Anura3D has not implemented any of them yet.

## 2.9. Anura3D one-phase single-point formulation

### 2.9.1. Governing equations

In Anura3D the governing equations describe the motion of the considered bodies. These are conservation equations of mass (Eq. 2.1) and momentum (Eq. 2.2), more commonly known as the Navier-Stokes equations in CFD:

$$\frac{\partial \rho}{\partial t} + \rho \nabla \cdot \mathbf{v} = 0 \tag{2.1}$$

$$\rho \mathbf{a} = \nabla \cdot \sigma + \rho \mathbf{g} \tag{2.2}$$

where $\rho$ is the material density, $t$ is time, $\mathbf{v}$ is the velocity, $\mathbf{a}$ is the acceleration, $\sigma$ is the Cauchy stress tensor and $\mathbf{g}$ is the body force exerted, for example, by gravity. The Cauchy stress tensor can be decomposed into $\sigma = p + \sigma_{dev}$, where $p$ is the material pressure and the subscript $(_{dev})$ indicates the deviatoric component of the Cauchy stress tensor. For fluids, which is relevant for the next chapter where water flows are analyzed, it is possible to introduce the dynamic viscosity $\mu$ by defining $\sigma_{dev} = \mu \dot{\varepsilon}_{dev}$, where $\dot{\varepsilon}_{dev}$ is the shear strain rate.

Considering weakly compressible fluids, the mass density is related to the fluid pressure as:

$$\frac{\partial \rho}{\partial t} = \frac{1}{c}\frac{\partial p}{\partial t}; \qquad c = \sqrt{\frac{K}{\rho}} \tag{2.3}$$

where $c$ is the compression wave velocity and $K$ is the bulk modulus of the fluid.

The nonlinear convective term is not present (in Eq. 2.2) as a result of the Lagrangian framework [43]. Instead, the positions of the MPs are updated each time step.

### 2.9.2. Numerical algorithm

The governing equations are discretized in space and time using “standard” FEM techniques. A mixed Gauss algorithm is used, in which integration is at the element’s Gauss point locations for a fully filled element, and at the material points for partially filled elements, e.g. at fluid free-surfaces. This leads to smoother stress fields and mitigates some effects of grid crossing errors [2]. Tetrahedral elements with linear shape functions are used here.

MPM requires an additional solution domain discretization compared to FEM, that consists of a cluster of MPs. It is assumed that each MP corresponds to a fixed mass representative volume of the continuum body $\Omega$, with the initial volume $V_p^0$, where the superscript $(^0)$ indicates the time step and the subscript $(_p)$ indicates the MP values, and it is calculated as:

$$V_p^0 = \frac{1}{n_{ep}} \int_{d\Omega_e} d\Omega \approx \frac{1}{n_{ep}} \sum_{q=1}^{n_{eq}} w_q |\mathbf{J}(\mathbf{x}_q)| \tag{2.4}$$

where $n_{ep}$ is the number of material points per element, $n_{eq}$ is the number of integration points (i.e. Gauss points or MPs) per element, $d\Omega_e$ is the volume associated with the $e^{th}$ tetrahedral element, so that $\Omega = \bigcup_{el=1}^{n_{el}} \Omega_{el}$, $w_q$ is the local integration weight associated with the integration point $(_q)$, $\mathbf{J}$ is the Jacobian matrix, and $\mathbf{x}_q$ is the position vector.

Information can be mapped between points and nodes by linear interpolation with the same shape functions used for the mapping between global and local coordinate systems. This process is done in fully filled elements to map information to the integration point locations prior to numerical integration. For example, when mapping information between nodes and MPs, a displacement field **u** can be written as:

$$\mathbf{u}_p(\mathbf{x}_p) \approx \mathbf{N}_j(\mathbf{x}_p)\mathbf{u}_j(t) \tag{2.5}$$

in which the subscript $(_j)$ indicates the nodal values and **N** is the interpolation function (from the combination of linear shape functions of the nodes evaluated in the global coordinate system). The same interpolation can be applied for other quantities (i.e. acceleration, mass, stress, etc.).

The details of the mathematical framework, including a description of the computational cycle can be found in, e.g., [10]. Using the constitutive equation (Eq. 2.3) and the standard finite element method (FEM) spatial discretisations, the weak form of the momentum balance equation (Eq. 2.2) can be written as:

$$\mathbf{M}_j^t \mathbf{a}_j^t = \mathbf{F}_j^{int,t} + \mathbf{F}_j^{ext,t} \tag{2.6}$$

where **M** is the lumped mass matrix, $\mathbf{F}^{int}$ and $\mathbf{F}^{ext}$ are the internal and external nodal forces and **a** is the vector of nodal accelerations. These are respectively defined as:

$$\mathbf{M}_j^t = \sum_{j=1}^{n_n} \sum_{q=1}^{n_{eq}} \mathbf{N}_j(\mathbf{x}_q) m_q \Big|_t \tag{2.7}$$

$$\mathbf{F}_j^{int,t} = \sum_{j=1}^{n_n} \sum_{q=1}^{n_{eq}} \mathbf{B}_j^T(\mathbf{x}_q) \sigma_q V_q \Big|_t \tag{2.8}$$

$$\mathbf{F}_j^{ext,t} = \sum_{j=1}^{n_n} \sum_{q=1}^{n_{eq}} m_q \mathbf{N}_j(\mathbf{x}_q) \mathbf{g} \Big|_t + \sum_{j=1}^{n_n} \mathbf{f}_j^{ext} \Big|_t \tag{2.9}$$

where **B** is the strain-displacement matrix, $\mathbf{f}_j^{ext}$ are the prescribed boundary nodal tractions, $n_n$ is the number of nodes per element and $m_q$ is the mass associated with the integration point under consideration.

The general MPM explicit numerical algorithm is as follows:

1. Map the information carried by the MPs to the background mesh using linear shape functions;
2. Determine the lumped mass matrix (Eq. 2.7), the internal force $\mathbf{F}^{int}$ (Eq. 2.8) and external force $\mathbf{F}^{ext}$ (Eq. 2.9) vectors at the nodes;
3. Compute the nodal acceleration field from (Eq. 2.6), imposing zero acceleration at the inflow nodes (see Fig. 3.1a);
4. MP velocities are updated using the nodal acceleration as:

$$\mathbf{v}_p^{t+1} = \mathbf{v}_p^t + \Delta t \sum_{j=1}^{n_n} \mathbf{N}_j(\mathbf{x}_p)\mathbf{a}_j^t \tag{2.10}$$

5. The MP positions are updated:

$$\mathbf{x}_p^{t+1} = \mathbf{x}_p^t + \Delta t \sum_{j=1}^{n_n} \mathbf{N}_j(\mathbf{x}_p)\mathbf{v}_j^{t+1} \tag{2.11}$$

6. The incremental MP strains are calculated as:

$$\Delta\varepsilon_p^{t+1} = \mathbf{B}(\mathbf{x}_p)\Delta\mathbf{u}_j^{t+1} \tag{2.12}$$

7. The stresses are derived from the constitutive relation (Eq. 2.3);
8. Determine the density of the MPs, which is used to update the MP's volumes, as:

$$\rho_p^{t+1} = \frac{\rho_p^t}{1 + \Delta\varepsilon_{vol,p}^{t+1}} \tag{2.13}$$

   where $\varepsilon_{vol,p}^{t+1}$ is the incremental volumetric strain.

In order to solve the system of governing equations, it is possible to distinguish three kinds of BCs: essential (Dirichlet, displacement), natural (Neumann, force) or a linear combination of the two (Newton/Robin). Other state variables, i.e. initial velocities and pressure in this case, also need to be initialised. Further, strain and pressure smoothing procedures can be used to mitigate the stress oscillations due to grid crossing [30].

The critical time step should satisfy the so-called *Courant-Friedrichs-Levy (CFL)* condition [12], meaning that the time increment should not exceed a certain value depending on material density, stiffness and the minimum size of the elements in order to ensure the stability of the explicit integration scheme:

$$\Delta t_{crit} = \frac{l_e}{c_p} \tag{2.14}$$

where $\Delta t$ is the critical time step, $l_e$ is the minimum length of the element. In our study, a reduction factor $\alpha_{Courant}$ is introduced in the above expression to obtain the time step size (i.e. $\Delta t = \alpha_{Courant} \times \Delta t_{crit}$).

## 2.10. Two-phase single-point formulation

When considering the interaction between the solid phase and the liquid phase components in a saturated porous material (i.e. soil), the MPM implementation requires a hydro-mechanical coupling. Anura3D includes two distinct approaches, the two-phase single-point and the double point formulations [21]. Both approaches in the current implementation consider weakly compressible fluids, although in the single-point approach, the behaviour of the saturated porous media is led by the kinematics of the solid skeleton, while the liquid volume is described with respect of the solid motion. Each MP represents a saturated soil volume $V_{MP}$ carrying the information of both phases:

$$V_{MP} = V_S^{MP} + V_L^{MP} \tag{2.15}$$

where the subscripts S and L refer to the solid and liquid phases, respectively.

In this formulation, the solid mass per material point (MP) remains constant during the computation, while the total MP mass may vary due to liquid inflow or outflow. This assumption is valid when porosity gradients are relatively small but introduces errors—dependent on the accuracy of the liquid mass balance—when materials with differing porosity come into contact. Spatial variations in density and porosity are neglected, and soil grains are treated as incompressible.

The liquid flow is assumed to be laminar and stationary within the low-velocity regime, with the interaction between solid and liquid phases governed by Darcy's law. Both the liquid's dynamic viscosity and its intrinsic permeability are considered constant, and shear stresses in the liquid phase are neglected. According to Terzaghi's theory [47], the mechanical behavior of the soil skeleton is described in terms of effective stresses.

### 2.10.1. Governing equations

In the two-phase single-point formulation, the governing equations consist of the dynamic momentum balance of the liquid phase, the dynamic momentum balance of the mixture, the mass balance equations, and the constitutive laws of both phases. As a result, all dynamic terms are considered, with the accelerations of the solid skeleton $a_S$ and the pore liquid $a_L$ serving as the primary unknowns.

The dynamic momentum balance equation for the mixture can be written as:

$$n_S \rho_S \mathbf{a}_S = \nabla \cdot \sigma + (n_S \rho_S + n_L \rho_L)\mathbf{g} \tag{2.16}$$

where $\rho_S$ and $\rho_L$ are the solid and liquid density, while $n_S$ and $n_L$ are the volumetric concentration ratio of the solid and the liquid phases, respectively. The dynamic momentum balance equation of the liquid phase per unit of liquid volume can be expressed as:

$$\rho_L \mathbf{a}_L = \nabla p_L - \mathbf{f}_L^d + \rho_L \mathbf{g} \tag{2.17}$$

where $\mathbf{f}_L^d$ is the drag force, and $p_L$ is the liquid pressure. For a more detailed explanation of its numerical implementation, please refer to [21].

### 2.10.2. Main features

Besides the above mentioned formulations implemented in Anura3D, what makes this software implementation particularly suitable to geotechnical applications is the possibility to use advanced constitutive models for soil that account for the critical state soil mechanics theory [53], often referred to as steady state soil mechanics theory. Additionally, Anura3D offers several analyses tools that are useful to describe the construction stages of geotechnical problems such as excavations, loading conditions (drained or undrained) and loading procedures (gravity loading and K0 procedure).

The constitutive models selected in this dissertation, for describing soil behaviour features typical of large deformation problems, have been chosen with increasing degree of complexity, from the simplest to the more advanced, with the aim to contain the computational cost of the analyses. Linear elastic constitutive models are frequently used in feasibility studies and in the preliminary phases of nonlinear analyses to gain confidence in the selected modelling approach.

The application of linear constitutive models is particularly evident in an academic environment for educational purposes. But also in engineering practice, in order to reduce the costs associated with nonlinear analyses, the design often follows just the linear analyses by applying high coefficients for safety so that the nonlinear analysis would be redundant. The high coefficients of safety however hinders the assessment of the resisting mechanisms of a structure, and hence its constituent materials' mechanical performance. Furthermore, in order to simulate a failure, a nonlinear analysis becomes necessary.

Once more, for simplicity, linear elastic perfectly plastic constitutive models, such as the Mohr-Coulomb model, are frequently used in engineering practice to assess the stability of a soil structure as it is capable to model the ultimate strength of the material. However the ability of such simple constitutive models to model real soil behavior is limited. Especially when dealing with hardening or softening materials subjected to large strains, constitutive models that take account of gain/losses of material strength at large deformations become necessary, as will be shown in Chapter 5 of this dissertation.

Because flow slides may occur in dense sands, as previously discussed in Section 2.2.2, the necessity for a more advance constitutive model led the author to select the Mohr-Coulomb strain-softening (MCSS) model. This constitutive model was selected because it requires a relatively small number of input parameters and with a clear physical meaning. These parameters are the peak and residual values of friction angle, cohesion and dilatancy, plus the $\eta$ parameter that controls the softening behaviour.

Conveniently, the softening behaviour expires when the strength parameters reach their residual values, allowing the material mobilized to flow at a lower resistance than the rest of the soil body. This behaviour allows the generation of preferential surfaces of shear, similar to what is observed in soil laboratory and field experiments. It also suppresses the generation of excess water pressure when large strains are reached, allowing the soil body to find a new equilibrium configuration. However, the thickness of the shear bands have the same size as the element where they take place. Hence the results of models that employ the MCSS model are mesh dependent and a regularization technique should be used [35].

Among other features that contributed to the preference for Anura3D for this research project, the 'excavation tool' allows removing MPs from the computational domain, mimicking in the numerical model the excavation process that would occur in physical models. However, the MPs are removed instantaneously, so that the full process is not described in detail, but it yields acceptable results as first approximation of the solution for many geotechnical problems such as deep excavations and undercutting of slopes.

## 2.11. CUR113 guidelines, Eurocode 7 and PERC

In the Netherlands, the "best practices" for under water sand slopes in quarries are described by the CUR113 [16]. These recommendations are based on the results of soil surveys, analysis of the failure mechanism and risk considerations. Although the European Commission took the initiative to establish a set of harmonized technical rules for designing construction works, these rules were initially intended as an alternative to the national regulations in force in Member States and were ultimately meant to replace them. Hence, geotechnical design practices are ruled by Eurocode 7 [9] by means of the limit state design philosophy.

According to these guidelines, slope design must demonstrate that ground deformations will not require a serviceability limit state in structures or infrastructure located on or near the analyzed ground. This requirement arises because available numerical methods generally do not provide reliable predictions of deformations in natural slopes. To prevent the need of serviceability limit states, one of the following measures should be applied:

1. Limiting the mobilised shear strength;
2. When the prediction of geotechnical behaviour is difficult, observing the movements and specifying actions to reduce or stop them, if necessary (i.e. use the "Observational Method", in which the design is reviewed during construction).

The calculation model may consist of any of the following: an analytical model; a semi-empirical model; a numerical model. Any calculation model shall be either accurate or err on the side of safety. Results of computational models should include the range of uncertainty in the results of the method of analysis and any systematic errors known to be associated with the method of analysis. Numerical methods can be appropriate if compatibility of strains or the interaction between the structure and the soil at a limit state are considered. The selection of characteristic values for geotechnical parameters shall take account of the following. These prescriptions are directly taken from Eurocode 7 [9]:

- geological and other background information, such as data from previous projects;
- the variability of the measured property values and other relevant information, e.g. from existing knowledge;
- the extent of the field and laboratory investigation;
- the type and number of samples;
- the extent of the zone of ground governing the behaviour of the geotechnical structure at the limit state being considered;
- the ability of the geotechnical structure to transfer loads from weak to strong zones in the ground.

The costs associated with the use of advanced numerical methods is generally justified for high consequence class (e.g. CC3, very high risk) structures which are generally associated with complex design situations (Geotechnical Category, GC3). In the latest generation of Eurocodes, partial safety factors for actions and resistances are directly linked to these Consequence Classes. Hence, Consequence Classes help guiding the designer in deciding the appropriate level of conservatism and intensity of ground investigations. Decisions are often made with simplistic models, minimum soil data and with relatively high uncertainty, hence use high factors of safety. Establishing a widely available, cheap and consistent assessment tool for large deformations geotechnical safety assessments (e.g. slope failures), promises to sharpen the design of high Consequence Class and Geotechnical Category problems and also to decrease the uncertainties related to quantitative forecasts of consequences of failure and improvement of current design standards.

However, the application of such advanced numerical solutions is not only relegated to CC3 structures. For example, adopting the terminology of the PERC International Reporting Standards 2021 [1], in the mining industry, there is a need to reduce the risk concerning the selection of appropriate Modifying Factors for the quantification of Mineral Reserves, among others (see Figure 2.8). The Modifying Factors depend upon the level of understanding of each relevant element. A clear and demonstrable relationship between the project context and the identified factors must be established. The depth and scope of analysis should be proportionate to the project's stage of development, with any data gaps explicitly identified and disclosed. Variations in Environmental, Social, and Governance considerations may

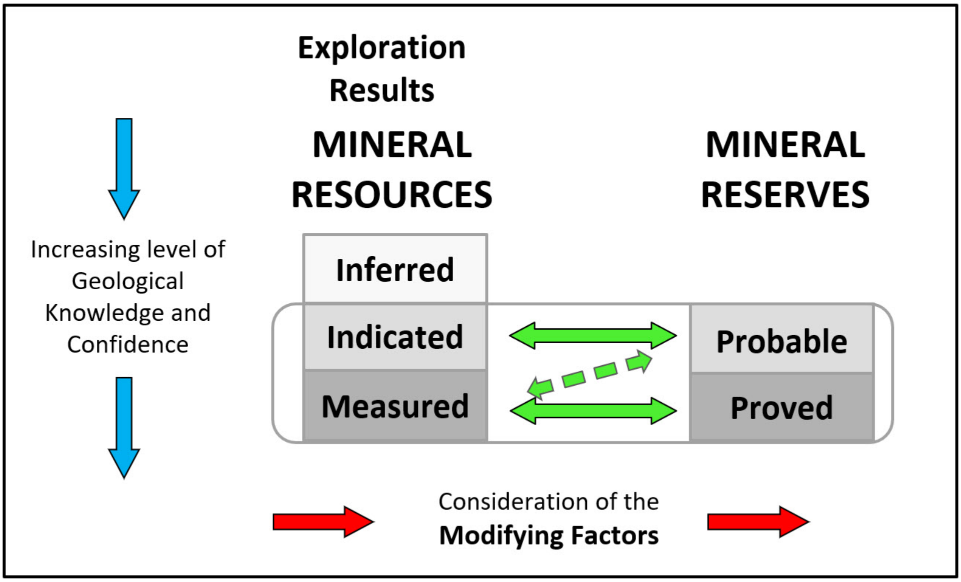

Figure 2.8: The general relationship between Exploration Results, Mineral Resources and Mineral Reserves according to the Pan-European Reserves and Resources Reporting Committee's (PERC 2022) guide to public reporting for mineral companies in Europe [1].

independently constitute, or contribute to, material changes that significantly influence the project schedule, capital and operating costs, and potentially the overall feasibility of project advancement. Accordingly, the uncertainties associated with the Modifying Factors should be systematically evaluated and transparently addressed in the reporting of Mineral Resources and Mineral Reserves. Therefore advancing the methodology for slope safety assessments does not only represent a technical solution but also a legal one, including in CC1 sand quarries.

## 2.12. Summary

In the first part of this chapter, flow slide phenomena are defined by means of a typological classification based on widespread definitions in geotechnical engineering by [24]. Then the possible triggering mechanisms and physical onset processes are described. Dutch and European ruling codes for site investigation and the assessment of geotechnical parameters are indicated and commented.

The second part of chapter describes the literature review of the numerical method for the analysis of flow slides. The alternatives to the MPM method as well as the successful applications of MPM are listed from existing literature and the main feature and assumptions are highlighted. The results from this literature review are useful to identify an MPM formulation for an accurate, cheap, consistent visualization of the hydro-mechanical stress-displacement fields for a sand flow slide, from initiation of the failure up to deposition of the sediments.

The author's conclusion is that Anura3D is a promising and robust investigation tool, and it is considered a valid support for the analysis of geotechnical large deformation problems at the engineering scale. However, there is limited literature about the robustness, advantages and limitations of Anura3D when applied to soil and water interaction problems. The lack of well established benchmarks hinders the quantitative assessment of the numerical solutions errors. For rigorous validation, verification activities are first recommended in order to ensure that the software implementation is doing what it is intended for. Unfortunately this requires analytical solutions that are available for a very small number of problems.

Once the modeller has built confidence in his modelling strategies, he may attempt validation against more complex experiments that, in flow-slide case studies, are challenging due to the lack of similarities among experiments. To further complicate the validation procedure, one has to account for the different scales at which the phenomena take place (time scale, geometrical scale). From a physical perspective, there is no investigation protocol to analyse flow-slide phenomena because of the intrinsic variability of the material involved and difficulties of having accessible and reliable investigation tools. This is particularly challenging for simultaneously underground and underwater environments that characterise these phenomena.

## References

[1] Pan european reserves and resources reporting committee. perc reporting standard. 2021.

[2] I. K. J. Al-Kafaji. *Formulation of a Dynamic Material Point Method ( MPM ) for Geomechanical Problems*. PhD thesis, University of Stuttgart. 2013.

[3] Anura3D. Anura3d mpm research community, 2017.

[4] S. S. Bandara. Material point method to simulate large deformation problems in fluid-saturated granular medium. page 292, 2013.

[5] K. Been and M. G. Jefferiest. A state parameter for sands. *Géotechnique*, 35:99–112, 1985.

[6] M. Bendixen, J. Best, C. Hackney, and L. L. Iversen. Time is running out for sand. *Nature*, 571:29–31, 2019.

[7] J. H. V. D. Berg, A. V. Gelder, and D. R. Mastbergen. The importance of breaching as a mechanism of subaqueous slope failure in fine sand. *Sedimentology*, 49:81–95, 2002.

[8] M. Bolognin, M. Martinelli, K. J. Bakker, and S. N. Jonkman. Validation of material point method for soil fluidisation analysis. *Procedia Engineering*, 175:233–241, 2017.

[9] A. J. Bond, B. Schuppener, G. Scarpelli, T. L. L. Orr, S. Dimova, B. Nikolova, and A. V. Pinto. Eurocode 7: Geotechnical design worked examples, 2013.

[10] F. Ceccato, A. Yerro, A. Chmelnizkij, E. J. Fern, M. Martinelli, and A. Rohe. Scientific manual mpm software – anura3d, 2017.

[11] R. Courant. Variational methods for the solution of problems of equilibrium and vibrations. Technical report, New York University, 1943.

[12] R. Courant, K. Friedrichs, H. Lewy, and H. Lewyt. On the partial difference equations of mathematical physics. *IBM Journal of Research and Development*, 11:215–234, 3 1967.

[13] D. M. Cruden and D. J. Varnes. Landslide types and processes. *Special Report - National Research Council, Transportation Research Board*, 1996.

[14] D. M. Cruden and D. J. Varnes. *Landslides: Investigation and Mitigation*. Springer, 1996.

[15] S. Cuomo, P. Ghasemi, M. Martinelli, and M. Calvello. Simulation of liquefaction and retrogressive slope failure in loose coarse-grained material. *International Journal of Geomechanics*, 19:04019116, 10 2019.

[16] CUR-commissie. *CUR 113 Oeverstabiliteit bij zandwinputten*. 2008.

[17] J. M. Duncan. State of the art: Limit equilibrium and finite-element analysis of slopes. *Journal of Geotechnical Engineering*, 122:577–596, 7 1996.

[18] J. T. Eggenhuisen and W. D. Mccaffrey. The vertical turbulence structure of experimental turbidity currents encountering basal obstructions: Implications for vertical suspended sediment distribution in non-equilibrium currents. *Sedimentology*, 59:1101–1120, 2012.

[19] M. Farias and D. Naylor. Safety analysis using finite elements. *Computers and Geotechnics*, 22:165–181, 1 1998.

[20] E. J. Fern, D. A. de Lange, C. Zwanenburg, J. A. M. Teunissen, A. Rohe, K. Soga, D. A. D. Lange, C. Zwanenburg, J. A. M. Teunissen, A. Rohe, and K. Soga. Experimental and numerical investigations of dyke failures involving soft materials. *Engineering Geology*, 219:130–139, 3 2016.

[21] J. Fern, A. Rohe, K. Soga, E. Alonso, A. Rohe, K. Soga, and E. Alonso. *The Material Point Method for Geotechnical Engineering: a Practicle Guide*. CRC Press, 1st editio edition, 2019.

[22] D. V. Griffiths and P. A. Lane. Slope stability analysis by finite elements. *Géotechnique*, 49:387–403, 1999.

[23] S. A. Hall, N. Lenoir, and G. Viggiani. Full-field characterisation of strain localisation evolution in sand under triaxial loading by in- situ x-ray microtomography and 3d-volumetric digital image correlation. *71st EAGE Conference & Exhibition*, pages 1–5, 2009.

[24] O. Hungr, S. Leroueil, and L. Picarelli. The varnes classification of landslide types, an update. *Landslides*, 11:167–194, 2014.

[25] J. N. Hutchinson. General report: Morphological and geotechnical parameters of landslides in relation to geology and hydrogeology. In *Landslides, Proc 5th Int. Symp. On Landslides*, volume 1, pages 3–35, 1988.

[26] L. Li, C. Tang, W. Zhu, and Z. Liang. Numerical analysis of slope stability based on the gravity increase method. *Computers and Geotechnics*, 36:1246–1258, 9 2009.

[27] J. Locat and H. J. Lee. Submarine landslides: advances and challenges 1. *Canadian Geotechnical Journal*, 1:193–212, 2002.

[28] S. Ma, X. Zhang, and X. M. Qiu. Comparison study of mpm and sph in modeling hypervelocity impact problems. *International Journal of Impact Engineering*, 36:272–282, 2 2009.

[29] J. Maertens, G. V. Alboom, K. Haelterman, and J. Couck. Stability of underwater slopes realized by means of a suction dredger. In *Proceedings of the 17th International Conference on Soil Mechanics and Geotechnical Engineering: The Academia and Practice of Geotechnical Engineering*, 2009.

[30] M. Martinelli. 2 layer formulation: Joint mpm software., 2015.

[31] D. Mastbergen, G. van den Ham, M. Groot, T. van der Kaaij, and G. Peelen. Retrograding breach flow slides in the netherlands, observations and numerical modeling. In *IAS , 19th International Sedimentological Congress19th International Sedimentological Congress*, 2014.

[32] D. R. Mastbergen, K. Beinssen, and Y. Nédélec. Watching the beach steadily disappearing: The evolution of understanding of retrogressive breach failures. *Journal of Marine Science and Engineering*, 7:368, 10 2019.

[33] P. Peduzzi. Sand, rarer than one thinks. Technical report, UNEP Global Enviromental Alert Service (GEAS), 2014.

[34] C. V. Rhee. Slope failure by unstable breaching. *Maritime Engineering*, 168:84–92, 2015.

[35] J. G. Rots, P. Nauta, G. M. A. Kusters, and J. Blaauwendraad. and fracture localization in concrete. 1985.

[36] J. W. T. A. T. T. Rudnicki. *Fundamentals of continuum mechanics*. John Wiley & Sons Inc, 1 edition, 2015.

[37] K. Schellbach. Probleme der variationsrechnung. *Journal für die reine und angewandte Mathematik (Crelles Journal)*, 1851:293–363, 1 1851.

[38] J. Silva. *The influence of underwater embankment properties on breaching failures*. PhD thesis, Utrecht University 2020.

[39] D. E. Smith, S. Shi, R. A. Cullingford, A. G. Dawson, S. Dawson, C. R. Firth, I. D. L. Foster, P. T. Fretwell, B. A. Haggart, L. K. Holloway, and D. Long. The holocene storegga slide tsunami in the united kingdom. *Quaternary Science Reviews*, 23:2291–2321, 12 2004.

[40] K. Soga, E. Alonso, A. Yerro, K. Kumar, and S. Bandara. Trends in large-deformation analysis of landslide mass movements with particular emphasis on the material point method. *Géotechnique*, 66:248–273, 3 2016.

[41] T. P. Stoutjesdijk, M. B. D. Groot, and J. Lindenberg. Flow slide prediction method: influence of slope geometry, 2014.

[42] D. Sulsky, Z. Chen, and H. L. Schreyer. A particle method for history-dependent materials. *Computer Methods in Applied Mechanics and Engineering*, 118:179–196, 1994.

[43] D. Sulsky, S.-J. Zhou, and H. L. Schreyer. Application of a particle-in-cell method to solid mechanics. *Computer Physics Communications*, 87:236–252, 1995.

[44] U. G. Survey. Landslide types and processes. Technical report, USGS, 2004.

[45] T. Tang. Modeling of soil water interaction using openfoam modellierung von wasser-boden-interaktion mittels openfoam, 2016.

[46] D. R. Tappin, P. Watts, G. M. Mcmurtry, Y. Lafoy, and T. Matsumoto. The sissano, papua new guinea tsunami of july 1998, offshore evidence on the source mechanism. *Marine Geology*, 175:1–23, 2001.

[47] K. Terzaghi. Theoretical soil mechanics. *Géotechnique*, page 510, 1943.

[48] P. J. Vardon, B. Wang, and M. A. Hicks. Slope failure simulations with mpm. *Journal of Hydrodynamics*, 29:445–451, 6 2017.

[49] D. J. Varnes. Slope movement types and processes. *Transportation Research Board Special Report*, 1:11 – 33, 1978.

[50] T. Waltham. *Foundations of engineering geology.* Taylor & Francis Group, 3 edition, 2009.

[51] B. Wang, P. J. Vardon, and M. A. Hicks. Investigation of retrogressive and progressive slope failure mechanisms using the material point method. *Computers and Geotechnics*, 78:88–98, 2016.

[52] Z. Wieckowski. The material point method in large strain engineering problems. *Computer Methods in Applied Mechanics and Engineering*, 193:4417–4438, 2004.

[53] D. M. Wood. *Soil behaviour and critical state soil mechanics.* Cambridge University Press, 1 2014.

[54] Y. You. *Dynamics of dilative slope failure*. PhD thesis, The University of Texas at Austin. 2013.

[55] F. Zabala and E. E. Alonso. Progressive failure of aznalcóllar dam using the material point method. 61:795–808, 2011.

[56] F. Zhang, X. Zhang, K. Y. Sze, Y. Lian, Y. Liu, F. Zhang, X. Zhang, K. Y. Sze, Y. Lian, Y. Liu, F. Zhang, X. Zhang, K. Y. Sze, Y. Lian, and Y. Liu. Incompressible material point method for free surface flow. *Journal of Computational Physics*, 330:92–110, 2 2017.

# 3

# Development and validation of in/outflow boundary conditions

*This chapter describes the development and application of inflow and outflow boundary conditions (BCs) for the material point method (MPM) in order to simulate fluid flow problems. This corresponds to velocity and pressure controlled BCs. Due to the coupled Lagrangian and Eulerian description of the fluid motion in MPM it is necessary to add and remove material points, with appropriate kinematic properties, to and from the computational domain. The newly-developed BCs have been used to simulate uniform open channel flow and the phenomenon of free overfall in open channels, which is transient conditions leading to non-uniform flow due to a sudden bed level drop. It is shown that the numerical results predict well the flow geometry including end depth ratio, pressure distribution and accelerations, and therefore the velocities and displacements.*

## 3.1. Introduction

Free surface fluid flows are common problems in many fields of engineering. Several arbitrary Lagrangian-Eulerian (ALE) methods have been developed for fluid dynamics in recent years (e.g. [5, 9, 19]) to simulate free surface flow. The material point method (MPM) [17] is a specific variant of an ALE method.

---

Parts of this chapter have been published by Zhao X, **Bolognin M**, Liang D, Rohe A, & Vardon P J (2019). Development of in/outflow boundary conditions for MPM simulation of uniform and non-uniform open channel flows. Computers & Fluids, 179, 27–33.

*The main contribution of the author of this dissertation consisted of developing the theory and the implementation strategy for both inflow and outflow elements. Additionally, he selected a suitable analytical solution from literature and the benchmark problems for the overall validation.*

The position of the material is traced by the material points (MPs), so that no specific procedure is needed to capture or to trace interfaces. MPs can move through a fixed background mesh during the simulation and, consequently, in order to model continuous flows, MPs must be inserted into and/or removed from the domain at boundaries. This chapter describes the development, verification and validation of the velocity-controlled inflow and pressure-controlled outflow BCs for MPM. The implementation has been undertaken in the Anura3D software [2].

Originally, the modelling approach to simulate quasi-steady in/outflow conditions in MPM was to use large reservoirs in order to supply the domain of interest with MPs (e.g. [3, 11, 20]). This required a large reservoir, increasing the computational effort, only approximated steady conditions and limited the time able to be simulated. Being able to prescribe in/outflow BCs allows: (i) true steady-state conditions; (ii) a large reduction of computational cost; (iii) the simplification of the geometry; and (iv) improving the general applicability of the method.

The proposed algorithm allows the enforcement of different upstream and downstream conditions. For the purpose of model validation, the new BCs were applied for modelling eventual steady-state critical flow in an uniform open channel and free overfall, comparing the results with experimental measurements and analytical solutions.

This chapter is structured as follows: Section 3.2 discusses the development and implementation of the proposed in/outflow BCs; in Section 3.3 the new algorithm is verified by simulating a subcritical flow that requires proper simultaneous imposition of upstream and downstream BCs; in Section 3.4 the numerical results of a free overfall flow are compared with existing analytical and experimental results as validation; and the conclusions are presented in Section 3.5. For the theoretical and numerical formulation of MPM as implemented in Anura3D please look back to Chapter 2.9.

## 3.2. In/outflow boundary conditions

In order to facilitate inflow (or source-like) boundaries, one needs to impose an acceleration on the nodes of the inflow elements connected to the domain (see Fig. 3.1) at every time step. Additionally, to ensure mass continuity (and thus satisfying Eq. 2.1), MPs must be added and enter the domain. The acceleration, velocity and density of the generated MPs needs to be consistent with the BCs. A constant Dirichlet BC (i.e. fixed acceleration) should be applied to the nodes of the inflow elements by updating the acceleration **a** (as described in step 3 of Section 2.9.2). Conversely, an outflow BC requires imposing Neumann BCs (i.e. force) at the nodes of the outflow elements (see Fig. 3.1b), representing water pressure on the other side of the boundary. The combination of these two BCs enables the simulation of subcritical flow BCs.

Due to the Lagrangian-Eulerian description, new MPs need to be introduced at the inflow boundary. To facilitate this, an extra set of elements is added (shown in green in Fig. 3.1a) to the computational domain (shown in blue). At the beginning of the computational cycle, MPs are placed in the additional elements (called inflow elements) with prescribed velocity and zero acceleration. The inflow nodes that are shared with the elements of the computational domain (highlighted in Fig. 3.1a by red ellipses) have a prescribed acceleration so as to maintain the prescribed velocity field at the boundary.

When an inflow element is empty, new MPs will be introduced in the inflow elements at the same local position as the material which is initially discretized inside the domain, i.e. the Gauss point locations. The added MPs are released at the desired time step to ensure the fluid nodal density is maintained, i.e. at every $n^{th}$ time step, defined as:

$$n = \frac{\Delta L}{\mathbf{v}^0 \Delta t_i} \tag{3.1}$$

where $\Delta L$ is the element size in the direction parallel to the prescribed velocity vector, $\mathbf{v}^0$ is the prescribed input velocity and $\Delta t_i$ is the $i^{th}$ time step size.

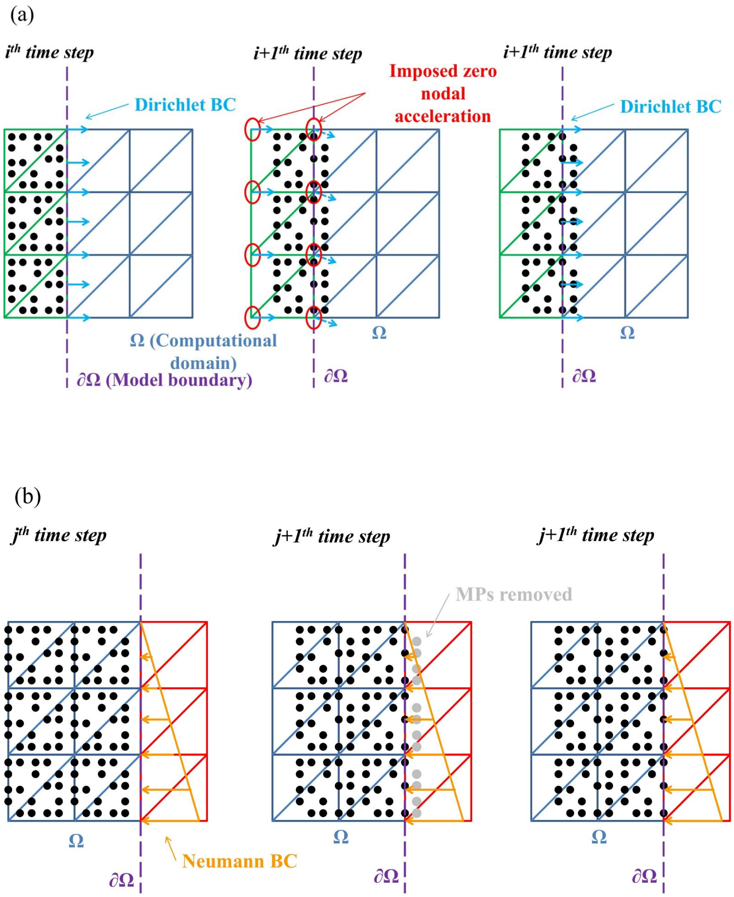

Figure 3.1: Illustration of the BCs: (a) Inflow BC, with inflow elements (green) and (b) outflow BC, with outflow elements (red).

For the outflow BC, additional outflow elements are introduced (Fig. 3.1b). Natural BCs are assigned on the nodes shared with the computational domain in step 2 of Section 2.9.2. As soon as an MP enters an outflow element it is removed from the computation.

## 3.3. Verification of boundary conditions

In order to verify the application of the in/outflow BCs a simple case is simulated. An initially empty domain is considered of $0.15 \times 0.15 \times 0.01$ m, in the x-, y-, z-directions, with frictionless walls, a prescribed horizontal inflow velocity of 1.0 m/s and a zero acceleration along the inflow boundary as indicated in Fig. 3.2a. The three-dimensional domain is discretised by linear tetrahedral elements and has a thickness of one element with only the front face shown in Fig. 3.2. The reduction factor for the time discretization $\alpha_{Courant}$ is fixed as 0.98. A band of outflow elements is attached to the right side of the computational mesh with a prescribed hydrostatic pressure. Outflow elements and their BCs are only activated when MPs enter the adjacent elements. The water is modelled by a Newtonian compressible constitutive model. It has an initial density $\rho^0$ = 1000 kg/m$^3$, dynamic viscosity $\mu$ = $1 \times 10^{-6}$ kPa·s and bulk modulus $K$ = 20000 kPa. The water bulk modulus was reduced by a factor of 100 from reality in order to increase the time step as an explicit integration scheme is adopted. It was pointed out in Liang (2010) [8], provided that the modeled water has a speed of sound at least an order of magnitude (over ten times) greater than the maximum flow velocity, its increased compressibility has negligible influence on the results.

The minimum time step is obtained as described in Section 2.9.2. Further, strain and pressure smoothing procedures are used to mitigate the stress oscillations due to grid crossing [10].

Fig. 3.2 shows the simulation results in terms of pressure (b) and velocity (c) at different time steps. After an initial time interval of transient moving water front, a steady uniform flow is achieved. It is worth mentioning that the prescribed Neumann BC at the outflow boundary nodes causes unreasonably high pressures near the bottom when the flow is not yet fully developed, which is especially evident at 0.15 s and 0.20 s. This is caused by the prescribed hydrostatic pressure which is initiated based on the final water depth. As the calculation continues, and the outlet water level keeps rising, this inconsistency vanishes. This phenomenon can be avoided if the hydrostatic pressure at the outflow elements would be updated during the calculation based on the water depth. However, the purpose of the present simulation is to verify the capabilities of the newly proposed in/outflow BCs. After 0.8 s it can be seen that a constant velocity, a hydrostatic pressure and a horizontal free surface are achieved, which proves the correctness of the applied boundary conditions.

## 3.4. Validation benchmark

In order to validate the theoretical formulation and numerical implementation of in/outflow BCs, a well-known open channel flow problem has been simulated. This

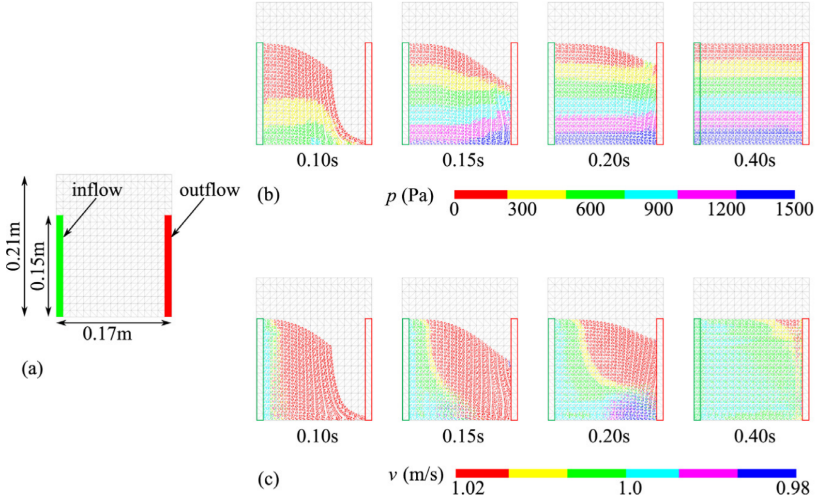

Figure 3.2: (a) Computational mesh of a rectangular channel and application of in/outflow BCs for the simulation of a subcritical flow. Representation of the fluid flow converging to a steady solution enforced by the downstream BC: (b) Pressure field; (c) Velocity field at different time steps.

is the situation where a fluid flow encounters a sudden drop in the bed, also known as a free overfall. The free overfall simulation is chosen as a validation benchmark for the in/outflow BCs since the rapid change in bed geometry is considered a stringent validation case.

### 3.4.1. Existing free overfall studies

Rouse (1936) [15] measured the pressure distribution in a steady horizontal rectangular free overfall using wall and bed piezometers. It was observed that a free overfall in rectangular channels could be used as a simple flow measuring device that required no calibration. Since then, due to its practical importance, many investigators have studied free overfall in various channels (e.g., [18], [14], [13]). In [13], water was supplied from a constant head tank fed by a pump, and the discharge was measured using a calibrated orifice meter installed in the supply line. At the channel's downstream end, the side walls extended beyond the brink to confine the nappe between them. The water surface profile was recorded with a point gauge, while pressure distributions were measured both at the end section and in the upstream region. When the free overfall enters the air, there is no reverse curve in the water surface until it strikes the bottom at a lower elevation. According to the momentum conservation law, provided that no external energy is added to the system, the water surface will seek its lowest possible energy configuration. The theoretical flow depth for parallel flows with a rectangular cross-section is then equal to the critical flow depth $y_c$, as shown in Fig. 3.3 [4], where $H$ is the total water head. The critical flow depth $y_c$ is expressed as $y_c = \sqrt[3]{\alpha(\bar{v}h_i)^2/g}$ , where $\bar{v}$ is the mean flow velocity of the cross-section, $h_i$ is the initial flow depth and $\alpha$ is the velocity coefficient which can be approximately taken as 1.0 .

For the free overfall flow and rapidly varied bed geometry problems, the actual surface follows the profile represented by the solid blue line in Fig. 3.3. Rouse (1936) [15] experimentally found that for almost horizontal geometries, the computed critical depth based on parallel flow assumption $y_c$ is about 1.4 times the brink depth $y_b$.

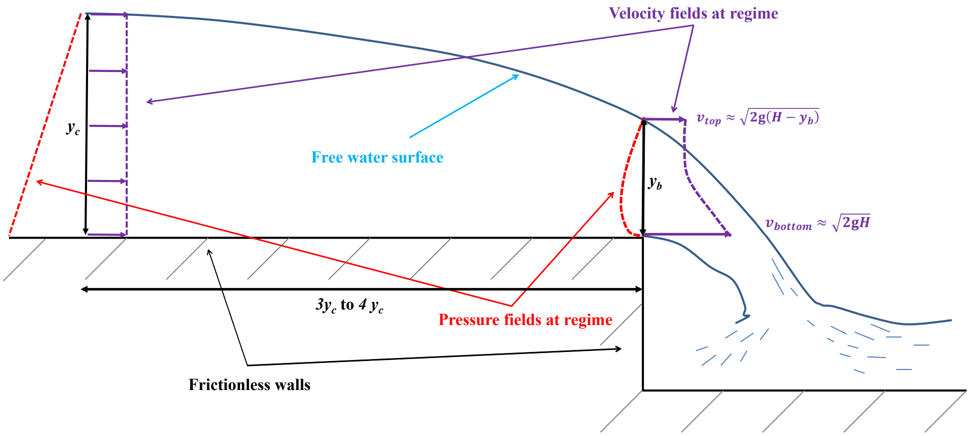

Figure 3.3: Free overfall problem.

Montes (1994) [12] proposed an analytical solution for the analysis of open channel flows near a discontinuity of the bed geometry (i.e. free overfall). Assuming the flow in each terminal section to be nearly parallel with the bottom, negligible viscous effects, irrotational flow and energy conservation, it is possible to use a potential-flow solution of the inverse type (a variant of Stokes inverse mapping [16]). The solution of the potential-flow equations was solved numerically by a finite difference grid (successive over relaxation method), and the unknowns (free-surface location, velocity and pressure fields) were determined by an iterative procedure. This solution is used as reference for the numerical solution as shown in Fig. 3.7 and 3.8.

Readers are referred to Dey (2002) [6] for a comprehensive review of the research on free overfall in rectangular open channels flows.

### 3.4.2. Computational setup

An initially empty domain is considered of $0.60 \times 0.15 \times 0.01$ m in the x-, y-, z-directions with a prescribed horizontal inflow velocity of 1.213 m/s, frictionless bottom and a zero acceleration along the inflow boundary indicated in green in Fig. 3.4. As in the subcritical flow case (Section 3.3), the three-dimensional domain is discretised by linear tetrahedral elements and has a thickness of one element with only the front face shown in Fig. 3.4. A layer of outflow elements are attached to the right side of the computational mesh (in red), with zero prescribed Neumann BCs at the nodes. The cross section for the analysis of the result around the brink are shown in Fig. 3.4. Frictional effects are neglected for all contact surfaces. The material properties (e.g. density, viscosity and bulk modulus) are as assigned in Section 3.3 and the time step is calculated as in Section 2.9.2. In the following section, the dependencies of the simulation results on the number of MPs per element and mesh size are evaluated.

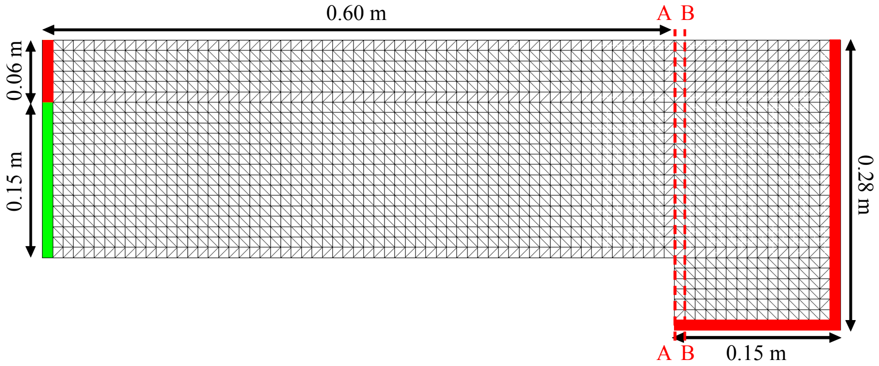

Figure 3.4: Computational mesh of a rectangular channel for free overfall simulation. The in/outflow BC elements are highlighted respectively in green and red. At the overfall brink two cross sections (A-A and B-B) are investigated.

## 3.4.3. Results

### Effect of mesh size and number of material points per element

A sensitivity study of the free overfall simulations by varying the computational mesh size and the initial number of material points per element (PPE) is given in this section. Figs. 3.5 and 3.6 show results of open channel flow simulations with an initial water depth of 0.15 m and a velocity of 1.213 m/s. Three mesh sizes are used: 0.03 m, 0.01 m and 0.005 m when studying the effect of the mesh size, and 4 PPEs are used as a first approximation (Fig. 3.5).

It can be observed that there are frequent pressure fluctuations when using finer meshes, which are attributed to grid-crossing errors. It is discussed in Guilkey et al. (2006) [7] and Al-Kafaji (2013) [1] that using a finer mesh causes more frequent migration of MPs between elements, and therefore the grid-crossing errors are more pronounced. The problem is more severe when the PPE is low [1] and the stiffness of the material is high. However, the mesh resolution plays an important role for the accuracy of the results: by decreasing the mesh size the brink height in the numerical solution converges to the analytical one (see Table 3.1, where 8 PPE are used).

Fig. 3.6 shows the comparison of simulations of open channel flow with four different values of PPE: 4, 8, 10 and 20 MPs per element, respectively for a mesh size of 0.03 m. It can be observed that 4 PPE is a too coarse discretisation as it emphasises the grid crossing error, while simulations with 8, 10 and 20 PPE produce much best results in terms of pressure distribution.

These results led to the conclusion that the nodal density oscillations are the

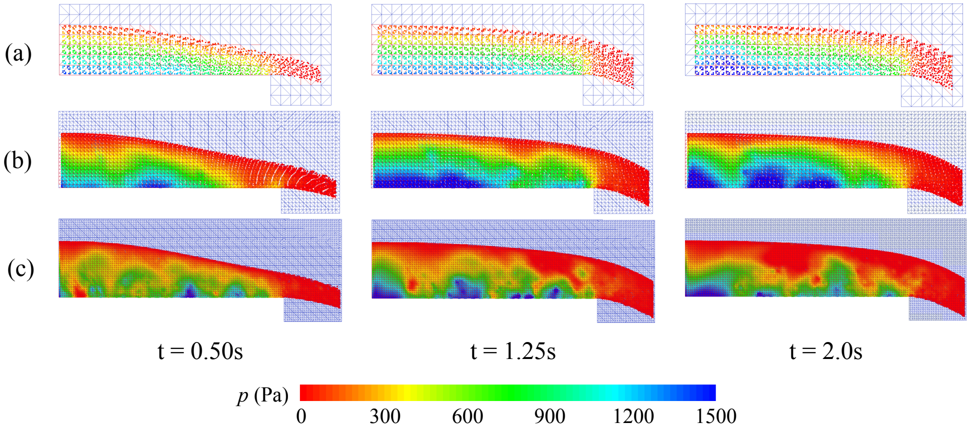

Figure 3.5: Comparison of open channel simulations with different mesh sizes. a) $\Delta L$ = 0.03 m; b) $\Delta L$ =0.01 m; c) $\Delta L$ = 0.005 m for different time instants.

main cause of pressure fluctuations due to the weakly compressible behaviour of the fluid. The change in calculated nodal density in this method is directly due to the proportional change in PPE in the elements surrounding the node, and therefore by increasing the PPE the oscillations are reduced. Table 3.1 gives a quantitative analysis of the brink depth relative error combining different mesh sizes and using 8 PPE. In this chapter, we propose to use a finer mesh because that improves the depth at the brink and the drawback of more pressure oscillation is compensated by introducing a higher number of PPE.

Table 3.1: Relative error of brink depth estimation using meshes with various sizes (8 PPE)

| Mesh size (m) | Time (s) | $y_b$ (m) | Analytical (m) | Error (%) |
|---|---|---|---|---|
| 0.03 | 2 | 0.1109 | 0.10725 | 3.44 |
| 0.01 | 2 | 0.1093 | 0.10725 | 1.90 |
| 0.005 | 2 | 0.1093 | 0.10725 | 1.88 |

### Pressure distribution at brink

The pressure distribution with the numerical solution provided by MPM is compared with laboratory measurements (Sec. 3.4.1) and the analytical solution. The pressure distribution at the brink (cross-section A-A in Fig. 3.4) is plotted with data from literature in Fig. 3.7, where $\gamma$ is the water unit weight and $y$ is the height of the MP above the brink. Note that the MPs selected for analysis are actually located within a thin area (about one fifth of the element size) in the flow direction containing the chosen cross-sections. From the comparison, it can be seen that, near the free surface, the numerical pressure distribution in both cross sections agree relatively well with experimental data obtained by other researchers. For the region near the bed, the numerical simulations seem to over-predict the pressure in cross section

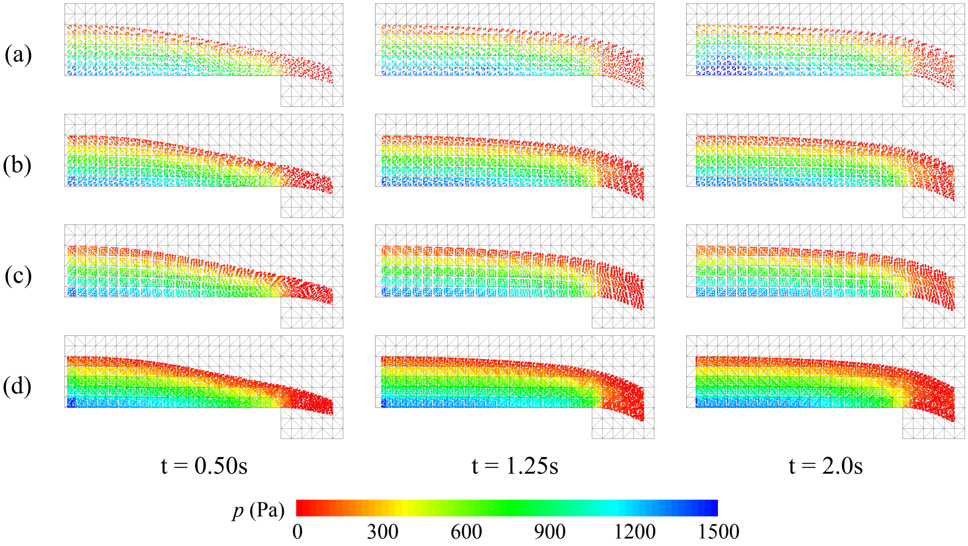

Figure 3.6: Comparison of open channel simulations with different PPEs. a) $PPE = 4$; b) $PPE = 8$; c) $PPE = 10$; d) $PPE = 20$ for different time instants.

A-A. This may be attributed to the vertical fixities applied on the corner nodes of the brink, which prevent the MPs from leaving the mesh. This vertical fixity also restricts the MP from moving freely downward once they pass the brink, within one element, causing the pressure near the bottom to increase. This can be shown by selecting MPs one element away (cross-section B-B in Fig. 3.4), where the influence of the vertical fixity is negligible, and the pressure distribution near the bed is significantly closer to the experimental results.

### Velocity distribution at brink

Fig. 3.8 shows the comparison of the velocity distribution with the results calculated by the semi-analytical solution given in [12], where $v$ and $v_c$ are the velocity and critical velocity, respectively. MPs are chosen in the same manner as in Fig. 3.7. It can be seen that the velocity close to the channel bed is slightly underestimated in cross-section A-A. Several factors may contribute to that: in experiments there is a slight contraction of the flow at the brink where the water detaches from the bed which is not occurring in the numerical simulation; the low order shape functions produce a slightly over stiff behaviour that reduces the velocity where the largest deformations occur. Last but not least, the impact of the fixity mentioned above also adds to underestimation of the velocity in cross-section A-A.

## 3.5. Conclusions

In/outflow BCs suitable for MPM simulations of open channel flow have been developed. These have been applied to the simulation of eventually steady subcritical flow and free overfalls in rectangular open channels to effectively validate the BCs.

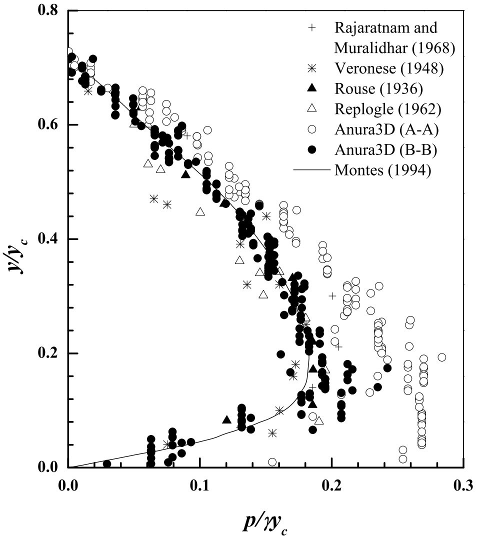

Figure 3.7: Pressure distribution at brink in rectangular overfall.

The brink depth, pressure distribution and velocities have been analysed for several geometries and flow velocities and a good agreement between the MPM results, analytical solutions and experimental results is seen. The BCs are considered validated and can be used to simulate a wide range of flow conditions.

# References

[1] I. K. J. Al-Kafaji. *Formulation of a Dynamic Material Point Method ( MPM ) for Geomechanical Problems*. PhD thesis, University of Stuttgart. 2013.

[2] Anura3D. Anura3d mpm research community, 2017.

[3] M. Bolognin, M. Martinelli, K. J. Bakker, and S. N. Jonkman. Validation of material point method for soil fluidisation analysis. *Procedia Engineering*, 175:233–241, 2017.

[4] V. T. Chow. *Open-channel hydraulics*. McGraw-Hill Book Company, reissue edition, 1959.

[5] M. Cremonesi, F. Ferri, and U. Perego. A basal slip model for lagrangian finite element simulations of 3d landslides. *International Journal for Numerical and Analytical Methods in Geomechanics*, 41:30–53, 2017.

[6] S. Dey. Free overall in open channels: State-of-the-art review. *Flow Measurement and Instrumentation*, 13:247–264, 2002.

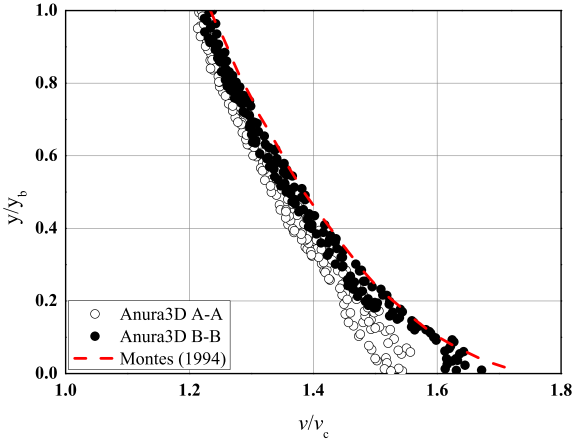

Figure 3.8: Fluid velocity at the brink. Comparison of analytical solution with MP velocity for steady state flow conditions.

[7] J. E. Guilkey, J. B. Hoying, and J. A. Weiss. Computational modeling of multicellular constructs with the material point method. *Journal of Biomechanics*, 39:2074–2086, 2006.

[8] D. Liang. Evaluating shallow water assumptions in dam-break flows. *Proceedings of the Institution of Civil Engineers - Water Management*, 163:227–237, 2010.

[9] J. Maljaars, R. J. Labeur, M. Möller, and W. Uijttewaal. Development of a hybrid particle-mesh method for simulating free-surface flows. *Journal of Hydrodynamics, Ser. B*, 29:413–422, 6 2017.

[10] M. Martinelli. 2 layer formulation: Joint mpm software., 2015.

[11] M. Martinelli, F. S. Tehrani, and V. Galavi. Analysis of crater development around damaged pipelines using the material point method. *Procedia Engineering*, 175:204–211, 1 2017.

[12] J. S. Montes. Potential-flow solution to 2d transition from mild to steep slope. *Journal of Hydraulic Engineering*, 120:601–621, 1994.

[13] N. Rajaratnam and D. Muralidhar. Characteristics of the rectangular free overfall. *Journal of Hydraulic Research*, 6:233–258, 1968.

[14] J. A. Replogle. Discussion on 'end depth at a drop in trapezoidal channels' by m.h. diskin. *Journal of the Hydraulics Division*, 88:161–165, 1962.

[15] H. Rouse. Discharge characteristics of the free overfall: Use of crest section as a control provides easy means of measuring discharge. *Civil Engineering ASCE*, 6:257–260, 1936.

[16] G. G. Stokes. *Supplement to a paper on the theory of oscillatory waves*, pages 314–326. Cambridge University Press.

[17] D. Sulsky, Z. Chen, and H. L. Schreyer. A particle method for history-dependent materials. *Computer Methods in Applied Mechanics and Engineering*, 118:179–196, 1994.

[18] A. Veronese. Rilievi sperimentali sugli sbocchi liberi. *L'Energia Elettrica*, pages 441–638, 1948.

[19] F. Zhang, X. Zhang, K. Y. Sze, Y. Lian, Y. Liu, F. Zhang, X. Zhang, K. Y. Sze, Y. Lian, Y. Liu, F. Zhang, X. Zhang, K. Y. Sze, Y. Lian, and Y. Liu. Incompressible material point method for free surface flow. *Journal of Computational Physics*, 330:92–110, 2 2017.

[20] X. Zhao and D. Liang. Mpm modelling of seepage flow through embankments. In *International Ocean and Polar Engineering Conference*, pages 1161–1165, 2016.

# 4

# Assessment of dike safety within the MPM framework

*Dike infrastructure is of vital importance for the safety against flooding. The standard methodologies for the assessment of dike safety for macrostability are based on limit equilibrium methods, which result in a safety factor (SF) against shear failure. The more advanced alternative consists of using the finite element method to compute the SF against shear failure. However, these approaches do not take into account the capacity of the dike to retain water, and are only concerned with the mechanical equilibrium of the dike's initial composition. With the recent advancements in the modelling of large deformations within geotechnical engineering, e.g. by means of the material point method (MPM), the post failure behaviour of the dike can be predicted. The MPM is a mesh-free method that has been developed to address the problem of large deformation on a continuum level. The MPM offers the possibility to redefine the concept of SF against shear failure. The initial shear failure of a dike does not necessarily lead to the loss of the dike's capability to retain water. In reality, after the initial shear failure the mass of soil will move and reach a new equilibrium position. This chapter presents the analysis of a progressive dike failure, in order to get a better insight of the post failure behaviour, and a proposal is made to better reflect on the concept of SF.*

---

Parts of this chapter have been published by Coelho B Z, **Bolognin M** , Aboufirass A, Rohe A, & Nuttall J D (2018). Assessment of dike safety within the framework of large deformation analysis with the material point method. NuMGe2018 Numerical Methods in Geotechnical Engineering IX (pp. 657–665).

*The main contribution of the author of this dissertation consisted of performing the first exploratory comparison (verification) of the MPM results with the numerical benchmark proposed by Hicks and Wong 1988 [3] by using the Mohr Coulomb constitutive model. This benchmark describes LEM and FEM results for the safety assessment of a submerged sandy slope by increasing the gravity multiplier. He contributed by selecting and analysing relevant literature, setting up an equivalent MPM numerical model and interpreting the results, including reproducing the LEM and FEM results from literature.*

## 4.1. Introduction

Slope stability of dikes is an important issue in geotechnical engineering as dikes are often the first line of defence against water flooding. Traditionally, slope stability analysis is carried out using LEM or FEM. In this chapter, MPM will be used to assess the stability of a dike. After an initial validation of the method against literature results, MPM will be applied to analyse a typical Dutch dike profile, and the differences with the standard methodologies will be highlighted and discussed.

## 4.2. Verification

The material point method (MPM) analyses have been performed with the software Anura3D [1]. The validation has been performed by simulating a slope previously presented by [3]. The cross-section of the 2D slope geometry and mesh for the MPM analysis are presented in Figure 4.1.

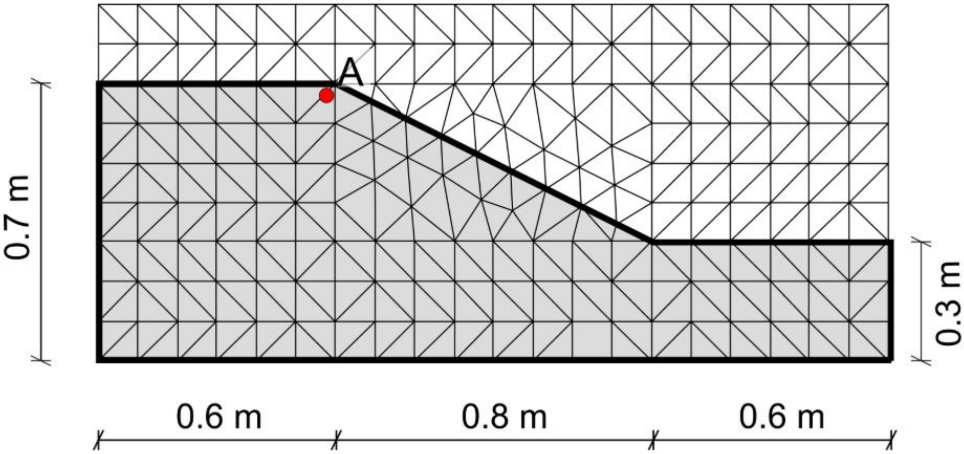

Figure 4.1: Cross-section of 2D slope geometry and mesh (based on [3]). The slope has been modelled with 3D tetrahedral elements, with a model thickness of one element in order to be equivalent to a 2D analysis.

The slope is assumed to be fully saturated with water, and the analysis is undrained. The system of equations is solved explicitly in the time domain. The domain was discretised using low-order tetrahedral elements (in total 1086 active elements), with initially 4 material points in each element. The displacements are constrained in both the vertical and horizontal directions for the bottom boundary, and the displacements are constrained in the horizontal direction along the vertical boundaries. The slope material has been modelled as a Mohr-Coulomb material (see Table 4.1).

The slope factor of safety (SF) was assessed by increasing the gravity multiplier, while keeping all material parameters constant. The SF is defined as the ratio between the gravity multiplier at the failure state and the initial gravity multiplier, i.e. 1g [4–6]. Figure 4.2 shows the vertical displacement for point A (see location

| Parameter | Value | Unit |
|---|---|---|
| Young's modulus | 1000 | $kPa$ |
| Volumetric weight | 20 | $kN/m^3$ |
| Poisson ratio | 0.3075 | - |
| Poisson ratio undrained | 0.499 | - |
| Cohesion | 0.6 | $kPa$ |
| Friction angle | 30 | $deg$ |
| Dilantancy angle | 0 | $deg$ |

Table 4.1: Parameters for Mohr-Coulomb material model

in Figure 4.1), located at the edge of the slope crest, obtained by finite element method (FEM) [3], MPM and limit equilibrium method (LEM). The LEM analysis were performed by using Bishop's method within the D-GeoStability software [2]. It follows that the results provided by the MPM calculation are in agreement with the results from the FEM analysis, up to the moment of failure (gravity multiplier of $\approx$ 2.3), which illustrates the correctness of the MPM solution for small strain analysis.

The FEM computation has the limitation of not providing any insight into the dike behaviour after the initial failure, while the MPM is able to simulate beyond this point. The LEM provides a result that is also in agreement with the FEM analysis. This shows that when the objective is to estimate the initial SF of slopes the LEM provides a good solution with fewer computational resources. Following the traditional design methodology it is assumed that the slope SF is 2.3. However, for this SF the vertical displacement of point A is only 0.08 mm (0.02% of the slope height), which means that the slope could still fulfill the structural function of retaining high water levels as well as the same slope before this initial failure. This will be further discussed in the next section.

## 4.3. Dike analysis and safety

### 4.3.1. Problem description

In order to illustrate the benefits of using the MPM for slope stability analysis, a generic dike section has been studied. The dike geometry corresponds to a typical Dutch dike section, with non symmetric inclination of the slopes (outer slope=1/4; inner slope=1/5). The dike was considered fully saturated with the water level placed at the height of the crest. The cross section of the 3D dike geometry and mesh for the MPM analysis are presented in Figure 4.3.

The system of equations is solved explicitly in the time domain. The domain was discretised using low-order tetrahedral elements (in total, 7017 active elements), with initially 4 material points in each element. The displacements are constrained in both vertical and horizontal directions for the bottom boundary, and the displacements are constrained in the horizontal direction along the vertical boundaries. The dike material was considered to be uniform and homogeneous, and has been modelled as a Mohr-Coulomb material (properties available in Table 4.2).

The mesh is refined in the area where higher shear strains are expected. The

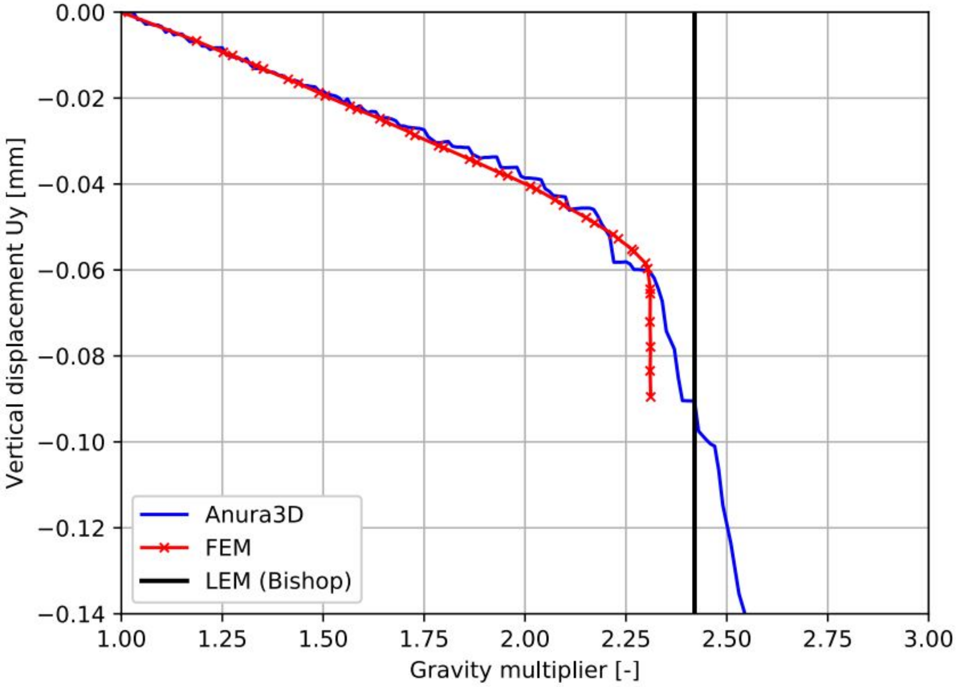

Figure 4.2: Comparison between FEM [3] MPM and LEM results for the vertical displacement of the slope crest.

application of distributed loads in the MPM is not straight forward, as the material points can move through the mesh. To overcome this issue, the water loading was modelled by representing the water reservoir as an elastic material, with the properties presented in Table 4.2. Note that the water is not infiltrating into the dike. Figure 4.4 shows the vertical effective stress and pore water pressure after the initialisation of gravity loading (gravity multiplier 1g).

It follows that the proposed methodology is appropriate to model the water loading. Similar to the slope presented in the previous section, the dike safety was assessed by increasing the gravity multiplier. However, as the aim of the analysis is to analyse dike deformation, a problem arises as the dike deformation incorporates both the deformation due to shearing and the deformation due to the elastic deformation caused by the gravity increase. In order to be able to distinguish between the two, an additional one-dimensional soil column subjected to gravity increase was computed with the MPM, and its results subtracted from the dike results. The results from the one-dimensional soil column correspond entirely to the deformation caused by the gravity increase, as no shearing occurs. Therefore, the results presented in the following section are corrected, and merely concern the shear deformation.

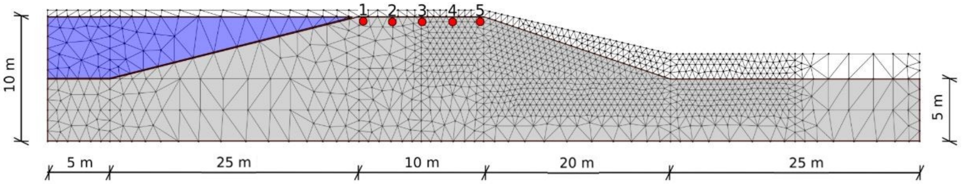

Figure 4.3: Cross section of a typical Dutch dike geometry and mesh.

| Material | Parameter | Value | Unit |
|---|---|---|---|
| Dike | Volumetric weight | 20 | $kN/m^3$ |
| | Young's modulus | 7500 | $kPa$ |
| | Poisson ratio | 0.33 | - |
| | Poisson ratio undrained | 0.499 | - |
| | Cohesion | 1 | $kPa$ |
| | Friction angle | 35 | $deg$ |
| | Dilatancy angle | 0 | $deg$ |
| Water | Volumetric weight | 10 | $kN/m^3$ |
| | Young's modulus | 150000 | $kPa$ |
| | Poisson ratio | 0 | - |
| | Poisson ratio undrained | 0.499 | - |

Table 4.2: Material parameters for the dike geometry modelled with MPM

### 4.3.2. Results

Figure 4.5 shows the vertical displacement of several points located along the dike crest, together with the SF obtained by means of the LEM. The locations of the points are indicated in Figure 4.3.

The dike crest exhibits higher displacements at points towards the inner slope. Point 1, which is located close to the outer slope and next to the water loading, has a smaller vertical deformation. For a gravity multiplier of 1.2, which corresponds to the SF according to the LEM analysis, the crest deformation is very small. This is further illustrated in Figure 4.6, which presents the vertical crest displacement for low values of the gravity multiplier.

For a gravity multiplier of 1.2 the maximum dike crest deformation occurs at point 5 and is smaller than 7 mm. This means that, if this dike was analysed following the standard methods, the dike would be considered to fail with a maximum displacement of 7 mm. However, for such a small deformation it can be expected that the dike still fulfills its primary function of retaining water. Figure 4.7 presents the dike crest profile at different levels of the gravity multiplier.

For a gravity multiplier of 1.2 the dike crest exhibits no visible displacement. At a gravity multiplier of 1.5 the dike crest starts to move, but only for the points closer to the inner slope. Only at a gravity multiplier of 3 is a clear movement of the entire dike crest identified. From the figure it is also found that the dike crest not only settles, but also elongates. The main advantage of the MPM for the analysis

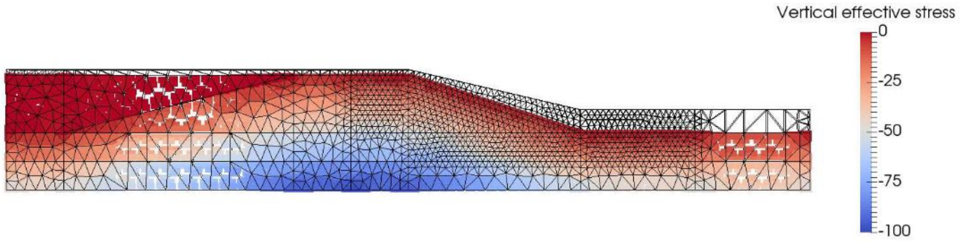

(a)

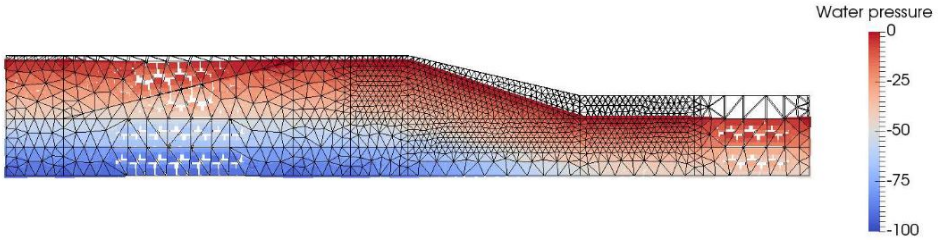

Figure 4.4: Initialisation stage: (a) vertical effective stress and (b) water pressure at gravity multiplier 1g.

of dike safety is related to the possibility of analysing beyond the initial failure.

As the gravity multiplier increases, the dike continuously deforms and reaches new equilibrium positions. This is because failure is progressive and not abrupt as is assumed by the LEM. From a safety point of view, if a maximum allowable displacement of the dike crest is defined, a new SF can be established based on this displacement criterion. For example, for this particular dike, if it would be acceptable to have a maximum crest displacement of 25 cm, the SF would be larger than 1.5, instead of 1.2 as defined from the LEM. The displacement and shear strain fields of the dike are presented in Figure 4.8, at different gravity multipliers.

The dike is found to exhibit a classic macro-stability failure by movement of the inner slope. Up to a gravity multiplier of 2 no significant displacement or shear bands occur. For gravity multipliers of 2 and higher, the formation of the shear band and its effects on the dike displacement are clearly visible.

### 4.3.3. Influence of Young's modulus

The standard methodology for dike safety assessment based on LEM does not take account of the dike deformation; hence the stiffness has no influence on the dike safety. However, when going towards an assessment based on displacement criteria, the stiffness is of importance, as it is fundamental to correctly model the displacement field. Therefore an analysis on the Young's modulus is performed in the range between 2500 and 15000 kPa. Figure 4.9 presents the results of the dike crest displacement for several cases.

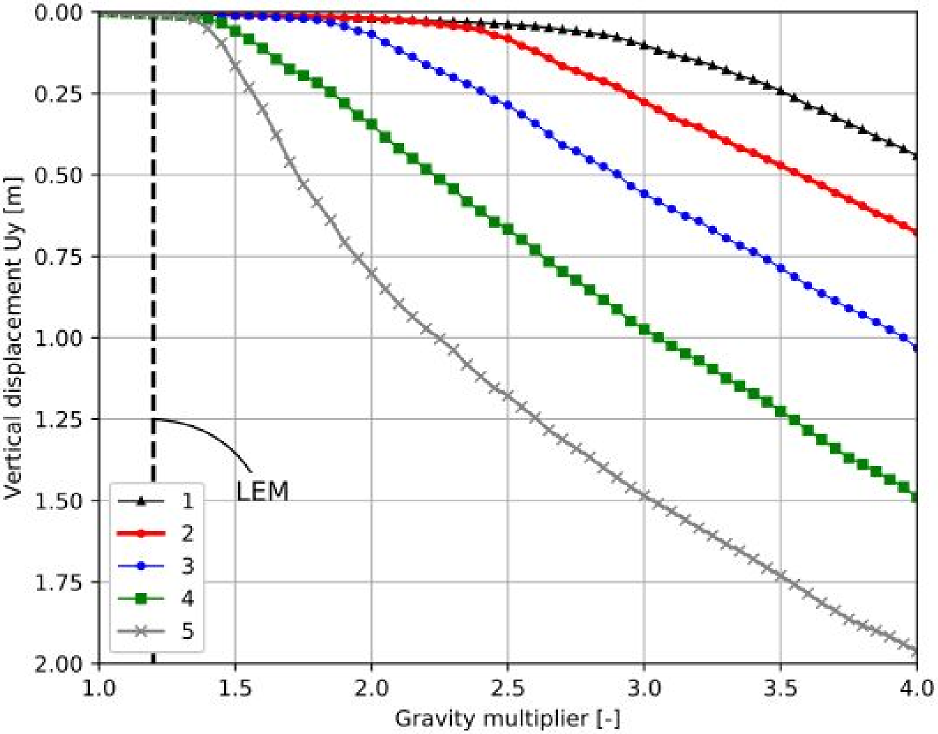

Figure 4.5: Vertical displacement for several points along the dike crest.

It is clear the effect of the Young's modulus on the dike crest displacement results. For low gravity multipliers (Figure 4.9a and 4.9b), the deformation pattern is the same for all Young's moduli, while the lower the Young's modulus the larger the crest deformation. As the gravity multiplier increases the deformation pattern changes. At a gravity multiplier of 2 (Figure 4.9c) the displacement at the outer slope is larger for the lower Young's modulus, although at the inner slope the displacement is larger for the larger Young's moduli. An inflection point is found halfway along the dike crest, where the influence of the Young's modulus on the displacement is inverted. This is likely caused by stress redistributions caused by the large deformations, and illustrates the complexity of large deformation analysis. For the higher gravity multipliers (4.9d, and 4.9e), this effect is enhanced, whereby higher crest displacements occur for higher Young's modulus.

These results illustrate the importance of correctly estimating the Young's modulus when performing more advanced computations by means of the MPM. Also, it shows that as the design shifts towards displacement criteria, more soil investigation is needed in order to be able to correctly parametrise the material models.

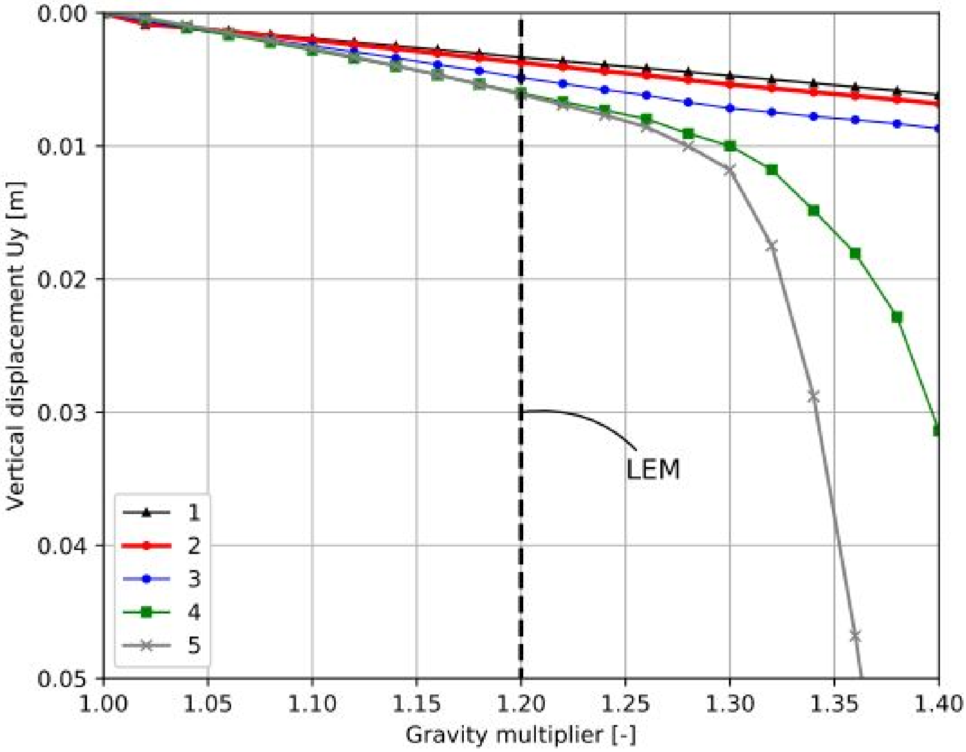

Figure 4.6: Vertical displacement for several points along the dike crest for low gravity multipliers.

## 4.4. Conclusions

This chapter presented the validation of the Anura3D MPM software, and dike safety analysis based on displacement criteria. The standard methodology for the assessment of dike safety is based on LEM, which does not take account of a deformation criterion. Based on MPM calculations it has been shown that, for the SF corresponding to the LEM, the dike crest displacements are very small. This means that the SF does not imply that the dike fails its requirement of retaining water, but just that an initial failure took place. After this initial failure the dike stabilises in a new equilibrium position.

The recent developments of the MPM enable one to look beyond this initial failure. From the analysed dike section, it has been shown that the dike continues deforming with increasing gravity, and that the dike failure is progressive. Profiles for the dike crest deformation were computed, which can be used to assess the dike safety by combining it with criteria for the maximum allowed displacement of the dike crest. Moving towards a displacement based safety assessment of dikes can have a positive impact for existing dikes, as it will provide a better prediction of their safety, as well as for dikes to be constructed, as it will allow for more economical designs.

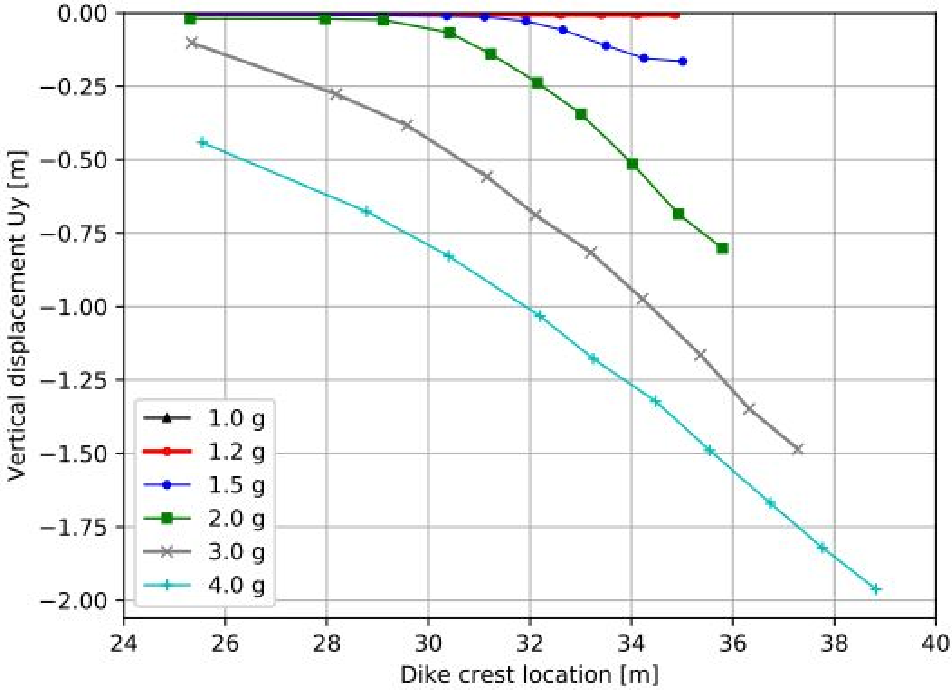

Figure 4.7: Dike crest profile for different values of gravity multiplier.

The analyses presented in this chapter can be considered as a first step in a transition towards a safety assessment based on displacement criteria. Future work concerns the definition of the maximum allowed crest displacement and this must be established within the probabilistic framework of dike safety. The transition towards displacement criteria is likely to require more and different soil investigations, in order to determine the stiffness parameters reliably.

## References

[1] Anura3D. Anura3d mpm research community, 2017.

[2] Deltares. Slope stability software for soft soil engineering. d-geo stability v16.1.1., 2016.

[3] M. A. Hicks and S. W. Wong. Static liquefaction of loose slopes. *Numerical Methods in Geomechanics*, I:1361–1367, 1988.

[4] L. Li, C. Tang, W. Zhu, and Z. Liang. Numerical analysis of slope stability based on the gravity increase method. *Computers and Geotechnics*, 36:1246–1258, 9 2009.

[5] C. C. Swan and Y.-K. Seo. Limit state analysis of earthen slopes using dual

continuum/fem approaches. *International Journal for Numerical and Analytical Methods in Geomechanics*, 23:1359–1371, 10 1999.

[6] H. Zheng, L. Tham, and D. Liu. On two definitions of the factor of safety commonly used in the finite element slope stability analysis. *Computers and Geotechnics*, 33:188–195, 4 2006.

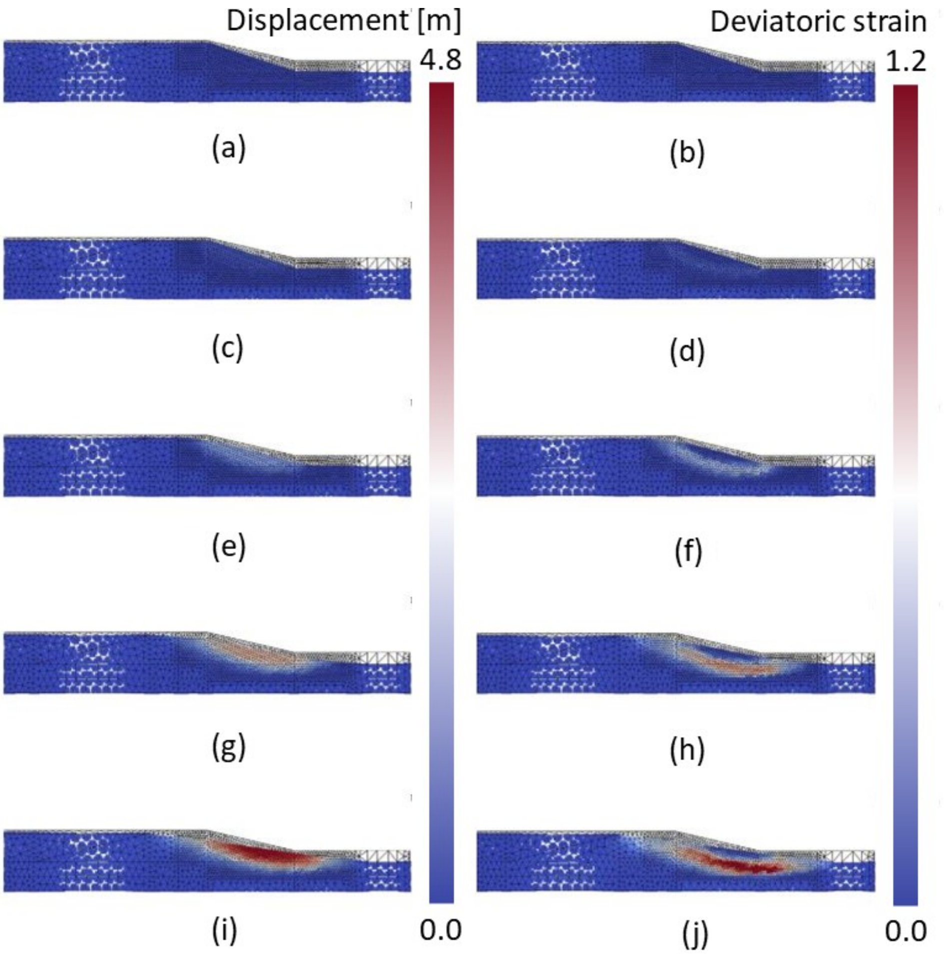

Figure 4.8: Displacement and deviatoric strain fields for different values of gravity: (a) and (b) 1.2g, (c) and (d) 1.5g, (e) and (f) 2g, (g) and (h) 3g, (i) and (j) 4g.

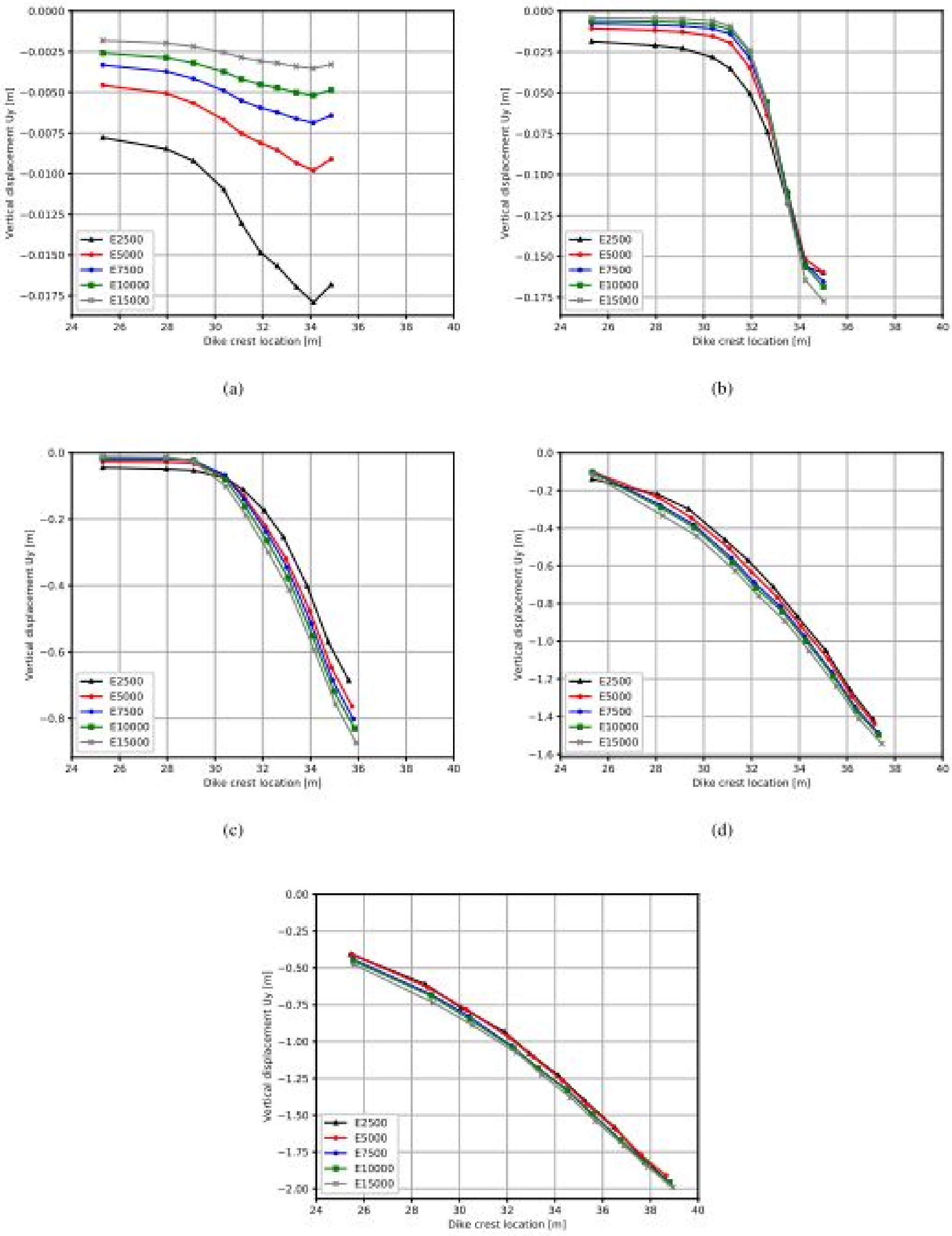

(a) (b)

(c) (d)

(e)

Figure 4.9: Effect of the Young's modulus on the crest profile for different values of gravity: (a) 1.2g, (b) 1.5g, (c) 2g, (d) 3g and (e) 4g.

# 5

# Field test above water of a complete slope failure: numerical analysis including kinematics

*In order to better understand (and assess) the risk or consequence of slope failure, it is important to understand the entire slope failure process, from initiation through to the final situation after slope failure. The assessment of slope stability for granular materials, i.e. failure initiation, is generally performed by using limit equilibrium methods (LEM) or the finite element method (FEM). The material point method (MPM) can also yield similar results; however, it can additionally compute the interim and consequences of the slope instability by taking into account large deformations. A large-scale field test and MPM simulations have been undertaken to investigate the slope failure phenomenon and the capability of MPM to simulate accurately the full process, including the kinematics of the failure. The instrumented slope is located well above the water table and in a uniform horizontal quartz sand layer. It is seen that MPM with a simple elastoplastic material model does not give realistic results in terms of geometry evolution during failure, leading to less steep final slopes than observed. A material model that is able to capture strain-softening behaviour during the failure process is necessary to achieve a kinematic and geometric evolution that is consistent with field measurements.*

## 5.1. Introduction

Predicting the consequences of a slope failure involves not only the prediction of the initial failure but also the evolution of the geometry and kinematics of the failing material during the slope failure. The prediction of initial failure has been investigated extensively in previous decades, and the behaviour is generally well captured using either limit equilibrium methods (LEM) (e.g. [8]), or with continuum numerical methods, for example the finite element method (FEM) with the strength reduction procedure (e.g. [21]). FEM has advantages in satisfying compatibility conditions for different soil layers and in not a priori defining slip circle shapes. However, these methods cannot account for large deformations.

The recent development of the material point method (MPM) allows the simulation of both the initiation and evolution of slope failures [14, 36] in a single framework. MPM is a continuum mechanics method, and because it utilises several features common to FEM, similar material models can be used. There are a wide number of recent developments and improvements ongoing in MPM: the development of implicit formulations (e.g. [27, 35, 38]), coupled hydromechanical formulations (e.g. [7, 37, 39]), unsaturated soil behaviour (e.g. [6, 37, 40]), numerical accuracy and robustness (e.g. [4, 22, 33]), and very large distortions (e.g. [31]), partly through collaborative software communities (e.g. [5, 11]).

Other methods, such as the discrete element method (e.g. [15, 43]), do not share the same continuum formulation and therefore require material models that are not frequently used for practical engineering purposes. In addition, the discrete element method becomes computationally expensive when applied to engineering-scale problems. Meanwhile, smoothed particle hydrodynamics (SPH) [13], although being a validated tool for large deformation analysis, falls short with respect to computational cost, stability and boundary treatment when compared to MPM [25, 30, 44].

One of the challenges for the development of MPM is the lack of analytical and experimental data sets to verify and validate large deformation behaviour, especially as elasto-plastic behaviour occurs. Compared to laboratory observations, field observations can provide additional insights into the role of scale effects in material behaviour and about processes that occur at the onset and during the evolution of a slope failure. A number of case studies have been presented in the literature where MPM has been used to simulate slope failure [24, 40–42]. Several have been reasonably successful in simulating the failure initiation and final deposition, although no measurements were available of the dynamic evolution of the failure. Therefore, the failure process, i.e. the kinematics and the material behaviour, could not be readily validated.

The main objective of this chapter is to present a full-scale slope failure coupled with a detailed geotechnical characterisation and monitoring campaign, and to analyse the failure with MPM models. In addition, the initiation of the slope failure has been simulated using traditional LEM and FEM methods, as generally suggested by design guidelines (e.g. the Dutch best practices guidelines (CUR113) [16] and the Eurocode [10]), as well as with MPM. The evolution of the slope failure predicted by MPM has been compared to the measured geometric and kinematic evolution in the field experiment. Two constitutive models are tested, these being a standard elasto-plastic soil model and the same model modified for large strains. The slope failure analyses presented are undertaken in a sandy slope above water as a first step toward the validation of MPM for underwater slides. A schematic of the validation workflow for this chapter is:

### Validation workflow

1. Site selection, desk study, soil investigation (Sections 5.2.1, 5.2.2, 5.2.3, 5.2.4)
2. Experimental and monitoring activities of slope failure (Sections 5.2.5, 5.2.6, 5.2.7)
3. Simplifying assumptions, numerical modelling and calibration of constitutive parameters from (1.) (Sections 5.3, 5.3.1, 5.3.2)
4. Preliminary numerical analyses with LEM and correction of apparent/peak cohesion assumed from (3.) to match field observations from (2.) for MC LEPP and MC SS constitutive relations (Sections 5.3.2, 5.3.3)
5. Numerical analyses and validation of FEM for the same constitutive relations used in (4.) (Sections 5.3.2, 5.3.4)
6. Numerical analyses and validation of MPM for the same constitutive relations used in (4.) (Sections 5.3.2, 5.3.5)
7. Discussion of complete slope failure process and conclusions (sections 5.3.5, 5.4)

## 5.2. Slope failure experiment

### 5.2.1. Introduction

The controlled slope failure experiment involved monitoring an artificially triggered slide in an uniform sand layer, from initiation through to deposition of the material. Slope failure was triggered by undercutting the slope toe with a wheel loader (a prior risk assessment had been performed). The main aim of the test was to monitor the evolution of the sliding soil mass geometry, velocity and acceleration during a slide at engineering scale, including triggering mechanism and onset and deposition of the sliding soil mass.

An accelerometer and a video camera were the primary monitoring tools used in this field test, which was the first test in a series to prepare for an underwater flowslide test. It offered an opportunity to monitor a slope failure where mostly dry material was involved, the phreatic water table being located well below the slope. However, a limited amount of pore water was present that affected soil behaviour. The slope was located in an active sand quarry, from here on called Site-A, as shown on the digital elevation map (DEM) in Figure 5.1. This map was generated from LiDAR point clouds provided by the Belgian National Geographic Institute and its nominal accuracy is $0.5$ m [3].

Sibelco generously granted access to its quarry facilities for the experimental programme conducted in the frame of this study. The company's support, infrastructure, and technical cooperation were instrumental in enabling the successful execution of the experimental campaign. The authors gratefully acknowledge Sibelco's valuable contribution, which significantly enhanced the practical relevance and feasibility of the research.

### 5.2.2. Geometry

The slopes in the Site-A sand quarry generally show gentler angles at the toe, due to loose material deposited from natural hillslope processes (i.e., recent erosion processes or small failures). With reference to Figures 5.1 and 5.2, this is most obvious in the C-C and D-D cross-sections, with the A-A cross-section transitioning more gradually from a shallow to a steep gradient (bottom to top). Meanwhile, the B-B cross-section represents a slope closer to a ramp and has an even shallow gradient throughout.

Differences in these typical geometry configurations may be due to variability in relative density and / or unsaturated water content, resulting in pressure gradients, both of which affect soil shear strength. The gentler gradients at the toe suggest that this material generally has a lower shear strength than in the main part of the slope body. As this material is presumed to be the result of natural hillslope processes, it is thought that the material softens as it fails. This also suggests that the soil in the main body of the slope will be dilative during failure.

The slope geometry selected as the best representation of the field experiment geometry is the C-C cross-section, shown in Figure 5.2. The soil layer is uniform sand and, as the sandy slopes are of similar height throughout the quarry, the steepest slope is likely to be the most unstable slope and therefore the easiest in which to trigger a failure. Additionally, it resembles the naturally occurring slope geometries at the excavation fronts during wheel loader mining activities in this quarry.

The slope for the test was selected by two criteria: the slope height should be greater than $10$ m and its cross-section should be reasonably regular for at least $20$ m along the length of the slope. The first criterion ensures that there is a significant effect of confining stresses in the deepest soil layers, giving this dataset additional value compared to laboratory experiments. The second criterion reduces the influence of three-dimensional effects.

The slope toe was removed with a wheel loader to trigger the failure: sand from the toe was excavated, thereby increasing the average angle of the slope until failure occurred. Wheel loaders allow the removal of large volumes of sand at each excavation step; hence it is a convenient tool for triggering the slide, as well as for mining activities and transporting the excavated material (e.g. to the conveyor-belts or dumper).

For safety reasons, it is not generally allowed to extract the sand below an overhang (no undermining), nor to excavate a slope higher than the excavating machine's reach. Normally such high slopes are mined in multiple benches for reducing the loading height. Details of Sibelco safety guidelines for their extraction operations with wheel loaders can be found in [32]. To allow the experiment to be performed with a high slope, a prior risk assessment with LEM calculations (and

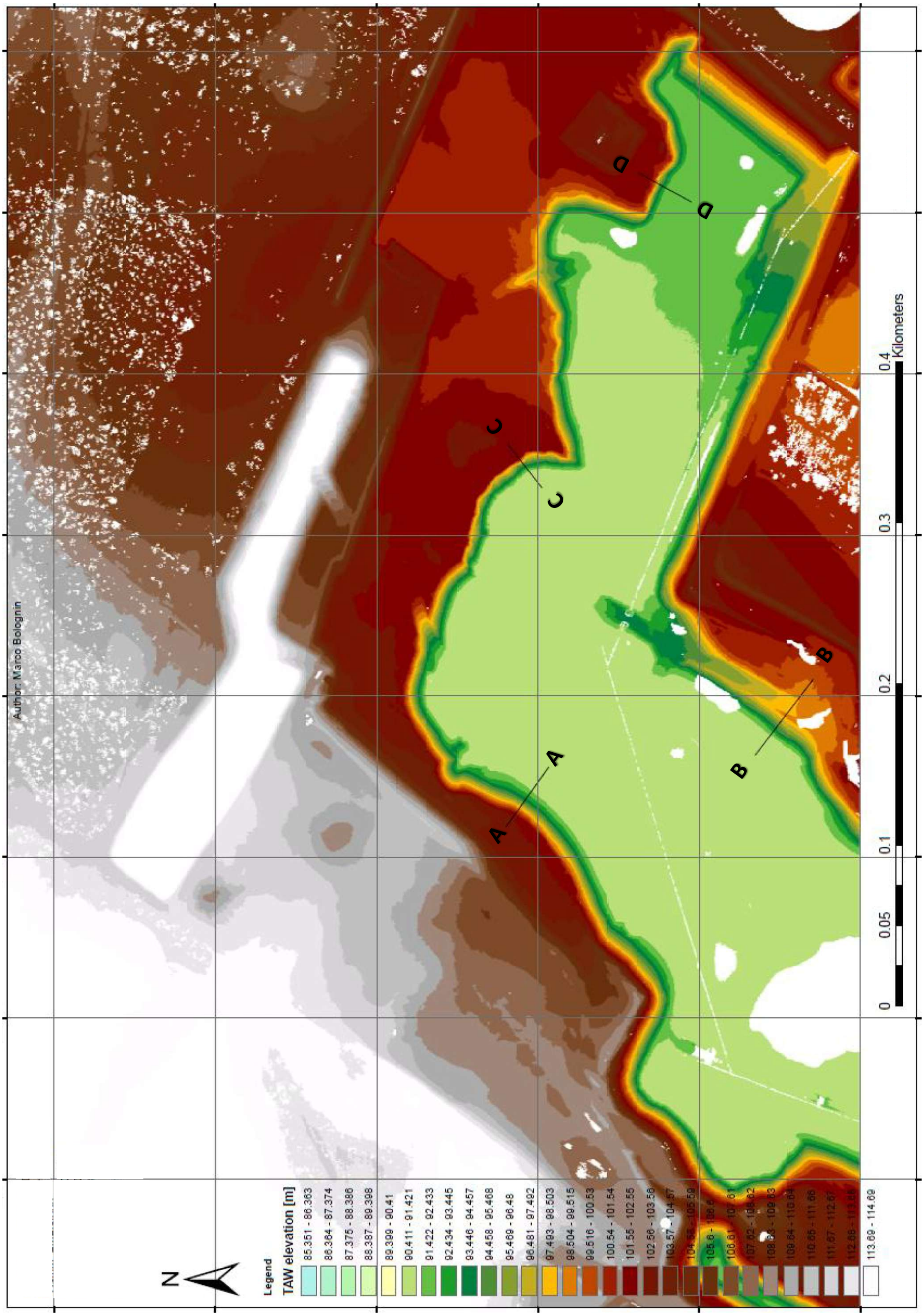

Figure 5.1: Digital elevation map of Site-A sand quarry generated from LiDAR data provided by the Belgian National Geographic Institute. Cross-sections extracted for the geometry selection are highlighted in black (A-A to D-D).

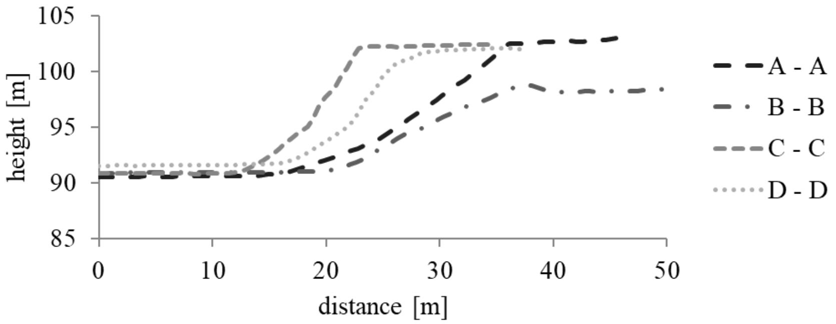

Figure 5.2: Cross-sections for the slope geometry selection in Site-A sand quarry.

later confirmed with MPM) was performed, and this was approved by the responsible Geotechnical Engineer from Sibelco who was also on watch during the experimental activities.

Additionally, the wheel loader operator was informed of the foreseen risk of the experimental activities and instructed to load in a perpendicular direction to the slope face while observing the slope carefully. Furthermore, large wheel loaders have a long reach and a high cab position which further reduces the risk of engulfment. The activities for the experiments were performed in a central area of the quarry so that their execution would be inconsequential for the final slope geometry of the quarry.

This toe undercutting triggering mechanism of a slope may also resemble the effects of natural erosion, i.e. due to water flows. A schematic geometry is shown in Figure 5.3, with $area\,A$ and $area\,B$ representing the excavated material. Several failures were triggered around the same site to ensure qualitative reproducibility of the slide in this quarry.

### 5.2.3. Site investigation and material parameter determination

From pre-existing geological investigations performed [34], the quarry is located in a thick homogeneous layer of pure quartz sand. A visual assessment in the field (and from available pictures) confirmed the geological interpretation, as the slopes appeared uniform without layering and white in colour. In addition, a high relative density was indicated by the steep slopes. Disturbed samples were retrieved with hand drills for the laboratory investigation, and the resulting borehole was subsequently used for the accelerometer installation and filled with sand spoil.

### 5.2.4. Laboratory investigation

From the retrived samples in the field, a grain size distribution, three-stage direct shear tests (DST) were undertaken at University of Liége [20] and three multi-stage DST at the Geo-Lab of TU-Delft [2].

The grain size distribution is shown in Figure 5.4. The uniformity and curva-

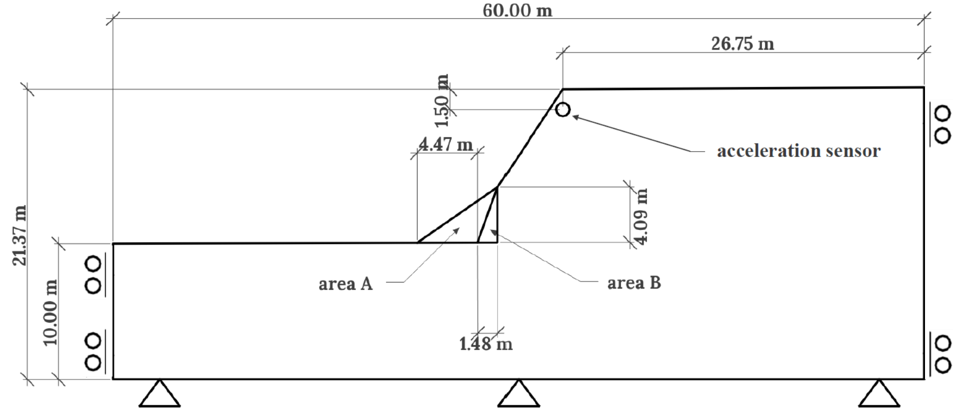

Figure 5.3: Geometry used for the slope stability analyses. $area\ A$ and $area\ B$ at the toe are removed in order to represent the excavation processes visible in Figure 5.7. The estimated initial position of the acceleration sensor is highlighted with a circle at the slope crest.

ture coefficients were calculated as $Cu = 1.5$ and $Cc = 0.9$ respectively, thereby classifying the soil as a uniformly graded sand.

The single-stage DST were performed on three different reconstituted samples following ISO 17892-10 [28]. The samples were pre-loaded with different vertical stresses ($85$ kPa, $171$ kPa and $341$ kPa) and the shearing velocity was kept constant throughout the experiment at $13$ mm/h. The samples were tested as received, and the in situ water content was assumed to be $2.5\%$ by weight. Other test data are shown in Table 5.1. The results are shown in Figure 5.5 and allowed the estimation of both the peak and residual values of friction and cohesion. The lines chosen for this interpretation are included in the figure.

Table 5.1: Test data from the single-stage and multi-stage DST tests. $H^*$ is the sample height; $\sigma'_y$ is the vertical effective stress; $\gamma$ is the bulk unit weight; $\gamma_d$ is the dry bulk unit weight; $\gamma_s$ is the sand grains unit weight; $w$ is the sample water content; and $n$ is the bulk porosity.

| Sample # | $H^*$ $(mm)$ | $\sigma'_y$ $(kPa)$ | $\gamma$ $(kN/m^3)$ | $\gamma_d$ $(kN/m^3)$ | $\gamma_s$ $(kN/m^3)$ | $w$ $(\%)$ | $n$ $(-)$ |
|---|---|---|---|---|---|---|---|
| 1 | 10 | 85 | 15.74 | 15.35 | 26.31 | $2.5^a$ | 0.417 |
| 2 | 10 | 171 | 15.59 | 15.21 | 26.31 | $2.5^a$ | 0.422 |
| 3 | 10 | 341 | 15.03 | 14.67 | 26.31 | $2.5^a$ | 0.442 |
| 4 | 20.9 | $26, 46, 66^b$ | 15.60 | 15.60 | 26.31 | 0.03 | 0.414 |
| 5 | 22.5 | $26, 46, 66^b$ | 15.42 | 15.42 | 26.31 | 0.02 | 0.407 |
| 6 | 23.5 | $26, 46, 66^b$ | 16.16 | 16.16 | 26.31 | 0.01 | 0.386 |

$^a$assumed value, $^b$multi-stage tests

The multi-stage DST were carried out on three samples with different initial dry densities (loose, medium and dense). As soon as the sample reached the peak value of shear resistance, i.e. when the horizontal strain increased with no increase

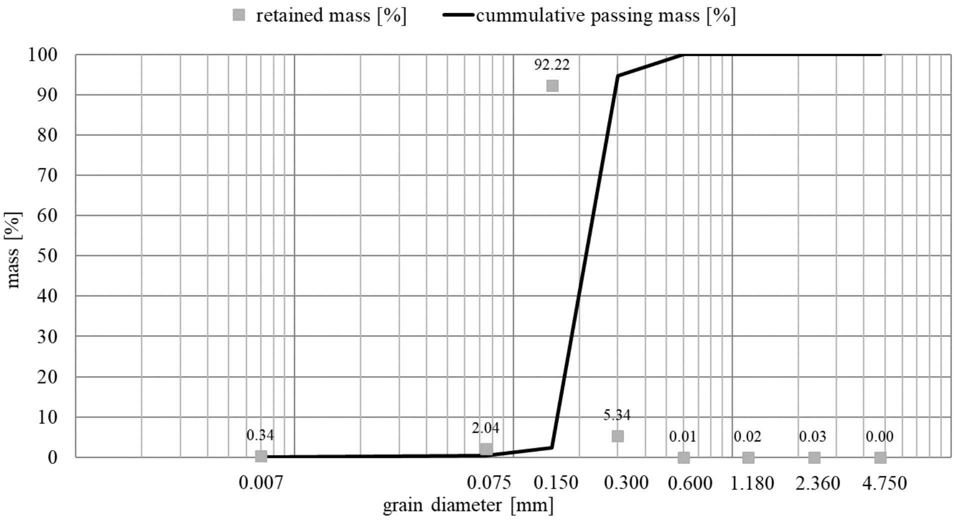

Figure 5.4: Grain size distribution for Site-A sand [20].

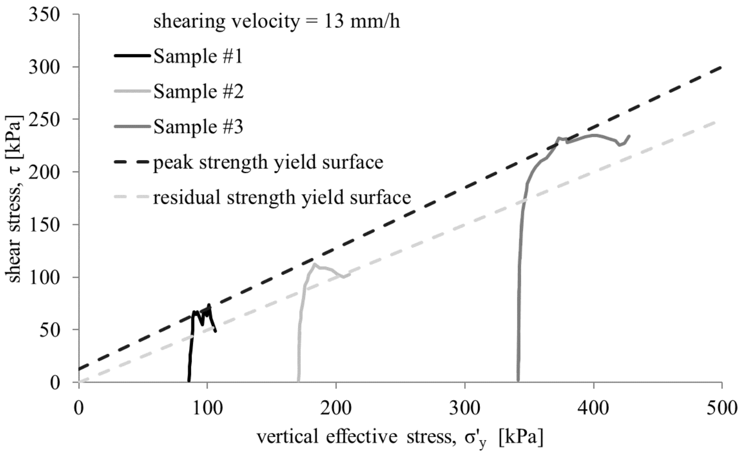

Figure 5.5: Single-stage DST results and the Mohr-Coulomb peak and residual failure envelopes [20].

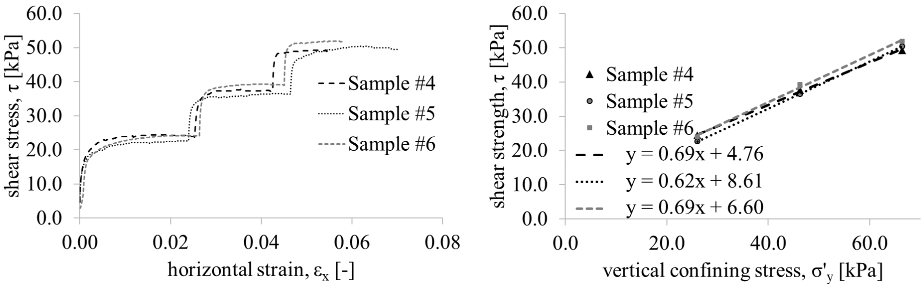

Figure 5.6: Multi-stage DST results. The shear strength values chosen for the soil parameter calibration are shown against the effective (normal) stress.

Table 5.2: Calibration of Site-A sand strength parameters from laboratory investigation.

| | Sample # | $\varphi$ (°) | $c$ (kPa) |
|---|---|---|---|
| Peak values from single-stage DST | 1, 2, 3 | 30 | 13 |
| Residual values from single-stage DST | 1, 2, 3 | 27 | 0 |
| Peak values from multi-stage DST | 4 | 32 | 9 |
| Peak values from multi-stage DST | 5 | 35 | 5 |
| Peak values from multi-stage DST | 6 | 35 | 7 |

in applied shear stress, the shearing of the sample was stopped and the vertical confining stress increased before shearing of the sample resumed.

Care was taken to avoid softening, observed at higher shear strains. Therefore, the test data do not show softening, preventing the assessment of residual strength parameters. However, these tests do allow the determination of peak values of friction and cohesion with a single sample. For this series of tests, the samples were fully dried and the water content was always below $0.03\%$ in weight. The vertical loads for the 3 loading stages were $26$ kPa, $46$ kPa and $66$ kPa, and the results are shown in Figure 5.6. Interpretation of the multi-stage DST suggests an average peak friction angle of $34°$ and an average value of (apparent) peak cohesion of $7$ kPa.

Material parameters determined for a Mohr-Coulomb failure envelope for both sets of tests are summarised in Table 5.2. The small discrepancies in the results highlight the sensitivity of the sand to the initial testing conditions and sample dimensions. Sand is generally considered a cohesionless material; however the observed cohesion may be attributed to the relative density and the water content. The water plays a double role: it acts as a lubricant between the sand grains reducing the angle of friction, while, at the same time, as it is unsaturated it creates menisci around the grains increasing the apparent cohesion.

The values of in situ unit weight have been estimated using available sand laboratory investigation data from another quarry (Site-D) that has a similar grain size distribution and chemical properties, by looking at the minimum and maximum values of unit weight recorded when applying the DGI method, 13.6 kN/m$^3$ and 16.7

kN/m$^3$, respectively [19]. Because the sand in the slope body is expected to be in a dense state, based on the observed steep slope angles, a value around the highest observed in the laboratory testing was selected, i.e. $\gamma_d$ of 16 kN/m$^3$.

Following this study, in situ investigations results were made available by Sibelco for Site-A by means of handheld devices (i.e. using a standard volume or with the water replacement test). Their investigations showed superficial density values of 1.526 t/m$^3$ with standard deviation of 0.031, validating the assumptions made for the selected value of density of the target sand slope.

### 5.2.5. Monitoring system

#### Acceleration/inclination sensor

As large deformation throughout the whole failure process is the focus here, inclinometers which are often used to measure the onset of slope failures cannot be used. An acceleration sensor was installed in the slope crest, $1.5$ m below the soil surface. The system comprised an accelerometer mounted in a cylindrical aluminium casing. The dimensions of the casing were $6$ cm in diameter and $10.5$ cm in height. Additionally, a magnetic compass was included in the casing in order to calculate the motion orientation and rotation.

As the material involved in the slide was unsaturated sand, the duration of the slide was expected to be short due to limited hydro-mechanical effects; hence high frequency sampling sensors were chosen. From laboratory experience, a measurement frequency of $100$ Hz was considered sufficient to distinguish and record the relevant changes in the different phases of the sand flow slide [26]. The range of accelerations necessary for capturing these phenomena is $\pm 1.0\ g$ as the only destabilising force on the slope was its self-weight. Assuming that the connection cables to the logger have a negligible effect on the sensor inertia, the accelerometer recorded the soil mass motion from onset to deposition. This sensor allows live monitoring of the measurements; hence the experiment could have stopped if a dangerous situation would have arisen (e.g. in the scenario that pre-failure displacements were detected).

#### Video Camera

The failure was recorded on video in order to capture the qualitative dynamic and kinematic features of the sliding event. The camera was positioned on the southern side of the experimental slope in order to compare the screenshots to simulation results.

### 5.2.6. Failure mode hypotheses

Undercutting the slope toe generates a steeper excavation front due to the apparent cohesion given by the suction from the unsaturated water content and the relatively high relative density. Repeated excavation steps increase the size of the excavation front and trigger a macro-instability of the slope that will result in a sliding soil mass bounded by an approximately circular slip surface. Dense sand is generally characterised as a frictional and stiff material. The high relative density, indicated by the high angle of repose of the initial slope, suggests a dilative behaviour. This

Figure 5.7: a) Slope profile before the last excavation step and assumed geometry used for the numerical simulation (schematic geometry in Figure 5.3 with $areaA$ removed); b) final slope profile, after the induced slope failure.

hints to (i) a failure localising to a shear band, which softens as the shear strains increase, (ii) leading to a log spiral shape of the failure surface (rather than a circular failure) [9], and (iii) involving the failure of initially intact soil blocks, which may then further break up as the failure progresses due to a reduction in confinement. As the most loaded soil is located in the deepest layers close to the vertical excavation front, the failure is expected to propagate from the bottom to the crest of the slope. The high slope angle also suggests that the failure surface will pass through the toe.

### 5.2.7. Results

The wheel loader filled its bucket multiple times to remove the loose sand deposited at the toe. As the wheel loader move backwards after every filling of the bucket (hence removing lateral soil support from the slope toe), thin layers of sand from the slope formed shallow slides depositing ahead the excavation wall. The excavation procedure continued, involving also the denser sand, until generating an almost vertical wall before triggering the slide. The excavation front before failure was similar in height to that of the wheel loader.

During all triggered slide events, the back scarps left by the slip surfaces were not smooth circles, but exhibited an irregular shape that can be approximated by a circle that fails in multiple blocks. This failure mechanism is generally a consequence of the presence of apparent cohesion in the granular material. The apparent cohesion was probably due to water suction which subsequently dissipates when large deformations occur.

Multiple slides were triggered to investigate the reproducibility of the experiment and to assess the reliability of the triggering method and monitoring system, and these resulted in similar failure modes. The first slide event was recorded with the acceleration sensor and the three dimensional accelerations are reported in Figure 5.8 in the global coordinate system. Details of the kinematics are discussed in Section 5.3.5, alongside the numerical analysis. The final slope is shown in Figure 5.7b.

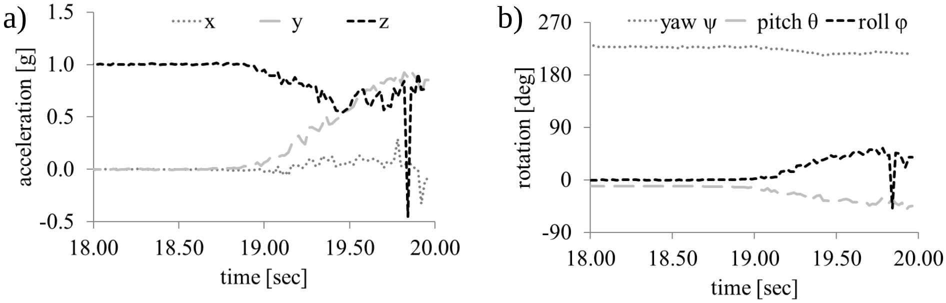

Figure 5.8: Data from the acceleration sensor during the first sliding event: a) the acceleration vector components expressed in the global coordinate system, where z is the vertical component; b) rotation angles, magnetic North corresponds to 0° yaw angle.

## 5.3. Numerical modelling

The desk study and experimental data are used for the validation of the numerical approaches. First, the results using LEM and FEM are compared in a fashion similar to [12, 17, 21, 23], and this comparison is then extended to MPM. The accuracy and performance of the methods are highlighted and discussed.

The dynamic explicit MPM implementation with linear mapping/interpolation functions is used, with 3-noded triangular elements and mixed-Gaussian integration [5]. The material behaviour is represented by different linear-elastic, plastic constitutive models, using a Mohr-Coulomb failure envelope, with the parameters chosen from data presented in Section 5.2.3.

### 5.3.1. Geometry

The slope geometry chosen for the numerical models is a schematisation of cross-section C-C in Figure 5.2. For FEM and MPM models, the initial stresses are generated using gravity loading. Then two further loading stages are modelled, by removing $area\ A$ and $area\ B$ sequentially from the toe, as indicated in Figure 5.3, to simulate the excavation process. For the LEM model, only the geometry after the first excavation step (without $area\ A$ in Figure 5.3) is considered, because it resembles the last observed stable configuration before failure.

### 5.3.2. Material models and parameter calibration

The soil slope is modeled as a homogeneous geotechnical layer, i.e. having uniform material parameters. Simple material models are used: the Mohr– Coulomb (MC) failure envelope is used in the LEM analyses and the Mohr– Coulomb linear-elastic, perfectly-plastic (MC LEPP) model is used in the FEM and MPM computations. Additionally, a more advanced constitutive model, Mohr–Coulomb Strain-Softening (MC SS), is used to simulate possible strain-softening effects due to the large strains occurring.

Note that most of the samples used in the shearing devices were tested at relatively high values of porosity and that the in situ sand is expected to be comparable to the higher densities tested in the laboratory. This is because loose sand cannot support stable slope angles that are higher than the angle of repose. It can also be observed (Table 5.1) that the dry unit weight of the samples for the single stage DST is lower than those for the multistage DST.

Higher soil unit weight is expected to enhance the dilative behaviour of the sand and, in turn, can generate more suction during initial loading (in those samples with sufficient water content), which will further increase the apparent cohesion present in the soil; as the shearing continues due to the large deformations, the water menisci around the grains can break, dissipating the suction. The peak friction angle was seen to be dependent on the initial dry unit weight as shown in Figure 5.9(b).

The friction angle is generally seen to increase with unit weight, although this variation is relatively small. As the in situ unit weight is thought to be at the higher end of that shown in the figure, a value of $34°$ has been selected. This value is supported by literature as the friction angle of pure quartz sand at the critical state is equal to around 33° [9]; therefore, assuming slightly higher values for a denser state is considered reasonable.

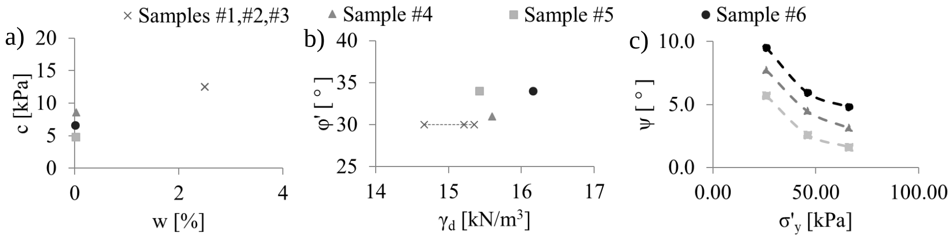

Figure 5.9: Variation of experimentally determined parameters against sample state: a) measured cohesion against water content; b) measured friction angle against dry unit weight; c) measured dilation angle against confining pressure.

Cohesion, or rather apparent cohesion, is seen in Figure 5.9(a) to be a function of water content, although it is not possible to estimate the maximum value of this function with the available data. The Poisson's ratio and Young modulus are assumed equal to 0.3 and 30.0 MPa, respectively, as these are relatively insensitive parameters for the analysis and are reasonable values for coarse spherically-grained sands [45].

Directly using any of the calibrated soil parameter sets from the laboratory investigation, for the LEM and FEM analyses, resulted in a factor of safety (SF) below 1.0 (i.e. an unstable slope). However, the slope in the field was stable before the experimental activities commenced and during the excavation of $area\ A$ of the toe (which implies SF $\geq 1$). Aside from 3D effects, this discrepancy may be attributed to small variations in the material parameters due to the sample unit weight and water content. Due to the limited available laboratory tests and difficulties in undisturbed field sampling, the apparent cohesion was recalibrated using LEM analyses: as the field evidence showed a stable slope during the first part of the toe excavation, the cohesion was gradually increased while computing the slope SF for the second geometry (after the first excavation stage), keeping constant the friction angle until achieving an SF equal to 1.0. For MC LEPP, this procedure was undertaken adopting a residual dilation angle of zero as for large strains a constant non-zero dilation angle results in unrealistic results.

This resulted in a value of apparent cohesion equal to 16.0 kPa, close to the peak value observed in the single-stage DST. For the MC SS model, a (peak) dilation angle of 5° was assumed, based on Figure 5.9c and a reasonable estimate of the confining stresses at the toe of the slope, which would be expected to suppress dilation to about 5°. This resulted in an initial value of peak cohesion of 14.0 kPa.

The residual value of friction angle estimated from the single-stage DST was 27°. However, the same inferences made for the MC LEPP calibration protocol about the initial sample unit weight also apply here. Therefore, in order not to underestimate the critical state friction angle, 33° was considered a reasonable value to use for the sand in the analysis, because the material is almost pure quartz sand [9]. The residual value of cohesion is assumed to be close to zero due to the granular material, but selected to be equal to $1$ kPa for numerical stability. The residual dilatancy is assumed to be zero, consistent with critical state soil mechanics.

In the MC SS constitutive model, the values of friction angle and cohesion decrease proportionally to the deviatoric strain of the material according the following relationship:

$$x' = x'_r + (x'_p - x'_r)e^{\eta \epsilon^p_{eq}} \tag{5.1}$$

where $\epsilon^p_{eq}$ is the deviatoric strain, $\eta$ is the shape factor to control the softening rate and $x'$ can be any of the shear strength parameters, i.e. $c'$, $\varphi'$ or $\psi'$.

The adoption of strain-softening constitutive models in standard FEM formulations leads to mesh dependency of the results [29], which can be overcome using regularisation techniques. A smeared crack approach is used in the FEM and MPM applications when using MC SS, by assuming that the energy dissipated by a theoretical discrete crack is equal to the total work dissipated by a shear band of arbitrary thickness. In FEM and MPM, the thickness of a shear band is approximated by the mesh size. By considering displacements large enough to reach residual strength values, a set of numerical shear tests with different element sizes has been compared for the calibration of $\eta$ using MPM.

A schematic representation of the computational model and boundary conditions of the numerical shear test is presented in Figure 5.10. Initially, empty elements are included (above and to the right of the soil specimen) in order to allow dilation and distortion of the soil sample during shearing. The boundary conditions are applied at the nodes: zero displacement in the horizontal and vertical directions was imposed at the base of the elements representing the soil sample, while on the top edge, after a first load step for the imposition of a constant vertical stress ($85$ kPa as in the laboratory test sample #1), it is then sheared with an applied constant horizontal velocity. As the model is shear rate independent, any shearing velocity yields the same solution. In order to quantify the mesh dependency of the numerical results, two different mesh sizes ($0.5$ m and $1$ m, respectively) were used.

In Figure 5.11, the effects of the two mesh sizes and different values of the shape factor on the shear strength estimation are compared. The shape factor was selected by comparing the numerical results with the experimental curves for the mesh size used in the model, such that a similar strength softening rate is achieved. Figure 5.12 shows that the obtained strength reduction rate with $\eta = 10.0$ and an element size of 0.5 m is comparable to the experimental result.

The full set of calibrated material properties for the MC LEPP and MC SS material models are reported in Table 5.3.

### 5.3.3. Slope stability assessment with LEM

LEM analyses have been performed using Bishop's modified method [8], as implemented in D-Geo-Stability [18]. The SF represents the value by which the original strength parameters ($c'$ and $\tan\varphi$) have been scaled down in order to bring the slope to the point of failure. A series of different slip circles (changing centres and

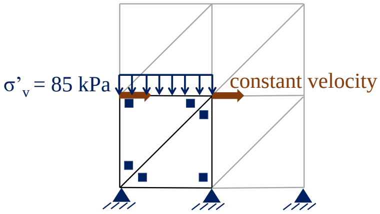

Figure 5.10: MPM computational domain, including boundary conditions, for shear test used for the calibration of MC SS parameters.

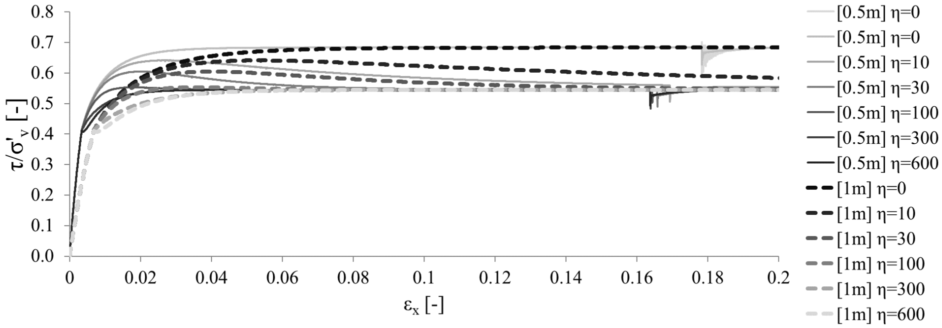

Figure 5.11: Comparison of numerical results for shear test, using different combinations of mesh size and shape factor for the calibration of MCSS parameters.

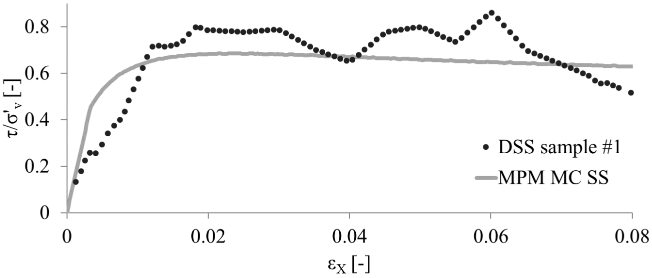

Figure 5.12: Comparison of computed response versus laboratory data for single-stage DST with initial confining stress of 85 kPa.

Table 5.3: Site-A sand geotechnical parameters after recalibration with LEM analysis to match field observations.

| *parameter* [unit] | $\gamma_d$ [kN/m$^3$] | $\varphi_p$ [°] | $c_p$ [kPa] | $\psi$ [°] | $\varphi_r$ [°] | $c_r$ [kPa] | $\psi_r$ [°] | $\eta$ [-] | $E$ [MPa] | $\nu$ [-] |
|---|---|---|---|---|---|---|---|---|---|---|
| MC LEPP | 16 | 34 | 16 | 0.0 | - | - | - | - | 30 | 0.3 |
| MC SS | 16 | 34 | 14 | 5.0 | 33 | 1.0 | 1.0 | 10 | 30 | 0.3 |

radii) are examined and the lowest value of SF is selected as the critical one. Each trial failure was discretised into 50 slices.

The results of the LEM analysis after the first excavation step are presented in Figure 5.13. In this figure the slip circle corresponding to the lowest SF is shown by the solid black line. The coordinates (Xm, Ym) represent the center coordinates of the critical slip circle. All slip circle centres considered in the analyses are indicated by black crosses and the tangent lines by light green horizontal lines.

The results using the shear strength properties from the MC LEPP model are plotted in Figure 5.13a and the results using the strength properties from the MC SS model are plotted in Figure 5.13b. The slope body colour coding represents the envelope of all the slip surfaces considered and corresponding value of SF. The results show agreement in the determination of the slip surfaces with the lowest SF, despite the differences in the input parameters, with both analyses predicting a shallow slip circle passing through the slope toe. The location of the sliding plane qualitatively matches the experimental results well. The dilation angle has a negligible effect in this case, due to the unconfined nature of the problem and no consideration of the ongoing deformation.

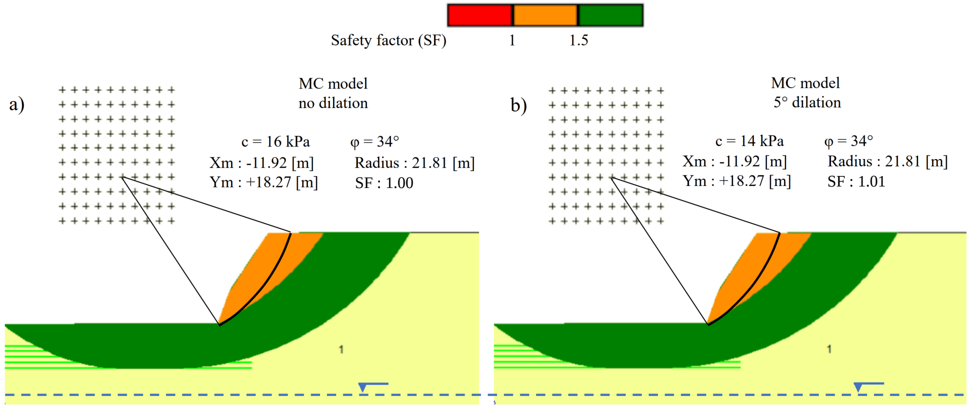

Figure 5.13: LEM results for the Site-A test slope analysis: a) using shear strength parameters without dilation; b) using shear strength parameters with dilation. The horizontal blue dashed line represents the considered ground water table.

### 5.3.4. Slope stability assessment with FEM

The slip surface has also been assessed with the FEM commercial code Plaxis2D [1]. In this approach, the shear strength parameters are progressively reduced until the slope is no longer stable.

The same set of soil parameters used for the LEM were used for the FEM simulations (see Table 5.3). The domain discretisation used $4^{th}$ order triangular elements and is shown in Figure 5.14.

The boundary conditions are applied to the edges of the model as indicated in Figure 5.3. The excavation is simulated by deactivating volumes (or areas in 2D)

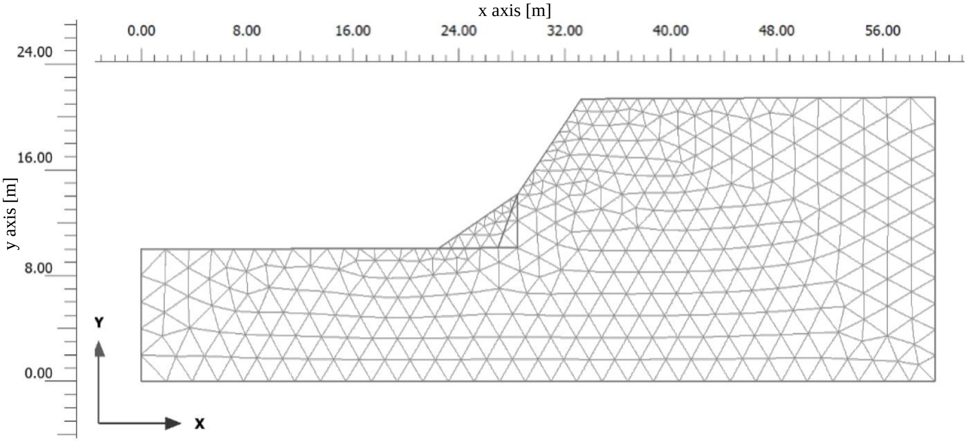

Figure 5.14: FEM mesh discretisation.

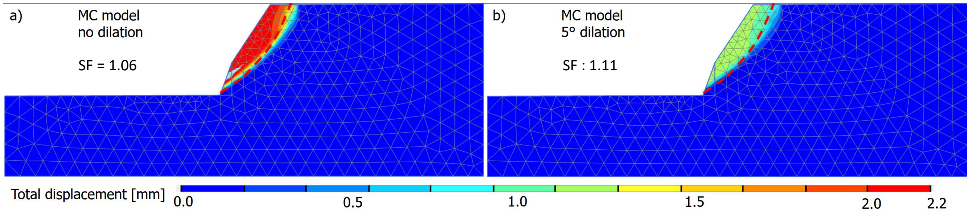

Figure 5.15: FEM results of total displacement after 1st excavation stage, compared to the predicted slip surface from LEM results (shown by the dashed red line): a) using shear strength parameters without dilation; b) using shear strength parameters with dilation.

of soil from the model instantaneously, thereby reducing the stabilising effect of the slope toe. The strength reduction method is used and failure is here defined as occurring when the determinant of the Jacobian of one of the mesh elements becomes negative.

After initialising the stresses by gravity loading, the toe is excavated in two steps. The slope SF after the first excavation step was calculated to be 1.06 for the MC without dilation and 1.11 for MC with dilation, which are both slightly larger than those calculated by LEM. The calculation stops when the second excavation step is modelled, indicating that the SF was already below 1. The shape and location of the slip circle is comparable to the LEM results, as seen in Figure 5.15. It can be concluded that LEM and FEM with the strength reduction method yield consistent solutions for the safety assessment of the slope considered. Additionally, they both predict well the shape of the initial slope failure.

### 5.3.5. Slope modelling with MPM

For the MPM analyses, the 2D version of the Anura3D software was used [5]. Linear mapping functions for the numerical integration and mapping algorithm are used, together with an explicit time integration scheme. An unstructured mesh with 3-noded triangular elements was used, with a refined mesh at the location of the expected slide, as shown in Figure 5.16. Considering that the elements in Plaxis have quadratic basis functions, a finer mesh is used for the MPM analyses (that use linear mapping functions). Three material points (MPs) initially per element were considered sufficient for the solution with the mixed Gaussian integration formulation, in which Gaussian integration is used for fully filled elements and material point integration for partially filled elements. For the time step size, the Courant number is kept as 0.98 to satisfy the Courant-Friedrichs-Lewy condition and a global damping coefficient of 0.05 was applied to introduce additional energy dissipation (i.e. due to the thermal effects of friction or to account for air drag, etc.). The boundary conditions and loading stages are consistent with the FEM model.

The results of the MPM simulation with the MC LEPP material model and parameters are shown in Figure 5.17, and the results with the MC SS material model and parameters are shown in Figure 5.18. In both analyses the slope was shown to be stable after the first excavation step ($areaA$ removed), but failed after the second excavation step ($areaB$ removed). The computed shape of the initial slip surface is in agreement with the LEM and FEM results for both analyses (with the LEM failure surface shown by a dotted red line for the end of the first excavation stage in each figure).

#### Kinematics of the slope failure with MPM

The results over time from the MC LEPP MPM simulation are presented in Figure 5.17. A slip surface is seen to propagate from the toe to the crest of the slope after the second excavation step (see Figure 5.17c,d); this stage corresponds to the beginning of failure in the field experiment. However, as soon as MPs move downward, the slope finds a new equilibrium state (Figure 5.17d). This is in contrast to field observations where, after the initial acceleration of the soil mass, a debris

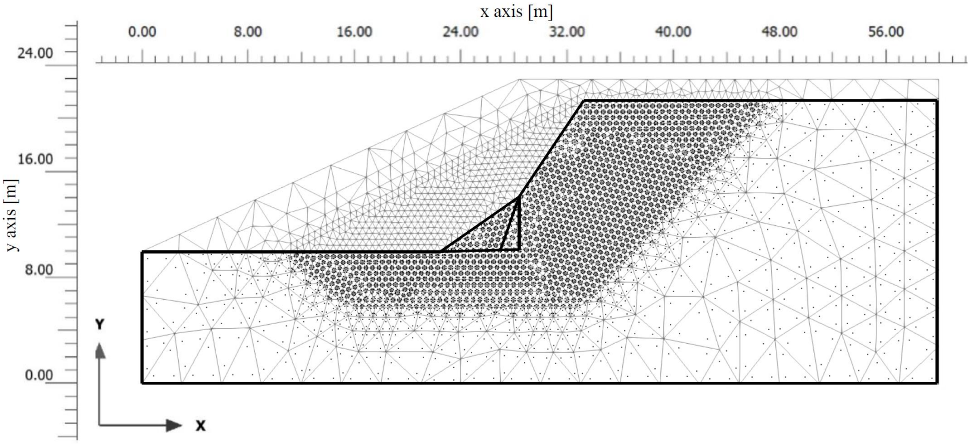

Figure 5.16: Mesh and material point discretisation used for the MPM analyses. The soil body is highlighted by the thick black lines.

flow resulted from the moving mass leaving a steep back-scarp in the upper part of the slope.

In order to conservatively assess the consequences of a possible run-out, the apparent cohesion was manually set to $0.0$ kPa after removing the last volume of soil from the toe. With this artefact the slope fails in about $5$ s, resulting in a relatively uniform slope with a lower angle of repose (see Figure 5.17h). This simulation indicates that even in the case that the soil layer would loose all its apparent cohesion (e.g. due to vibrations) and that the wheel loader could not move away in time, the wheel loader cabin would remain above the run-out profile (i.e. safe position for the operator). However, the final geometry overestimates the run-out and retrogression length and the shear band moves progressively further into the back-scarp, in contrast to what was observed during the experiment, suggesting that a main error source for this discrepancy is the constant value of the apparent cohesion throughout the soil body which is not representative for soil under large shear deformation.

In the analysis of kinematics for the simulation using MC SS as the material model, it is not required to adapt the soil parameters during the simulation. The kinematics, run-out and retrogression length are well captured, as shown in Figure 5.18. In Figure 5.18a, the deviatoric strain shows the simulated evolution of shear bands and deformation. An initial complete shear band is shown developing from 0.1 to 0.6 seconds. From 1.0 to 6.0 seconds a mass of soil is separated from the slope, leaving a steep back-scarp. At 6.0 seconds the final situation is shown. The simulation result can be compared to video stills from the test shown in Figure 5.18b. The failure surface from Figure 5.18a is superimposed on the video stills. It is clear that the kinematics of the failure process are well reproduced.

The displacements derived from the acceleration data are shown in Figure 5.19 (vertical displacement has a negative sign and horizontal displacement has a pos-

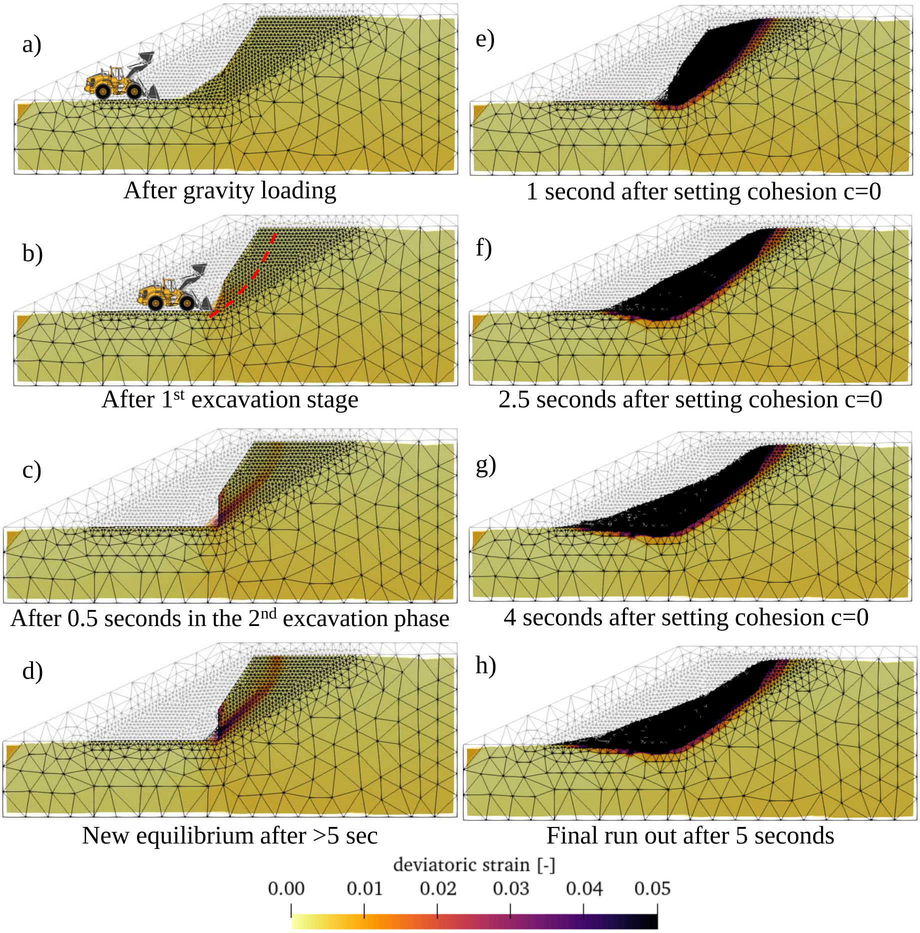

Figure 5.17: Deviatoric strain contour plots at various times from the MC LEPP MPM simulation. An image of the wheel loader to-scale is included in order to illustrate the excavation procedure.

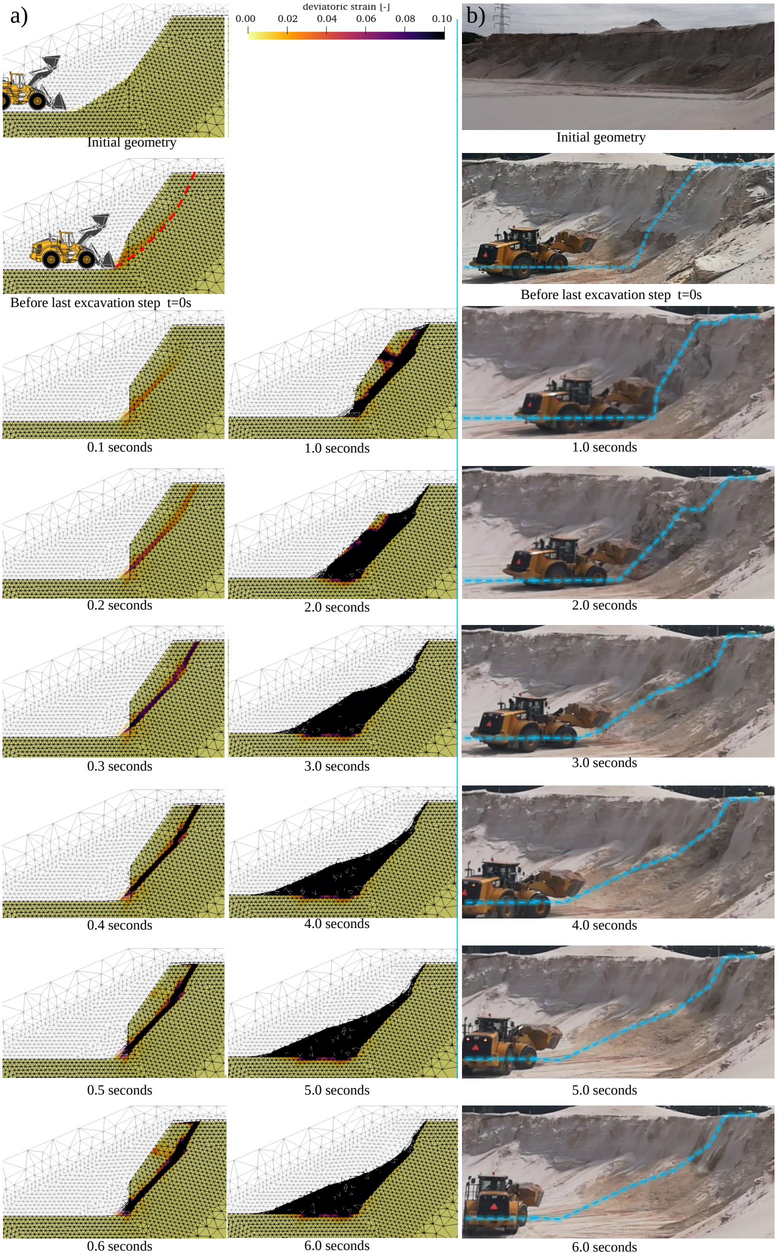

Figure 5.18: a) Deviatoric strain and slide slip surface propagation from the MC SS MPM simulation. An image of the wheel loader to-scale is included in order to illustrate the excavation procedure. b) observations from the field experiment in Site-A sand quarry.

itive sign) in comparison with the displacements of MPs located around the accelerometer sensor. The free-fall displacement is also plotted for reference. The softening rate makes a large difference in the early stage kinematics, so, to make the comparison between analyses more reasonable, the initial time (t=0) for plotting the displacement evolution from each of the simulations has been selected when the horizontal displacement is 0.5 m. The accelerometer, however, only measures until about 0.5 s, when the logging cable disconnected, so it is hard to make a full comparison of measured and modelled displacements.

It can be seen that the shape of the measured vertical displacement evolution is similar to that of the free-fall displacement, but with a less steep gradient, suggesting that the falling material continues to be supported by the remaining material in the slope. As the soil material is moving vertically it is also being translated horizontally. In the early stages, the two simulations have comparable results and reasonably match the accelerometer data. By comparing the results of the simulations with the video of the experiment, it is possible to conclude that the MC LEPP simulation overestimates the displacements observed in the field after the slope failure and that the MC SS simulation better captures the sliding kinematics.

To compare the impact of the $\eta$ parameter, an additional simulation with $\eta = 30$ has been undertaken, with the results also plotted in Figure 5.19. It is seen that the general kinematics are similar, with a limited reduction in the failure time observed. Therefore, the slope response is relatively insensitive to the softening rate.

The accelerations recorded by the sensor show significant noise, as indicated in Figure 5.8. The displacement curves shown in Figure 5.19 have been obtained by integrating the accelerations recorded during the induced sliding failure initiation only (after $19.0$ s from Figure 5.19). Moreover, the initial position of the sensor has some uncertainty as it was estimated based on the position of the hand drilling at the surface, although numerical simulation results suggest this impact is minor.

## 5.4. Summary and conclusions

In this chapter, the results of a slope failure field test are presented and compared with numerical results from LEM, FEM and MPM. Figure 5.20 provides an overview of this comparison. Very few large scale instrumented field tests are available that report failure kinematics.

All the numerical methods predicted comparable safety factors and slip surfaces, consistent with the field test. However, as the deformations become large, granular material properties continuously evolve, and both large deformation numerical models and non-linear large deformation constitutive models are necessary tools in order to obtain accurate stress-displacement forecasts.

MPM was shown to be able to simulate the dynamics of the full failure in terms of duration and displacements. Strain-softening was essential to capture the kinematics and the final geometry. Additional field monitoring programmes and site investigations should be performed to access the liquid phase contribution and to validate more complex constitutive formulations. The datasets collected during these experiments are available on the 4TU repository [https://data.4tu.nl/collections/a7f00e8a-cc10-45fd-a212-65ded27f7173].

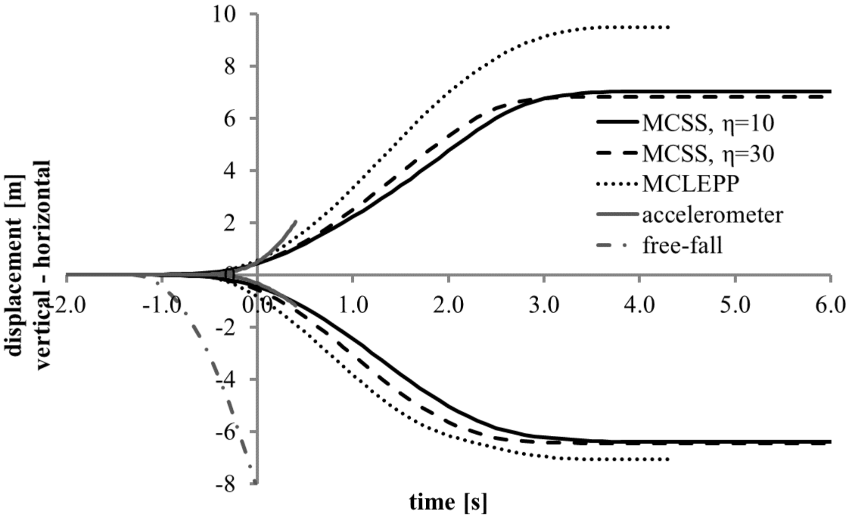

Figure 5.19: Comparison of derived displacements from the recorded accelerations in MPM simulations for the whole duration of the experiment.

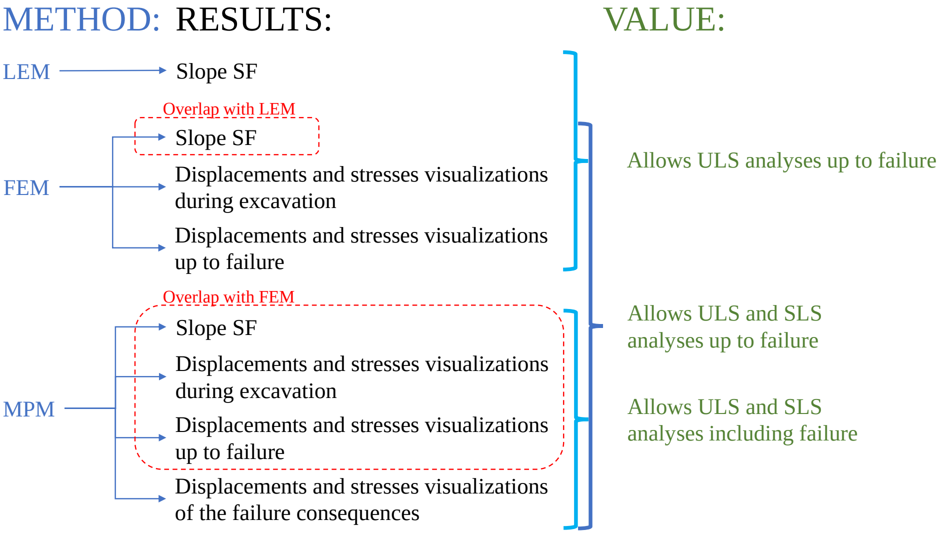

Figure 5.20: Comparison of the modelling approaches used, including the type of output and qualitative value for safety assessments.

# References

[1] Plaxis2d, 2016.

[2] Nl-ge-he-01-09072018 internal report data shear box. Technical report, TU Delft, 2018.

[3] Belgian national geographic institute, 2019.

[4] J. L. G. Acosta, P. J. Vardon, G. Remmerswaal, and M. A. Hicks. An investigation of stress inaccuracies and proposed solution in the material point method. *Computational Mechanics*, 65:555–581, 2020.

[5] Anura3D. Anura3d mpm research community, 2017.

[6] S. Bandara, A. Ferrari, and L. Laloui. Modelling landslides in unsaturated slopes subjected to rainfall infiltration using material point method samila. *International Journal for Numerical and Analytical Methods in Geomechanics*, 40:1358–1380, 2016.

[7] S. Bandara and K. Soga. Coupling of soil deformation and pore fluid flow using material point method. *Computers and Geotechnics*, 63:199–214, 2015.

[8] A. W. Bishop. The use of the slip circle in the stability analysis of slopes. *Géotechnique*, 5:7–17, 1955.

[9] M. D. Bolton. The strength and dilatancy of sands. *Geotechnique*, 36:65–78, 1986.

[10] A. J. Bond, B. Schuppener, G. Scarpelli, T. L. L. Orr, S. Dimova, B. Nikolova, and A. V. Pinto. Eurocode 7: Geotechnical design worked examples, 2013.

[11] R. Brannon. University of utah mpm code, 2018.

[12] Y.-L. Chang and T.-K. Huang. Slope stability analysis using strength reduction technique. *Journal of the Chinese Institute of Engineers*, 28:231–240, 2005.

[13] P. W. Cleary, M. Prakash, J. Ha, N. Stokes, and C. Scott. Smooth particle hydrodynamics: status and future potential, 2007.

[14] B. Z. Coelho, A. Rohe, A. Aboufirass, J. Nuttall, and M. Bolognin. Assessment of dike safety within the framework of large deformation analysis with the material point method. In Cardoso, editor, *NuMGe2018 Numerical Methods in Geotechnical Engineering IX*, pages 657–665. Taylor & Francis, 2018.

[15] P. A. Cundall and O. D. L. Strack. A discrete numerical model for granular assemblies, 1979.

[16] CUR-commissie. *CUR 113 Oeverstabiliteit bij zandwinputten*. 2008.

[17] E. Dawson, W. Roth, and A. Drescher. Slope stability analysis by strength reduction. *Geotechnique*, 49:835–840, 1999.

[18] Deltares. Slope stability software for soft soil engineering. d-geo stability v16.1.1., 2016.

[19] Fugro. Onderzoek zandgroeve ”site-d” nabij n136 - (b). Technical report, Fugro, 2018.

[20] Geo3. V3.1 cis res t/68543/000. Technical report, Liège University, 2018.

[21] D. V. Griffiths and P. A. Lane. Slope stability analysis by finite elements. *Géotechnique*, 49:387–403, 1999.

[22] C. Gritton and M. Berzins. Improving accuracy in the mpm method using a null space filter. *Computational Particle Mechanics*, 4:131–142, 1 2016.

[23] L. Li, C. Tang, W. Zhu, and Z. Liang. Numerical analysis of slope stability based on the gravity increase method. *Computers and Geotechnics*, 36:1246–1258, 9 2009.

[24] X. Li, Y. Wu, S. He, and L. Su. Application of the material point method to simulate the post-failure runout processes of the wangjiayan landslide. *Engineering Geology*, 212:1–9, 2016.

[25] S. Ma, X. Zhang, and X. M. Qiu. Comparison study of mpm and sph in modeling hypervelocity impact problems. *International Journal of Impact Engineering*, 36:272–282, 2 2009.

[26] A. Maghsoudloo, A. Askarinejad, R. D. Jager, F. Molenkamp, and M. Hicks. Experimental investigation of pore pressure and acceleration development in static liquefaction induced failures in submerged slopes. In *9th International Conference of Physical Modelling in Geotechnics*, 2018.

[27] Y. G. Motlagh and W. M. Coombs. An implicit high-order material point method. In *1st International Conference on the Material Point Method*, pages 8–13. Elsevier, 2017.

[28] NEN. Iso 17892-10:2018 - geotechnical investigation and testing — laboratory testing of soil — part 10: Direct shear tests. Technical report, NEN, 2018.

[29] J. Oliver and A. E. Huespe. Continuum approach to material failure in strong discontinuity settings. *Computer Methods in Applied Mechanics and Engineering*, 193:3195–3220, 2004.

[30] S. J. Raymond, B. Jones, and J. R. Williams. A strategy to couple the material point method (mpm) and smoothed particle hydrodynamics (sph) computational techniques. *Computational Particle Mechanics*, 5:49–58, 1 2018.

[31] A. Sadeghirad, R. M. Brannon, and J. E. Guilkey. Second-order convected particle domain interpolation (cpdi2) with enrichment for weak discontinuities at material interfaces. *International Journal for Numerical Methods in Engineering*, 95:928–952, 2013.

[32] R. Schmitz and M. Haggman. Geotechnical guideline 001 (gt 001 safeloadingheights rev 3). Technical report, Sibelco, 2018.

[33] Q. Tran and W. Sołowski. Temporal and null-space filter for the material point method. *International Journal for Numerical Methods in Engineering*, 120:328–360, 10 2019.

[34] M. van der Meulen, W. Westerhoff, A. Menkovic, S. Gruijters, C. Dubelaar, and D. Maljers. Silica sand resources in the netherlands. *Netherlands Journal of Geosciences*, 88:147–160, 11 2009.

[35] P. C. Wallstedt and J. E. Guilkey. An evaluation of explicit time integration schemes for use with the generalized interpolation material point method. *Journal of Computational Physics*, 227:9628–9642, 2008.

[36] B. Wang, P. J. Vardon, and M. A. Hicks. Investigation of retrogressive and progressive slope failure mechanisms using the material point method. *Computers and Geotechnics*, 78:88–98, 2016.

[37] B. Wang, P. J. Vardon, and M. A. Hicks. Rainfall-induced slope collapse with coupled material point method. *Engineering Geology*, 239:1–12, 5 2018.

[38] B. Wang, P. J. Vardon, M. A. Hicks, and Z. Chen. Development of an implicit material point method for geotechnical applications. *Computers and Geotechnics*, 71:159–167, 1 2016.

[39] Y.-S. Yang, T.-T. Yang, L.-C. Qiu, and Y. Han. Simulating the overtopping failure of homogeneous embankment by a double-point two-phase mpm. *Water*, 11:1636, 8 2019.

[40] A. Yerro, E. Alonso, and N. Pinyol. The material point method for unsaturated soils. *Géotechnique*, 65:201–217, 2015.

[41] A. Yerro, J. Bray, K. Soga, and J. Bray. Runout evaluation of the oso landslide with the material point method. *Can. Geotech. J.*, 12:1–14, 12 2018.

[42] A. Yerro, N. M. Pinyol, and E. E. Alonso. Internal progressive failure in deep-seated landslides. *Rock Mechanics and Rock Engineering*, 49:2317–2332, 2016.

[43] A. B. Yu. Discrete element method an effective way for particle scale research of particulate matter. *Engineering Computations*, 21:205–214, 2004.

[44] X. Zhao, D. Liang, and M. Martinelli. Numerical simulations of dam-break floods with mpm. In *Procedia Engineering*, volume 175, pages 133–140. Elsevier Ltd, 2017.

[45] Y. Zhou, B. Xu, A. Yu, and P. Zulli. An experimental and numerical study of the angle of repose of coarse spheres. *Powder Technology*, 125:45–54, 5 2002.

# 6

# Full size field experiment of submerged flowslides

*Underwater flowslides are major hazards, causing fatalities and economic losses worldwide; hence it is important to understand and predict their behaviour. Interpretation frameworks and numerical predictions have been developed to study these phenomena. However, validation studies are required to make these methods suitable for use in industry. As there are no analytical solutions for slope stability assessments, experiments are necessary for validation. In this chapter, a flowslide field experiment is presented with the aim of providing a dataset to validate numerical models for the simulation of flowslides in sandy slopes. A monitoring setup is designed and used to record the dynamic features of the partially submerged flowslide in an artificially induced slope failure in a sand quarry. The proposed experimental set up proved its effectiveness in capturing the main features of the occurring flowslide and its results are used as a benchmark for the preliminary simulation of the slope failure with MPM. The numerical model of the proposed experiment has been solved with a 2-phase 1-point MPM formulation, which finds reasonable agreement with field observations, such as the retrogressive failure mechanism, qualitative pore pressure fluctuations, and estimation of the retrogression length.*

## 6.1. Introduction

The value of quantitative landslide hazard assessment has been widely recognized, as it underpins management decisions, guides mitigation measures, and informs the allocation of resources. For more than a century, understanding the mechanical behaviour of coupled soil and water has been an active topic of research. Laboratory experiments are useful to investigate flowslides as complementary tests to full-scale experiments because scaling effects are generally not negligible when considering flowslides, or more generally, the mechanical interaction between soil and water.

The application of information and geospatial technologies such as remote sensing and geographic information systems (GIS) has greatly contributed to landslide hazard assessment studies over recent years. However, a detailed description of retrogressive breach failure (RBF) dynamics at field scale is lacking in the literature. This is in part due to the risks associated with monitoring activities in underwater environments and the difficulty of predicting when and where a landslide will activate. During marine sand dredging activities, however, slope failures are frequently used to steer sediments and water mixtures to the dredging equipment. Although this shows that the phenomenon is understood to some extent and can be somewhat controlled, large unintended RBFs are not rare during excavation activities. Once an RBF is triggered, it is usually impractical to stop it. Therefore, an assessment of the evolution from triggering to final deposition of material and a new stable situation is important. The uncertainty of the spatial extent and dynamics of such events may result in unwanted costs.

This chapter presents an experimental set of artificially triggered underwater flowslide fields to monitor the dynamics and morphology changes of the RBF of sand. The main aim of the test is to monitor during an RBF at full scale the failing soil mass geometry evolution, including triggering mechanism by dredging activities, and the onset and the deposition of the sliding soil mass. This is considered useful for the geotechnical characterisation of the soil material from back analyses, as well as for the validation of numerical and empirical solutions for slope failure forecasts.

The experimental slopes predominantly consisted of dense, saturated sand. The duration of the expected sand flow ranges from a few seconds (in the case of liquefaction occurrence) to hours (in the case of pure breaching occurrence) [5]. In practice, a retrogressive failure mechanism is more often observed, which is the result of a combination of the previously described mechanisms.

After preparation of the slopes for the experiment, a dredger excavated sand from the toe, thereby loading the sand body by its tendency to spread laterally because of its self weight. This tendency is translated in increasing suction due to the dilative behaviour of dense sand. In turn, the suction slowly dissipates as the ambient water flows into the sand body. Its dissipation rate depends on the sand strength (i.e. local porosity, friction, cohesion, bulk density, etc.) and the applied loads (i.e. pressure gradients, stress state, etc.). Because the sand particles at the interface between the steep sand slopes and the ambient water are unconfined on one side, these will move downwards by gravitational forces, sometimes resulting in accelerating turbidity currents. The turbidity current contributes to the erosion of the slope body, increasing the overall erosion rate, specially at the base of the slope due to the funnel shape of the scar. This often results in undercutting geometries that favour sliding events of sand blocks. The sediments from the collapsing slope will deposit at its base. This process locally generates soil masses in a loose state compared to the virgin sand slopes, which are therefore susceptible to sand liquefaction.

Low accuracy estimations only are possible due to the noise present in the measurements, the scarce redundancy of the monitoring tools and the missing bathymetric data, but the dataset presented in this chapter is considered sufficient to describe the main features characterizing the observed RBFs. After a detailed description of the field-experimental observations, an attempt is made to simulate the RBF with a coupled MPM formulation (as implemented in Anura3D) to explore the forecasting performances of the numerical model. This effort was made with the aim of validating MPM for flowslide phenomena.

## 6.2. Site description and monitoring system for the field experiments

Two quarries with similar soil properties were selected as sites to perform the proposed RBF full scale experiment: the north-east shore of Site-B sand quarry, and the north-west shore of Site-C sand quarry. The experimental investigations undertaken in this study were made possible through access to quarry facilities provided by Sibelco. The availability of the company's infrastructure, along with its technical assistance and institutional support, played a pivotal role in the effective realization of the testing program. From pre-existing geological investigations, the quarries are known to be located in horizontal layers of pure quartz sand for at least all the depth of the excavation permits (i.e. about -25m below water table).

A visual assessment of the pre-stripped areas that were prepared for the mining activities confirmed the geological interpretation, as they appeared uniform without layering and white in colour. In addition, a high relative density was indicated by earlier CPT investigations and by the typical retrogressive failure mode of the slopes during mining activities. The dense sand layers that characterise these quarries were expected to facilitate the RBF mechanism, as confirmed by mining experience in the surroundings. The slope failures were artificially triggered by undercutting the slope toe with a suction dredger. The slopes suitable for the test were selected to have a slope height greater than 7 m. This criterion ensures that there is a significant effect of confining stresses in the deepest soil layers and that there is enough potential energy for the resulting sediment flow to accelerate during the failure, giving to this dataset additional value compared to laboratory experiments. Multiple slope failures were monitored, on two sites with similar soil properties.

To enable the execution of experiments involving steep slope configurations, preliminary risk assessments were conducted using the Limit Equilibrium Method (LEM), with subsequent verification through Material Point Method (MPM) analyses. These assessments were reviewed and approved by the responsible geotechnical engineer from Sibelco, who was also present onsite to supervise the experimental activities. The experiments were carried out in a central zone of the quarry on temporary slopes to ensure that their implementation would not have any impact on the final slope geometry of the quarry.

A detailed description of both experimental sites and of the monitoring system that was used is reported in the following sections.

### 6.2.1. Site-B sand quarry

The slope selected for the first set of experiments was located in the north-east shore of Site-B sand quarry, shown in Figure 6.1-a. During desk study activities, grain size distributions, historical CPTs, geological interpretations and bathymetries have been collected to support the geotechnical interpretations presented in this chapter, and a selection of this data are reported in Appendix B in Figures 4, 5, 6 and 7. Additionally, triaxial, oedometer, grain size, grain shape and min-max density investigations [4] that were made in the same geological layer (i.e. Mol formation – Maatheide Member quartz sands) can be considered representative for this site.

Geological interpretations indicate that the horizontal sand layer of the Site-B quarry is composed of fine uniformly graded silica sand, from the top down to the full depth of the excavation, with possible occurrences of small clay lenses. Site-B quarry is an artificial lake as a result of past mining activities below the water table. The quarry is currently mined for sand production, mainly for the glass industry. This implies that the material resulting from mining activities is regularly analysed in the laboratory and with a high degree of purity. The sand has very high percentages in weight of pure quartz grains and it is mostly homogeneous in terms of grain size distribution. An envelope of the grain size distributions from samples extracted at every meter of depth in vertical drillings, up to -24 m below the water table, is presented in Figure 6.1-b.

The mean grain size is $d_{50} = 190$ $\mu$m and clay particles have not been found to be above 7% of the total weight. Hence the presence of fine particles can be disregarded for describing the geotechnical mechanical behaviour of the soil. The quarry maximum depth is 20 m below the free water level. The area had been stripped of the upper soil layers and vegetation in order to expose the pure quartz sand layer. The boundaries of the quarry have been constructed to have a 1:4 slope angle in order to guarantee stability. In fact, during preceding field experiments in the same geological layer, it was observed that following multiple slope failures triggered by a suction dredger, a slope angle of approximately 1:4 would occur [6]. Therefore slopes with an angle equal to or lower than this are considered to be in a stable configuration based on prior experience. However, excavation activities for dredging purposes within the boundaries of the quarry may generate steeper slopes.

From dredging experience, almost vertical breaching walls are temporarily achievable up to 5m in height before triggering a slope failure. The failure starts underwater and it slowly extends in a radial direction. If the disturbance of the slope reaches the shore, a gradual and progressive sliding of the unsaturated part of the slope occurs. Once the failure is initiated and sliding is observed on the shore, it is not possible to stop the erosion as long as a new equilibrium configuration of the slope is found.

In order to install monitoring tools in the target slope for the experiment, a mechanical excavator dug a 20m long trench parallel to the shore, until reaching the water table. This trench was useful for installing the fiber optic strain gauge in the saturated part of the slope, but also facilitated the use of hand drills for pushing the pore-pressure and acceleration sensors in boreholes below the water table.

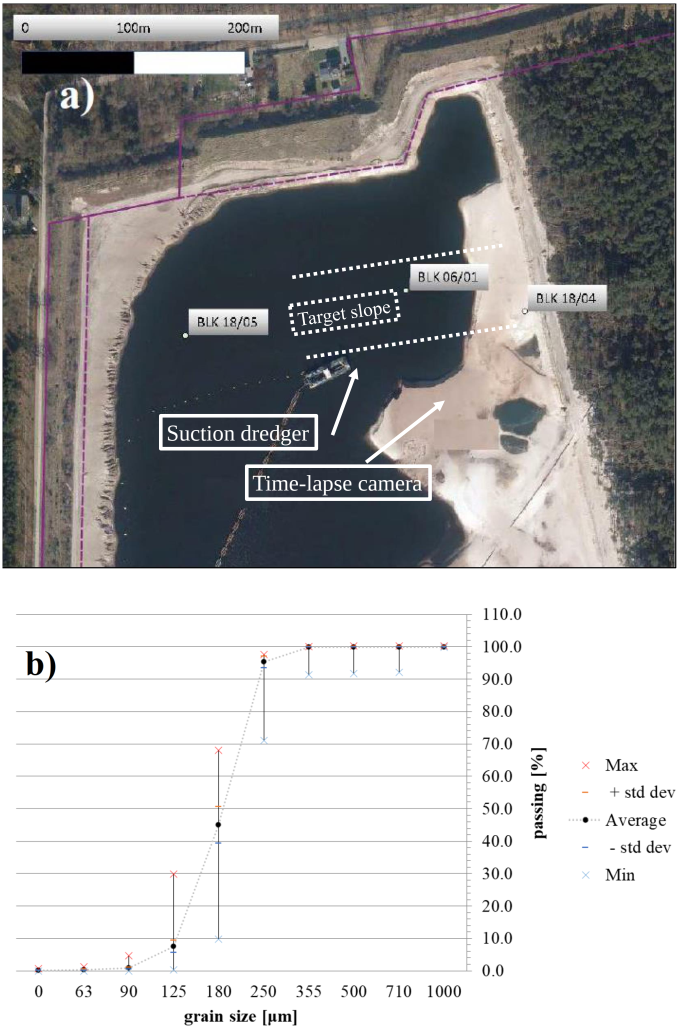

Figure 6.1: (a) Site-B, experiment site seen from Google Earth. The target slope for the experiment is indicated by the white dashed lines. The location of the drillings for the sample extraction is indicated in the map. (b) Grain size distribution envelope. Samples were previously washed of clay particles, although, they never exceeded 7% of the total weight.

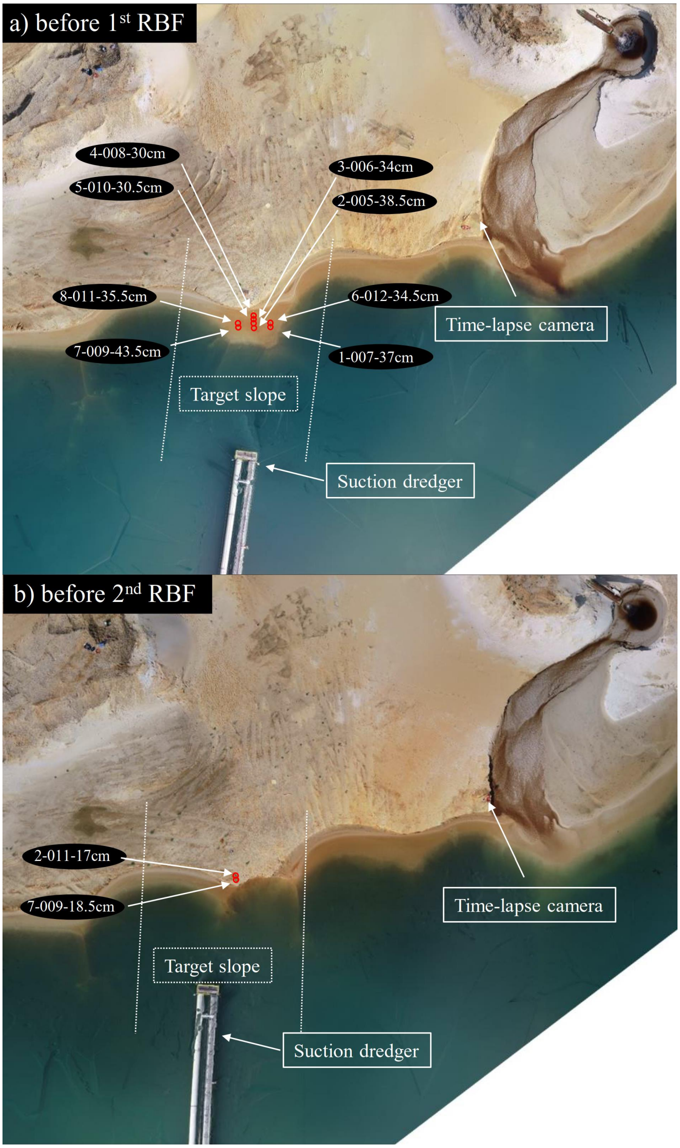

Figure 6.2: Figures from UAV photogrammetry of the Site-C test site before RBFs: (a) the instrumented slope is identified showing the positions of the sensors (in red) before the first RBF event, including depth of installation below water table; (b) the instrumented slope is identified showing the position before the second RBF event, including installation depth below water table.

The spoil of the hand-drilling activities was collected as soil samples. The target slope for the experiment was reasonably regular but did not have constant cross-sections in the perpendicular direction to the trench because the quarry is usually excavated with stationary dredgers: stationary dredgers use the concave shell shape of the back-scarp to guide the sand particles flow to the deepest part of the pit where the suction mouth is positioned.

At the beginning of the experimental dredging activities, the target slope was relatively far from the position of the instrumented trench and multiple RBFs were necessary to ensure that the triggered slope failure would involve also the buried sensors installed in the trench. The target slope superficial layer in the unsaturated part of the slope appeared homogeneous and white in color. However, the target slope was located near to a corner area of the shore where tridimensional effects of the failure could not be disregarded. The southern part of the shore corner area appeared darker in color and with local steep slope angles in the unsaturated part, suggesting the presence of lenses of cohesive material (see Figure 6.1-a).

### 6.2.2. Site-C sand quarry

A second set of experiments was performed in Site-C sand quarry. This sand quarry was also generated by dredging excavations, but it is only 8 meters deep below free water (roughly half the depth of Site-B). Its sand layers included more lenses of loamy material compared to Site-B, which is more cohesive than pure silica sand. Submerged slope angles in this quarry have been observed as high as 1:1 from the bathymetry scanners, while appearing stable from the surface. The grain size and chemical analyses from sample extractions are presented in Appendix C. However, artificially triggered flowslides in this quarry had been observed to result in similar failure mechanisms and final morphology to those in Site-B.

The target slopes for the two RBF experiments are highlighted in Figure 6.2. The slopes were selected in an area that was easily accessible by car for transporting the monitoring equipment, and on a pre-stripped area from the overburden material (i.e. loamy and gravelly soil layers) with a shore geometry reasonably regular (or slightly convex, in order to reduce stabilizing tridimensional effects during the slope failure). The target slope crest for the first RBF experiment in Site-C, conversely to other experiments, had a sand platform just below the free water. This slope was selected for monitoring the first RBF because it allowed installing the pore-pressure sensors below water with reduced effort in the submerged sand platform. The second RFB experiment in Site-C, similarly to the experiments in Site-B, was performed in close proximity to the first RBF experiment, in a slope generated as result of the stationary dredger excavation from the toe of the first target slope.

### 6.2.3. Monitoring system

The monitoring system included tools for visualising the changing geometry during failure and sensors to provide quantitative estimations for the pre and post-failure behaviour. The tools typically had a high sampling frequency to be able to capture the motion of sand, ranging from very quick, such as liquefaction, to very slow, such as breaching. Moreover, the slope, being partially submerged, required different tools and technologies for monitoring its geometry, depending on the surrounding environmental conditions (i.e. above and below the water table).

| Sensor | What is observed | Remarks |
|---|---|---|
| Bathymetry scanner | Underwater 3D slope geometry | Suffers from scatter on sediment clouds |
| UAV photogrammetry | Above water slope geometry | Surveying missions trade accuracy for flight duration |
| Global Positioning System | Suction head position | Only available in Site-B |
| Time-lapse camera | Duration of the observed failure, the dredger relative position to the slope and in order to capture the qualitative features of the retrogressive sliding failure mechanism above water | Kept active during the entire experimental activities |
| Pore-pressure and acceleration sensor | Pore-pressure and acceleration at sensor position | Only available in Site-C experiments due to sensors not being watertight, needed steel cables to facilitate recovering activities |
| Fiber optic strain gauge | Pre-failure deformations | Only available in Site-B, needed thicker cable to avoid plastic strains during installation |

Table 6.1: Summary of monitoring system

### Bathymetry scanner

An echo-sounder bathymetry scanner mounted on the suction dredger records the underwater 3D slope geometries. Sounds wave were preferred in an underwater environment to light waves, as the latter often suffer from significant scattering and light diffusion that limits the operational distance of the system. The output of this monitoring tool is a geo referred 3D point-cloud. The coordinates and time of the measurements were stored in the memory unit of the device itself. Continuous measurements in real time were not made available. However, point clouds at different time intervals were made available and can be compared to reduce the uncertainties about the ongoing failure mechanism.

### UAV photogrammetry

The UAV equipped with HD camera (DJI Phantom 4) was used in order to monitor the geometry above water. The pictures collected were automatically combined by software (Pix4Dmapper v4.4.10) for the generation of geo-referred 3D point-clouds, providing ground control points. The UAV allowed capturing the whole area within the duration of a single flight (or mission), that lasted about 5 minutes per mission.

### Global Positioning System

The bathymetric data and the UAV maps were made using GPS sensors of the devices in order to assign to each point a set of coordinates. Additionally, a GPS sensor is also installed in the suction head in order to monitor its position through time (e.g. see Figure 6.8-a and 6.9).

### Time-lapse camera

The RBFs were recorded on video in order to measure the duration of the observed failure, the dredger relative position to the slope and in order to capture the qualitative features of the retrogressive sliding failure mechanism above water. A time lapse camera (Brinno BCC200) was therefore installed in the proximity of the test areas. The device was set-up to collect a picture every 15 seconds. Additionally, short videos have been captured by smartphone, from which it is possible to have a qualitative understanding of the RBF in real time.

### Pore-pressure transducer and acceleration sensor

Pore-pressure transducers and triaxial acceleration sensors pairs were installed in the slope crest, below the ground water table. The transducers were mounted together with triaxial accelerometers in an aluminium cylindrical casing as shown in Figure 6.3. The dimensions of the casing were 6 cm in diameter and 10.5 cm high. The hole at the centre of the bottom black disc allows water entering to be in contact with the pressure sensor. The casing also allows the integration of ballast for sensor density adjustments. Density adjustments were desireable to adjust the sensor density as close as possible to the bulk density of the flowing soil, so that the sensor would move with a minimal relative velocity to it.

As the sensor casings are buried by turbidity currents during the execution of the experiment, a steel cable connection with an anchor is also installed to facilitate the sensors retrieval. From laboratory experience, a measurement frequency of 100 Hz was considered sufficient to distinguish and record the relevant changes of the different failure phases of the sand flow slide [7]. Pore pressure, acceleration and time are automatically stored by the data logger. Pore pressure readings are used to quantify the in situ dilation behaviour of the dense sand, which would manifest itself in excess pore-pressures.

As the focus of this experiment is large deformations throughout the whole failure process, inclinometers, which are often used to measure the onset of slope failures, cannot be used. Assuming that the sensor cables have negligible effect on the sensor inertia to motion, acceleration data in time aims at estimating translational velocity of the soil mass motion, from onset to deposition. The acceleration data estimates also the angular variation of the soil mass in which the sensor is buried. Hence, the accelerometer sensor provides soil pre-failure signals similarly to an inclinometer.

Hand drilled boreholes were dug to install the sensors (so that heavy machinary was not brought close to the slope), which limited the vertical depth of installation, but reduced the disturbance of the surrounding soil. Hence it was possible to install only one sensor in each (relatively shallow) borehole excavated with the hand-drill available on site. This resulted in arrays of sensors only in the two horizontal directions. Additional arrays in the vertical direction are recommended for a future study to better investigate the failure geometry and pore pressure distribution during failure.

Figure 6.3: Aluminium cylindrical casing containing the pore pressure transducers assembled by Dr. Bertges.

### Fiber optic strain gauge

As pre-failure deformations are likely to appear at the top of the slope just before failure, a 100 $m$ long strain gauge (i.e. a fiber optic cable with a diameter $\phi = 900$ $\mu m$ including jacket and core diameter $\phi_C = 8.2$ $\mu m$) was buried at the slope crest in a 20 $m$ long trench visible in figures 6.4 and 6.5, parallel to the shore and below the water table. A cable with a small diameter was selected among others in the attempt of capturing very small strains. After installing the fiber optic cable on the bottom of the trench, a sand embankment of about 1 $m$ was relocated on top of the cable to ensure enough bonding between the cable and the surrounding soil. The logger (i.e. the fTB 2505, fibrisTerre Systems GmbH) was manually activated at regular intervals and when the slope geometry changes become visible in the unsaturated part.

## 6.3. Experimental protocol

Failure dynamics are strongly influenced by the materials involved in the phenomena and their state (i.e. initial density and loading conditions). Moreover typical geotechnical investigations only provide limited information about the subsurface: they are often constrained by high costs and they are subjected to inherent uncertainties (i.e. the natural variability of soil properties and the interpretation of the in-situ and laboratory tests); hence one cannot guarantee in advance when and where a flowslide will occur. However, from dredging experience in the selected quarries, and due to the anticipated high in-situ relative density of the sand, an RBF is the most likely mechanism to occur.

A 4-step experimental protocol was proposed in order to reduce the risk of triggering the failure before the intended time and to capture the failure dynamics as described in subsections 6.3.2 - 6.3.5. This protocol facilitates in capturing at least the geometry before and after slope failure with modular accuracy, both in space and time.

The accuracy of the photogrammetry (i.e. measurements from the UAV), for example, increases by reducing the altitude at which the drone hovers over the surveyed area. However, as a consequence of lower flight altitude, more pictures are needed to cover the same area; hence increasing the time of the surveying mission. Because the RBF keeps evolving during the surveying activities, it will be more challenging to distinguish which part of the slope collapsed into the lake during lengthy missions. Conversely, by increasing the flight altitude of the UAV, the measurements will be less accurate, but because the surveying mission will be brief, it is more favourable for capturing the dynamics of the RBF. Another way to control the accuracy in space and time is varying the redundancy and/or the frequency of the observations.

### 6.3.1. Triggering mechanism

The triggering mechanism selected for the experiment is undercutting the target slope toe with a stationary suction dredger. The dredging activity can generate an almost vertical excavation front, due to the apparent soil cohesion generated by the excess water pressure during shearing of the dense sand. The breaching wall may appear stable, especially from the surface, but a slow process of erosion (i.e. breaching) will take place as the excess pore pressure dissipates. A continuous excavation can gradually increase the receding breaching wall height, eventually triggering a macro-instability (i.e. sliding) of the slope. The sliding soil mass, when occurring in continuous and homogeneous sandy slopes, is predicted to be bounded by an approximately shell-shaped slip surface.

Undercutting the slope with dredging equipment is proposed to: (i) yield a local slope failure initially bounded by a shear band, which softens as shear strains increase; (ii) lead to a log spiral shape of the shear band (rather than a circular failure) [3]; (iii) have initially intact soil blocks moving as a rigid bodies, which may then further break as the failure progresses. From dredging experience in similar slopes, this triggering mechanism produces RBFs with similar dynamics and post-failure morphology, indicating the potential for the reproducibility of the experimental results. As the soil volumes with the highest concentration of shear stresses are located in the deep soil layers close to the vertical excavation front, the slip surface is expected to propagate from the toe to the crest of the slope.

### 6.3.2. Step #1: installation of monitoring equipment

The selected test site was stripped of its overburden to reveal the sandy soil layer below and remove the superficial organic and waste material, in order to improve the predictability of the failure, with the intention of stimulating a RBF. The video camera was installed and activated in a safe location close to the target slope, but outside the intended flowslide area, in order to record all the preparation activities on the field while reducing the chances to bury it in the case of an uncontrolled breaching.

Afterward, an excavator prepares a trench on top of the selected slope for the test, to facilitate the installation of the fibre optic strain gauge and pore pressure transducers below the water table. The trench should be as close as possible to the shoreline in order to reduce the duration of the following preparation activities; however it should be sufficiently far from it in order to reduce the risk of the slope collapsing and in turn the loss of the excavator inside the lake, as vibrations and additional top load from the trench excavation activities could trigger liquefaction flowslides. After the successful installation of the intended monitoring tools, a first 'monitoring step' is proposed to capture the initial geometry, before performing any dredging activity. This is done by taking measurements, at least once, from each tool (i.e., pore-pressure and acceleration sensors, bathymetry scanner, GPS, fibre-optical stain gauge, and UAV).

The pore-pressure and acceleration sensors when activated have an automatic logging at 100Hz. The bathymetry scanner was continuously measuring the slope geometries surrounding the dredger, offering underwater images to the dredger operator, while its GPS position is automatically logged. The fibre optic strain gauge logging duration is short and can be set for automatic logging. However, due to the numerous uncertainties (i.e. duration of excavation activities, of the sliding process, and amplitude of prefailure cracking, among others) and in order to contain the amount of data to interpret, it was preferred activating it only when considered opportune (i.e. at regular intervals during the excavation by the dredger and more frequently when soil blocks were observed falling into the lake).

The UAV logging missions were also of variable duration due to the large size of the experiment. Additionally, one should consider the trade-off between accuracy of the measurements and duration of the UAV mission. Hence, also the UAV logging missions were also performed when considered opportune rather then at fixed time intervals or on a fixed area. Figure 6.4-a provides a schematic representation of the field conditions and the expected outcome for this monitoring step.

### 6.3.3. Step #2: slope geometry preparation

In order to increase the probability of triggering an RBF large enough to involve the monitoring tools installed in the instrumented trench, the selected slope for the experiment was further prepared by excavating the toe with the suction dredger in the perpendicular direction of the slope. Hence, before the beginning of the excavation activities, the pore pressure sensors, acceleration sensors and time lapse camera are activated to record respectively the excess pore water pressure evolution, eventual soil mass movements and shore geometry evolution in time. No significant readings are expected in this monitoring step for the final outcome of the experiment. However, one cannot exclude the occurrence of a larger failure than expected when undercutting the slope toe. Hence, these sensors were activated to record possible uncontrolled slope failures.

The excavation for the target slope preparation generates a vertical breaching wall in the location of the slope toe that propagates uphill as shown in Figure 6.4-b. The falling unconfined sediments from the breaching wall generate turbidity currents that accelerate the slope erosion process, especially at the toe where these are channeled by the concave morphology of the scarp. The suction head excavation is sustained by the dredging operator up to the point that small sliding events become visible at the slope crest due to overhanging of soil masses [2]. At this point, large amounts of sediments flow down-slope; hence the erosion process tends to expire as gentler slopes are formed by the depositing sediments close to the target slope toe. The erosion process was fostered by continuous excavation of sand from the toe, in such a way that the shoreline moved close to the instrumented trench. The experience of the dredger operator is used to control, at least in part, the failure morphology.

Before the shore line advances too close to the instrumented trench, the excavation stops and the breaching wall finds a new equilibrium configuration with slope angles of about 1:4 as shown in Figure 6.4-c. At this point it is possible to perform a second 'monitoring step' where all of the monitoring tools are read to obtain a panoptic view of the resulting slope in a stable configuration.

### 6.3.4. Step #3: bottom floor preparation

In order to obtain a full slope susceptible to breaching, from bottom to top (i.e. toe to crest), the quarry bottom floor should be further excavated to remove the deposited loose sediments from the previously triggered flowslide. This guarantees that incoming sediments from subsequent flowslide phenomena can move with low shear resistance once the turbidity currents are triggered, hence reducing self-stabilising effects that could stop the slope failure before the receding shoreline reaches the sensors installed in the instrumented trench.

The pore pressure sensors, acceleration sensors and time lapse camera are activated again for precaution and excavation of the bottom floor and of part of the virgin soil (so to obtain steep slope angles) is performed. Once the quarry floor is reestablished and clean from recently deposited sediments, the target slope is ready for the intended RBF experiment, with a slope geometry resembling that shown in Figure 6.4-d. At this point, it is possible to perform the third 'monitoring step' where all of the monitoring tools are read to obtain a panoptic view of the target slope in a configuration susceptible to breaching.

### 6.3.5. Step #4: trigger and final geometry

At this stage, the slope is ready to have the toe undercut as the trigger for the main RBF event. The pore pressure sensors, acceleration sensors, and time lapse camera are activated again before the dredger starts excavating the slope toe perpendicularly to the shore for the triggering mechanism. When the breaching wall reaches heights close to 5m, large sliding events should become visible from above the water surface, as previously observed during mining activities. As soon as the dredger operator is able to observe the superficial sliding occurrence of sand blocks from the shore into the lake, he stops the suction head and lifts it above the water surface to guarantee that the RBF dynamics are fostered by the sand mass self-weight only and that the excavation does not further foster the slope failure. During the slide the slope geometry evolution is monitored with the time lapse camera, UAV and bathymetry, while the motion of sand blocks and pore-pressure fluctuations are monitored by the acceleration and pore-pressure sensors. The RBF will then continue and self-expire when the slope reaches a new equilibrium configuration, with a final geometry that resambles that shown in Figure 6.4-e. After this, it is finally possible to perform a last 'monitoring step' where all of the monitoring tools are read, to conclude the experiment by capturing the geometry of the slope after the last RBF.

### 6.3.6. Notes about the proposed experimental set up

The excavation activities for sand production are expensive for dredging companies due to the amount of personnel and machinery required. The dredging activities were roughly performed as during ordinary industrial practice (i.e. dredging from the quarry's slope toes, rather than accurately preparing the slope geometry for the experiment). However the dredging activities were stopped as planned when the slope crest was observed collapsing into the water, allowing the RBF events to be monitored with minimal hindrance on the production.

Due to turbidity currents, fine sediments are suspended in the water for relatively long periods of time, favoring segregation and also hindering the performance of the bathymetry scanner. The suspended sediment cloud can be mistaken as the bottom floor of the quarry. However, the redundancy of the 3D point-cloud data set enables quantitative estimations of the sensor performance, including bottom floor accuracy. Pore pressure data sets provide quantitative estimations of the suction generated during failure. A direct consequence of the dilative behaviour of the failing dense sand is the generation of excess water pressure (suction) in the slope body that allows the RBF to take place rather than yielding a sliding event as expected in subaerial slopes (i.e. as presented in Chapter 5 of this dissertation).

As the RBF approaches the pore pressure sensors, these are dragged downslope by the turbidity currents, allowing measurements of the pore pressure generated by the deposition of sediment concentrated flows in the proximity of the slope toe.

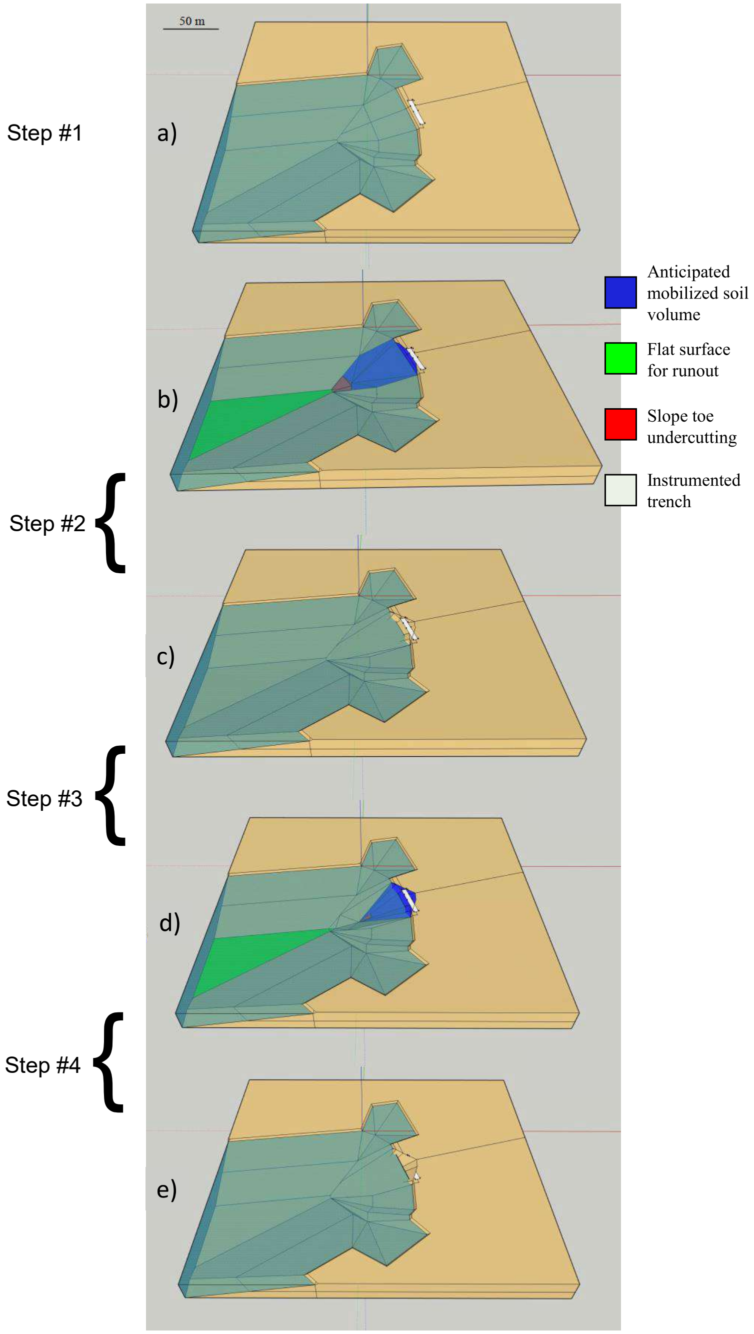

Figure 6.4: 3D sketches of the proposed 4 step experimental set up for monitoring RBF dynamics. The Site-B quarry geometry is used as an example: a) is the slope configuration after excavation of the trench parallel to the shore; b) illustrates the anticipated volumes of sand involved in the first RBF to bring the shore close to the instrumented trench; c) is the new equilibrium configuration after the first RBF event; d) represents the slope configuration under which it is susceptible to breaching for the whole depth; e) anticipated final geometry after the last RBF.

## 6.4. Results of monitoring activities in Site-B

The slope selected for the RBF experimental set-up was located at the north-east shore of the Site-B quarry where the overburden was already removed to allow mining. The trench for the sensors installation was also prepared in advance, near a corner slope of the quarry that was easily accessible for the excavator available on site, as visible in figure 6.1-a.

Two RBF events were triggered in sequence following the experimental protocol described above (i.e. experimental steps from #1 to #4). As the UAV surveying missions last just a few minutes, multiple images of the unsaturated backscarp were captured during each RBF, to describe the evolution of the failure as observed from above water (i.e. the ”dry” part of the quarry).

### 6.4.1. Observations during first RBF

Figure 6.5 shows the digital surface model of the (unsaturated) ”dry” part of the slope as captured by five UAV surveying missions and its evolution in time during the first RBF (i.e. experimental steps #1 and #2). Figure 6.5-a shows the shore during continuous excavation activities of the target slope toe to trigger the first RBF, around the time (8:30am) when the first soil block was observed splashing from the shore into the water. No changes of the slope geometry above water were observed up to this moment. The initial shore line is highlighted by the dashed line as reference.

The occurrence of the RBF becomes evident once multiple sand blocks started falling from the shore (i.e. the unsaturated back-scarp) into the lake water, generating a thin floating layer made of air bubbles along with organic material and small sediments, previously trapped between sand grains (e.g. as visible in Figure 6.5-b). The soil blocks splashing into the water were also clear signals for the surveyors to carry on UAV surveying missions and fiber optic tool logging's in sequence until no more slope movements are observed.

Figure 6.5-b shows the retrogression of the shore after about 45 minutes: part of the shoreline closest to the dredger head ”disappeared” into the water. Figure 6.5-c shows the shore after about 75 minutes. This picture also shows that the failure spreads radially and that the erosion process was still active because of the abundant floating layer around the failing shoreline. During the first RBF event, the dredger continued excavating intermittently during the observed failure, to foster the failure by reducing the self stabilising effects of the depositing sediments at the slope toe, so that the back-scarp approached the trench where other sensors were installed, but without involving the instrumented trench in the slope failure. The duration of the excavation activities necessary to achieve this was controlled by the dredger operator mining experience in this quarry, and the observed RBF lasted about 90 minutes. The maximum retrogression length of the shore is about 19 m.

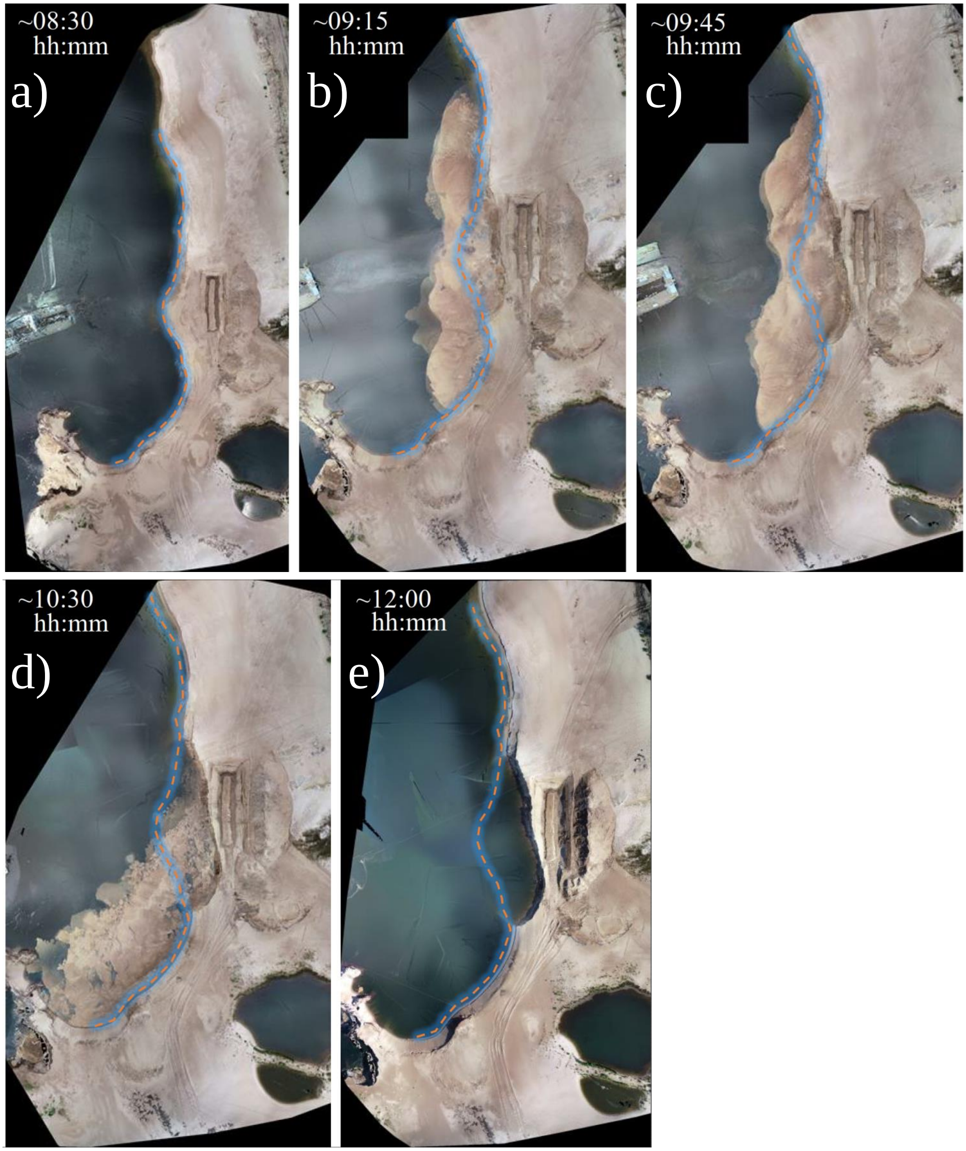

Figure 6.5: Overview of the first RBF in Site-B from UAV photogrammetry. The orange dashed line highlights the shoreline shape before the first RBF experiment.

Figure 6.5-d shows the shore after 120 minutes. From this image it is possible to confirm that the dredging activities are terminated as the dredging vessel retracted in order to allow the slope to find a new equilibrium configuration and slow down the erosion process, at least above the water surface. However a significant part of the floating layer was still in suspension and drifting around carried by the lake currents. Hence, it is clear that the deposition of at least part of the sediments occurred outside the monitored area.

Figure 6.5-e shows the shore geometry after 210 minutes from the beginning of the RBF and after 135 minutes from the observed end of the RBF. The geometry of the shore is basically unchanged since 9:45am and the floating layer has completely deposited into the lake. At this point the slope is considered stable as it found a new equilibrium configuration and it is deemed ready for the second RBF (i.e. experimental steps #3 and #4)

### 6.4.2. Observations during second RBF

After the preparation of the bottom floor of the quarry for the second RBF event (i.e. experimental step #3), the dredger operator triggered the second RBF by excavating in the perpendicular direction to the shore (i.e experimental step #4), while the time-lapse camera kept recording. This time, in contrast to the first RBF, the dredger operator stopped excavating as soon as the first sand blocks were observed splashing into the water, by pulling the suction head above the water (as visible in Appendix D, Figure 14). The RBF occurred for several minutes, up to about 90 minutes, fostered only by the self weight of the sediments and the relatively steep slope geometry. An overview of the evolution of the RBF in time is presented in Figure 6.6, again using UAV photogrammetry.

Figure 6.6-a shows the shoreline as before the beginning of the second RBF. A dashed line is drawn on the shoreline initial position as reference.

Figure 6.6-b shows the shoreline at around 14:30, when the first sand blocks were observed falling into the lake from the backscarp. Similar to what happened during the first RBF, sediments floating and drifting on the water surface were making the underwater erosion processes evident by highlighting the ripples caused by water turbulence.

Figure 6.6-c shows the shoreline at around 14:45 retracting radially from the location where the first sand blocks were observed splashing into the water. From this image it is possible to observe that the floating layer has already drifted far away by the quarry currents (i.e. wind and water currents).

Figure 6.6-d shows the shoreline after about 1 hour from the start of the RBF, when the frequency of the sand blocks falling from the back-scarp gradually decreased down to a stop. Hence, the floating sediments slowly disappeared by sinking or drifting onto the surrounding shore, indicating that the slope found a new equilibrium configuration after the RBF.

Figure 6.6-e shows the shoreline at around 16:45, when most sediments have been deposited and no significant changes of the slope geometry have occurred for a sustained amount of time. The maximum retrogression length of the shore is about 13 m.

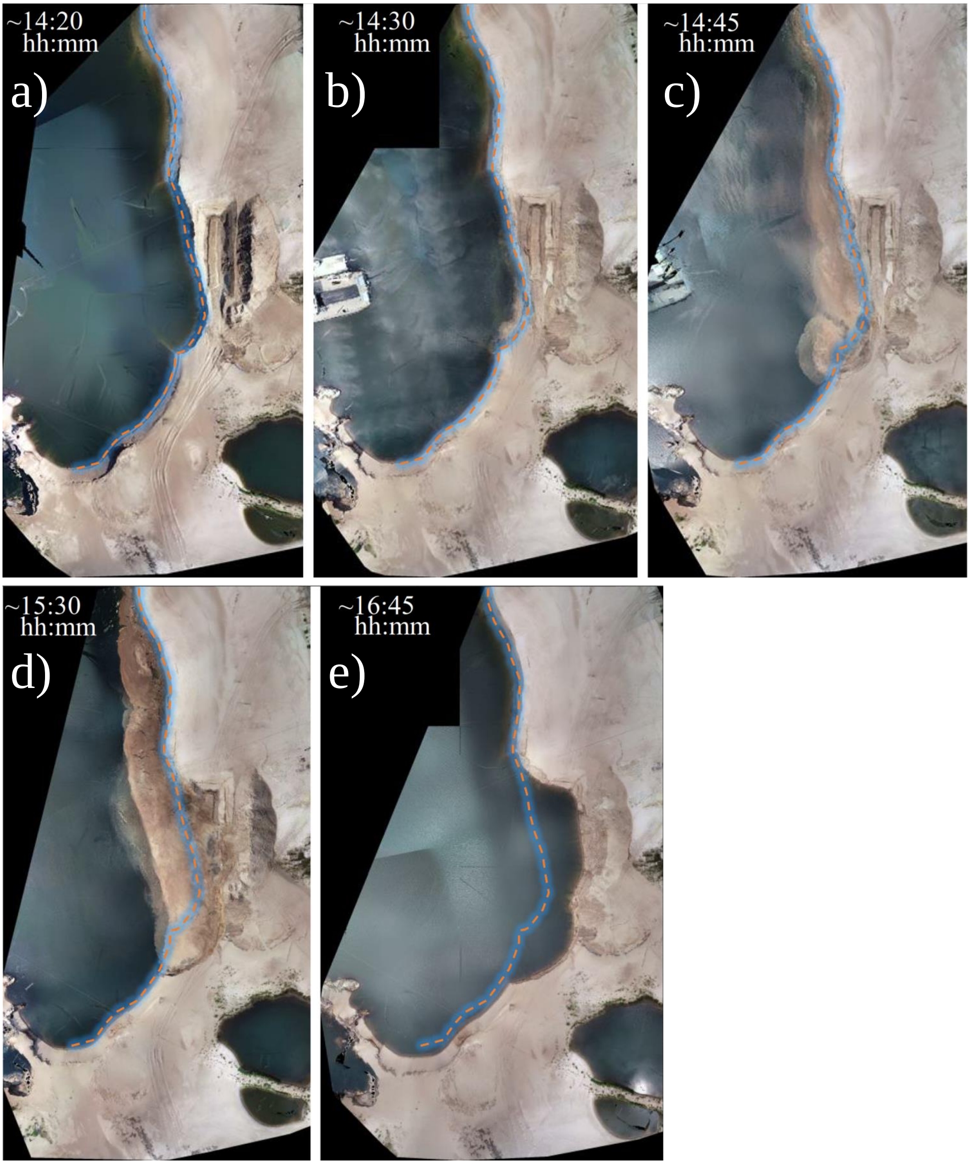

Figure 6.6: Overview of the second RBF in Site-B from UAV photogrammetry. The orange dashed line highlights the shoreline shape before the second RBF experiment.

### 6.4.3. Data analysis

By combining the available point clouds generated by echo sounder bathymetry with UAV digital surface models using $CloudCompare^{TM}$ (as in this dissertation, or similar geospatial software) it is possible, after post-processing, to generate panoptic views of the slope geometry at different moments in time. The resulting panoptic view of the full target slope for the experiment before and after the dredging activities is shown in Figure 6.7. Figure 6.7-a shows the target slope panoptic view before any excavation activities. The contour lines indicate the z coordinate and the dashed line indicate the location of the shoreline (i.e. water table). Figure 6.7-b shows the bathymetry recorded after the first RBF event. From this figure it is possible to observe that the excavation front at the slope toe presents steep geometries, well above the friction angle of the sand.

The 3D point-clouds post-processing data also allow for automatic visualizations of the dip angles (e.g. Figure 6.8-a), which highlights the changes in slope angles and the susceptible areas for RBFs (i.e. darker shades of red). Figure 6.8-a shows submerged slope angles before the experimental step #4, apparently stable and with a steepness above $45^{\circ}$. It is also possible to observe extreme slopes nearby the suction head GPS recorded position, touching $70^{\circ}$ where the RBF was initiated. The surroundings present gentler slope angles, but sometimes larger than the soil angle of internal friction which suggests the presence of some apparent cohesion in the sand layer of this quarry. The slopes do not show a gradual change of slope angle but a rather step-wise change. This is not only due to the excavation method used in this quarry (where RBF are often triggered to drive sand into the suction head), but also due to the fact that sediments move suspended in turbidity currents, and by accelerating down slope they gain enough momentum to deposit far from their origin and settle with a slope angle as small as $2^{\circ}$.

By comparing the last panoptic geometry to the one obtained before the RBF event, it is possible to perform estimations of the mobilised volumes of sand during the RBF. Figure 6.8-b shows in orange where most of the sediments settled and in blue the eroded volumes of sand during the triggering and following excavation activities. A large amount of sediment deposited just behind the depression caused by continuous excavation of the suction head (as also visible in Figures 6.7-b and 6.8-b) that was kept active to promote failure close to the instrumented trench, as explained in Experimental step #2. Figure 6.8-b also shows that part of the southern slope was involved during the RBF. Hence, it is reasonable speculating that the southern slope erosion contributed to decelerate the RBF thanks to the abutment effect that the new forming slopes near the toe have on the target slope.

Quantitative estimations of the mobilised sediments are reported in Table 6.2. About 12.000 $m^3$ were mobilized during each RBF. From this table it is possible to appreciate that both RBF events have a negative volume balance, meaning that part of the sediment was removed from the monitored area. This is partially justified by the fact that part of the mobilized sediments were collected by the suction head, and that another part was deposited by the turbidity currents outside of the surface area taken in the analysis. Because the slope selected as the experiment site was close to a shore corner, the sediment contributions from surrounding slopes, especially underwater, are more prominent, hence possibly influencing the RBF on the target slope due to its ”abutment effect”.

After the experimental step #2, additional excavation activities for removing the sand deposits from the bottom of the quarry were performed, as described in experimental step #3. This was done in order to facilitate the run out for a second RBF event. The time-lapse camera kept recording during the ”floor cleaning” excavations, while UAV and fibre optic tools were logged regularly to record possible developments of the slope geometry; however, no significant changes were recorded.

Figure 6.7-c shows the geometry of the target slope before triggering the second RBF. This geometry, due to the steep slopes close to the instrumented trench, is particularly susceptible to RBFs prone to involve also the instrumented trench.

By comparing the panoptic geometry obtained after the experimental step #3 (i.e. 6.7-c) to the one obtained after the experimental step #4 (i.e. 6.7-d), it is possible to perform estimations of the mobilised volumes of sand during the second RBF, as shown in Figure 6.8-c. This figure shows the slope eroded by the second RBF in shades of blue and, in shades of red, the location where most of the sediments settled. It is also possible to see that not only the target east slope but also part of the south shore was eroded away during the experiment. Additionally, from this figure it is possible to observe via the dispersed shades of yellow that some of the mobilized sediments deposited far from their origin. It is not possible to determine the complete trajectory of the sediments from the data made available, but it is reasonable to also speculate that some of them deposited outside the monitored area (i.e. surface analysed).

In Figure 6.8, the A-A cross section is arbitrarily selected in the centre of the backscarp to use for the MPM validation exercise, and is highlighted by the black dashed lines. Two lines in close proximity are used to ensure that enough points are taken from the point clouds to draw a continuous vertical profile. The vertical profile is reported in Figure 6.9. The profile lines appear thicker in the presence of slopes with a dip angle rather perpendicular than parallel to the cross section, but it indicates the location of the bottom floor with reasonable accuracy for the simulation of the RBF at this scale. The location of the suction head is also highlighted with a scale of grays as in the previous figure, and helps to identify the sand volumes removed by the suction head that triggered the flowslide.

The fibre optic surveys (shown in Appendix A, Figure 1) that were performed during the Site-B experiment showed very localised displacements (crack patterns, as shown in the Appendix A, Figure 2), although these cracks appear to be either present since the installation or rapidly occurring, hindering the interpretation of the data. Ultimately, for this experiment the fibre optic readings reliably indicate only the time at which the cable breaks during the second RBF.

The pore pressure and acceleration sensors were installed in the trench just below the water table in the boreholes from hand drills. The casing of these sensors was found not to be water-tight during the installation in Site-B, and the electronics subsequently failed. Therefore, no data set from pore pressure and acceleration sensors was produced in Site-B.

The time-lapse camera was turned on and left active for all the duration of the experiment. An overview of the camera images is presented in the appendix in figures 13 and 14.

The analyses of the experimental results performed so far allow for low accuracy estimations only, but the datasets here presented are considered sufficient to describe the main features of the monitored RBFs, such as macro geometry changes in time and duration of the event. Additional postprocessing of the collected data (e.g. comparing multiple point clouds or manually selecting ground control points) can improve the accuracy of the description of the RBF experiments here presented, but it is beyond the scope of this study.

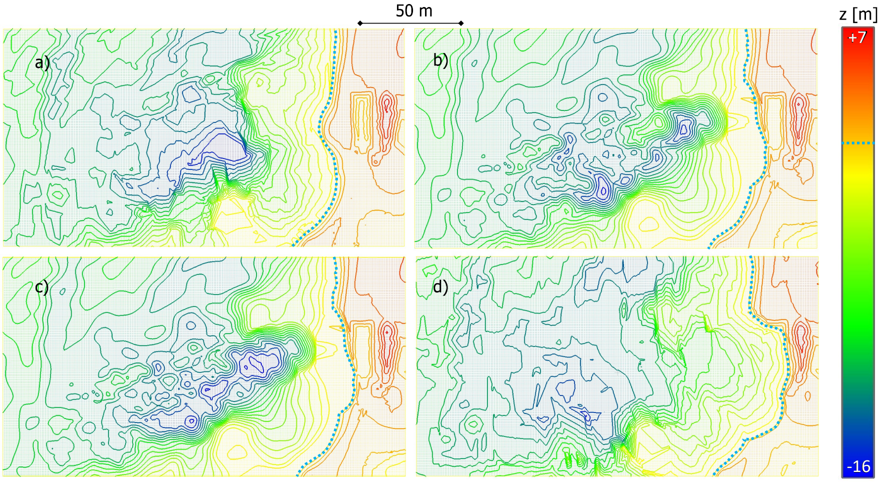

Figure 6.7: Panoptic views of the partially submerged slope at Site-B, obtained by merging bathymetries and UAV photogrammetry point-clouds: a) initial panoptic view ; b) panoptic view after 1st slide; c) panoptic view before 2nd slide; d) final panoptic view. Contour lines every 1 m. Water table is indicated with a dashed cyan line.

| RBF event #1 | | | RBF event #2 | | |
|---|---|---|---|---|---|
| volume difference | -6287 | $m^3$ | volume difference | -2741 | $m^3$ |
| surface analysed | 21222 | $m^2$ | surface analysed | 21384 | $m^2$ |
| deposited volume | 5111 | $m^3$ | deposited volume | 10083 | $m^3$ |
| eroded volume | 11399 | $m^3$ | eroded volume | 12823 | $m^3$ |

Table 6.2: Results from volume estimation in Site-B experiment by comparing panoptic views visible in Figure 6.7-a-b and in Figure 6.7-c-d respectively.

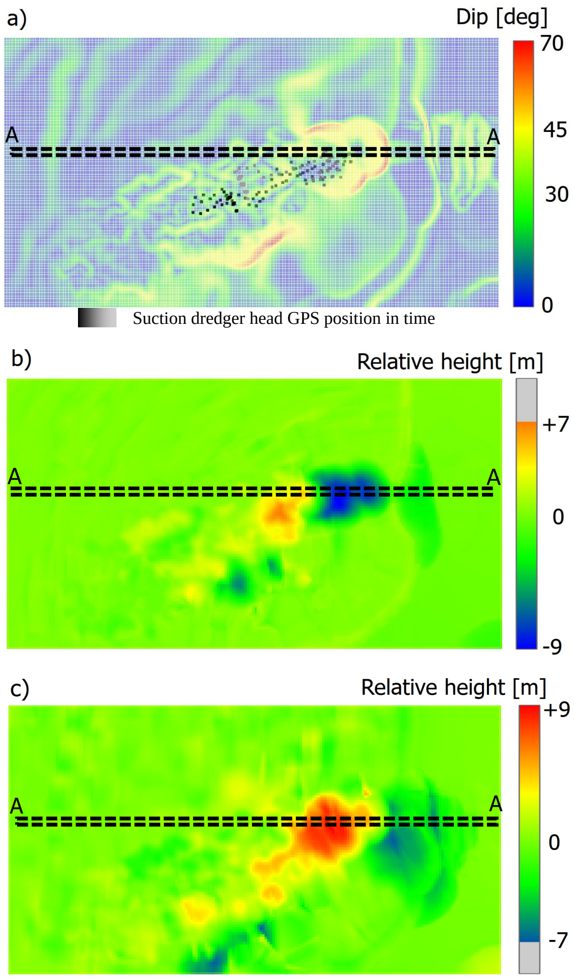

Figure 6.8: Slope steepness and RBF event volume analyses: a) dip angles of partially submerged slope before 2nd slide, the suction head GPS location through time is indicated with scale of grey (from black to gray); b) volume analysis after 1st slide: c) volume analysis after 2nd slide. The cross-section A-A of Figure 6.9 is highlighted here with black dashed lines.

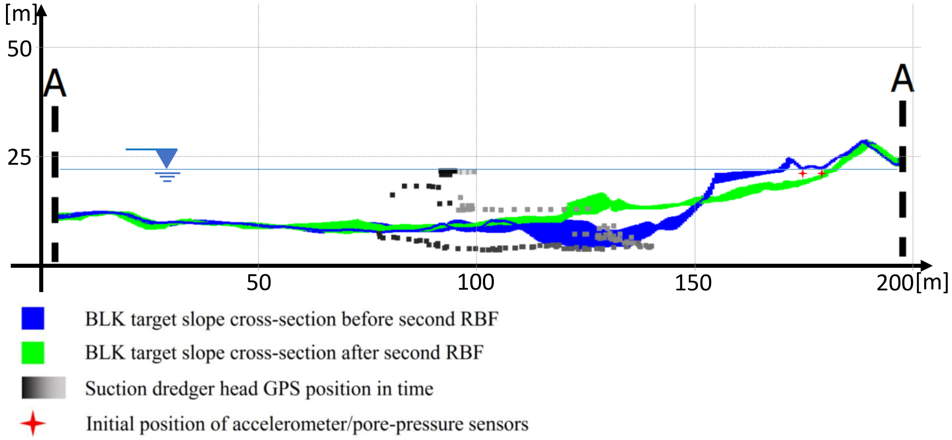

Figure 6.9: Point cloud from combination of bathymetry and UAV data, representing target cross section of the second RBF in Site-B. The cross-section is overlapped with the suction head GPS location through time, indicated with scale of grey (from black to gray).

## 6.5. Results of monitoring activities in Site-C

A new set of experiments was proposed to monitor RBF events during dredging activities also in Site-C, with the aim of including an analysis of pore pressure and acceleration data. Not all monitoring tools available in Site-B were also available in Site-C and even the selected slopes had different geometries, but it is considered very valuable adding a description of the evolution of pore-pressures and of the sediment accelerations to better understand the stress state of the soil before, during, and after the slope failures. Pore water affects effective stresses in the soil, which in turn modifies its strength, influencing the failure mechanisms and their sequence. However, on their own they do not clearly indicate underwater soil motion, and hence they need to be interpreted together with acceleration data. Because the geological layer and mining experiences of the two quarries were very similar, the pore pressure and acceleration logs, which are the focus of this set of experiments, are deemed to provide at least a quantitative description of the main characteristics of the failure.

Since it was considered not economically convenient to prepare the target slope before the experiments, it was decided to perform the experiments in a previously stripped area of the quarry that was ready for dredging activities and easily accessible for the surveyors. The ground level is 5m above the free water surface of the lake and the area near the shore was stripped by 4.5m, leaving the free water surface of the lake at about 50cm below the shore surface level. This was shallower in Site-C than in Site-B, allowing us to install sensors below water with hand drills and without mechanical excavators. In Site-C it was not possible to use the fiber optic strain gauge because the fiber optic cable was damaged and partially lost during the experiment in Site-B, and the results were not conclusive. However, during these experiments the pore-pressure and acceleration sensors were logged, unlike in the Site-B experience.

When arriving on site, a sand platform was present in the location selected for the experiments where the coast line was convex rather than concave. Hence it was deemed advantageous to install the buried sensors there to reduce the three-dimensional self-stabilizing effects of the run-out. The target slope, buried sensors and time-lapse camera locations are indicated in Figure 6.2-a. The sensors are in an orthogonal grid, spaced 0.5m distance north-south and 2m east-west from each other. The time-lapse camera was active for the entire duration of the experimental protocol. The pore pressure sensors were installed below the water table with a hand drill as deep as possible before the borehole collapses; hence, only a few dozens of cm.

The relatively smaller slope height required fewer excavation activities by the suction dredger to destabilize the slope. Hence, experimental step #2 was not required and allowed us to perform experimental steps #3 and #4 twice in sequence on the same day. Before triggering the RBF, the bottom floor preparation (i.e. experimental step #3) was performed and measurements were taken from the bathymetry scanner and UAV to capture the geometry of the slope. While the bathymetry data made available were insufficient or corrupted to measure the slope below water, the UAV missions allowed for the monitoring of the slope area near the shore from above water.

### 6.5.1. Observations during first RBF

For the first time in Site-C, experimental step #4 was performed: the triggered RBF involved the slope body where the pore-pressure sensors were installed. Figure 6.10 highlights the evolution of the target slope geometry in time during the first RBF as observed from five UAV missions. The blue dashed line highlights the lake water surface position, and the green dashed line, the target slope before the first RBF event. The evolution over time of the slope erosion is visible only in the slope crest from UAV photogrammetry (both above water and few centimeters below the free water surface).

The first image in Figure 6.10 (9:42 am) depicts the initial shape of the slope, capturing the moment after the installation of the sensors and the beginning of the excavation process. In the second image (11:31 am), the excavation process happening perpendicular to the shoreline can be seen with the suction dredger moving closer to the foreshore as the suction head undercuts the slope toe. The first RBF becomes apparent at around 11:53 am, with air bubbles emerging on the water surface from the underwater breaching wall (as visible in the third image in Figure 6.10 11:58 am), and it took about 30 minutes for the breaching wall to reach the slope crest, causing some sand blocks to fall into the lake before expiring. This was a clear sign for the suction dredger to stop the dredging and retract the suction head.

From the UAV images it is not easy to observe what happens underwater, but the evolution of the back-scarp circular shape of the shore close to the slope crest, that is typical of these phenomena, is evident (as visible in the fourth image at 12:24 pm). After 20 minutes there were no more changes in the geometry, indicating that the RBF was over and most of the suspended sediments settled (seen in the last image in Figure 6.10 at 12:54 pm).

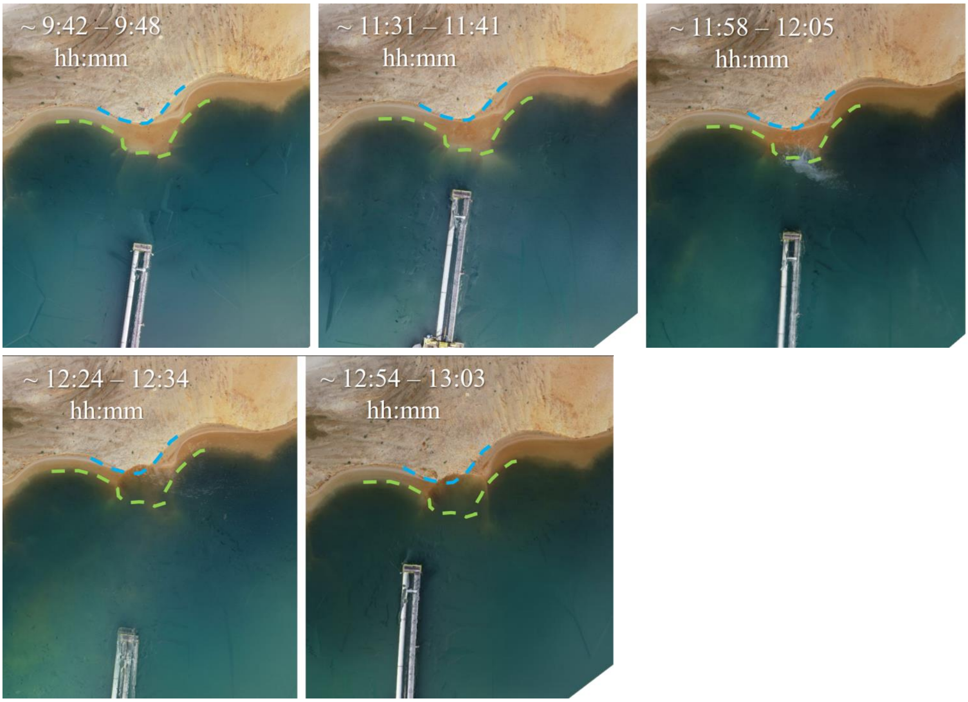

Figure 6.10: Overview of the first RBF in Site-C from UAV photogrammetry. The blue dashed line highlights the shoreline before the first RBF event. The green dashed line highlights the submerged sand platform shape before the first RBF.

After the first observable RBF, about 3 hours were spent recovering and reinstalling the pore-pressure sensors in the proximity of the first back-scarp. This time also ensured that the underwater failure had stopped, finding a new equilibrium configuration for the slope. Six of the pore pressure and acceleration sensors were lost during the recovery attempt because of improper connection to the steel cable meant for this purpose. However, it was possible to retrieve two sensors and reinstall them on the left convex slope adjacent to the back-scarp of the first RBF, as indicated in Figure 6.2-b.

### 6.5.2. Observations during second RBF

The initial shape of the stable slope before the second RBF is visible in Figure 6.11 at 12:54 pm, with the blue dashed line indicating the foreshore location for the second experiment. The excavation activities trigger the second RBF started around 15:00, first to clean the bottom of the quarry from the sediment previously mobilized (i.e. a second experimental step #3) and then to trigger the slide (i.e. a second experimental step #4).

The occurrence of the second RBF became evident at around 16:00, with the air bubble emerging on the water surface (as seen in Figure 6.11 at 16:15 pm). The air bubble from the breaching wall appears as a white floating layer close to the shore and part of the slope crest is already eroded away, particularly in close proximity to the installed sensors.

At 16:15 the dredger operator noticed sand blocks falling into the lake from the back-scarp, stopped excavating and moved away from the target slope to allow the failure to expire fostered only by its self-weight. The third image at 16:34 pm depicts the ongoing RBF process, as is evident from the sand sediment cloud of the turbidity currents and floating material. A larger portion of the slope was involved in the second RBF compared to the first RBF (as visible in Figure 6.11 at 17:45 pm), possibly due to the temporary support that the unsaturated part of the slope provided. Once the suction in the unsaturated part dissipated, the additional strength provided by the unsaturated part also disappeared resulting in a larger slope failure.

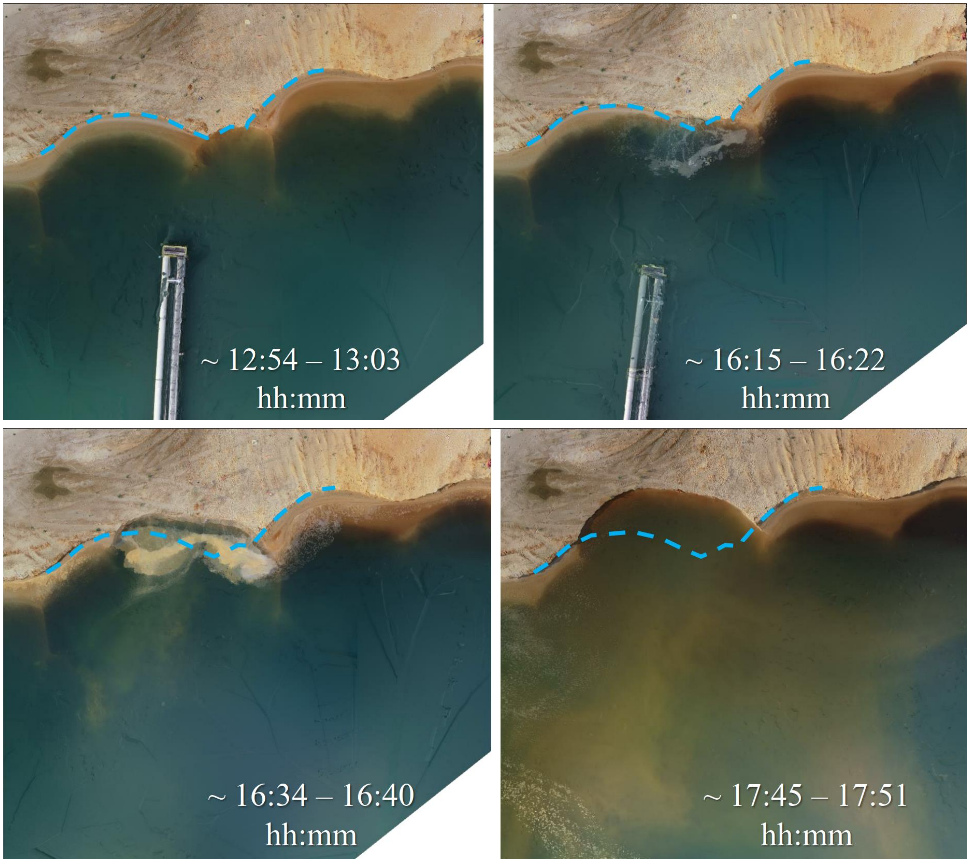

Figure 6.11: Overview of the second RBF in Site-C from UAV photogrammetry. The blue dashed line highlights the shoreline before the second RBF event.

Based on UAV photogrammetry data, which only shows the slope surface area but not the underwater geometry, we estimate the second RBF to be around four times the first, not accounting for the underwater volume that was mobilized. This estimation is made by observing the shape of the back scarp which is 4.7m wide above water for the first RBF, with a radius of approximately 5.6m. Similarly, the second RBF has a 17.1m wide back scarp with a radius of approximately 20.5m. The suspended sediments on the water surface during the second RBF, that lasted about 30 minutes, were more numerous due to more frequent splashing of sand blocks in the water. The last frame at 17:45 pm shows part of the sediments that were still suspended near the shore and it appears clear that at least part of them deposited far from their origin.

### 6.5.3. Data analysis

Unfortunately, the bathymetry data made available for the Site-C experiment were found insufficient or corrupted for the purpose of building multiple panoptic views and consequently performing volume analyses. Only a panoptic view of the target slope geometry after the second RBF was reconstructed and is presented in Figure 6.12, alongside a screenshot of the continuous data-stream as visible from the command console of the suction dredger. An overview of the monitored features for each experiment is reported in Table 6.3.

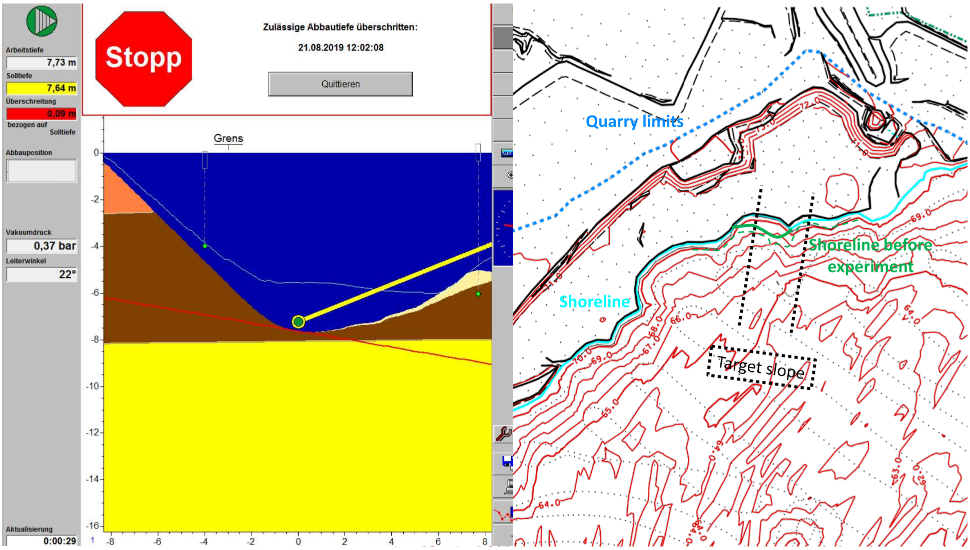

Zulässige Abbautiefe überschritten:
21.08.2019 12:02:08

Arbeitstiefe 7,73 m
Solltiefe 7,64 m
Überschreitung 0,09 m bezogen auf Solltiefe
Abbauposition
Vakuumdruck 0,37 bar
Leiterwinkel 22°
Aktualisierung 0:00:29

Figure 6.12: On the left, a screenshot of the target slope cross-section from the bathymetry scanner used in Site-C before the experiment. On the right, a bathymetric map of the Site-C quarry after the experiment: the continuous green line indicates the shoreline geometry before the experiment; the dashed green line indicates the geometry of the sand platform just below the water table, which is also visible in Figure 6.2 and 6.11.

### Pore pressure interpretations

The pore pressure evolution in time during the experimental protocol activities is shown in Figure 6.13. Each sensor pressure data log is plotted against time. The names of the sensors buried, which indicate their installation depth below the water surface, and their initial location, are presented in Figure 6.2.

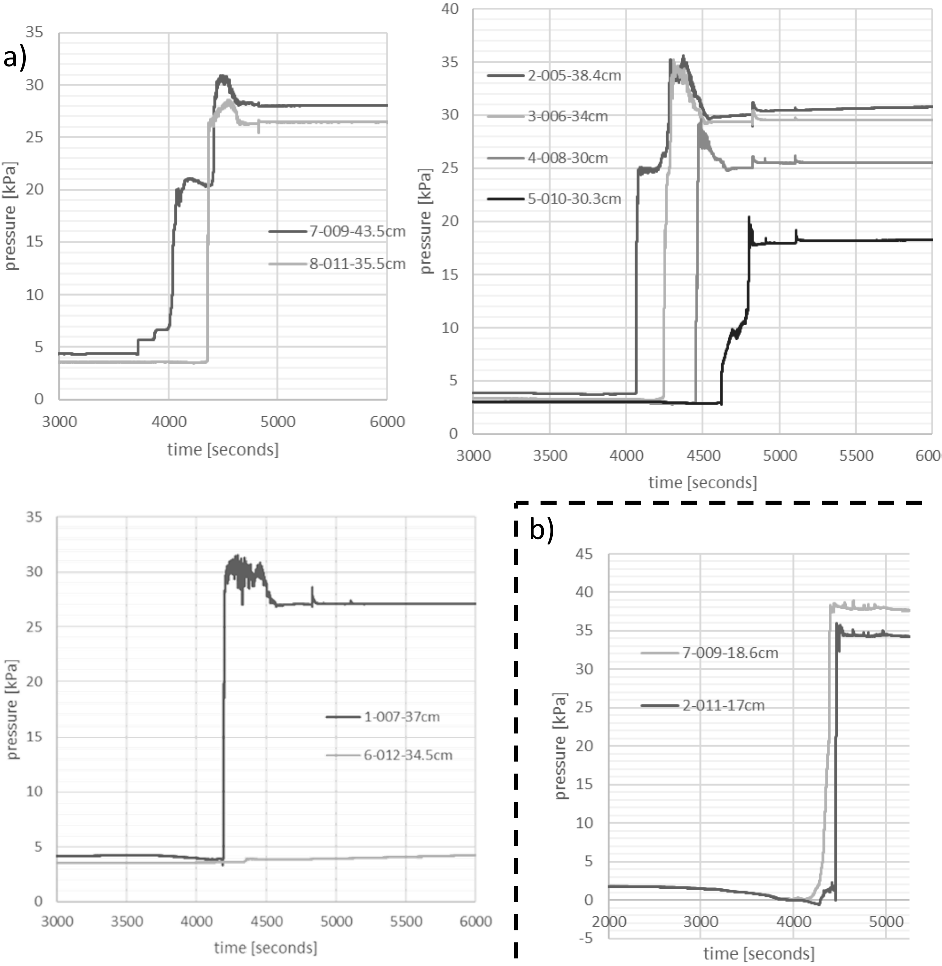

Figure 6.13: Plots from pressure sensors during RBF: a) data set collected during the first RBF event; b) data set collected during the second RBF event.

The horizontal lines at the beginning and at the end of the pressure data sets represent hydrostatic pressure conditions, hence their depth below the water table. As the breaching wall generated by the suction dredger approaches the sensor positions, we can observe some excess water pressure build-up due to the dilative behavior of dense sand. This effect is visible during the first RBF (Figure 6.13-a), but is more pronounced in the second one (Figure 6.13-b). After this, there is a rapid increase of pressure due to the fact that the sensors fell freely under gravity until reaching the bottom of the slope. There are multiple features of the RBF captured by the pore pressure data.

Firstly, the dilative behavior of sand due to the tendency of the slope to spread after undercutting of the toe, which is visible by the decrease of pore pressure before a sharp increase in pore pressure. Secondly, the sharp increase in pore pressure represents the sensor falling downslope among the sand sediments (e.g. at 4700 seconds for sensor 5-010 in Figure 6.13-a). This sudden increase sometimes presents stepwise trends until settling in a new spot (e.g. bottom of the quarry). These steps may represent either that the connection cables got stuck in the sand at the crest, slowing down the fall, or that the sensors may be slowed down by local gentler gradients of the underwater slope geometry.

In Figure 6.13 it is visible how each sensor has settled at a different depth due to the fact that the retrogressive pattern of the slope failure involves the sensors sequentially in time, leaving them on the newly deposited sediment bed coming from the RBF. It is possible to observe that the slope failure occurs retrogressively and also radially by comparing the time stamp at which the sudden increase of water pressure occurs in each sensor. Next, following the rapid increase of pressure we observe a slower build-up and dissipation of pore water pressure from the sensor readings. These signals are typical of hydraulic jump and sand consolidating from the turbidity currents. In Figure 6.13 this corresponds to the maximum pore pressure readings, i.e. the first peaks.

Fourthly, we observe local peaks that follow the first maximum peaks, and these occur simultaneously in all sensors. These signals are visible, e.g., at around 4800 seconds and 5100 seconds of the first RBF. This pattern (i.e. sudden increase of pore pressure and slow dissipation) recalls that of a liquefaction slide pressure signal, as presented in the laboratory experience from Chapter 2 in figure 2.6. Hence, a liquefaction slide appears to occur due to the overloading of the depositing loose sediments, since the pressure peaks are visible simultaneously by multiple sensors. Following these signals in the data, it can be seen that the pore pressure readings show horizontal lines which indicate no movement was detected until the end of the experiment.

### Acceleration data interpretations

Similarly to the pore pressure readings, the accelerometer data in the Z direction through time is shown in Figures 6.14-a and -b.

For the accelerometer data, only the Z direction from the sensor log is presented in this chapter to make the figure plots more readable. The noise in the accelerometer data readings does not allow reliable velocity estimations; however, changes in the average line clearly indicate the time in which the sensors are in motion. By combining the observations from the pore pressure and accelerometer data over time, it is possible to speculate about what happened to the buried sensors.

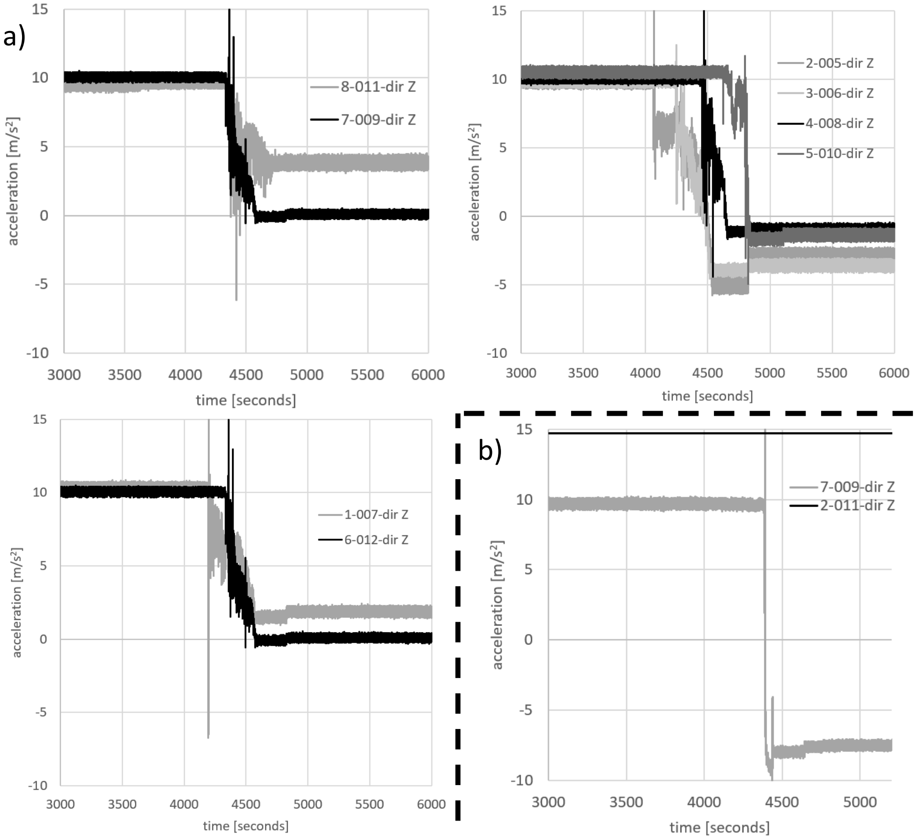

Figure 6.14: Plots from accelerometers during RBF: a) data set collected during the first RBF event; b) data set collected during the second RBF event.

The horizontal lines at the beginning and at the end of the acceleration data sets represent at rest (i.e. not in motion) conditions for the sensor. The interpretation of the features from the pore pressure sensor about the RBF is supported by changes of the accelerometer data around the same time. For example, sensor 3-006 data registers no movement until 4250 seconds, which corresponds to the sudden increase of pore pressure, indicating downwards motion of the sensor in the quarry. It reaches a new equilibrium at around 4500 seconds, which is interrupted around 4800 seconds for the final equilibrium position. This interruption corresponds to local peaks of the pore pressures, indicating the occurrence of liquefaction slides involving the sensor.

Finally we can observe that pore pressure sensor 6-012 and accelerometer 2-011 did not work or got damaged due to the unique pattern of their readings compared to others. Other observations are also supported by the UAV photogrammetry maps, such as the slow retrogressive and radial evolution of the failure.

| **Location and date** | **Site-B 28-29 May '19** | **Site-C 21 Aug '19** |
|---|---|---|
| **Slope Height** | 18 $m$ | 8 $m$ |
| **Material** | quartz sand | quartz sand |
| **Average Grain Size** | 0.19 $mm$ | 0.18 $mm$ |
| **Monitored Features:** | **1st RBF - slope experiment 1** | |
| *Bathimetry* | ✓ | x |
| *UAV Digital Elevation Model* | ✓ | ✓ |
| *Panoptic View* | ✓ | x |
| *Gps Head Position* | ✓ | x |
| *Pore-pressure and acceleration* | x | ✓(x8 sensors) |
| *Timelapse video* | ✓ | ✓ |
| *Excavation method* | continuous suction | suction interrupted as soon as RBF triggered |
| *Volume* | 11399 $m^3$ | N/A |
| *Max Retrogressive length* | 19 $m$ | 0.5 $m$ |
| *Slope failure duration* | 90 $min$ | 30 $min$ |
| | **2nd RBF - slope experiment 2** | |
| *Bathimetry* | ✓ | x |
| *UAV Digital Elevation Model* | ✓ | ✓ |
| *Panoptic View* | ✓ | x |
| *GPS Suction head position* | ✓ | x |
| *Pore-pressure and accelerations* | x | ✓(x2 sensors) |
| *Timelapse video* | ✓ | ✓ |
| *Excavation method* | suction interrupted as soon as RBF triggered | suction interrupted as soon as RBF triggered |
| *Volume* | 12823 $m^3$ | N/A |
| *Max Retrogressive lenght* | 13 $m$ | 4 $m$ |
| *Slope failure duration* | 60 $min$ | 30 $min$ |

Table 6.3: Overview of the Site-B and Site-C experiments

# 6.6. Numerical simulation

## 6.6.1. Introduction

In order to validate Anura3D for RBF, field-scale experiments are necessary in addition to laboratory experiments as presented in previous chapters. This is because scale effects for this phenomenon are not negligible. Hence, a preliminary modelling exercise was made by taking the results of the second RBF event in Site-B presented in Section 6.4 as a benchmark.

The results of the MPM simulation are compared with more established numerical results (i.e., FEM strength reduction method) and also with the field experiment results. The A-A cross-section was arbitrarily selected for this validation exercise and is shown in Figure 6.9. A 2D plane strain cross-section is computationally cheaper and simpler to model than the full 3D slope as an exploratory attempt. While the RBF monitored was influenced by 3D effects of the sliding process, a 2D model allows one to judge qualitatively the performance of Anura3D in capturing the RBF features such as pore-pressure fluctuations, retrogressive patterns and shape of failure. This cross section was selected as a slice of the 3D panoptic view (i.e. point cloud) because it is roughly in the middle of the target slope and perpendicular to the shore. During the second RBF, the dredger lifted the suction head above the water table as soon as the operator observed soil blocks falling into the water from the unsaturated back-scarp. This means that after triggering the RBF, the sediments moved due to the self weight (and not because of ongoing undercutting).

This RBF event is better suited to be simulated by Anura3D compared to other RBFs monitored during the experiments because of the available bathymetry before and after the main sliding event and because sand volumes were not continuously removed in order to foster the failure. Hence, it requires one single excavation phase to model the triggering mechanism, after which the RBF takes place. The comparison of numerical slope evolution and monitoring data is considered useful for assessing the performance of the 2D, two-phase, one-point MPM formulation as an investigation tool for RBFs and partially for its validation for breaching flowslides at real scale.

Because there are no analytical solutions for slope instability problems, the RBF is first investigated with a FEM strength reduction analysis, as is common in mining practice. A phased construction analysis appears the most simple modelling strategy in order to consider realistic stress conditions during the calculations. The computational mesh geometry used for the FEM and MPM simulations (that are visible respectively in figures 6.15 and 6.16) is simplified by linearizing the local slope gradients (as these could act as weak points of the slope that could trigger premature global failures in the simulation). For the FEM model, only the initiation of the slide can be computed (owing to the limitation of the small strain assumption) by removing soil elements from the slope toe to simulate the excavation of the suction dredger.

As in the first simulation attempt, the soil is simply modelled as a dense, isotropic, fully saturated homogeneous sand material below the water table and completely dry above the water table. The laboratory test data made available for Site-B (i.e.

Table 6.4: Mohr-Coulomb strain softening parameters used for the FEM and MPM simulations of the Site-B experiment.

| *parameter* [unit] | $\gamma_d$ [kN/m$^3$] | $\varphi_p$ [°] | $c_p$ [kPa] | $\psi$ [°] | $\varphi_r$ [°] | $c_r$ [kPa] | $\psi_r$ [°] | $\eta$ [-] | $E$ [MPa] | $\nu$ [-] |
|---|---|---|---|---|---|---|---|---|---|---|
| MC SS | 16 | 35 | 8 | 5.0 | 33 | 1.0 | 1.0 | 500 | 30 | 0.3 |

grain size distributions) were not considered sufficient for a thorough calibration of the slope material. The sandy soil behaviour was simulated with a Mohr-Coulomb Strain-Softening (MC SS) constitutive relationship calibrated from field evidence in dry conditions: the peak and residual friction angle, dilatancy, and dry density are the same as selected for the pure quartz sand presented in Chapter 5 of this dissertation.

Additional laboratory tests were performed to adjust the calibration on Site-D sand samples (i.e., triaxial and oedometer tests in loose, medium and dense samples, grain size, unit weight, Proctor test). However, a thorough calibration of the soil model is not the main aim of this study. Therefore, as a first simulation attempt, the calibration of the soil strength parameters performed in Section 5.3.2 is considered a good approximation for this site as well. Only the initial value of (apparent) cohesion was adjusted/increased (in other words, recalibrated). This was done because of the evidence in the field: the steep slope angle, well above the sand friction angle, that were observed during the field experiment would not be stable otherwise. Also the DST presented in Table 5.2 shows the presence of apparent cohesion in the material samples. The full set of soil parameters used in the following analyses for the MC SS material model are here reported in Table 6.4 for reference.

The 2D two-phase one-point MPM formulation with linear triangular elements was selected among others for simplicity and because it was already validated for liquefaction flowslides at the laboratory scale [9].

## 6.6.2. Validation of the numerical solutions

### FEM simulation

By using the soil parameters presented in Table 6.4, the FEM with strength reduction method is applied to estimate the slope safety factor before excavation activities to trigger the RBF. In Figure 6.15 the hydrostatic pressures are plotted as vectors on the soil boundaries. The location of the water table coincide with the top right corner of the model geometry. Therefore, only the dunes of soil above water table around the instrumented trench are modelled as dry material.

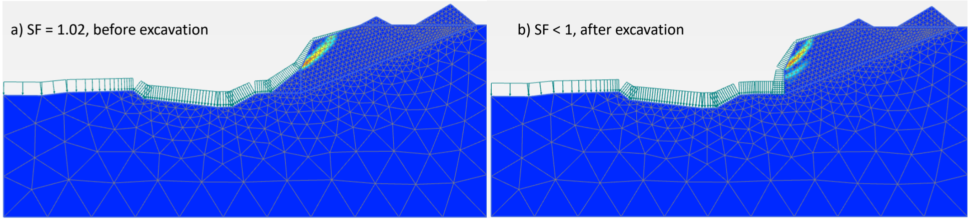

Figure 6.15: FEM with strength reduction method results for the 2nd RBF event in Site-B. The deviatoric strain is plotted to compare the initial sliding surface with MPM simulations.

The loading phases of the FEM analysis can be summarised as follows. During the first phase, the initialisation of the stresses is performed under drained conditions, with gravity loading, after which the strain and displacements in the model are reset to zero. The initial slope model corresponds to the linearised slope geometry obtained at the end of experimental step #3. Because this geometry was generated by continuous excavation of the slope toe, it is considered very susceptible to RBF and just in equilibrium. The value of apparent cohesion was incrementally changed starting from zero during the stress initialization until a stable geometry was found (at $c_p = 8kPa$). Following this, a dummy phase is run to ensure that equilibrium is reached and that the slope is stable in the new state. In the third phase, the strength reduction method is used to check the slope safety factor before toe excavation (see Figure 6.15 -a). With these soil strength parameters and linearised geometry, the slope is just in equilibrium before the toe excavation step (i.e. with a slope safety factor = 1.02).

A fourth phase is calculated starting from the stress state of the second phase, where the behaviour of the undrained soil is activated and the excavation of the toe is performed to assess the pre-failure strains and to forecast the failure surface in the slope. To mimic the triggering mechanism (i.e., toe excavation), some soil volumes were removed from the slope toe. This excavation phase initially left a 5 m tall vertical soil wall without lateral support. The soil in the proximity of the wall base will tend to shear due to the self-weight of the slope, and the FEM solution of this excavation phase diverges, indicating that the slope is ongoing large deformations. The results of the phased excavation analysis performed with Plaxis are shown in Figure 6.15-b. It is not clear however how far the RBF will extend uphill, nor about the consequences of the sliding process (i.e. duration of the failure and sediment trajectory and deposition). The highest values of deviatoric strain indicated in red shows the occurrence of a shear band in the steepest part of the slope.

Hence, this FEM simulation predicts the log spiral shape of the first sliding soil mass. This is much larger from the observed shape during the experiment because of unavoidable abstractions (e.g. element size, instantaneous removal of the toe, 3D effects, water turbidity effects, etc.) between the model and the experiment. However, the log spiral shape of the sliding blocks is captured as expected by the soil model because of the soil material involved.

### MPM simulation

In order to compare the MPM solution to the FEM results, an equivalent phased analysis procedure was performed. The same geometrical (e.g., linearization of the slope) and modelling considerations (e.g., hydrostatic pressures and dry soil volumes) were made to have comparable models. The mesh refinement also has a similar size (i.e., about 1 m) where soil displacements are expected. Note that a mesh discretization of the non-soil domain in MPM is necessary to allow the points representing the slope material to move among adjacent elements during the calculation. The stress initialization was performed by a gravity loading drained analysis and by resetting the displacements and strains at the end of it to zero. A second dummy phase, similar to the FEM phased modelling procedure, was also here run to ensure equilibrium steady state conditions before the excavation phase.

The soil parameters are the same to those used in the FEM model. The geometry also is very similar, with the difference that the vertical breaching wall is not generated by removing soil volumes from the toe (as done in the FEM model), but by deactivating a vertical boundary condition that restrains horizontal displacements during the gravity loading procedure. This difference is expected to not significantly affect the results.

In Figures 6.16 and 6.17, the main results of the MPM analysis performed with Anura3D are presented. Figure 6.16 shows the soil that moves and softens due to the deviatoric strain developed after the removal of the toe. It is seen that as soon as the vertical boundary is removed, a soil body with a very similar shape to that forecasted by the FEM analysis starts moving downslope. However, not only is the soil above the slip surface moving, but also the surrounding soil. At the same time, a large portion of the slope develops excess pore water pressure as a result of the dilative behaviour of the dense sand during shearing.

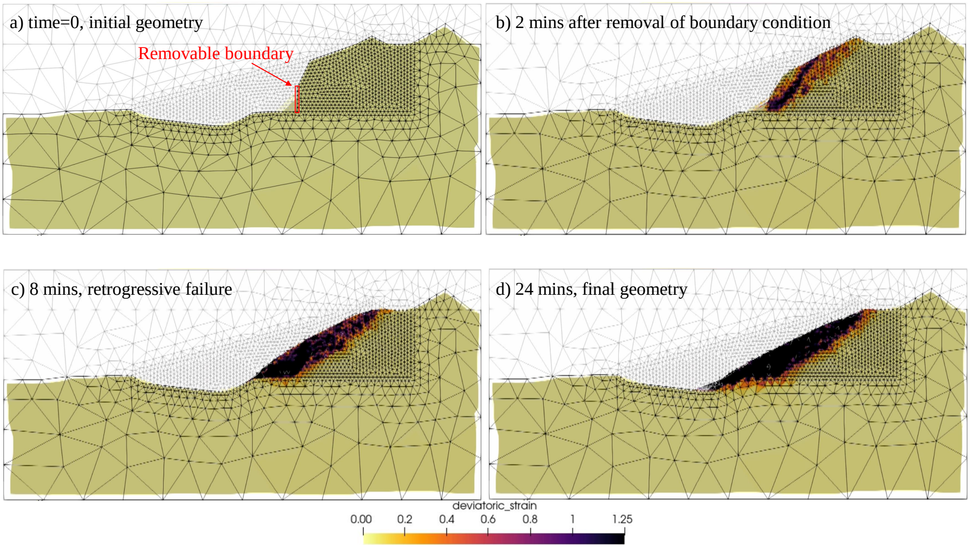

Figure 6.16: MPM results of the 2nd RBF event in Site-B. The deviatoric strain is plotted to compare the initial sliding surface with FEM simulations.

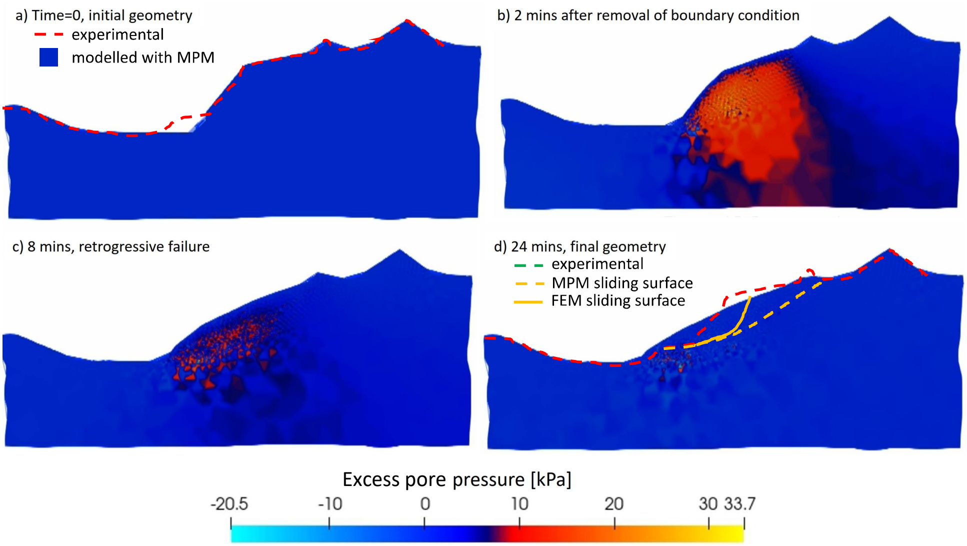

Figure 6.17: MPM results of the 2nd RBF event in Site-B. The excess pore pressure results show unrealistic pressure oscillations.

Figure 6.17 shows the evolution of the excess pore water pressure generated during the failure. As MPM allows for large deformations, the simulation continues for a relatively long time, showing the full retrogressive failure pattern typical of these sliding phenomena. During this time, the excess pore water pressure that was generated in the slope body slowly dissipates, decreasing the (transient) apparent strength of the material, and expiring after about 24 minutes. Qualitatively MPM well captures the slope failure and provides equivalent and additional insight compared to the FEM analysis.

While the results of the FEM analysis are seen to only capture the initial sliding surface geometry, from the MPM results it is possible to observe the evolution of the failure until deposition of the mobilised sediments. FEM and MPM analyses predict similar initial sliding surfaces, as shown in Figures 6.15-b and 6.16-b.

There are some key similarities with the observed experimental results:

- the shape of the sliding surfaces resemble that of a log spiral in accordance with the results of Bolton [3].
- The full retrogression length of the observed RBF (i.e. 13m) is close to that of the MPM (i.e. 8m).
- The RBF lasted for about 1 hour in the field, and in the MPM results a new stable configuration is found after 24 minutes. Despite the fact that the duration does not match quantitatively, this can be considered similar because the MPM predicts a slow failure rate of the slope typical of RBF, unlike other failing mechanisms often associated with sandy slopes. Additionally, permeabilities could easily vary by more than a magnitude of 2.
- The pore pressure rises before failure of the slope in both the experimental and numerical results.

The overall phenomenon is qualitatively well described. Quantitatively, the results of strains and displacements are equivalent to the FEM until failure, and after failure, the retrogressive failure is captured to some extent, allowing a better estimation of the retrogression length of the failure.

However there are also considerable differences:

- The final slope geometry differs to a certain extent from those observed during the experiment presenting a steeper slope and shorter run out. Potentially, this is because the hydraulic effects are neglected by the used MPM formulation, among other reasons.
- The slope failure in the field, after triggering mechanism, occurred with multiple small retrogressive slidings events from the backscarp slope but MPM results clearly shows only 2 major sliding surfaces. This is due to the fact that MPM uses a minimum element size of 1 m, while sand in real RBF can move grain by grain. It is reasonable to speculate that by refining the mesh size (e.g to the size of the turbidity flow) the accuracy of the results will increase.

The stress field in the MPM simulation presents a checker-board pattern, with oscillations, mostly in the range 5-10 kPa, during the failure. This is evident in the water pressure plots in Figure 6.17-b-c. The appearance of this spatial stress distribution is mainly due to the linear shape functions that were used for numerical integration.

## 6.7. Discussion

### 6.7.1. Experimental measurements considerations

The presented experimental set up and monitoring protocol facilitated capturing a new experimental dataset of RBF at full scale, with adjustable accuracy, both in space and time. Increasing the redundancy of the monitoring tools would increase the overall accuracy of the measurements and amend possible data loss.

The limited time and resources made available for this pilot experiment were the main bottlenecks that hindered the complete success of the monitoring activities, because the tools deployed proved their effectiveness, and despite some data set being lost (i.e. bathymetries from Site-C, pore pressure readings from Site-B), the resulting dataset were sufficient for the validation of numerical solutions. Pore pressure readings would have not been lost in Site-B due to water breach if prior water-testing and calibration of the sensors in the laboratory would have been performed. Pore pressure sensors would have not been lost if properly installed to steel cables meant for that purpose. However, a pontoon with a mechanical arm for the recovery process is advised as they can be buried under several meters of sand. The fiber optic strain gauge installation process generated plastic strains that hindered the readings. This could be prevented by using thicker cables and/or a different installation technique.

A large part of the challenges in performing these experiments came by the uncertainties of yielding useful results by following this experimental protocol. Despite these challenges, the experimental protocols successfully recorded several features of the RBF and can be used as a case study for future research as a proof of concept. Drones, including underwater drones, have become increasingly more accessible making them a promising addition to aid the monitoring setup.

Steeper slopes than the angle of repose of the material were recorded after experimental step #3, which indicates the presence of apparent cohesion in the material even if saturated sand is deemed a cohesion-less material.

### 6.7.2. Numerical modelling considerations

The soil parameters and material behavior have been approximated by using the soil investigation performed in the previous chapter and by adjusting the cohesion to have stable geometries as observed in the experiment. This was considered a reasonable choice because of similar chemical properties and grain size analyses. However, the soil material behaviour should be better calibrated by making full use of the investigation performed in Site-D [4] and possibly including layering and variability. Also more advanced constitutive models for sand are available and are expected to improve the outcomes of the analysis, even though they often require additional efforts for the procurement and calibration. The MCSS model was here chosen because is often used in literature and mining practice, and its parameter calibration is relatively straightforward. However it has no stress dependent strength parameters which makes it less accurate compared to other models, especially when the scale of the slope is very large.

As the sand in the slope body is expected to be in a dense state, a unit weight value around the highest observed in laboratory tests was selected, that is, $\gamma_d$ 16 kN / m$^3$. The steep slopes in the bathymetry may also indicate that there were still active breaching slopes underwater or simple measurements errors (e.g. ghost clouds), even though these scenarios are unlikely due to the relatively long period of time between experimental steps that would allow active breaches the time to expire, and because stable steep slopes were also observed above water for a relatively long period of time. Hence, accounting for apparent cohesion in the constitutive model of sand is considered reasonable. It was decided to adjust the cohesion parameter to fit field observations also because, while the friction angle of sand is expected to be roughly constant at constant stress levels, the value of cohesion may vary due to presence of fine particles, cementation processes, or suction. However, more detailed site investigations, interpretations, and assessments with different constitutive models are expected to yield better and more reliable results from the simulated slope models, but at a cost that was not well suited for this research project.

The undrained conditions in the FEM analysis after the excavation phase are questionable considering the relatively coarse material. However, the sensors recorded build-up and dissipation of water pressure during experiments (both at laboratory and field scale), indicating that even though the excess pore pressure is expected to dissipate quickly, the excess pore pressure should not be neglected. Drained calculations can be used as an alternative scenario, but not always more conservative. The excess water pressure recorded in the experiments is expected to briefly increase the material strength (depending on the dissipation rate). However, the temporarily stronger material may generate steeper slope geometries during RBF sliding events, which in turn would favour faster turbidity currents, which could promote undercutting of the slope. Conversely, a drained calculation, as implemented in Plaxis or Anura3D (i.e. disregarding pore water pressure changes), would not account for the transient soil strength increase, and hence would not be able to capture the steep slope geometries occurring in the observed sliding surface.

FEM was a useful framework to workout the slope stability problem, allowing estimating the factor of safety (useful to manage failure risk) and to assess the failure mechanism by forecasting the occurrence of sliding in the slope body, the concentration of strain in the shear band and the generation of excess pore water pressure due to the dilating sand behaviour. However, FEM cannot give information about the evolution of the failure after the occurrence of the first slide due to the small deformation assumption, hindering the assessment of the retrogression length of the RBF.

The MPM simulation shows a steeper final slope angle as a result of the RBF and a retrogression length smaller than that observed in the field. Among the contributing factors for this discrepancy, it is worth mentioning that the hydrodynamic effects were neglected by the selected 2-phase, 1-point formulation. The 2D two-phase one-point MPM formulation with linear triangular elements was selected among others for simplicity and because it has already been validated for liquefaction flowslides at laboratory scale. However, its coupled formulation does not account for the fluid phase with a separate set of material points but, together with the solid phase, in the same material point, meaning that the hydrodynamic effects generated by free water flows (e.g. turbidity currents) are neglected. The use of more complex formulations (e.g., the 2-phase 2-point formulation) are expected to yield better results by including some of the hydrodynamic effects.

The 2D plane-strain analysis for homogeneous slope bodies is an acceptable abstraction, but the analysis of 3D geometry effects should also be included for a thorough validation. The stress oscillations observable in MPM simulations are a known feature of linear shape functions and grid crossing MPs, but these can be mitigated with solutions available in literature (e.g. [1]). Liquefaction events of the deposited sand is not observed in the MPM simulation, but it could be due to the relatively coarse mesh and relatively simple constitutive model that accounts for positive dilative behaviour only and does not perform well for sedimentation processes. In fact, MC dilatancy sign is constant and cannot capture the contraction of the loosened parts once large strains have been reached.The mesh used in the presented models is relatively crude considering that the thickness of the shear band depends on the element size. Hence, refinement would help capturing multiple slides typical of RBFs and better model the failure geometry.

The MPM simulation can be considered at least partially validated for the analysis of flowslide phenomena at the engineering scale, by providing equivalent results up to the moment of failure to traditional assessment methods; additionally, allowing a better estimation of the retrogression length for RBFs while capturing important features of the phenomena such as the generation of excess pore water pressure during failure and retrogressive features.

## 6.8. Conclusions

This chapter presented a real-scale experimental set up for monitoring sand RBF dynamics and morphology. A new experimental dataset was collected by undertaking several field tests in quarries, with RBFs triggered by dredging activities. The RBFs were triggered by undercutting a previously instrumented underwater slope with a suction dredger. The triggered RBF mobilised a large shell-shaped volume of soil from the slope body, of approximately 12,000 $m^3$, depositing its sediments on a wide area at the slope base. The experimental setup proved its effectiveness in recording the main features of an RBF at field scale, and the results are considered useful for the analysis of RBFs. The main observed features are:

- triggering mechanism (GPS tracking of the suction head and mining experience was used to induce a slope failure at a location and time predefined for the experiment);
- slow retrogressive radial failure pattern (combination of UAV and bathimetric

data allowed one to generate a panoptic view of the submerged sand slopes at different moments in time, these flowslides took about 60 minutes to expire in multiple slides, while the dry sand slope collapsed in bulk in about 6 seconds as seen in chapter 5);

- mobilized volumes and sediment trajectories (the digital elevation models of the slopes allowed one to quantify the amount of sediment eroded and deposited from the area in the analysis and to speculate about their trajectories);
- pore pressure evolution (stress state of the soil can be understood and compared to similar laboratory scale experimental work presented in [8]).

In particular, the results are considered useful for the geotechnical investigation and characterisation of the slope body material from back analyses, as well as for the validation of numerical solutions for flowslide phenomena. FEM is a well-known and powerful interpretation tool for geotechnical problems and is capable to calculate the limit states of the initial slope failure. However, once the RBF is triggered it does not predicts its consequences, limiting our understanding of the impact and extent of the overall failure phenomena. MPM allows analysis, not only of the prefailure displacements and limit states with performances comparable to FEM, but it also enables estimations of RBF evolution and consequences with reasonable agreement with experimental results.

MPM is therefore considered a useful framework for the analysis of many engineering problems, such as the safety assessment of slope geometries in the mining industry and offshore structures. The datasets collected during these experiments are available on the 4TU repository [https://data.4tu.nl/collections/a7f00e8a-cc10-45fd-a212-65ded27f7173].

## References

[1] L. G. Acosta, P. J. Vardon, and M. A. Hicks. Composite material point method (cmpm) to improve stress recovery for quasi-static problems. *Procedia Engineering*, 175:324–331, 1 2017.

[2] S. Alhaddad, R. J. Labeur, and W. Uijttewaal. Large-scale experiments on breaching flow slides and the associated turbidity current. *Journal of Geophysical Research: Earth Surface*, 125, 10 2020.

[3] M. D. Bolton. The strength and dilatancy of sands. *Geotechnique*, 36:65–78, 1986.

[4] Fugro. Onderzoek zandgroeve ”site-d” nabij n136 - (b). Technical report, Fugro, 2018.

[5] O. Hungr, S. Leroueil, and L. Picarelli. The varnes classification of landslide types, an update. *Landslides*, 11:167–194, 2014.

[6] J. Maertens, G. V. Alboom, K. Haelterman, and J. Couck. Stability of underwater slopes realized by means of a suction dredger. In *Proceedings of the 17th*

*International Conference on Soil Mechanics and Geotechnical Engineering: The Academia and Practice of Geotechnical Engineering*, 2009.

[7] A. Maghsoudloo, A. Askarinejad, R. D. Jager, F. Molenkamp, and M. Hicks. Experimental investigation of pore pressure and acceleration development in static liquefaction induced failures in submerged slopes. In *9th International Conference of Physical Modelling in Geotechnics*, 2018.

[8] J. Silva. *The influence of underwater embankment properties on breaching failures*. PhD thesis, Utrecht University 2020.

[9] T. P. Stoutjesdijk, M. B. D. Groot, and J. Lindenberg. Flow slide prediction method: influence of slope geometry, 2014.

# 7

# Conclusions and Recommendations

The main goal of this research project is to validate numerical soluitions for sand flow-slides in flood defenses. The proposed numerical solutions should offer an accurate, cheap, consistent visualization of hydro-mechanical stress-displacement fields, from initiation of the failure up to deposition of the sediments. Hence, the Material Point Method (MPM) numerical framework was applied for fluid flows and slope stability problems, above and under the water table. These analyses are compared, where possible, to analytical solutions, and numerical and experimental benchmarks.

The literature review, in addition to providing familiarity with the theoretical background, provides a summary of some of the drawbacks of the existing methods. In fact, despite impressive performances of MPM for the solution of complex engineering and computer graphics problems, it still suffers from several numerical shortcomings, such as stability issues, inaccurate mapping of the Material Points (MPs) data, and nonphysical oscillations that arise when MPs travel from one element to another. This led to a cautious application of the method, exploring physics-based governing equations and benchmarks of increasing complexity in order to gain a feeling of the capabilities.The validations described in this dissertation are two-dimensional problems and are considered increasingly complex and complementary to those already available in literature. Two-dimensional problems were selected as convenient abstractions from a computational prospective and as propaedeutic for successful three-dimensional studies.

First, only the fluid phase is validated using analytical benchmarks for water flows. After this, only the solid phase is validated by comparing MPM simulations with numerical exercises and a field experiment. Finally a coupled (solid and liquid phase) MPM formulation was used to simulate a full scale flowslide field experiment. These steps, and how they answer the main research questions, are detailed in the following section. Comprehensive calibration of the slope material parameters was not pursued, as a deliberate decision was made to allocate the available resources within the scope of this study in a rational and efficient manner. For practical engineering applications, the proposed methodology would necessitate the development of a robust database with an adequate sample size and strong statistical reliability. Furthermore, its implementation should be carried out in accordance with applicable local regulations and standards.

## 7.1. Conclusions by Research Questions

1. **How is it possible to simulate fluid flows while adding/removing material points in/from the computational domain in the Anura3D framework? (Chapter 3)**

   To study water flows, it is desirable to be able to introduce MPs in the computational domain at a controlled rate. This feature was not available in Anura3D and it was decided to develop and implement it, also because it would enable less computationally expensive modelling strategies. The implementation of new Boundary Conditions (BCs) allows simulating both transient and steady-state flow conditions in an efficient manner, because the MPs that exit the area of interest are automatically removed from the computational domain while the pressure controlled BC accurately mimics the downstream conditions. At the same time, the velocity-controlled BC introduces MPs at the desired rate and state, removing the need of a large upstream reservoir to supply the domain of interest. In order to answer the first research question, the following sub-questions needed to be addressed.

   - **What boundary conditions should be applied?**

     The MPM is used to solve the underlying ordinary differential equations of the problem in the analysis, by applying appropriate BCs. Hence, subcritical fluid flows or Brink flow models can be solved by using two types of BCs: Dirichlet BCs at the inflow, to specify the values of the solution itself, since the inflow is a known quantity of these types of problems (easily measurable in experimental facilities); and Neumann BCs at the outflow as this affects the geometry of the flow upstream. These types of BCs are frequently used in FEM analyses. However, when large deformations occur in the MPM framework, special care must be taken to add and remove MPs to and from the computational domain. This requires adapting the BCs for MPM applications, features that were not previously available. New BCs (here called in/outflow BCs) were developed and implemented.

   - **What integration scheme is required?**

     Explicit methods are more common as these are well suited to analyse fast nonlinear dynamic problems. However, when using explicit integration schemes, the convergence of the solution is not guaranteed. Hence, special care has to be paid to select satisfactory and sufficient numerical features to favor convergence of the solution, such as: type of elements, type of shape functions, size of the discretization, number of MPs per element, time step size, material parameters, smoothing techniques, etc. A number of numerical features have been tested and proved to be successful. These are presented during the validation exercises of Sections 3.3 and 3.4.

- **If required, what smoothing technique improves the results?**

  Once the opportune integration scheme is selected, Anura3D yields good results for open channel flows. However, the simulation results were affected by considerable stress oscillations concealing the linear flow features that were expected to be observed in the problems in analysis. The application of strain and pressure smoothing procedures as described in [5] were proven successful in improving the quality of the solution as shown in 3.4.3.

Free open channel flows were used as benchmarks due to the complex flow fields and were successfully simulated.

2. **How can Anura3D be validated for slope failure analyses? (Chapter 4)**

   Validation exercises are usually performed against certain analytical solutions where possible. When these were not available, as in the case of slope stability analysis, LEM and FEM numerical computations, and field experiments have been carried out. The validation benchmarks gradually increased in complexity, starting from laboratory scale slopes up to engineering scale dike profiles. By performing verification studies against established numerical solutions available in literature 4.2, and by being able to simulate also the interim and morphology post-failure as shown in Section 4.3, the following sub questions were answered:

   - **Does Anura3D yield comparable results to traditional LEM and FEM for the safety assessment of slopes?**

     The results comparison of LEM, FEM and MPM calculations were found in agreement when replicating the numerical benchmark proposed by Hicks and Wong 1988 [4], up to the moment of failure (gravity multiplier of ≈ 2.3), which illustrates the correctness of the MPM solution for small strain analysis. The LEM and FEM computations have the limitation of not providing any insight into the dike behaviour after the initial failure, while the MPM is able to simulate beyond this point. Since MPM unlocks the ability to assess the new slope equilibrium configuration after an initial failure, it could indicate whether the slope could still fulfill its structural function (i.e. retaining high water levels ) as before an initial slide, leading to the following research questions.

   - **Does initial shear failure of a dike lead to the loss of the dike's capability to retain water?**

It is shown that, based on MPM calculations of a typical dutch dike profile under increasing gravity load (e.g. in a centrifuge test), for slope failures (i.e SF < 1 from the LEM), the dike crest displacements are progressive up to high values of gravity loads. The dike crest displacements start small, and are measurable in centimeters up to 2g. Hence a SF smaller than one does not imply that the dike fails its requirement of retaining water, but just that an initial failure took place. In other words, the initial shear failure of the dike in the analysis did not lead to the loss of the dike's capability to retain water. This is because, after this initial failure, the numerical slope always found a new equilibrium configuration in the range of the sensitivity study here presented. Hence the computed dike crest deformation with MPM can be used to assess the dike safety performances, by combining the analyses results with new criteria for the maximum allowed displacement of the dike crest. This aligns with the conclusions of Remmerswaal [6].

- **What are the opportunities that the MPM solutions offer to better reflect on the concept of safety factor?**

  Moving towards a displacement based safety assessment of dikes can have a positive impact for existing dikes, as it will provide a better prediction of their safety. Also, for dikes to be constructed, it will allow for more economical designs. This aligns with the conclusions of Remmerswaal [6], where he finds that the assessment of the initial failure consequences leads to a significant reduction in the computed probability of flooding due to dyke slope failure. The analyses presented in this dissertation can be considered as a first step in a transition towards a safety assessment based on displacement criteria.

Following these theoretical exercises, a large scale field experiment and numerical simulations have been undertaken to investigate the slope failure process and the capability of MPM to simulate accurately the full process, including the kinematics of the failure. This was done because it is important to understand the entire slope failure process, from initiation through to the final situation after slope failure, in order to better understand (and assess) the risk or consequence of slope failure.

3. **How can full scale slope failures be simulated, including the forecast of its initial instability, kinematics and final geometry? (Chapter 5)**

   The simulation of a dry slope (i.e. above water) sliding phenomenon requires accurate modelling abstractions and detailed experimental protocols. Hence, a detailed geotechnical characterization and monitoring campaign were proposed in Chapter 5 and performed in a open pit quarry of quartz sand. Additionally, it is essential to adopt a constitutive behaviour for the material in the analysis that captures to an acceptable degree of accuracy the stress-strain behaviour of the material that constitutes the slope itself. Hence the following subquestion was formulated as follows:

- **What are the material model requirements for accurate displacement forecasts of slope failure consequences?**

  Two constitutive models have been tested for answering this question, these being a standard elasto-plastic MC soil model and the same model modified for large strains, aka MCSS. These were chosen among others because they are readily available in Anura3D, relative simplicity of the constitutive relations, relative simplicity of the calibration procedures, and because of their wide spread use in literature and geotechnical practice. They predicted comparable initial slip surface geometries as those observed in the field test. However, to better capture the kinematics and the final geometry of dense sand embankments failures, strain-softening constitutive behaviour was essential. This proved that also a dry slope failure can be accurately simulated by MPM models, predicting well the geometry and the duration of the failure.

Because both phases of the mixture, solid and fluid, were separately simulated with a good degree of accuracy (i.e in Chapter 3 and 5 of this dissertation), a further step was taken towards making Anura3D available for dike safety assessments by using a coupled formulation of fluids plus solids. Hence the final research question was formulated:

4. **How can Anura3D be validated for submerged flowslide dynamics and morphology against full scale experiments? (Chapter 6)**

It is generally difficult to know when and where a submerged flowslide will occur. During marine sand dredging activities, however, submerged slopes failures are frequently used to steer sediments and water mixtures to the dredging equipment. Because it was made possible to monitor mining activities of an industry partner of this project, it was decided to devise and perform a slope instability experiment in a submerged quarry to validate an MPM coupled formulation. To answer the final research question, the following sub-questions needed to be addressed:

- **How can underwater mining activities be monitored as experiments / case-studies to validate Anura3D for flowslides?**

  A geotechnical characterization and experimental protocol to monitor the failing soil mass geometry, velocity and acceleration evolution during a retrogressive breach failure at full scale, including triggering mechanism, onset and deposition of the sliding soil mass, was devised and presented in Chapter 6, proving its effectiveness. Multiple surveying technologies (i.e. bathymetry scanner, UAV photogrammetry, GPS, time lapse camera, porepressure, acceleration sensors, strain gauge) were deployed producing a dataset that can be used for the validation of numerical and empirical geotechnical and fluid dynamics solutions for the analyses of flowslide phenomena. The strain gauge fiber optic cable diameter was too thin for this set of experiments, hindering the interpretation of the dataset. Not all bathymetric data were made available and the porepressure water tight seal failed during Site-B experiments. However multiple experiments have been performed allowing to access the performance of each sensor technology here presented.

- **What monitoring tools and experimental protocols are required to produce an useful dataset for the validation of the numerical solution?**

  From an experimental perspective, this dissertation identifies the main physical variables that drive the flow-slide phenomena, including monitoring tools for its investigation at engineering scale. Experimental protocols have been developed to monitor the main features of flowslides in sand mining activities. For saturated quartz sand slopes, the main physical variables are the soil grain size, its initial density, and stress state, besides the three-dimensional geometry of the slope. Hence, for the grain size and initial density, standard field and laboratory investigations on soil samples extracted from the relevant geological layer in analysis have been carried out. For the three dimensional slope geometry, GPS, bathimetry scanner and UAV photogrammetry were used. The stress state in the saturated soil required developing and deploying Lagrangian sensors to monitor the pore pressure oscillations during failure. A selection of the data collected in the field experiments have been analysed and compared to numerical studies for their validation, highlighting their effectiveness.

Finally, a preliminary MPM simulation was compared with an underwater flow-slide field experiment. MPM allowed analyzing, not only pre-failure displacements and stress states similarly to FEM, but it enabled better estimations of RBF consequences, capturing also the retrogressive failure mechanism. Similarly to the third research question (Chapter 5), good agreement was achieved between field observations and MPM predictions in terms of the shapes of sliding surfaces, overall retrogression length, duration of the RBF, and pore pressure evolution. The remaining discrepancies are mostly attributed to simplifications in the modelling procedure and superficial investigation data rather than numerical artefacts. However, this should be better investigated in future studies, especially because this coupled formulation presents shortcomings in capturing the hydrodynamic effects of the RBF. The data set of the experiments provides the basis for further validation of MPM.

The results of this exploratory application of Anura3D to a flowslide field experiment demonstrate that advanced numerical solutions allow highly complex problems to be managed, possibly replacing physical experimental facilities. Anura3D proved to be a robust investigation tool and a valid support for the design and optimisation of modern projects. This is because it offers an accurate, cheap, consistent visualisation of hydro-mechanical stress-displacement fields for sand flow-slides, from initiation of the failure up to deposition of the sediments. MPM is therefore considered a useful framework for the analysis of many engineering problems, such as the safety assessment of slope geometries in the mining industry and offshore structures. It holds promise to help with the study of flood defences, accessing not only the consequences of slope failures but possibly redefining safety assessment criteria.

## 7.2. Recommendations for future work

The recommendations for further model development, calibration and its application in the future are presented in this section.

### 7.2.1. Model development

MPM currently presents different numerical artifacts and convergence challenges. Among the acknowledged sources of errors of the Anura3D implementation there is the linearity of the shape functions. Higher-order shape functions are available in literature and are deemed to increase the accuracy of the solution while reducing the stress oscillations when used in combination with higher order elements. It is recommended to implement higher-order shape functions and higher-order elements in MPM to improve the stability of the method, its convergence rate and yield solutions less prone to spurious shear. In addition, a quadrilateral geometrical shape of the elements is recommended to be implemented to increase the accuracy of the solution. Different integration schemes and mapping techniques should also be assessed and compared, contributing to existing work in this direction [1].

Chapter 5 showed that the selection of an advanced constitutive model is necessary for an accurate forecast of stress-displacements in flow-slide problems. Many constitutive models are available that better apply to specific problems. An ideal MPM software should be able to apply these different approaches and compare them to prove the predictive capacity of the method, although only a small number of them are already implemented in Anura3D. It is recommended to implement commonly used constitutuve models for FEM in MPM software.

It is recommended to use advanced non-linear constitutive models to improve the applicability and accuracy of MPM simulations for current engineering problems. In fact, examples of ongoing studies such as the PM4Sand [2] and Monot constitutive models [3] already showed advantages when compared to more traditional alternatives for the forecast of excess pore pressure during shearing.

### 7.2.2. Model Calibration

While further mathematical studies are desirable, validation benchmarks with field experiments are necessary to increase the reliability of MPM applications to hydro geotechnical problems. Despite the abundant number of well established field and laboratory investigation protocols (such as ISO or ASTM) to master the details of a large number of soil parameters (certainly larger than what is critical) there is a lack of experimental protocols for the safety assessment of underwater sand slopes problems and the calibrations of suitable soil models which hampers the complete validation of numerical and empirical solutions for slope stability at an engineering scale. It is recommended that the investigation and calibration protocols should be standardized to guide the engineer to a proper application of the numerical tool.

This dissertation has the ambition to represent a pilot step in this direction.

From a physical experimental perspective, it is suggested to perform additional postprocessing of the collected data (e.g. comparing multiple point clouds or manually selecting ground control points) to improve the accuracy of the description of the RBF experiments here presented.

### 7.2.3. Application of MPM to Industry Cases

Even though the fluid flows presented in Chapter 3 have been successfully validated, it is recommended to perform further studies of water flows with different geometries, especially for 3D domains. The in/outflow BCs can be adjusted to simulate unsteady or steady-state fluid or solid MPs sinks/sources, such as leaking, rainfalls or avalanches, generally improving the applicability of the method for flow-slide related problems. Including application to other failure mechanisms of slopes and dikes than instability such as piping, scouring and turbidity currents. It is recommend to explore such research directions in future work.

The successful application of the MPM needs to satisfy several numerical requirements (such as appropriate discretization of the domain, adopt opportune Courant number values to prevent divergence, etc.) as well as accurately calibrated constitutive models. However, even numerically sound abstractions and properly calibrated material models may not perform perfectly: prediction errors occur due to several sources of uncertainties such as bifurcation of the solution, incompleteness of the underlining physics of the governing equation, measurement errors, etc. Hence, the main challenge in applying MPM to engineering practice is to be able to distinguish and quantify between numerical artefacts and modelling errors. It is recommended therefore to compose an extensive validation database of numerical benchmarks against analytical solutions and experimental data to help in this process.

It is recommended to perform thorough convergence analyses in order to increase confidence in MPM applications to hydro geotechnical problems. To do so, the type and size of mesh elements in use must be able to capture the expected solution in the limit of a mesh refinement process, by being larger than the representative volume of soil and possibly smaller than the shear bend size or than the required accuracy of the solution. For MPM, not only the background mesh, but also the MPs discretization should be adequate. Once the convergence analysis provides an order of magnitude for the numerical artefacts, it is recommended that the investigator couple the numerical analyses with a probabilistic tool to perform sensitivity studies. This is because sensitivity studies allow reducing the risk of modelling errors by focusing the investigations on the driving parameters.

In Anura3D, the initial MPs location inside the elements is now fixed and predefined. This results in structured MPs patterns which may lead to errors due to simultaneous grid crossing. It is recommended to allow adjusting the initial MPs locations to minimize the occurrence of grid crossing errors and limiting their impact on the accuracy of the overall solution. It is also recommended to refine the background mesh discretization when localization happens.

The Fortran code had several drawbacks in terms of good coding practices and standards which hinders its readability and maintainability. It is therefore suggested to rewrite the code following best practices[1]. Moreover, to leverage the rapid advancements in high-performance computing, which are delivering orders-of-magnitude improvements in computational power, it is recommended that the software architecture be designed to support parallelization. As computational power is ever increasing and new technologies are continuously emerging, the importance of deterministic solutions that currently have a too high computational cost should not be overlooked for future applications.

Despite the thorough validation of the MPM method still requires considerable efforts, it offers the opportunity to establish a cheap and consistent assessment tool for the visualization of hydro-mechanical stress-displacement fields for the slope safety assessment, especially when compared to more simplistic methods commonly used in engineering practice. Additionally it promises to successful explore new research directions, including quantitative forecasts of the slope failure consequences and improvement of current design standards.

## References

[1] J. L. G. Acosta, P. J. Vardon, G. Remmerswaal, and M. A. Hicks. An investigation of stress inaccuracies and proposed solution in the material point method. *Computational Mechanics*, 65:555–581, 2020.

[2] N. Dinesh, S. Banerjee, and K. Rajagopal. Performance evaluation of pm4sand model for simulation of the liquefaction remedial measures for embankment. *Soil Dynamics and Earthquake Engineering*, 152, 2022.

[3] M. A. Hicks. Experience in calibrating the double-hardening constitutive model Monot. *International Journal for Numerical and Analytical Methods in Geomechanics*, 27(13):1123–1151, 2003.

[4] M. A. Hicks and S. W. Wong. Static liquefaction of loose slopes. *Numerical Methods in Geomechanics*, I(1):1361–1367, 1988.

[5] M. Martinelli. 2 Layer Formulation: Joint MPM Software. Technical report, Deltares, Delft, 2015.

[6] G. Remmerswaal, P. J. Vardon, and M. A. Hicks. Evaluating residual dyke resistance using the random material point method. *Computers and Geotechnics*, 133:104034, 5 2021.

---

[1] E.g. `https://everythingfunctional.gitlab.io/fortran-style-guide/`

# Appendix-a

The fiber optic readings (Figure 1) that were performed during the experiment in Site-B, showed very localised displacements (crack patterns, Figure 2), however these cracks were either present since the installation or occurred almost instantaneously, hindering the interpretation of the data. It is not possible to distinguish between cracks and random errors of the device. It is reasonable to assume that the installation procedure was the primary cause for most of these patterns, causing plastic strains along the probe, thereby preventing us from capturing the slope displacement evolution. As the cable ended up buried under the sediments, it was not possible to recover it and further analyse it. Ultimately, for this attempt the fibre optic readings indicate reliably only the time at which the cable breaks during the RBF.

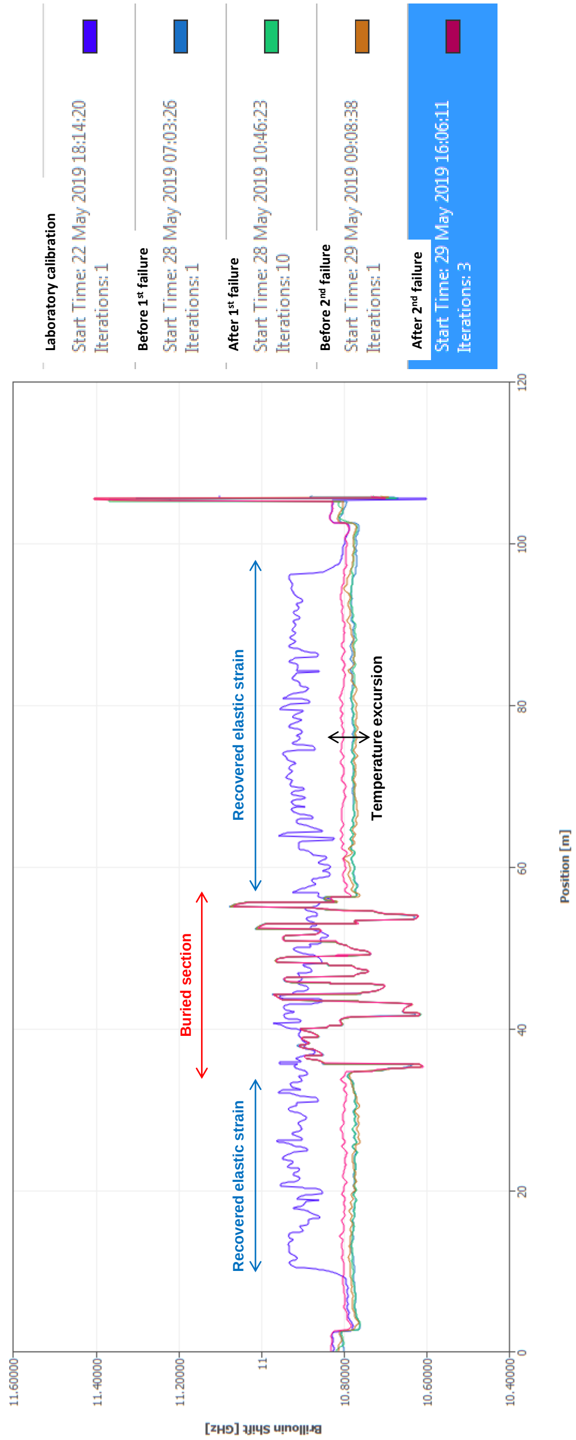

Figure 1: Raw data from fibre optic strain gauge installed in the trench parallel to the shore in Site-B.

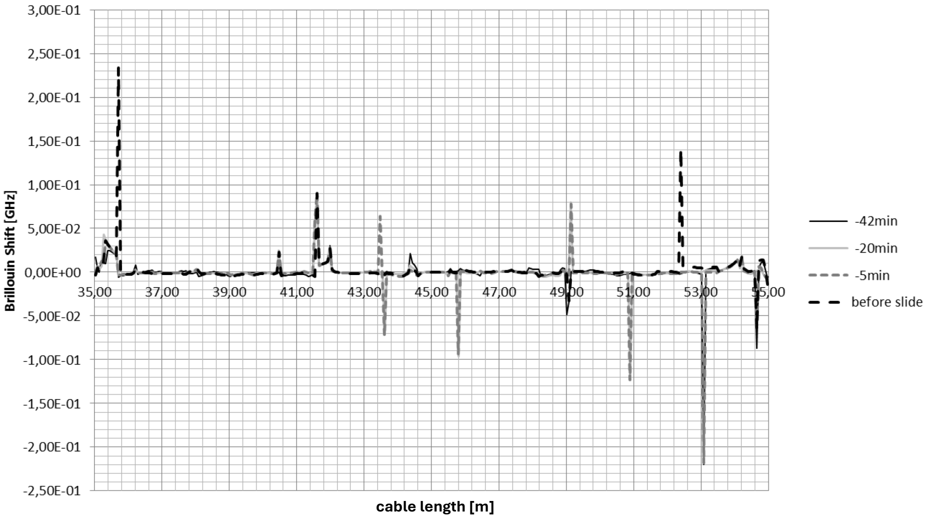

Figure 2: Frequency shift evolution before cable loss.

# Appendix-b

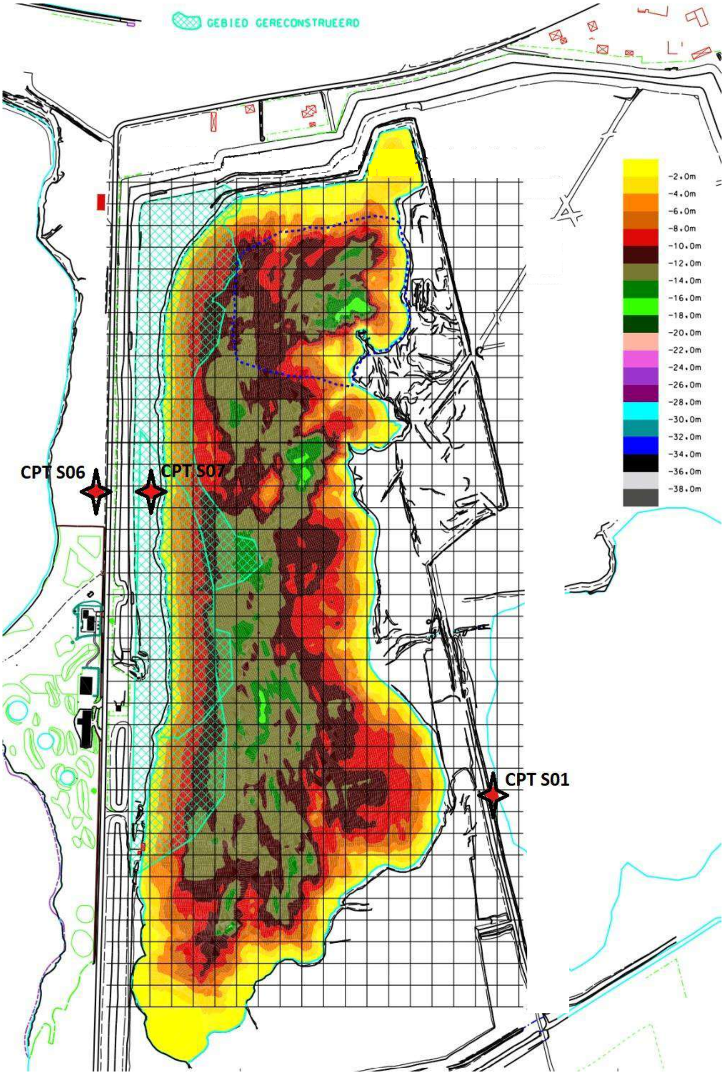

Figure 3: Panoptic view of the Site-B quarry before the experiment. CPT S01, S06, S07 investigations are higlighted on the map.

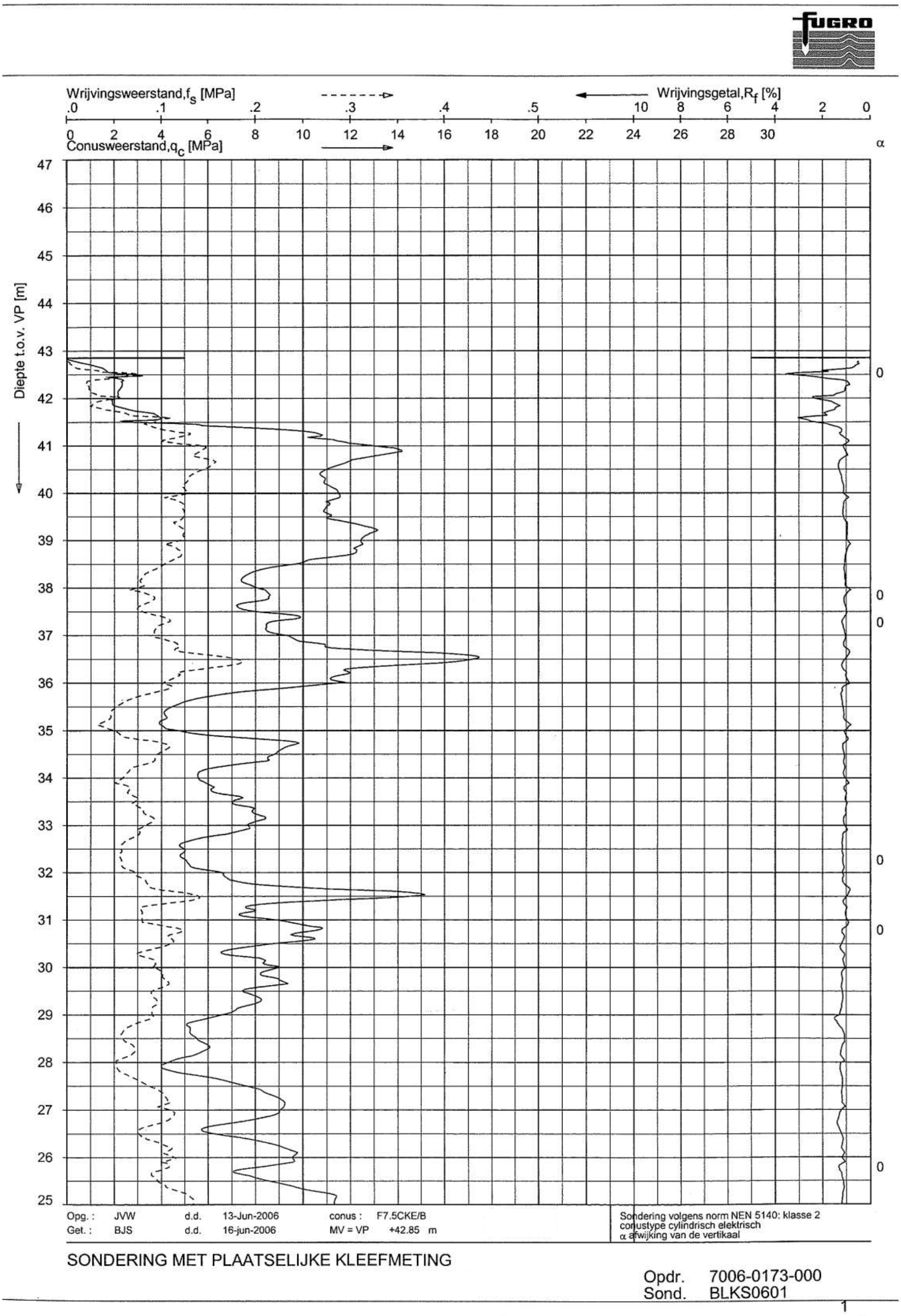

Opg. : JVW d.d. 13-Jun-2006 conus : F7.5CKE/B
Get. : BJS d.d. 16-jun-2006 MV = VP +42.85 m

Sondering volgens norm NEN 5140: klasse 2
conustype cylindrisch elektrisch
α afwijking van de vertikaal

SONDERING MET PLAATSELIJKE KLEEFMETING

Opdr. 7006-0173-000
Sond. BLKS0601

Figure 4: CPT S01 data collected by Fugro in 2013.

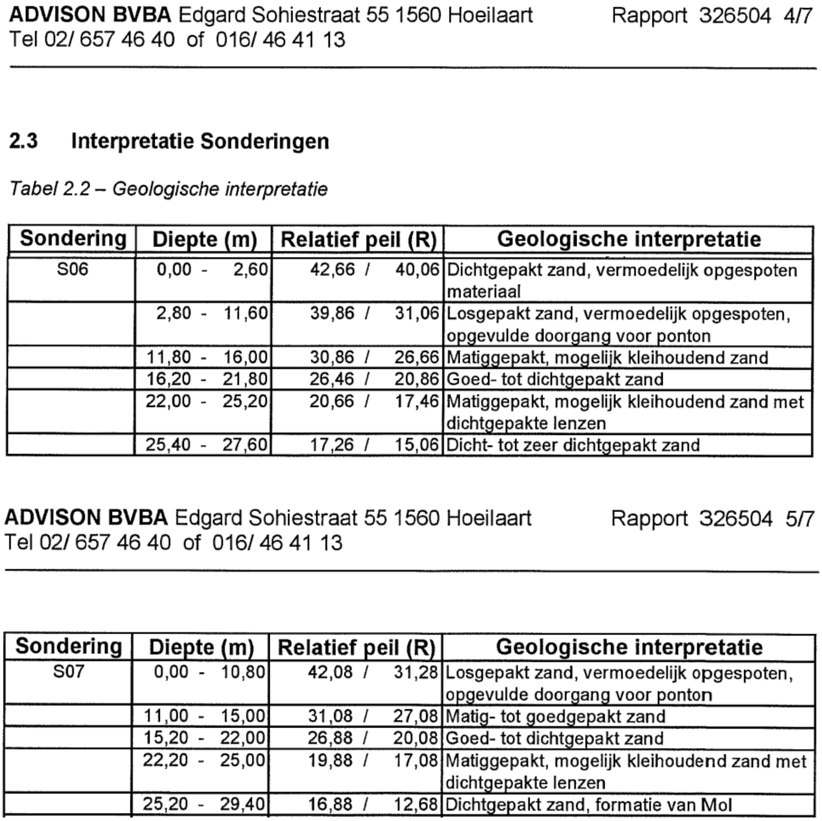

**ADVISON BVBA** Edgard Sohiestraat 55 1560 Hoeilaart Rapport 326504 4/7
Tel 02/ 657 46 40 of 016/ 46 41 13

**2.3 Interpretatie Sonderingen**

*Tabel 2.2 – Geologische interpretatie*

| Sondering | Diepte (m) | Relatief peil (R) | Geologische interpretatie |
|---|---|---|---|
| S06 | 0,00 - 2,60 | 42,66 / 40,06 | Dichtgepakt zand, vermoedelijk opgespoten materiaal |
| | 2,80 - 11,60 | 39,86 / 31,06 | Losgepakt zand, vermoedelijk opgespoten, opgevulde doorgang voor ponton |
| | 11,80 - 16,00 | 30,86 / 26,66 | Matiggepakt, mogelijk kleihoudend zand |
| | 16,20 - 21,80 | 26,46 / 20,86 | Goed- tot dichtgepakt zand |
| | 22,00 - 25,20 | 20,66 / 17,46 | Matiggepakt, mogelijk kleihoudend zand met dichtgepakte lenzen |
| | 25,40 - 27,60 | 17,26 / 15,06 | Dicht- tot zeer dichtgepakt zand |

**ADVISON BVBA** Edgard Sohiestraat 55 1560 Hoeilaart Rapport 326504 5/7
Tel 02/ 657 46 40 of 016/ 46 41 13

| Sondering | Diepte (m) | Relatief peil (R) | Geologische interpretatie |
|---|---|---|---|
| S07 | 0,00 - 10,80 | 42,08 / 31,28 | Losgepakt zand, vermoedelijk opgespoten, opgevulde doorgang voor ponton |
| | 11,00 - 15,00 | 31,08 / 27,08 | Matig- tot goedgepakt zand |
| | 15,20 - 22,00 | 26,88 / 20,08 | Goed- tot dichtgepakt zand |
| | 22,20 - 25,00 | 19,88 / 17,08 | Matiggepakt, mogelijk kleihoudend zand met dichtgepakte lenzen |
| | 25,20 - 29,40 | 16,88 / 12,68 | Dichtgepakt zand, formatie van Mol |

Figure 5: Geological interpretations for CPTs S06, S07 performed by Advison in 2004.

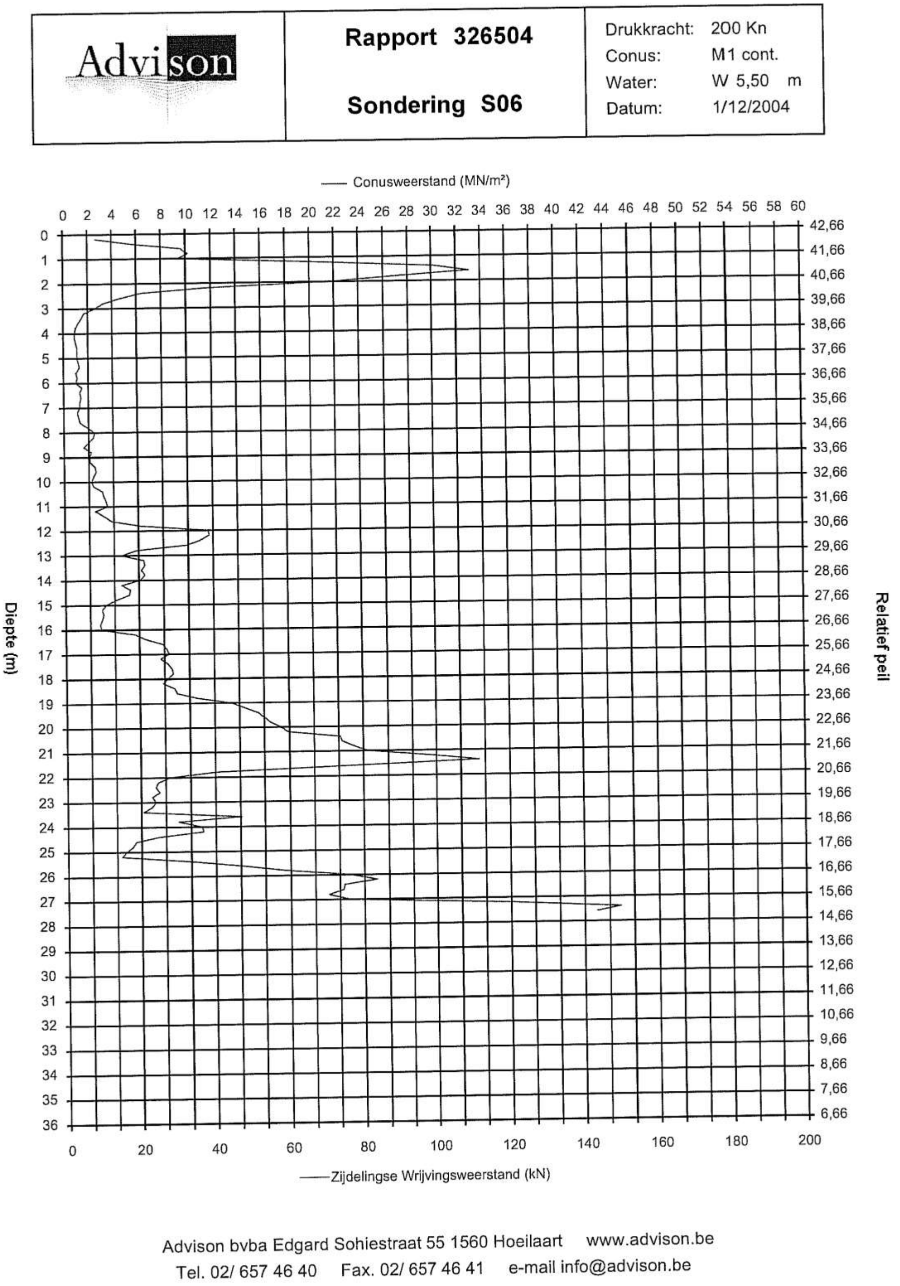

Advison

**Rapport 326504**

**Sondering S06**

Drukkracht: 200 Kn
Conus: M1 cont.
Water: W 5,50 m
Datum: 1/12/2004

Advison bvba Edgard Sohiestraat 55 1560 Hoeilaart www.advison.be
Tel. 02/ 657 46 40 Fax. 02/ 657 46 41 e-mail info@advison.be

Figure 6: CPT S06 data collected by Advison in 2004.

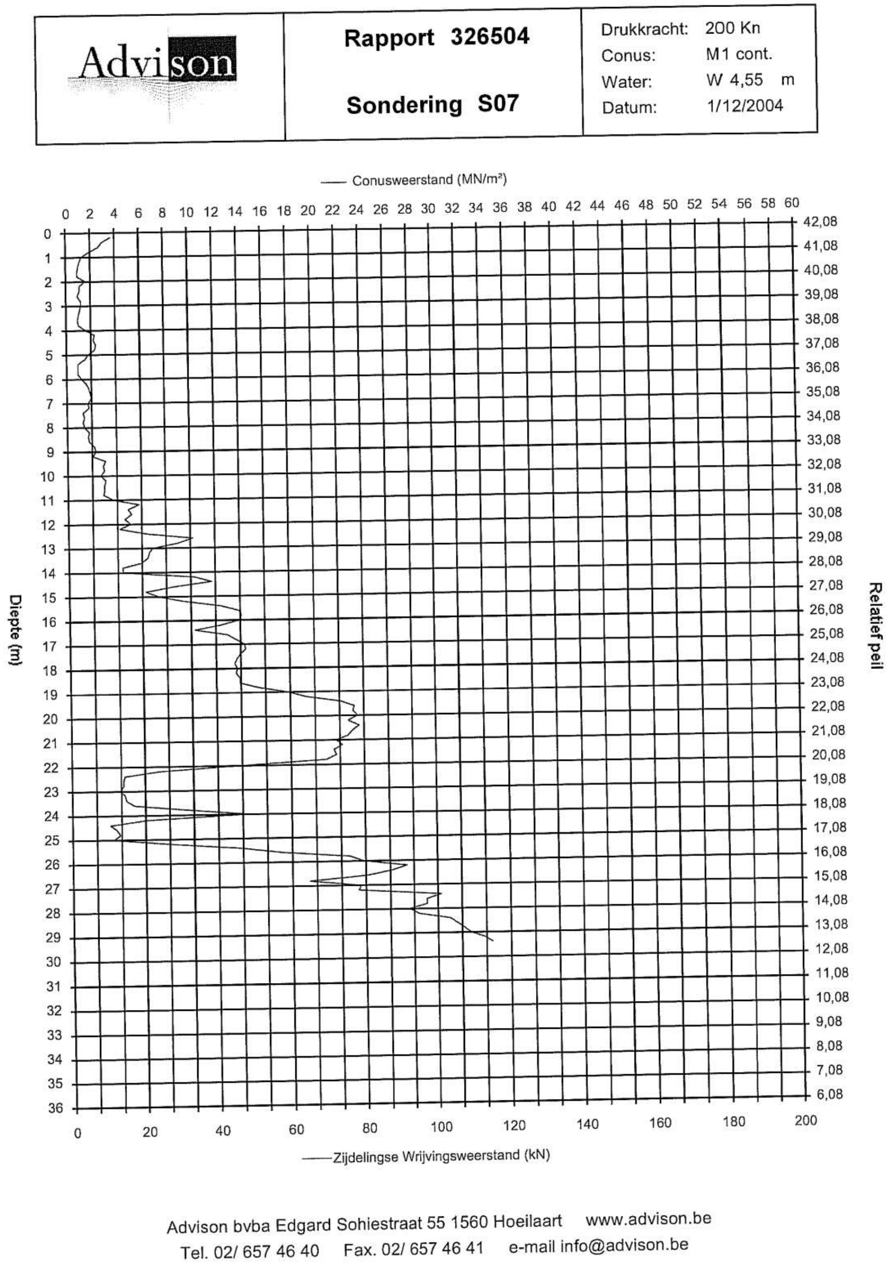

Advison

**Rapport 326504**

**Sondering S07**

Drukkracht: 200 Kn
Conus: M1 cont.
Water: W 4,55 m
Datum: 1/12/2004

Advison bvba Edgard Sohiestraat 55 1560 Hoeilaart www.advison.be
Tel. 02/ 657 46 40 Fax. 02/ 657 46 41 e-mail info@advison.be

Figure 7: CPT S07 data collected by Advison in 2004.

# Appendix-c

The coordinates of the drillings are around the Site-C at a maximum distance of 230 m between each other, and investigating the same geological layer.

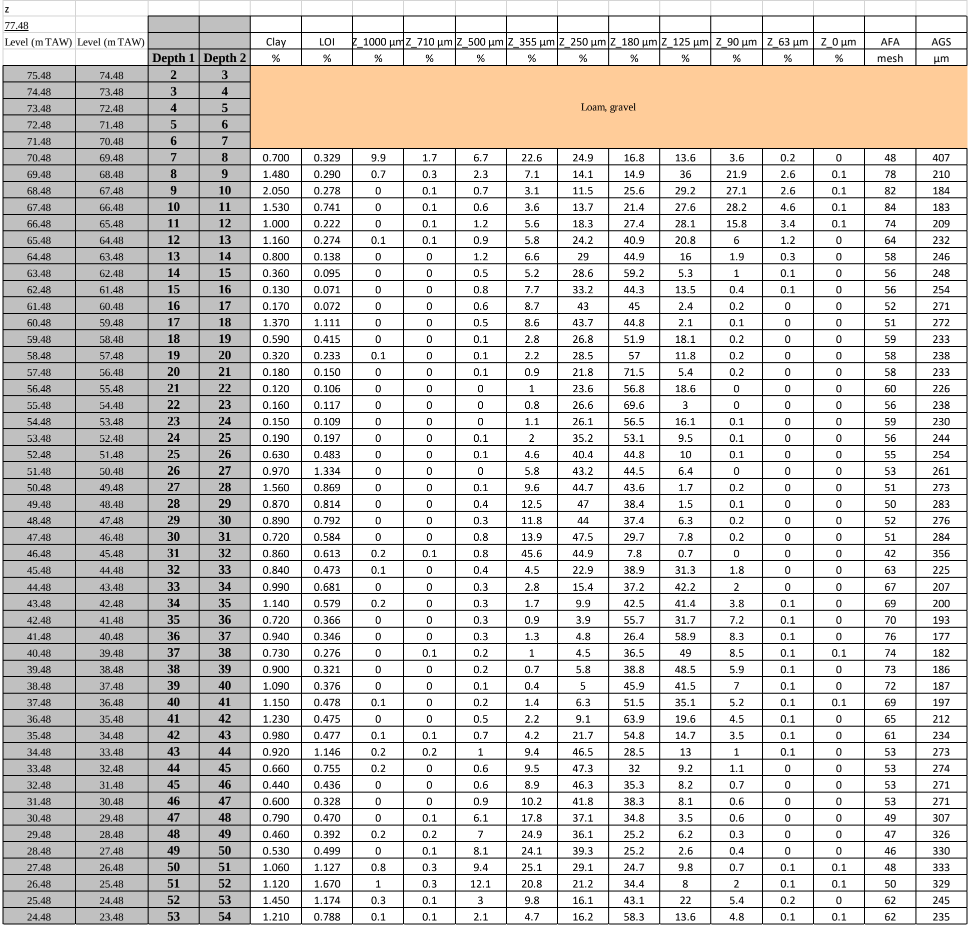

| z | | | | | | | | | | | | | | | | |
|---|---|---|---|---|---|---|---|---|---|---|---|---|---|---|---|---|
| 77.48 | | | | | | | | | | | | | | | | |
| Level (m TAW) | Level (m TAW) | | | Clay | LOI | Z_1000 µm | Z_710 µm | Z_500 µm | Z_355 µm | Z_250 µm | Z_180 µm | Z_125 µm | Z_90 µm | Z_63 µm | Z_0 µm | AFA | AGS |
| | | Depth 1 | Depth 2 | % | % | % | % | % | % | % | % | % | % | % | % | mesh | µm |
| 75.48 | 74.48 | 2 | 3 | Loam, gravel | | | | | | | | | | | | | |
| 74.48 | 73.48 | 3 | 4 | | | | | | | | | | | | | | |
| 73.48 | 72.48 | 4 | 5 | | | | | | | | | | | | | | |
| 72.48 | 71.48 | 5 | 6 | | | | | | | | | | | | | | |
| 71.48 | 70.48 | 6 | 7 | | | | | | | | | | | | | | |
| 70.48 | 69.48 | 7 | 8 | 0.700 | 0.329 | 9.9 | 1.7 | 6.7 | 22.6 | 24.9 | 16.8 | 13.6 | 3.6 | 0.2 | 0 | 48 | 407 |
| 69.48 | 68.48 | 8 | 9 | 1.480 | 0.290 | 0.7 | 0.3 | 2.3 | 7.1 | 14.1 | 14.9 | 36 | 21.9 | 2.6 | 0.1 | 78 | 210 |
| 68.48 | 67.48 | 9 | 10 | 2.050 | 0.278 | 0 | 0.1 | 0.7 | 3.1 | 11.5 | 25.6 | 29.2 | 27.1 | 2.6 | 0.1 | 82 | 184 |
| 67.48 | 66.48 | 10 | 11 | 1.530 | 0.741 | 0 | 0.1 | 0.6 | 3.6 | 13.7 | 21.4 | 27.6 | 28.2 | 4.6 | 0.1 | 84 | 183 |
| 66.48 | 65.48 | 11 | 12 | 1.000 | 0.222 | 0 | 0.1 | 1.2 | 5.6 | 18.3 | 27.4 | 28.1 | 15.8 | 3.4 | 0.1 | 74 | 209 |
| 65.48 | 64.48 | 12 | 13 | 1.160 | 0.274 | 0.1 | 0.1 | 0.9 | 5.8 | 24.2 | 40.9 | 20.8 | 6 | 1.2 | 0 | 64 | 232 |
| 64.48 | 63.48 | 13 | 14 | 0.800 | 0.138 | 0 | 0 | 1.2 | 6.6 | 29 | 44.9 | 16 | 1.9 | 0.3 | 0 | 58 | 246 |
| 63.48 | 62.48 | 14 | 15 | 0.360 | 0.095 | 0 | 0 | 0.5 | 5.2 | 28.6 | 59.2 | 5.3 | 1 | 0.1 | 0 | 56 | 248 |
| 62.48 | 61.48 | 15 | 16 | 0.130 | 0.071 | 0 | 0 | 0.8 | 7.7 | 33.2 | 44.3 | 13.5 | 0.4 | 0.1 | 0 | 56 | 254 |
| 61.48 | 60.48 | 16 | 17 | 0.170 | 0.072 | 0 | 0 | 0.6 | 8.7 | 43 | 45 | 2.4 | 0.2 | 0 | 0 | 52 | 271 |
| 60.48 | 59.48 | 17 | 18 | 1.370 | 1.111 | 0 | 0 | 0.5 | 8.6 | 43.7 | 44.8 | 2.1 | 0.1 | 0 | 0 | 51 | 272 |
| 59.48 | 58.48 | 18 | 19 | 0.590 | 0.415 | 0 | 0 | 0.1 | 2.8 | 26.8 | 51.9 | 18.1 | 0.2 | 0 | 0 | 59 | 233 |
| 58.48 | 57.48 | 19 | 20 | 0.320 | 0.233 | 0.1 | 0 | 0.1 | 2.2 | 28.5 | 57 | 11.8 | 0.2 | 0 | 0 | 58 | 238 |
| 57.48 | 56.48 | 20 | 21 | 0.180 | 0.150 | 0 | 0 | 0.1 | 0.9 | 21.8 | 71.5 | 5.4 | 0.2 | 0 | 0 | 58 | 233 |
| 56.48 | 55.48 | 21 | 22 | 0.120 | 0.106 | 0 | 0 | 0 | 1 | 23.6 | 56.8 | 18.6 | 0 | 0 | 0 | 60 | 226 |
| 55.48 | 54.48 | 22 | 23 | 0.160 | 0.117 | 0 | 0 | 0 | 0.8 | 26.6 | 69.6 | 3 | 0 | 0 | 0 | 56 | 238 |
| 54.48 | 53.48 | 23 | 24 | 0.150 | 0.109 | 0 | 0 | 0 | 1.1 | 26.1 | 56.5 | 16.1 | 0.1 | 0 | 0 | 59 | 230 |
| 53.48 | 52.48 | 24 | 25 | 0.190 | 0.197 | 0 | 0 | 0.1 | 2 | 35.2 | 53.1 | 9.5 | 0.1 | 0 | 0 | 56 | 244 |
| 52.48 | 51.48 | 25 | 26 | 0.630 | 0.483 | 0 | 0 | 0.1 | 4.6 | 40.4 | 44.8 | 10 | 0.1 | 0 | 0 | 55 | 254 |
| 51.48 | 50.48 | 26 | 27 | 0.970 | 1.334 | 0 | 0 | 0 | 5.8 | 43.2 | 44.5 | 6.4 | 0 | 0 | 0 | 53 | 261 |
| 50.48 | 49.48 | 27 | 28 | 1.560 | 0.869 | 0 | 0 | 0.1 | 9.6 | 44.7 | 43.6 | 1.7 | 0.2 | 0 | 0 | 51 | 273 |
| 49.48 | 48.48 | 28 | 29 | 0.870 | 0.814 | 0 | 0 | 0.4 | 12.5 | 47 | 38.4 | 1.5 | 0.1 | 0 | 0 | 50 | 283 |
| 48.48 | 47.48 | 29 | 30 | 0.890 | 0.792 | 0 | 0 | 0.3 | 11.8 | 44 | 37.4 | 6.3 | 0.2 | 0 | 0 | 52 | 276 |
| 47.48 | 46.48 | 30 | 31 | 0.720 | 0.584 | 0 | 0 | 0.8 | 13.9 | 47.5 | 29.7 | 7.8 | 0.2 | 0 | 0 | 51 | 284 |
| 46.48 | 45.48 | 31 | 32 | 0.860 | 0.613 | 0.2 | 0.1 | 0.8 | 45.6 | 44.9 | 7.8 | 0.7 | 0 | 0 | 0 | 42 | 356 |
| 45.48 | 44.48 | 32 | 33 | 0.840 | 0.473 | 0.1 | 0 | 0.4 | 4.5 | 22.9 | 38.9 | 31.3 | 1.8 | 0 | 0 | 63 | 225 |
| 44.48 | 43.48 | 33 | 34 | 0.990 | 0.681 | 0 | 0 | 0.3 | 2.8 | 15.4 | 37.2 | 42.2 | 2 | 0 | 0 | 67 | 207 |
| 43.48 | 42.48 | 34 | 35 | 1.140 | 0.579 | 0.2 | 0 | 0.3 | 1.7 | 9.9 | 42.5 | 41.4 | 3.8 | 0.1 | 0 | 69 | 200 |
| 42.48 | 41.48 | 35 | 36 | 0.720 | 0.366 | 0 | 0 | 0.3 | 0.9 | 3.9 | 55.7 | 31.7 | 7.2 | 0.1 | 0 | 70 | 193 |
| 41.48 | 40.48 | 36 | 37 | 0.940 | 0.346 | 0 | 0 | 0.3 | 1.3 | 4.8 | 26.4 | 58.9 | 8.3 | 0.1 | 0 | 76 | 177 |
| 40.48 | 39.48 | 37 | 38 | 0.730 | 0.276 | 0 | 0.1 | 0.2 | 1 | 4.5 | 36.5 | 49 | 8.5 | 0.1 | 0.1 | 74 | 182 |
| 39.48 | 38.48 | 38 | 39 | 0.900 | 0.321 | 0 | 0 | 0.2 | 0.7 | 5.8 | 38.8 | 48.5 | 5.9 | 0.1 | 0 | 73 | 186 |
| 38.48 | 37.48 | 39 | 40 | 1.090 | 0.376 | 0 | 0 | 0.1 | 0.4 | 5 | 45.9 | 41.5 | 7 | 0.1 | 0 | 72 | 187 |
| 37.48 | 36.48 | 40 | 41 | 1.150 | 0.478 | 0.1 | 0 | 0.2 | 1.4 | 6.3 | 51.5 | 35.1 | 5.2 | 0.1 | 0.1 | 69 | 197 |
| 36.48 | 35.48 | 41 | 42 | 1.230 | 0.475 | 0 | 0 | 0.5 | 2.2 | 9.1 | 63.9 | 19.6 | 4.5 | 0.1 | 0 | 65 | 212 |
| 35.48 | 34.48 | 42 | 43 | 0.980 | 0.477 | 0.1 | 0.1 | 0.7 | 4.2 | 21.7 | 54.8 | 14.7 | 3.5 | 0.1 | 0 | 61 | 234 |
| 34.48 | 33.48 | 43 | 44 | 0.920 | 1.146 | 0.2 | 0.2 | 1 | 9.4 | 46.5 | 28.5 | 13 | 1 | 0.1 | 0 | 53 | 273 |
| 33.48 | 32.48 | 44 | 45 | 0.660 | 0.755 | 0.2 | 0 | 0.6 | 9.5 | 47.3 | 32 | 9.2 | 1.1 | 0 | 0 | 53 | 274 |
| 32.48 | 31.48 | 45 | 46 | 0.440 | 0.436 | 0 | 0 | 0.6 | 8.9 | 46.3 | 35.3 | 8.2 | 0.7 | 0 | 0 | 53 | 271 |
| 31.48 | 30.48 | 46 | 47 | 0.600 | 0.328 | 0 | 0 | 0.9 | 10.2 | 41.8 | 38.3 | 8.1 | 0.6 | 0 | 0 | 53 | 271 |
| 30.48 | 29.48 | 47 | 48 | 0.790 | 0.470 | 0 | 0.1 | 6.1 | 17.8 | 37.1 | 34.8 | 3.5 | 0.6 | 0 | 0 | 49 | 307 |
| 29.48 | 28.48 | 48 | 49 | 0.460 | 0.392 | 0.2 | 0.2 | 7 | 24.9 | 36.1 | 25.2 | 6.2 | 0.3 | 0 | 0 | 47 | 326 |
| 28.48 | 27.48 | 49 | 50 | 0.530 | 0.499 | 0 | 0.1 | 8.1 | 24.1 | 39.3 | 25.2 | 2.6 | 0.4 | 0 | 0 | 46 | 330 |
| 27.48 | 26.48 | 50 | 51 | 1.060 | 1.127 | 0.8 | 0.3 | 9.4 | 25.1 | 29.1 | 24.7 | 9.8 | 0.7 | 0.1 | 0.1 | 48 | 333 |
| 26.48 | 25.48 | 51 | 52 | 1.120 | 1.670 | 1 | 0.3 | 12.1 | 20.8 | 21.2 | 34.4 | 8 | 2 | 0.1 | 0.1 | 50 | 329 |
| 25.48 | 24.48 | 52 | 53 | 1.450 | 1.174 | 0.3 | 0.1 | 3 | 9.8 | 16.1 | 43.1 | 22 | 5.4 | 0.2 | 0 | 62 | 245 |
| 24.48 | 23.48 | 53 | 54 | 1.210 | 0.788 | 0.1 | 0.1 | 2.1 | 4.7 | 16.2 | 58.3 | 13.6 | 4.8 | 0.1 | 0.1 | 62 | 235 |

Figure 8: Grain size analysis from $LBU05 - 25$ in Site-C sand quarry.

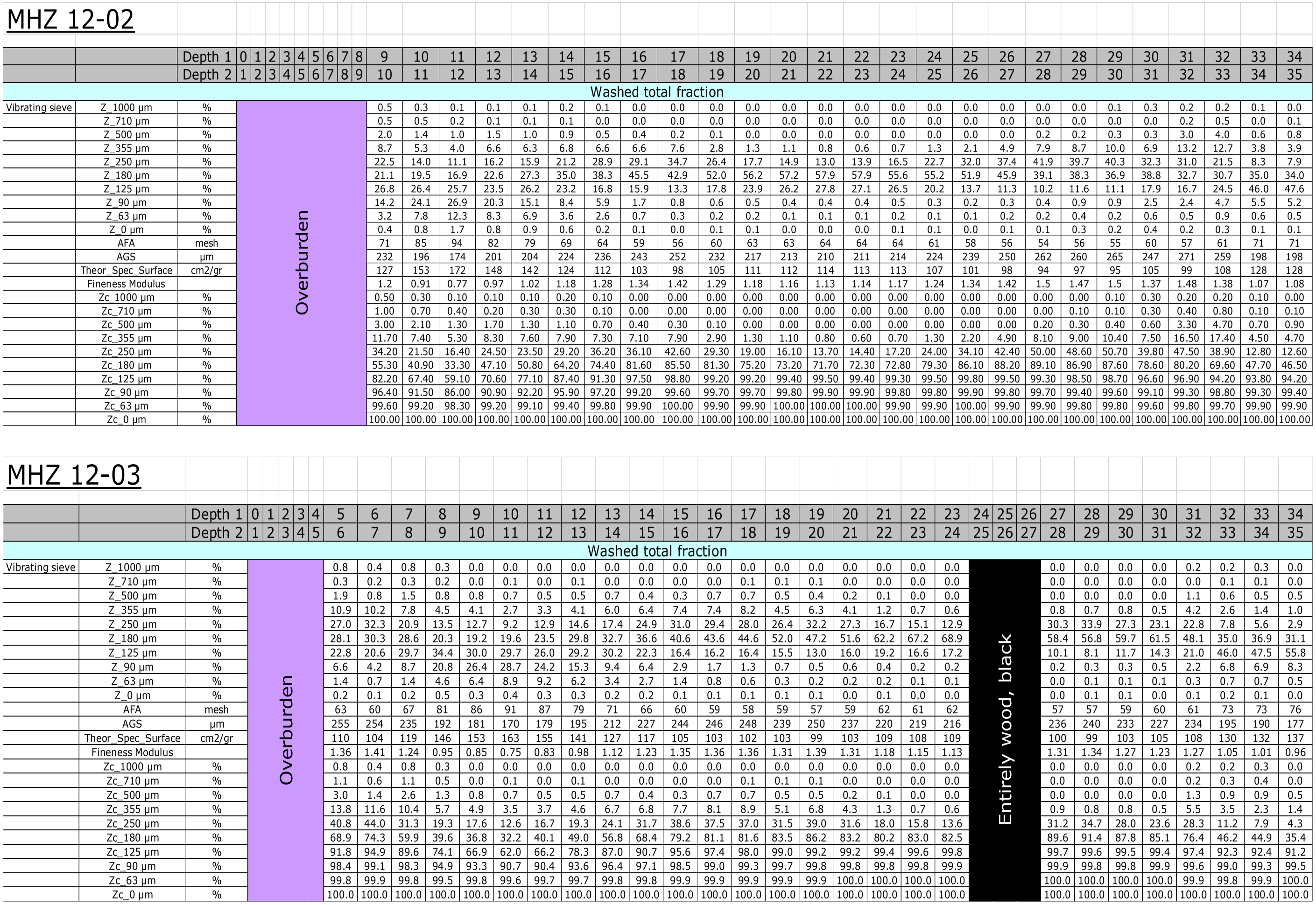

MHZ 12-02

| | | Depth 1 | 0 | 1 | 2 | 3 | 4 | 5 | 6 | 7 | 8 | 9 | 10 | 11 | 12 | 13 | 14 | 15 | 16 | 17 | 18 | 19 | 20 | 21 | 22 | 23 | 24 | 25 | 26 | 27 | 28 | 29 | 30 | 31 | 32 | 33 | 34 |
|---|---|---|---|---|---|---|---|---|---|---|---|---|---|---|---|---|---|---|---|---|---|---|---|---|---|---|---|---|---|---|---|---|---|---|---|---|---|
| | | Depth 2 | 1 | 2 | 3 | 4 | 5 | 6 | 7 | 8 | 9 | 10 | 11 | 12 | 13 | 14 | 15 | 16 | 17 | 18 | 19 | 20 | 21 | 22 | 23 | 24 | 25 | 26 | 27 | 28 | 29 | 30 | 31 | 32 | 33 | 34 | 35 |
| Washed total fraction | | | | | | | | | | | | | | | | | | | | | | | | | | | | | | | | | | | | | |
| Vibrating sieve | Z_1000 µm | % | Overburden | | | | | | | | | 0.5 | 0.3 | 0.1 | 0.1 | 0.1 | 0.2 | 0.1 | 0.0 | 0.0 | 0.0 | 0.0 | 0.0 | 0.0 | 0.0 | 0.0 | 0.0 | 0.0 | 0.0 | 0.0 | 0.0 | 0.1 | 0.3 | 0.2 | 0.2 | 0.1 | 0.0 |
| | Z_710 µm | % | | | | | | | | | | 0.5 | 0.5 | 0.2 | 0.1 | 0.1 | 0.1 | 0.0 | 0.0 | 0.0 | 0.0 | 0.0 | 0.0 | 0.0 | 0.0 | 0.0 | 0.0 | 0.0 | 0.0 | 0.0 | 0.0 | 0.0 | 0.0 | 0.2 | 0.5 | 0.0 | 0.1 |
| | Z_500 µm | % | | | | | | | | | | 2.0 | 1.4 | 1.0 | 1.5 | 1.0 | 0.9 | 0.5 | 0.4 | 0.2 | 0.1 | 0.0 | 0.0 | 0.0 | 0.0 | 0.0 | 0.0 | 0.0 | 0.0 | 0.2 | 0.2 | 0.3 | 0.3 | 3.0 | 4.0 | 0.6 | 0.8 |
| | Z_355 µm | % | | | | | | | | | | 8.7 | 5.3 | 4.0 | 6.6 | 6.3 | 6.8 | 6.6 | 6.6 | 7.6 | 2.8 | 1.3 | 1.1 | 0.8 | 0.6 | 0.7 | 1.3 | 2.1 | 4.9 | 7.9 | 8.7 | 10.0 | 6.9 | 13.2 | 12.7 | 3.8 | 3.9 |
| | Z_250 µm | % | | | | | | | | | | 22.5 | 14.0 | 11.1 | 16.2 | 15.9 | 21.2 | 28.9 | 29.1 | 34.7 | 26.4 | 17.7 | 14.9 | 13.0 | 13.9 | 16.5 | 22.7 | 32.0 | 37.4 | 41.9 | 39.7 | 40.3 | 32.3 | 31.0 | 21.5 | 8.3 | 7.9 |
| | Z_180 µm | % | | | | | | | | | | 21.1 | 19.5 | 16.9 | 22.6 | 27.3 | 35.0 | 38.3 | 45.5 | 42.9 | 52.0 | 56.2 | 57.2 | 57.9 | 57.9 | 55.6 | 55.2 | 51.9 | 45.9 | 39.1 | 38.3 | 36.9 | 38.8 | 32.7 | 30.7 | 35.0 | 34.0 |
| | Z_125 µm | % | | | | | | | | | | 26.8 | 26.4 | 25.7 | 23.5 | 26.2 | 23.2 | 16.8 | 15.9 | 13.3 | 17.8 | 23.9 | 26.2 | 27.8 | 27.1 | 26.5 | 20.2 | 13.7 | 11.3 | 10.2 | 11.6 | 11.1 | 17.9 | 16.7 | 24.5 | 46.0 | 47.6 |
| | Z_90 µm | % | | | | | | | | | | 14.2 | 24.1 | 26.9 | 20.3 | 15.1 | 8.4 | 5.9 | 1.7 | 0.8 | 0.6 | 0.5 | 0.4 | 0.4 | 0.4 | 0.5 | 0.3 | 0.2 | 0.3 | 0.4 | 0.9 | 0.9 | 2.5 | 2.4 | 4.7 | 5.5 | 5.2 |
| | Z_63 µm | % | | | | | | | | | | 3.2 | 7.8 | 12.3 | 8.3 | 6.9 | 3.6 | 2.6 | 0.7 | 0.3 | 0.2 | 0.2 | 0.1 | 0.1 | 0.1 | 0.2 | 0.1 | 0.1 | 0.2 | 0.2 | 0.4 | 0.2 | 0.6 | 0.5 | 0.9 | 0.6 | 0.5 |
| | Z_0 µm | % | | | | | | | | | | 0.4 | 0.8 | 1.7 | 0.8 | 0.9 | 0.6 | 0.2 | 0.1 | 0.0 | 0.1 | 0.1 | 0.0 | 0.0 | 0.0 | 0.1 | 0.1 | 0.0 | 0.1 | 0.1 | 0.3 | 0.2 | 0.4 | 0.2 | 0.3 | 0.1 | 0.1 |
| | AFA | mesh | | | | | | | | | | 71 | 85 | 94 | 82 | 79 | 69 | 64 | 59 | 56 | 60 | 63 | 63 | 64 | 64 | 64 | 61 | 58 | 56 | 54 | 56 | 55 | 60 | 57 | 61 | 71 | 71 |
| | AGS | µm | | | | | | | | | | 232 | 196 | 174 | 201 | 204 | 224 | 236 | 243 | 252 | 232 | 217 | 213 | 210 | 211 | 214 | 224 | 239 | 250 | 262 | 260 | 265 | 247 | 271 | 259 | 198 | 198 |
| | Theor_Spec_Surface | cm2/gr | | | | | | | | | | 127 | 153 | 172 | 148 | 142 | 124 | 112 | 103 | 98 | 105 | 111 | 112 | 114 | 113 | 113 | 107 | 101 | 98 | 94 | 97 | 95 | 105 | 99 | 108 | 128 | 128 |
| | Fineness Modulus | | | | | | | | | | | 1.2 | 0.91 | 0.77 | 0.97 | 1.02 | 1.18 | 1.28 | 1.34 | 1.42 | 1.29 | 1.18 | 1.16 | 1.13 | 1.14 | 1.17 | 1.24 | 1.34 | 1.42 | 1.5 | 1.47 | 1.5 | 1.37 | 1.48 | 1.38 | 1.07 | 1.08 |
| | Zc_1000 µm | % | | | | | | | | | | 0.50 | 0.30 | 0.10 | 0.10 | 0.10 | 0.20 | 0.10 | 0.00 | 0.00 | 0.00 | 0.00 | 0.00 | 0.00 | 0.00 | 0.00 | 0.00 | 0.00 | 0.00 | 0.00 | 0.00 | 0.10 | 0.30 | 0.20 | 0.20 | 0.10 | 0.00 |
| | Zc_710 µm | % | | | | | | | | | | 1.00 | 0.70 | 0.40 | 0.20 | 0.30 | 0.30 | 0.10 | 0.00 | 0.00 | 0.00 | 0.00 | 0.00 | 0.00 | 0.00 | 0.00 | 0.00 | 0.00 | 0.00 | 0.00 | 0.10 | 0.10 | 0.30 | 0.40 | 0.80 | 0.10 | 0.10 |
| | Zc_500 µm | % | | | | | | | | | | 3.00 | 2.10 | 1.30 | 1.70 | 1.30 | 1.10 | 0.70 | 0.40 | 0.30 | 0.10 | 0.00 | 0.00 | 0.00 | 0.00 | 0.00 | 0.00 | 0.00 | 0.00 | 0.20 | 0.30 | 0.40 | 0.60 | 3.30 | 4.70 | 0.70 | 0.90 |
| | Zc_355 µm | % | | | | | | | | | | 11.70 | 7.40 | 5.30 | 8.30 | 7.60 | 7.90 | 7.30 | 7.10 | 7.90 | 2.90 | 1.30 | 1.10 | 0.80 | 0.60 | 0.70 | 1.30 | 2.20 | 4.90 | 8.10 | 9.00 | 10.40 | 7.50 | 16.50 | 17.40 | 4.50 | 4.70 |
| | Zc_250 µm | % | | | | | | | | | | 34.20 | 21.50 | 16.40 | 24.50 | 23.50 | 29.20 | 36.20 | 36.10 | 42.60 | 29.30 | 19.00 | 16.10 | 13.70 | 14.40 | 17.20 | 24.00 | 34.10 | 42.40 | 50.00 | 48.60 | 50.70 | 39.80 | 47.50 | 38.90 | 12.80 | 12.60 |
| | Zc_180 µm | % | | | | | | | | | | 55.30 | 40.90 | 33.30 | 47.10 | 50.80 | 64.20 | 74.40 | 81.60 | 85.50 | 81.30 | 75.20 | 73.20 | 71.70 | 72.30 | 72.80 | 79.30 | 86.10 | 88.20 | 89.10 | 86.90 | 87.60 | 78.60 | 80.20 | 69.60 | 47.70 | 46.50 |
| | Zc_125 µm | % | | | | | | | | | | 82.20 | 67.40 | 59.10 | 70.60 | 77.10 | 87.40 | 91.30 | 97.50 | 98.80 | 99.20 | 99.20 | 99.40 | 99.50 | 99.40 | 99.30 | 99.50 | 99.80 | 99.50 | 99.30 | 98.50 | 98.70 | 96.60 | 96.90 | 94.20 | 93.80 | 94.20 |
| | Zc_90 µm | % | | | | | | | | | | 96.40 | 91.50 | 86.00 | 90.90 | 92.20 | 95.90 | 97.20 | 99.20 | 99.60 | 99.70 | 99.70 | 99.80 | 99.90 | 99.90 | 99.80 | 99.80 | 99.90 | 99.80 | 99.70 | 99.40 | 99.60 | 99.10 | 99.30 | 98.80 | 99.30 | 99.40 |
| | Zc_63 µm | % | | | | | | | | | | 99.60 | 99.20 | 98.30 | 99.20 | 99.10 | 99.40 | 99.80 | 99.90 | 100.00 | 99.90 | 99.90 | 100.00 | 100.00 | 100.00 | 99.90 | 99.90 | 100.00 | 99.90 | 99.90 | 99.80 | 99.80 | 99.60 | 99.80 | 99.70 | 99.90 | 99.90 |
| | Zc_0 µm | % | | | | | | | | | | 100.00 | 100.00 | 100.00 | 100.00 | 100.00 | 100.00 | 100.00 | 100.00 | 100.00 | 100.00 | 100.00 | 100.00 | 100.00 | 100.00 | 100.00 | 100.00 | 100.00 | 100.00 | 100.00 | 100.00 | 100.00 | 100.00 | 100.00 | 100.00 | 100.00 | 100.00 |

MHZ 12-03

| | | Depth 1 | 0 | 1 | 2 | 3 | 4 | 5 | 6 | 7 | 8 | 9 | 10 | 11 | 12 | 13 | 14 | 15 | 16 | 17 | 18 | 19 | 20 | 21 | 22 | 23 | 24 | 25 | 26 | 27 | 28 | 29 | 30 | 31 | 32 | 33 | 34 |
|---|---|---|---|---|---|---|---|---|---|---|---|---|---|---|---|---|---|---|---|---|---|---|---|---|---|---|---|---|---|---|---|---|---|---|---|---|---|
| | | Depth 2 | 1 | 2 | 3 | 4 | 5 | 6 | 7 | 8 | 9 | 10 | 11 | 12 | 13 | 14 | 15 | 16 | 17 | 18 | 19 | 20 | 21 | 22 | 23 | 24 | 25 | 26 | 27 | 28 | 29 | 30 | 31 | 32 | 33 | 34 | 35 |
| Washed total fraction | | | | | | | | | | | | | | | | | | | | | | | | | | | | | | | | | | | | | |
| Vibrating sieve | Z_1000 µm | % | Overburden | | | | | 0.8 | 0.4 | 0.8 | 0.3 | 0.0 | 0.0 | 0.0 | 0.0 | 0.0 | 0.0 | 0.0 | 0.0 | 0.0 | 0.0 | 0.0 | 0.0 | 0.0 | 0.0 | 0.0 | Entirely wood, black | | | 0.0 | 0.0 | 0.0 | 0.0 | 0.2 | 0.2 | 0.3 | 0.0 |
| | Z_710 µm | % | | | | | | 0.3 | 0.2 | 0.3 | 0.2 | 0.0 | 0.1 | 0.0 | 0.1 | 0.0 | 0.0 | 0.0 | 0.0 | 0.1 | 0.1 | 0.1 | 0.0 | 0.0 | 0.0 | 0.0 | | | | 0.0 | 0.0 | 0.0 | 0.0 | 0.0 | 0.1 | 0.1 | 0.0 |
| | Z_500 µm | % | | | | | | 1.9 | 0.8 | 1.5 | 0.8 | 0.8 | 0.7 | 0.5 | 0.5 | 0.7 | 0.4 | 0.3 | 0.7 | 0.7 | 0.5 | 0.4 | 0.2 | 0.1 | 0.0 | 0.0 | | | | 0.0 | 0.0 | 0.0 | 0.0 | 1.1 | 0.6 | 0.5 | 0.5 |
| | Z_355 µm | % | | | | | | 10.9 | 10.2 | 7.8 | 4.5 | 4.1 | 2.7 | 3.3 | 4.1 | 6.0 | 6.4 | 7.4 | 7.4 | 8.2 | 4.5 | 6.3 | 4.1 | 1.2 | 0.7 | 0.6 | | | | 0.8 | 0.7 | 0.8 | 0.5 | 4.2 | 2.6 | 1.4 | 1.0 |
| | Z_250 µm | % | | | | | | 27.0 | 32.3 | 20.9 | 13.5 | 12.7 | 9.2 | 12.9 | 14.6 | 17.4 | 24.9 | 31.0 | 29.4 | 28.0 | 26.4 | 32.2 | 27.3 | 16.7 | 15.1 | 12.9 | | | | 30.3 | 33.9 | 27.3 | 23.1 | 22.8 | 7.8 | 5.6 | 2.9 |
| | Z_180 µm | % | | | | | | 28.1 | 30.3 | 28.6 | 20.3 | 19.2 | 19.6 | 23.5 | 29.8 | 32.7 | 36.6 | 40.6 | 43.6 | 44.6 | 52.0 | 47.2 | 51.6 | 62.2 | 67.2 | 68.9 | | | | 58.4 | 56.8 | 59.7 | 61.5 | 48.1 | 35.0 | 36.9 | 31.1 |
| | Z_125 µm | % | | | | | | 22.8 | 20.6 | 29.7 | 34.4 | 30.0 | 29.7 | 26.0 | 29.2 | 30.2 | 22.3 | 16.4 | 16.2 | 16.4 | 15.5 | 13.0 | 16.0 | 19.2 | 16.6 | 17.2 | | | | 10.1 | 8.1 | 11.7 | 14.3 | 21.0 | 46.0 | 47.5 | 55.8 |
| | Z_90 µm | % | | | | | | 6.6 | 4.2 | 8.7 | 20.8 | 26.4 | 28.7 | 24.2 | 15.3 | 9.4 | 6.4 | 2.9 | 1.7 | 1.3 | 0.7 | 0.5 | 0.6 | 0.4 | 0.2 | 0.2 | | | | 0.2 | 0.3 | 0.3 | 0.5 | 2.2 | 6.8 | 6.9 | 8.3 |
| | Z_63 µm | % | | | | | | 1.4 | 0.7 | 1.4 | 4.6 | 6.4 | 8.9 | 9.2 | 6.2 | 3.4 | 2.7 | 1.4 | 0.8 | 0.6 | 0.3 | 0.2 | 0.2 | 0.2 | 0.1 | 0.1 | | | | 0.0 | 0.1 | 0.1 | 0.1 | 0.3 | 0.7 | 0.7 | 0.5 |
| | Z_0 µm | % | | | | | | 0.2 | 0.1 | 0.2 | 0.5 | 0.3 | 0.4 | 0.3 | 0.3 | 0.2 | 0.2 | 0.1 | 0.1 | 0.1 | 0.1 | 0.1 | 0.0 | 0.1 | 0.0 | 0.0 | | | | 0.0 | 0.1 | 0.1 | 0.0 | 0.1 | 0.2 | 0.1 | 0.0 |
| | AFA | mesh | | | | | | 63 | 60 | 67 | 81 | 86 | 91 | 87 | 79 | 71 | 66 | 60 | 59 | 58 | 59 | 57 | 59 | 62 | 61 | 62 | | | | 57 | 57 | 59 | 60 | 61 | 73 | 73 | 76 |
| | AGS | µm | | | | | | 255 | 254 | 235 | 192 | 181 | 170 | 179 | 195 | 212 | 227 | 244 | 246 | 248 | 239 | 250 | 237 | 220 | 219 | 216 | | | | 236 | 240 | 233 | 227 | 234 | 195 | 190 | 177 |
| | Theor_Spec_Surface | cm2/gr | | | | | | 110 | 104 | 119 | 146 | 153 | 163 | 155 | 141 | 127 | 117 | 105 | 103 | 102 | 103 | 99 | 103 | 109 | 108 | 109 | | | | 100 | 99 | 103 | 105 | 108 | 130 | 132 | 137 |
| | Fineness Modulus | | | | | | | 1.36 | 1.41 | 1.24 | 0.95 | 0.85 | 0.75 | 0.83 | 0.98 | 1.12 | 1.23 | 1.35 | 1.36 | 1.36 | 1.31 | 1.39 | 1.31 | 1.18 | 1.15 | 1.13 | | | | 1.31 | 1.34 | 1.27 | 1.23 | 1.27 | 1.05 | 1.01 | 0.96 |
| | Zc_1000 µm | % | | | | | | 0.8 | 0.4 | 0.8 | 0.3 | 0.0 | 0.0 | 0.0 | 0.0 | 0.0 | 0.0 | 0.0 | 0.0 | 0.0 | 0.0 | 0.0 | 0.0 | 0.0 | 0.0 | 0.0 | | | | 0.0 | 0.0 | 0.0 | 0.0 | 0.2 | 0.2 | 0.3 | 0.0 |
| | Zc_710 µm | % | | | | | | 1.1 | 0.6 | 1.1 | 0.5 | 0.0 | 0.1 | 0.0 | 0.1 | 0.0 | 0.0 | 0.0 | 0.0 | 0.1 | 0.1 | 0.1 | 0.0 | 0.0 | 0.0 | 0.0 | | | | 0.0 | 0.0 | 0.0 | 0.0 | 0.2 | 0.3 | 0.4 | 0.0 |
| | Zc_500 µm | % | | | | | | 3.0 | 1.4 | 2.6 | 1.3 | 0.8 | 0.7 | 0.5 | 0.5 | 0.7 | 0.4 | 0.3 | 0.7 | 0.7 | 0.5 | 0.5 | 0.2 | 0.1 | 0.0 | 0.0 | | | | 0.0 | 0.0 | 0.0 | 0.0 | 1.3 | 0.9 | 0.9 | 0.5 |
| | Zc_355 µm | % | | | | | | 13.8 | 11.6 | 10.4 | 5.7 | 4.9 | 3.5 | 3.7 | 4.6 | 6.7 | 6.8 | 7.7 | 8.1 | 8.9 | 5.1 | 6.8 | 4.3 | 1.3 | 0.7 | 0.6 | | | | 0.9 | 0.8 | 0.8 | 0.5 | 5.5 | 3.5 | 2.3 | 1.4 |
| | Zc_250 µm | % | | | | | | 40.8 | 44.0 | 31.3 | 19.3 | 17.6 | 12.6 | 16.7 | 19.3 | 24.1 | 31.7 | 38.6 | 37.5 | 37.0 | 31.5 | 39.0 | 31.6 | 18.0 | 15.8 | 13.6 | | | | 31.2 | 34.7 | 28.0 | 23.6 | 28.3 | 11.2 | 7.9 | 4.3 |
| | Zc_180 µm | % | | | | | | 68.9 | 74.3 | 59.9 | 39.6 | 36.8 | 32.2 | 40.1 | 49.0 | 56.8 | 68.4 | 79.2 | 81.1 | 81.6 | 83.5 | 86.2 | 83.2 | 80.2 | 83.0 | 82.5 | | | | 89.6 | 91.4 | 87.8 | 85.1 | 76.4 | 46.2 | 44.9 | 35.4 |
| | Zc_125 µm | % | | | | | | 91.8 | 94.9 | 89.6 | 74.1 | 66.9 | 62.0 | 66.2 | 78.3 | 87.0 | 90.7 | 95.6 | 97.4 | 98.0 | 99.0 | 99.2 | 99.2 | 99.4 | 99.6 | 99.8 | | | | 99.7 | 99.6 | 99.5 | 99.4 | 97.4 | 92.3 | 92.4 | 91.2 |
| | Zc_90 µm | % | | | | | | 98.4 | 99.1 | 98.3 | 94.9 | 93.3 | 90.7 | 90.4 | 93.6 | 96.4 | 97.1 | 98.5 | 99.0 | 99.3 | 99.7 | 99.8 | 99.8 | 99.8 | 99.8 | 99.9 | | | | 99.9 | 99.8 | 99.8 | 99.9 | 99.6 | 99.0 | 99.3 | 99.5 |
| | Zc_63 µm | % | | | | | | 99.8 | 99.9 | 99.8 | 99.5 | 99.8 | 99.6 | 99.7 | 99.7 | 99.8 | 99.8 | 99.9 | 99.9 | 99.9 | 99.9 | 99.9 | 100.0 | 100.0 | 100.0 | 100.0 | | | | 100.0 | 100.0 | 100.0 | 100.0 | 99.9 | 99.8 | 99.9 | 100.0 |
| | Zc_0 µm | % | | | | | | 100.0 | 100.0 | 100.0 | 100.0 | 100.0 | 100.0 | 100.0 | 100.0 | 100.0 | 100.0 | 100.0 | 100.0 | 100.0 | 100.0 | 100.0 | 100.0 | 100.0 | 100.0 | 100.0 | | | | 100.0 | 100.0 | 100.0 | 100.0 | 100.0 | 100.0 | 100.0 | 100.0 |

Figure 9: Grain size analysis from $MHZ1202 - 03$ in Site-C sand quarry.

| Drill | Depth 1 | Depth 2 | Clay | Vibrating sieve | | | | | | | | | | | | | |
|---|---|---|---|---|---|---|---|---|---|---|---|---|---|---|---|---|---|
| | | | < 25µm | 1000 | 710 | 500 | 355 | 250 | 180 | 125 | 90 | 63 | 0 | AFA | AGS | hSpecSu | FinMod |
| | m | m | % | % | % | % | % | % | % | % | % | % | % | mesh | µm | cm2/gr | |
| MHZ_16_06 | 0.0 | 1.0 | 3.27 | 6.8 | 1.3 | 5.2 | 17.3 | 29.3 | 17.6 | 10.7 | 5.3 | 2.7 | 3.8 | 62 | 350 | 116 | 1.68 |
| MHZ_16_06 | 1.0 | 2.0 | 1.97 | 5.5 | 4.0 | 14.4 | 26.6 | 28.6 | 13.0 | 4.5 | 1.7 | 0.9 | 0.8 | 44 | 425 | 75 | 2.05 |
| MHZ_16_06 | 2.0 | 3.0 | 1.78 | 19.8 | 5.4 | 10.6 | 18.3 | 20.9 | 13.2 | 6.1 | 2.5 | 1.4 | 1.8 | 44 | 531 | 80 | 2.25 |
| MHZ_16_06 | 3.0 | 4.0 | | | | | | | | | | | | | | | |
| MHZ_16_06 | 4.0 | 5.0 | 0.45 | 0.2 | 0.3 | 1.3 | 10.6 | 31.0 | 30.7 | 20.6 | 4.1 | 0.8 | 0.3 | 60 | 254 | 105 | 1.40 |
| MHZ_16_06 | 5.0 | 6.0 | 0.47 | 0.1 | 0.1 | 1.7 | 12.3 | 30.4 | 29.6 | 22.3 | 3.0 | 0.4 | 0.2 | 59 | 258 | 103 | 1.43 |
| MHZ_16_06 | 6.0 | 7.0 | 1.80 | 0.1 | 0.2 | 2.3 | 15.1 | 30.6 | 26.1 | 21.5 | 3.5 | 0.4 | 0.2 | 58 | 267 | 101 | 1.47 |
| MHZ_16_06 | 7.0 | 8.0 | 1.11 | 0.1 | 0.1 | 2.1 | 12.5 | 27.7 | 26.4 | 25.5 | 4.8 | 0.6 | 0.2 | 61 | 253 | 107 | 1.39 |
| MHZ_16_06 | 8.0 | 9.0 | 0.72 | 0.1 | 0.2 | 1.1 | 7.9 | 20.3 | 28.0 | 35.0 | 6.5 | 0.7 | 0.2 | 67 | 226 | 119 | 1.24 |
| MHZ_16_06 | 9.0 | 10.0 | 0.99 | 0.2 | 0.1 | 2.2 | 6.0 | 13.3 | 16.6 | 28.3 | 24.7 | 7.5 | 1.1 | 86 | 194 | 156 | 0.91 |
| MHZ_16_06 | 10.0 | 11.0 | 0.83 | 0.0 | 0.3 | 0.5 | 4.9 | 11.2 | 18.7 | 28.0 | 27.9 | 7.8 | 0.6 | 88 | 179 | 159 | 0.81 |
| MHZ_16_06 | 11.0 | 12.0 | 0.42 | 0.0 | 0.0 | 0.6 | 5.4 | 14.6 | 26.8 | 28.3 | 17.1 | 6.5 | 0.6 | 80 | 195 | 144 | 0.97 |
| MHZ_16_06 | 12.0 | 13.0 | 0.48 | 0.0 | 0.1 | 0.8 | 8.0 | 14.6 | 27.9 | 33.1 | 10.6 | 4.2 | 0.5 | 74 | 209 | 132 | 1.09 |
| MHZ_16_06 | 13.0 | 14.0 | 0.48 | 0.5 | 0.2 | 1.6 | 7.2 | 18.5 | 32.3 | 29.2 | 7.7 | 2.2 | 0.6 | 69 | 228 | 123 | 1.20 |
| MHZ_16_06 | 14.0 | 15.0 | 0.57 | 0.1 | 0.0 | 0.6 | 5.2 | 21.9 | 45.9 | 23.5 | 2.1 | 0.4 | 0.1 | 62 | 230 | 109 | 1.26 |
| MHZ_16_06 | 15.0 | 16.0 | 0.23 | 0.0 | 0.0 | 0.4 | 4.6 | 25.8 | 45.4 | 22.6 | 1.0 | 0.2 | 0.1 | 61 | 233 | 107 | 1.30 |
| MHZ_16_06 | 16.0 | 17.0 | 0.09 | 0.0 | 0.1 | 0.8 | 6.9 | 26.7 | 45.4 | 19.1 | 0.8 | 0.1 | 0.1 | 59 | 244 | 103 | 1.34 |
| MHZ_16_06 | 17.0 | 18.0 | 0.08 | 0.0 | 0.0 | 0.4 | 7.0 | 32.1 | 44.3 | 15.6 | 0.5 | 0.1 | 0.0 | 57 | 249 | 99 | 1.39 |
| MHZ_16_06 | 18.0 | 19.0 | 0.10 | 0.0 | 0.0 | 0.1 | 6.5 | 31.7 | 47.1 | 14.1 | 0.3 | 0.0 | 0.0 | 57 | 247 | 98 | 1.38 |
| MHZ_16_06 | 19.0 | 20.0 | 2.31 | 0.7 | 0.8 | 1.0 | 4.9 | 26.2 | 45.0 | 19.4 | 1.1 | 0.3 | 0.6 | 60 | 249 | 107 | 1.35 |
| MHZ_16_06 | 20.0 | 21.0 | 0.82 | 0.3 | 0.3 | 0.4 | 1.9 | 16.7 | 53.1 | 26.0 | 0.9 | 0.1 | 0.2 | 63 | 222 | 112 | 1.20 |
| MHZ_16_06 | 21.0 | 22.0 | 0.35 | 0.0 | 0.1 | 0.0 | 2.5 | 26.8 | 52.3 | 17.8 | 0.4 | 0.0 | 0.0 | 59 | 233 | 104 | 1.29 |
| MHZ_16_06 | 22.0 | 23.0 | 0.16 | 0.0 | 0.0 | 0.0 | 3.6 | 36.5 | 48.2 | 11.5 | 0.2 | 0.0 | 0.0 | 56 | 247 | 97 | 1.40 |
| MHZ_16_06 | 23.0 | 24.0 | 0.39 | 0.0 | 0.1 | 0.1 | 3.5 | 35.2 | 48.5 | 12.3 | 0.2 | 0.0 | 0.0 | 56 | 246 | 98 | 1.39 |
| MHZ_16_06 | 24.0 | 25.0 | 0.61 | 0.0 | 0.0 | 0.1 | 7.7 | 41.0 | 41.0 | 9.9 | 0.2 | 0.1 | 0.1 | 54 | 261 | 94 | 1.49 |
| MHZ_16_06 | 25.0 | 26.0 | 0.91 | 0.0 | 0.0 | 0.3 | 12.8 | 46.8 | 31.7 | 7.9 | 0.3 | 0.1 | 0.1 | 52 | 279 | 89 | 1.60 |
| MHZ_16_06 | 26.0 | 27.0 | 0.71 | 0.0 | 0.0 | 0.2 | 9.2 | 41.5 | 37.8 | 10.7 | 0.4 | 0.1 | 0.1 | 54 | 264 | 94 | 1.51 |
| MHZ_16_06 | 27.0 | 28.0 | 1.04 | 0.0 | 0.0 | 0.4 | 10.0 | 38.2 | 37.4 | 13.0 | 0.7 | 0.1 | 0.1 | 55 | 262 | 95 | 1.48 |
| MHZ_16_06 | 28.0 | 29.0 | 1.12 | 0.0 | 0.1 | 0.5 | 9.1 | 37.0 | 38.4 | 13.7 | 0.9 | 0.1 | 0.1 | 56 | 259 | 96 | 1.46 |
| MHZ_16_06 | 29.0 | 30.0 | 0.90 | 0.1 | 0.1 | 0.3 | 6.2 | 38.2 | 39.4 | 14.3 | 1.1 | 0.1 | 0.1 | 56 | 254 | 98 | 1.44 |
| MHZ_16_06 | 30.0 | 31.0 | 1.00 | 0.1 | 0.1 | 1.8 | 9.4 | 24.5 | 38.0 | 23.5 | 2.1 | 0.3 | 0.2 | 60 | 247 | 106 | 1.35 |
| MHZ_16_06 | 31.0 | 32.0 | 1.11 | 0.1 | 0.0 | 0.2 | 2.1 | 9.3 | 38.8 | 43.7 | 4.8 | 0.5 | 0.2 | 71 | 195 | 127 | 1.07 |
| MHZ_16_06 | 32.0 | 33.0 | 0.92 | 0.1 | 0.1 | 0.1 | 0.9 | 3.1 | 26.1 | 59.4 | 9.0 | 0.8 | 0.3 | 78 | 173 | 142 | 0.95 |
| MHZ_16_06 | 33.0 | 34.0 | 0.68 | 0.0 | 0.0 | 0.2 | 0.5 | 2.9 | 25.1 | 61.4 | 8.9 | 0.7 | 0.3 | 79 | 170 | 143 | 0.94 |
| MHZ_16_06 | 34.0 | 35.0 | 0.73 | 0.1 | 0.1 | 0.1 | 0.9 | 2.9 | 21.7 | 62.7 | 10.5 | 0.8 | 0.2 | 80 | 170 | 145 | 0.93 |
| MHZ_16_07 | 0.0 | 1.0 | 2.95 | 10.2 | 2.8 | 6.7 | 11.4 | 15.0 | 17.5 | 18.8 | 10.5 | 4.6 | 2.7 | 67 | 363 | 124 | 1.58 |
| MHZ_16_07 | 1.0 | 2.0 | 3.96 | 17.6 | 1.6 | 3.9 | 8.2 | 15.9 | 18.1 | 16.7 | 9.3 | 4.6 | 4.0 | 67 | 411 | 127 | 1.70 |
| MHZ_16_07 | 2.0 | 3.0 | 4.27 | 22.5 | 5.0 | 9.9 | 13.1 | 14.1 | 13.1 | 11.9 | 6.1 | 2.6 | 1.8 | 50 | 527 | 92 | 2.14 |
| MHZ_16_07 | 3.0 | 4.0 | 4.40 | 9.3 | 2.4 | 5.3 | 9.2 | 15.0 | 17.2 | 20.6 | 12.4 | 5.6 | 3.2 | 72 | 336 | 135 | 1.46 |
| MHZ_16_07 | 4.0 | 5.0 | | | | | | | | | | | | | | | |
| MHZ_16_07 | 5.0 | 6.0 | | | | | | | | | | | | | | | |
| MHZ_16_07 | 6.0 | 7.0 | | | | | | | | | | | | | | | |
| MHZ_16_07 | 7.0 | 8.0 | | | | | | | | | | | | | | | |
| MHZ_16_07 | 8.0 | 9.0 | 0.92 | 4.1 | 0.6 | 2.7 | 11.4 | 22.2 | 24.0 | 25.1 | 8.0 | 1.5 | 0.5 | 63 | 286 | 112 | 1.43 |
| MHZ_16_07 | 9.0 | 10.0 | 1.23 | 1.1 | 0.5 | 1.6 | 5.2 | 11.3 | 16.1 | 30.5 | 23.1 | 8.6 | 2.0 | 89 | 197 | 163 | 0.90 |
| MHZ_16_07 | 10.0 | 11.0 | 1.08 | 0.0 | 0.0 | 0.9 | 3.1 | 7.7 | 16.4 | 27.8 | 35.7 | 7.9 | 0.5 | 94 | 164 | 168 | 0.69 |
| MHZ_16_07 | 11.0 | 12.0 | 1.05 | 0.1 | 0.2 | 1.9 | 5.9 | 11.3 | 16.8 | 23.4 | 29.7 | 9.8 | 0.8 | 90 | 185 | 162 | 0.81 |
| MHZ_16_07 | 12.0 | 13.0 | 1.81 | 0.0 | 0.0 | 0.2 | 2.4 | 7.8 | 18.2 | 29.4 | 28.9 | 11.4 | 1.7 | 97 | 159 | 177 | 0.69 |
| MHZ_16_07 | 13.0 | 14.0 | 0.72 | 0.0 | 0.1 | 0.7 | 8.3 | 13.9 | 26.2 | 29.1 | 15.4 | 6.0 | 0.3 | 77 | 205 | 138 | 1.02 |
| MHZ_16_07 | 14.0 | 15.0 | 0.49 | 0.0 | 0.0 | 0.3 | 4.4 | 22.5 | 40.8 | 24.0 | 5.8 | 2.1 | 0.2 | 66 | 221 | 118 | 1.19 |
| MHZ_16_07 | 15.0 | 16.0 | 0.28 | 0.6 | 0.2 | 0.7 | 5.0 | 22.1 | 37.6 | 24.6 | 6.1 | 2.5 | 0.6 | 67 | 228 | 120 | 1.22 |
| MHZ_16_07 | 16.0 | 17.0 | 0.29 | 0.2 | 0.1 | 0.7 | 4.1 | 20.1 | 41.7 | 27.0 | 4.3 | 1.4 | 0.3 | 66 | 222 | 117 | 1.20 |
| MHZ_16_07 | 17.0 | 18.0 | 0.15 | 0.2 | 0.1 | 0.7 | 6.4 | 30.2 | 39.3 | 18.6 | 3.1 | 1.1 | 0.3 | 61 | 243 | 107 | 1.34 |
| MHZ_16_07 | 18.0 | 19.0 | 0.44 | 0.0 | 0.0 | 0.5 | 8.5 | 38.5 | 37.8 | 13.4 | 0.9 | 0.3 | 0.1 | 56 | 259 | 97 | 1.47 |
| MHZ_16_07 | 19.0 | 20.0 | 0.85 | 0.0 | 0.0 | 0.2 | 5.6 | 28.5 | 44.5 | 19.6 | 1.1 | 0.3 | 0.1 | 59 | 238 | 104 | 1.33 |
| MHZ_16_07 | 20.0 | 21.0 | 0.57 | 0.0 | 0.0 | 0.0 | 1.8 | 19.6 | 53.2 | 24.3 | 0.8 | 0.2 | 0.1 | 63 | 219 | 111 | 1.20 |
| MHZ_16_07 | 21.0 | 22.0 | 0.36 | 0.0 | 0.0 | 0.0 | 1.2 | 17.3 | 53.9 | 26.7 | 0.6 | 0.1 | 0.1 | 63 | 215 | 112 | 1.18 |
| MHZ_16_07 | 22.0 | 23.0 | 0.25 | 0.0 | 0.0 | 0.0 | 1.0 | 15.3 | 55.5 | 27.5 | 0.5 | 0.1 | 0.1 | 64 | 212 | 113 | 1.16 |
| MHZ_16_07 | 23.0 | 24.0 | 0.44 | 0.0 | 0.0 | 0.0 | 0.2 | 6.2 | 50.6 | 41.9 | 0.7 | 0.1 | 0.1 | 68 | 193 | 123 | 1.05 |
| MHZ_16_07 | 24.0 | 25.0 | 0.21 | 0.0 | 0.0 | 0.0 | 0.5 | 11.3 | 55.6 | 31.9 | 0.5 | 0.1 | 0.1 | 65 | 205 | 117 | 1.11 |
| MHZ_16_07 | 25.0 | 26.0 | 0.44 | 0.0 | 0.0 | 0.0 | 2.0 | 26.7 | 51.2 | 19.6 | 0.3 | 0.1 | 0.1 | 60 | 230 | 106 | 1.28 |
| MHZ_16_07 | 26.0 | 27.0 | 0.78 | 0.0 | 0.0 | 0.1 | 7.1 | 41.8 | 38.5 | 12.0 | 0.3 | 0.1 | 0.1 | 55 | 259 | 95 | 1.49 |
| MHZ_16_07 | 27.0 | 28.0 | 0.89 | 0.0 | 0.0 | 0.2 | 6.7 | 37.6 | 41.7 | 13.1 | 0.4 | 0.1 | 0.1 | 56 | 254 | 97 | 1.44 |
| MHZ_16_07 | 28.0 | 29.0 | 1.12 | 0.0 | 0.0 | 0.2 | 8.7 | 39.1 | 38.2 | 12.7 | 0.6 | 0.2 | 0.2 | 55 | 259 | 96 | 1.47 |
| MHZ_16_07 | 29.0 | 30.0 | 1.75 | 0.0 | 0.0 | 0.4 | 10.7 | 41.4 | 35.8 | 10.7 | 0.5 | 0.2 | 0.3 | 54 | 267 | 94 | 1.52 |
| MHZ_16_07 | 30.0 | 31.0 | 2.42 | 0.0 | 0.0 | 0.3 | 10.3 | 35.2 | 35.9 | 15.8 | 1.6 | 0.5 | 0.5 | 58 | 256 | 102 | 1.43 |
| MHZ_16_07 | 31.0 | 32.0 | 1.55 | 0.0 | 0.0 | 0.3 | 8.6 | 36.5 | 36.5 | 15.1 | 1.7 | 0.6 | 0.7 | 59 | 253 | 103 | 1.43 |
| MHZ_16_07 | 32.0 | 33.0 | 2.12 | 0.2 | 0.0 | 0.5 | 8.8 | 32.9 | 35.1 | 19.3 | 2.4 | 0.4 | 0.4 | 59 | 250 | 104 | 1.40 |
| MHZ_16_07 | 33.0 | 34.0 | 0.84 | 0.1 | 0.4 | 1.0 | 8.2 | 24.6 | 31.4 | 29.5 | 4.0 | 0.5 | 0.3 | 63 | 237 | 112 | 1.31 |
| MHZ_16_07 | 34.0 | 35.0 | 1.45 | 0.0 | 0.0 | 0.1 | 2.6 | 12.4 | 30.8 | 48.7 | 4.6 | 0.5 | 0.3 | 72 | 195 | 129 | 1.10 |

Significant amount of gravel, lignite or clay in sample, analysis not performed

Figure 10: Grain size analysis from $MHZ1606$ in Site-C sand quarry.

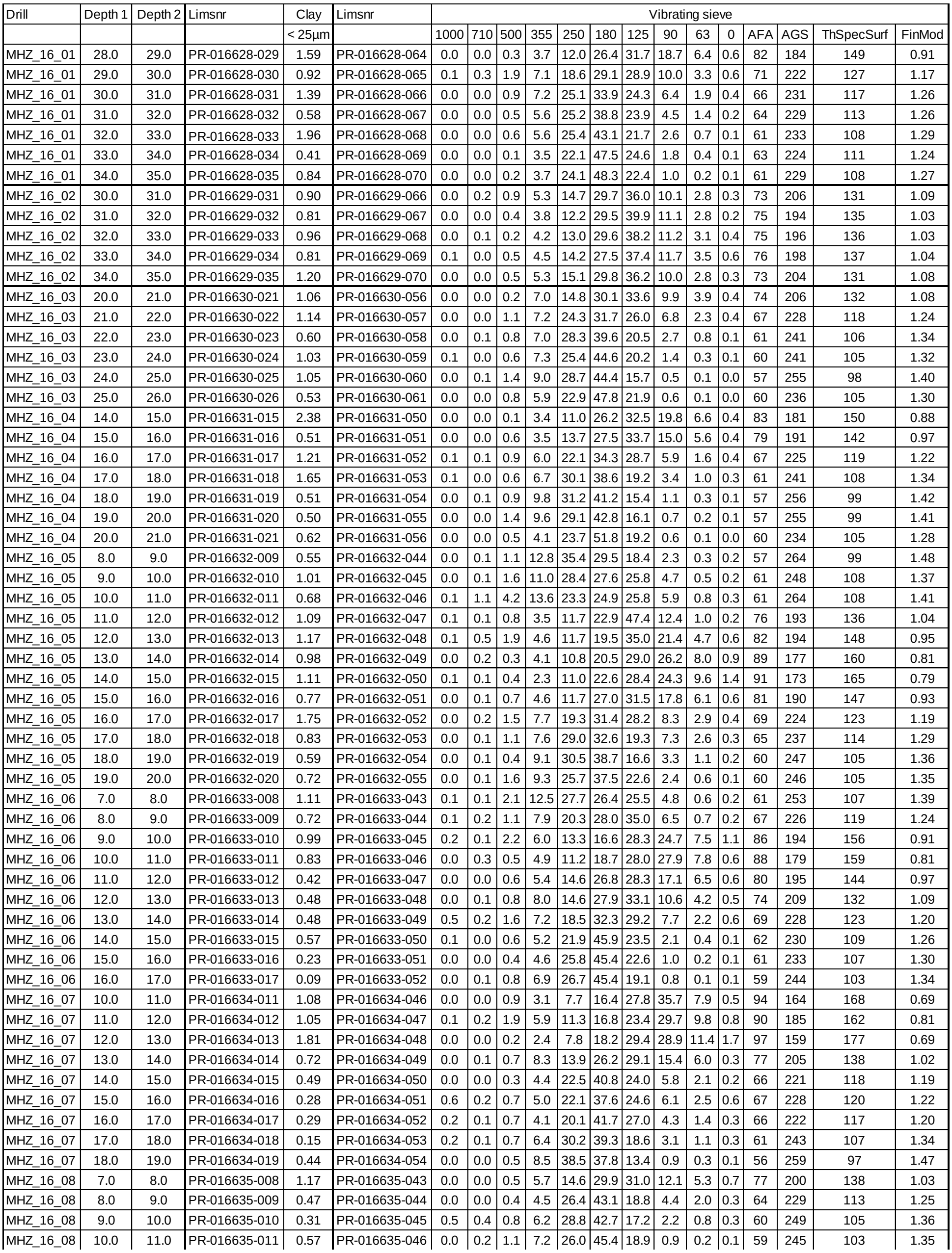

| Drill | Depth 1 | Depth 2 | Limsnr | Clay | Limsnr | Vibrating sieve | | | | | | | | | | | | | |
|---|---|---|---|---|---|---|---|---|---|---|---|---|---|---|---|---|---|---|---|
| | | | | < 25µm | | 1000 | 710 | 500 | 355 | 250 | 180 | 125 | 90 | 63 | 0 | AFA | AGS | ThSpecSurf | FinMod |
| MHZ_16_01 | 28.0 | 29.0 | PR-016628-029 | 1.59 | PR-016628-064 | 0.0 | 0.0 | 0.3 | 3.7 | 12.0 | 26.4 | 31.7 | 18.7 | 6.4 | 0.6 | 82 | 184 | 149 | 0.91 |
| MHZ_16_01 | 29.0 | 30.0 | PR-016628-030 | 0.92 | PR-016628-065 | 0.1 | 0.3 | 1.9 | 7.1 | 18.6 | 29.1 | 28.9 | 10.0 | 3.3 | 0.6 | 71 | 222 | 127 | 1.17 |
| MHZ_16_01 | 30.0 | 31.0 | PR-016628-031 | 1.39 | PR-016628-066 | 0.0 | 0.0 | 0.9 | 7.2 | 25.1 | 33.9 | 24.3 | 6.4 | 1.9 | 0.4 | 66 | 231 | 117 | 1.26 |
| MHZ_16_01 | 31.0 | 32.0 | PR-016628-032 | 0.58 | PR-016628-067 | 0.0 | 0.0 | 0.5 | 5.6 | 25.2 | 38.8 | 23.9 | 4.5 | 1.4 | 0.2 | 64 | 229 | 113 | 1.26 |
| MHZ_16_01 | 32.0 | 33.0 | PR-016628-033 | 1.96 | PR-016628-068 | 0.0 | 0.0 | 0.6 | 5.6 | 25.4 | 43.1 | 21.7 | 2.6 | 0.7 | 0.1 | 61 | 233 | 108 | 1.29 |
| MHZ_16_01 | 33.0 | 34.0 | PR-016628-034 | 0.41 | PR-016628-069 | 0.0 | 0.0 | 0.1 | 3.5 | 22.1 | 47.5 | 24.6 | 1.8 | 0.4 | 0.1 | 63 | 224 | 111 | 1.24 |
| MHZ_16_01 | 34.0 | 35.0 | PR-016628-035 | 0.84 | PR-016628-070 | 0.0 | 0.0 | 0.2 | 3.7 | 24.1 | 48.3 | 22.4 | 1.0 | 0.2 | 0.1 | 61 | 229 | 108 | 1.27 |
| MHZ_16_02 | 30.0 | 31.0 | PR-016629-031 | 0.90 | PR-016629-066 | 0.0 | 0.2 | 0.9 | 5.3 | 14.7 | 29.7 | 36.0 | 10.1 | 2.8 | 0.3 | 73 | 206 | 131 | 1.09 |
| MHZ_16_02 | 31.0 | 32.0 | PR-016629-032 | 0.81 | PR-016629-067 | 0.0 | 0.0 | 0.4 | 3.8 | 12.2 | 29.5 | 39.9 | 11.1 | 2.8 | 0.2 | 75 | 194 | 135 | 1.03 |
| MHZ_16_02 | 32.0 | 33.0 | PR-016629-033 | 0.96 | PR-016629-068 | 0.0 | 0.1 | 0.2 | 4.2 | 13.0 | 29.6 | 38.2 | 11.2 | 3.1 | 0.4 | 75 | 196 | 136 | 1.03 |
| MHZ_16_02 | 33.0 | 34.0 | PR-016629-034 | 0.81 | PR-016629-069 | 0.1 | 0.0 | 0.5 | 4.5 | 14.2 | 27.5 | 37.4 | 11.7 | 3.5 | 0.6 | 76 | 198 | 137 | 1.04 |
| MHZ_16_02 | 34.0 | 35.0 | PR-016629-035 | 1.20 | PR-016629-070 | 0.0 | 0.0 | 0.5 | 5.3 | 15.1 | 29.8 | 36.2 | 10.0 | 2.8 | 0.3 | 73 | 204 | 131 | 1.08 |
| MHZ_16_03 | 20.0 | 21.0 | PR-016630-021 | 1.06 | PR-016630-056 | 0.0 | 0.0 | 0.2 | 7.0 | 14.8 | 30.1 | 33.6 | 9.9 | 3.9 | 0.4 | 74 | 206 | 132 | 1.08 |
| MHZ_16_03 | 21.0 | 22.0 | PR-016630-022 | 1.14 | PR-016630-057 | 0.0 | 0.0 | 1.1 | 7.2 | 24.3 | 31.7 | 26.0 | 6.8 | 2.3 | 0.4 | 67 | 228 | 118 | 1.24 |
| MHZ_16_03 | 22.0 | 23.0 | PR-016630-023 | 0.60 | PR-016630-058 | 0.0 | 0.1 | 0.8 | 7.0 | 28.3 | 39.6 | 20.5 | 2.7 | 0.8 | 0.1 | 61 | 241 | 106 | 1.34 |
| MHZ_16_03 | 23.0 | 24.0 | PR-016630-024 | 1.03 | PR-016630-059 | 0.1 | 0.0 | 0.6 | 7.3 | 25.4 | 44.6 | 20.2 | 1.4 | 0.3 | 0.1 | 60 | 241 | 105 | 1.32 |
| MHZ_16_03 | 24.0 | 25.0 | PR-016630-025 | 1.05 | PR-016630-060 | 0.0 | 0.1 | 1.4 | 9.0 | 28.7 | 44.4 | 15.7 | 0.5 | 0.1 | 0.0 | 57 | 255 | 98 | 1.40 |
| MHZ_16_03 | 25.0 | 26.0 | PR-016630-026 | 0.53 | PR-016630-061 | 0.0 | 0.0 | 0.8 | 5.9 | 22.9 | 47.8 | 21.9 | 0.6 | 0.1 | 0.0 | 60 | 236 | 105 | 1.30 |
| MHZ_16_04 | 14.0 | 15.0 | PR-016631-015 | 2.38 | PR-016631-050 | 0.0 | 0.0 | 0.1 | 3.4 | 11.0 | 26.2 | 32.5 | 19.8 | 6.6 | 0.4 | 83 | 181 | 150 | 0.88 |
| MHZ_16_04 | 15.0 | 16.0 | PR-016631-016 | 0.51 | PR-016631-051 | 0.0 | 0.0 | 0.6 | 3.5 | 13.7 | 27.5 | 33.7 | 15.0 | 5.6 | 0.4 | 79 | 191 | 142 | 0.97 |
| MHZ_16_04 | 16.0 | 17.0 | PR-016631-017 | 1.21 | PR-016631-052 | 0.1 | 0.1 | 0.9 | 6.0 | 22.1 | 34.3 | 28.7 | 5.9 | 1.6 | 0.4 | 67 | 225 | 119 | 1.22 |
| MHZ_16_04 | 17.0 | 18.0 | PR-016631-018 | 1.65 | PR-016631-053 | 0.1 | 0.0 | 0.6 | 6.7 | 30.1 | 38.6 | 19.2 | 3.4 | 1.0 | 0.3 | 61 | 241 | 108 | 1.34 |
| MHZ_16_04 | 18.0 | 19.0 | PR-016631-019 | 0.51 | PR-016631-054 | 0.0 | 0.1 | 0.9 | 9.8 | 31.2 | 41.2 | 15.4 | 1.1 | 0.3 | 0.1 | 57 | 256 | 99 | 1.42 |
| MHZ_16_04 | 19.0 | 20.0 | PR-016631-020 | 0.50 | PR-016631-055 | 0.0 | 0.0 | 1.4 | 9.6 | 29.1 | 42.8 | 16.1 | 0.7 | 0.2 | 0.1 | 57 | 255 | 99 | 1.41 |
| MHZ_16_04 | 20.0 | 21.0 | PR-016631-021 | 0.62 | PR-016631-056 | 0.0 | 0.0 | 0.5 | 4.1 | 23.7 | 51.8 | 19.2 | 0.6 | 0.1 | 0.0 | 60 | 234 | 105 | 1.28 |
| MHZ_16_05 | 8.0 | 9.0 | PR-016632-009 | 0.55 | PR-016632-044 | 0.0 | 0.1 | 1.1 | 12.8 | 35.4 | 29.5 | 18.4 | 2.3 | 0.3 | 0.2 | 57 | 264 | 99 | 1.48 |
| MHZ_16_05 | 9.0 | 10.0 | PR-016632-010 | 1.01 | PR-016632-045 | 0.0 | 0.1 | 1.6 | 11.0 | 28.4 | 27.6 | 25.8 | 4.7 | 0.5 | 0.2 | 61 | 248 | 108 | 1.37 |
| MHZ_16_05 | 10.0 | 11.0 | PR-016632-011 | 0.68 | PR-016632-046 | 0.1 | 1.1 | 4.2 | 13.6 | 23.3 | 24.9 | 25.8 | 5.9 | 0.8 | 0.3 | 61 | 264 | 108 | 1.41 |
| MHZ_16_05 | 11.0 | 12.0 | PR-016632-012 | 1.09 | PR-016632-047 | 0.1 | 0.1 | 0.8 | 3.5 | 11.7 | 22.9 | 47.4 | 12.4 | 1.0 | 0.2 | 76 | 193 | 136 | 1.04 |
| MHZ_16_05 | 12.0 | 13.0 | PR-016632-013 | 1.17 | PR-016632-048 | 0.1 | 0.5 | 1.9 | 4.6 | 11.7 | 19.5 | 35.0 | 21.4 | 4.7 | 0.6 | 82 | 194 | 148 | 0.95 |
| MHZ_16_05 | 13.0 | 14.0 | PR-016632-014 | 0.98 | PR-016632-049 | 0.0 | 0.2 | 0.3 | 4.1 | 10.8 | 20.5 | 29.0 | 26.2 | 8.0 | 0.9 | 89 | 177 | 160 | 0.81 |
| MHZ_16_05 | 14.0 | 15.0 | PR-016632-015 | 1.11 | PR-016632-050 | 0.1 | 0.1 | 0.4 | 2.3 | 11.0 | 22.6 | 28.4 | 24.3 | 9.6 | 1.4 | 91 | 173 | 165 | 0.79 |
| MHZ_16_05 | 15.0 | 16.0 | PR-016632-016 | 0.77 | PR-016632-051 | 0.0 | 0.1 | 0.7 | 4.6 | 11.7 | 27.0 | 31.5 | 17.8 | 6.1 | 0.6 | 81 | 190 | 147 | 0.93 |
| MHZ_16_05 | 16.0 | 17.0 | PR-016632-017 | 1.75 | PR-016632-052 | 0.0 | 0.2 | 1.5 | 7.7 | 19.3 | 31.4 | 28.2 | 8.3 | 2.9 | 0.4 | 69 | 224 | 123 | 1.19 |
| MHZ_16_05 | 17.0 | 18.0 | PR-016632-018 | 0.83 | PR-016632-053 | 0.0 | 0.1 | 1.1 | 7.6 | 29.0 | 32.6 | 19.3 | 7.3 | 2.6 | 0.3 | 65 | 237 | 114 | 1.29 |
| MHZ_16_05 | 18.0 | 19.0 | PR-016632-019 | 0.59 | PR-016632-054 | 0.0 | 0.1 | 0.4 | 9.1 | 30.5 | 38.7 | 16.6 | 3.3 | 1.1 | 0.2 | 60 | 247 | 105 | 1.36 |
| MHZ_16_05 | 19.0 | 20.0 | PR-016632-020 | 0.72 | PR-016632-055 | 0.0 | 0.1 | 1.6 | 9.3 | 25.7 | 37.5 | 22.6 | 2.4 | 0.6 | 0.1 | 60 | 246 | 105 | 1.35 |
| MHZ_16_06 | 7.0 | 8.0 | PR-016633-008 | 1.11 | PR-016633-043 | 0.1 | 0.1 | 2.1 | 12.5 | 27.7 | 26.4 | 25.5 | 4.8 | 0.6 | 0.2 | 61 | 253 | 107 | 1.39 |
| MHZ_16_06 | 8.0 | 9.0 | PR-016633-009 | 0.72 | PR-016633-044 | 0.1 | 0.2 | 1.1 | 7.9 | 20.3 | 28.0 | 35.0 | 6.5 | 0.7 | 0.2 | 67 | 226 | 119 | 1.24 |
| MHZ_16_06 | 9.0 | 10.0 | PR-016633-010 | 0.99 | PR-016633-045 | 0.2 | 0.1 | 2.2 | 6.0 | 13.3 | 16.6 | 28.3 | 24.7 | 7.5 | 1.1 | 86 | 194 | 156 | 0.91 |
| MHZ_16_06 | 10.0 | 11.0 | PR-016633-011 | 0.83 | PR-016633-046 | 0.0 | 0.3 | 0.5 | 4.9 | 11.2 | 18.7 | 28.0 | 27.9 | 7.8 | 0.6 | 88 | 179 | 159 | 0.81 |
| MHZ_16_06 | 11.0 | 12.0 | PR-016633-012 | 0.42 | PR-016633-047 | 0.0 | 0.0 | 0.6 | 5.4 | 14.6 | 26.8 | 28.3 | 17.1 | 6.5 | 0.6 | 80 | 195 | 144 | 0.97 |
| MHZ_16_06 | 12.0 | 13.0 | PR-016633-013 | 0.48 | PR-016633-048 | 0.0 | 0.1 | 0.8 | 8.0 | 14.6 | 27.9 | 33.1 | 10.6 | 4.2 | 0.5 | 74 | 209 | 132 | 1.09 |
| MHZ_16_06 | 13.0 | 14.0 | PR-016633-014 | 0.48 | PR-016633-049 | 0.5 | 0.2 | 1.6 | 7.2 | 18.5 | 32.3 | 29.2 | 7.7 | 2.2 | 0.6 | 69 | 228 | 123 | 1.20 |
| MHZ_16_06 | 14.0 | 15.0 | PR-016633-015 | 0.57 | PR-016633-050 | 0.1 | 0.0 | 0.6 | 5.2 | 21.9 | 45.9 | 23.5 | 2.1 | 0.4 | 0.1 | 62 | 230 | 109 | 1.26 |
| MHZ_16_06 | 15.0 | 16.0 | PR-016633-016 | 0.23 | PR-016633-051 | 0.0 | 0.0 | 0.4 | 4.6 | 25.8 | 45.4 | 22.6 | 1.0 | 0.2 | 0.1 | 61 | 233 | 107 | 1.30 |
| MHZ_16_06 | 16.0 | 17.0 | PR-016633-017 | 0.09 | PR-016633-052 | 0.0 | 0.1 | 0.8 | 6.9 | 26.7 | 45.4 | 19.1 | 0.8 | 0.1 | 0.1 | 59 | 244 | 103 | 1.34 |
| MHZ_16_07 | 10.0 | 11.0 | PR-016634-011 | 1.08 | PR-016634-046 | 0.0 | 0.0 | 0.9 | 3.1 | 7.7 | 16.4 | 27.8 | 35.7 | 7.9 | 0.5 | 94 | 164 | 168 | 0.69 |
| MHZ_16_07 | 11.0 | 12.0 | PR-016634-012 | 1.05 | PR-016634-047 | 0.1 | 0.2 | 1.9 | 5.9 | 11.3 | 16.8 | 23.4 | 29.7 | 9.8 | 0.8 | 90 | 185 | 162 | 0.81 |
| MHZ_16_07 | 12.0 | 13.0 | PR-016634-013 | 1.81 | PR-016634-048 | 0.0 | 0.0 | 0.2 | 2.4 | 7.8 | 18.2 | 29.4 | 28.9 | 11.4 | 1.7 | 97 | 159 | 177 | 0.69 |
| MHZ_16_07 | 13.0 | 14.0 | PR-016634-014 | 0.72 | PR-016634-049 | 0.0 | 0.1 | 0.7 | 8.3 | 13.9 | 26.2 | 29.1 | 15.4 | 6.0 | 0.3 | 77 | 205 | 138 | 1.02 |
| MHZ_16_07 | 14.0 | 15.0 | PR-016634-015 | 0.49 | PR-016634-050 | 0.0 | 0.0 | 0.3 | 4.4 | 22.5 | 40.8 | 24.0 | 5.8 | 2.1 | 0.2 | 66 | 221 | 118 | 1.19 |
| MHZ_16_07 | 15.0 | 16.0 | PR-016634-016 | 0.28 | PR-016634-051 | 0.6 | 0.2 | 0.7 | 5.0 | 22.1 | 37.6 | 24.6 | 6.1 | 2.5 | 0.6 | 67 | 228 | 120 | 1.22 |
| MHZ_16_07 | 16.0 | 17.0 | PR-016634-017 | 0.29 | PR-016634-052 | 0.2 | 0.1 | 0.7 | 4.1 | 20.1 | 41.7 | 27.0 | 4.3 | 1.4 | 0.3 | 66 | 222 | 117 | 1.20 |
| MHZ_16_07 | 17.0 | 18.0 | PR-016634-018 | 0.15 | PR-016634-053 | 0.2 | 0.1 | 0.7 | 6.4 | 30.2 | 39.3 | 18.6 | 3.1 | 1.1 | 0.3 | 61 | 243 | 107 | 1.34 |
| MHZ_16_07 | 18.0 | 19.0 | PR-016634-019 | 0.44 | PR-016634-054 | 0.0 | 0.0 | 0.5 | 8.5 | 38.5 | 37.8 | 13.4 | 0.9 | 0.3 | 0.1 | 56 | 259 | 97 | 1.47 |
| MHZ_16_08 | 7.0 | 8.0 | PR-016635-008 | 1.17 | PR-016635-043 | 0.0 | 0.0 | 0.5 | 5.7 | 14.6 | 29.9 | 31.0 | 12.1 | 5.3 | 0.7 | 77 | 200 | 138 | 1.03 |
| MHZ_16_08 | 8.0 | 9.0 | PR-016635-009 | 0.47 | PR-016635-044 | 0.0 | 0.0 | 0.4 | 4.5 | 26.4 | 43.1 | 18.8 | 4.4 | 2.0 | 0.3 | 64 | 229 | 113 | 1.25 |
| MHZ_16_08 | 9.0 | 10.0 | PR-016635-010 | 0.31 | PR-016635-045 | 0.5 | 0.4 | 0.8 | 6.2 | 28.8 | 42.7 | 17.2 | 2.2 | 0.8 | 0.3 | 60 | 249 | 105 | 1.36 |
| MHZ_16_08 | 10.0 | 11.0 | PR-016635-011 | 0.57 | PR-016635-046 | 0.0 | 0.2 | 1.1 | 7.2 | 26.0 | 45.4 | 18.9 | 0.9 | 0.2 | 0.1 | 59 | 245 | 103 | 1.35 |

Figure 11: Part 1 of $MAMODtest$ in Site-C sand quarry.

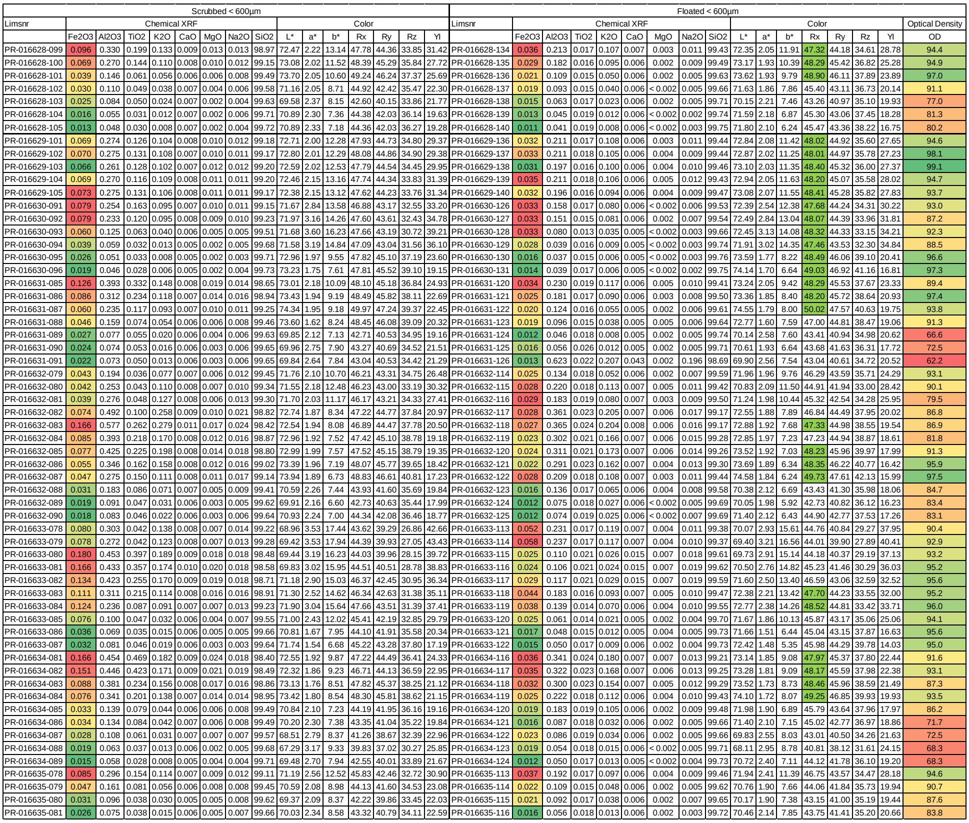

| Scrubbed < 600µm | | | | | | | | | | | | | | | | Floated < 600µm | | | | | | | | | | | | | | | | |
|---|---|---|---|---|---|---|---|---|---|---|---|---|---|---|---|---|---|---|---|---|---|---|---|---|---|---|---|---|---|---|---|---|
| Limsnr | Chemical XRF | | | | | | | | Color | | | | | | | Limsnr | Chemical XRF | | | | | | | | Color | | | | | | | Optical Density |
| | Fe2O3 | Al2O3 | TiO2 | K2O | CaO | MgO | Na2O | SiO2 | L* | a* | b* | Rx | Ry | Rz | YI | | Fe2O3 | Al2O3 | TiO2 | K2O | CaO | MgO | Na2O | SiO2 | L* | a* | b* | Rx | Ry | Rz | YI | OD |
| PR-016628-099 | 0.096 | 0.330 | 0.199 | 0.133 | 0.009 | 0.013 | 0.013 | 98.97 | 72.47 | 2.22 | 13.14 | 47.78 | 44.36 | 33.85 | 31.42 | PR-016628-134 | 0.036 | 0.213 | 0.017 | 0.107 | 0.007 | 0.003 | 0.011 | 99.43 | 72.35 | 2.05 | 11.91 | 47.32 | 44.18 | 34.61 | 28.78 | 94.4 |
| PR-016628-100 | 0.069 | 0.270 | 0.144 | 0.110 | 0.008 | 0.010 | 0.012 | 99.15 | 73.08 | 2.02 | 11.52 | 48.39 | 45.29 | 35.84 | 27.72 | PR-016628-135 | 0.029 | 0.182 | 0.016 | 0.095 | 0.006 | 0.002 | 0.009 | 99.49 | 73.17 | 1.93 | 10.39 | 48.29 | 45.42 | 36.82 | 25.28 | 94.9 |
| PR-016628-101 | 0.039 | 0.146 | 0.061 | 0.056 | 0.006 | 0.006 | 0.008 | 99.49 | 73.70 | 2.05 | 10.60 | 49.24 | 46.24 | 37.37 | 25.69 | PR-016628-136 | 0.021 | 0.109 | 0.015 | 0.050 | 0.006 | 0.002 | 0.005 | 99.63 | 73.62 | 1.93 | 9.79 | 48.90 | 46.11 | 37.89 | 23.89 | 97.0 |
| PR-016628-102 | 0.030 | 0.110 | 0.049 | 0.038 | 0.007 | 0.004 | 0.006 | 99.58 | 71.16 | 2.05 | 8.71 | 44.92 | 42.42 | 35.47 | 22.30 | PR-016628-137 | 0.019 | 0.093 | 0.015 | 0.040 | 0.006 | < 0.002 | 0.005 | 99.66 | 71.63 | 1.86 | 7.86 | 45.40 | 43.11 | 36.73 | 20.14 | 91.1 |
| PR-016628-103 | 0.025 | 0.084 | 0.050 | 0.024 | 0.007 | 0.002 | 0.004 | 99.63 | 69.58 | 2.37 | 8.15 | 42.60 | 40.15 | 33.86 | 21.77 | PR-016628-138 | 0.015 | 0.063 | 0.017 | 0.023 | 0.006 | 0.002 | 0.005 | 99.71 | 70.15 | 2.21 | 7.46 | 43.26 | 40.97 | 35.10 | 19.93 | 77.0 |
| PR-016628-104 | 0.016 | 0.055 | 0.031 | 0.012 | 0.007 | 0.002 | 0.006 | 99.71 | 70.89 | 2.30 | 7.36 | 44.38 | 42.03 | 36.14 | 19.63 | PR-016628-139 | 0.013 | 0.045 | 0.019 | 0.012 | 0.006 | < 0.002 | 0.002 | 99.74 | 71.59 | 2.18 | 6.87 | 45.30 | 43.06 | 37.45 | 18.28 | 81.3 |
| PR-016628-105 | 0.013 | 0.048 | 0.030 | 0.008 | 0.007 | 0.002 | 0.004 | 99.72 | 70.89 | 2.33 | 7.18 | 44.36 | 42.03 | 36.27 | 19.28 | PR-016628-140 | 0.011 | 0.041 | 0.019 | 0.008 | 0.006 | < 0.002 | 0.003 | 99.75 | 71.80 | 2.10 | 6.24 | 45.47 | 43.36 | 38.22 | 16.75 | 80.2 |
| PR-016629-101 | 0.069 | 0.274 | 0.126 | 0.104 | 0.008 | 0.010 | 0.012 | 99.18 | 72.71 | 2.00 | 12.28 | 47.93 | 44.73 | 34.80 | 29.37 | PR-016629-136 | 0.032 | 0.211 | 0.017 | 0.108 | 0.006 | 0.003 | 0.011 | 99.44 | 72.84 | 2.08 | 11.42 | 48.02 | 44.92 | 35.60 | 27.65 | 94.6 |
| PR-016629-102 | 0.070 | 0.275 | 0.131 | 0.108 | 0.007 | 0.010 | 0.011 | 99.17 | 72.80 | 2.01 | 12.29 | 48.08 | 44.86 | 34.90 | 29.38 | PR-016629-137 | 0.033 | 0.211 | 0.018 | 0.105 | 0.006 | 0.004 | 0.009 | 99.44 | 72.87 | 2.02 | 11.25 | 48.01 | 44.97 | 35.78 | 27.23 | 98.1 |
| PR-016629-103 | 0.066 | 0.261 | 0.128 | 0.102 | 0.007 | 0.012 | 0.012 | 99.20 | 72.59 | 2.02 | 12.53 | 47.79 | 44.54 | 34.45 | 29.95 | PR-016629-138 | 0.031 | 0.197 | 0.016 | 0.100 | 0.006 | 0.004 | 0.010 | 99.46 | 73.10 | 2.03 | 11.35 | 48.40 | 45.32 | 36.00 | 27.37 | 99.1 |
| PR-016629-104 | 0.069 | 0.270 | 0.116 | 0.109 | 0.008 | 0.011 | 0.011 | 99.20 | 72.46 | 2.15 | 13.16 | 47.74 | 44.34 | 33.83 | 31.39 | PR-016629-139 | 0.035 | 0.211 | 0.018 | 0.106 | 0.006 | 0.005 | 0.012 | 99.43 | 72.94 | 2.05 | 11.63 | 48.20 | 45.07 | 35.58 | 28.02 | 94.7 |
| PR-016629-105 | 0.073 | 0.275 | 0.131 | 0.106 | 0.008 | 0.011 | 0.011 | 99.17 | 72.38 | 2.15 | 13.12 | 47.62 | 44.23 | 33.76 | 31.34 | PR-016629-140 | 0.032 | 0.196 | 0.016 | 0.094 | 0.006 | 0.004 | 0.009 | 99.47 | 73.08 | 2.07 | 11.55 | 48.41 | 45.28 | 35.82 | 27.83 | 93.7 |
| PR-016630-091 | 0.079 | 0.254 | 0.163 | 0.095 | 0.007 | 0.010 | 0.011 | 99.15 | 71.67 | 2.84 | 13.58 | 46.88 | 43.17 | 32.55 | 33.20 | PR-016630-126 | 0.033 | 0.158 | 0.017 | 0.080 | 0.006 | < 0.002 | 0.006 | 99.53 | 72.39 | 2.54 | 12.38 | 47.68 | 44.24 | 34.31 | 30.22 | 93.0 |
| PR-016630-092 | 0.079 | 0.233 | 0.120 | 0.095 | 0.008 | 0.009 | 0.010 | 99.23 | 71.97 | 3.16 | 14.26 | 47.60 | 43.61 | 32.43 | 34.78 | PR-016630-127 | 0.033 | 0.151 | 0.015 | 0.081 | 0.006 | 0.002 | 0.007 | 99.54 | 72.49 | 2.84 | 13.04 | 48.07 | 44.39 | 33.96 | 31.81 | 87.2 |
| PR-016630-093 | 0.060 | 0.125 | 0.063 | 0.040 | 0.006 | 0.005 | 0.005 | 99.51 | 71.68 | 3.60 | 16.23 | 47.66 | 43.19 | 30.72 | 39.21 | PR-016630-128 | 0.033 | 0.080 | 0.013 | 0.035 | 0.005 | < 0.002 | 0.003 | 99.66 | 72.45 | 3.13 | 14.08 | 48.32 | 44.33 | 33.15 | 34.21 | 92.3 |
| PR-016630-094 | 0.039 | 0.059 | 0.032 | 0.013 | 0.005 | 0.002 | 0.005 | 99.68 | 71.58 | 3.19 | 14.84 | 47.09 | 43.04 | 31.56 | 36.10 | PR-016630-129 | 0.028 | 0.039 | 0.016 | 0.009 | 0.005 | < 0.002 | 0.003 | 99.74 | 71.91 | 3.02 | 14.35 | 47.46 | 43.53 | 32.30 | 34.84 | 88.5 |
| PR-016630-095 | 0.026 | 0.051 | 0.033 | 0.008 | 0.005 | 0.002 | 0.003 | 99.71 | 72.96 | 1.97 | 9.55 | 47.82 | 45.10 | 37.19 | 23.60 | PR-016630-130 | 0.016 | 0.037 | 0.015 | 0.006 | 0.005 | < 0.002 | 0.003 | 99.76 | 73.59 | 1.77 | 8.22 | 48.49 | 46.06 | 39.10 | 20.41 | 96.6 |
| PR-016630-096 | 0.019 | 0.046 | 0.028 | 0.006 | 0.005 | 0.002 | 0.004 | 99.73 | 73.23 | 1.75 | 7.61 | 47.81 | 45.52 | 39.10 | 19.15 | PR-016630-131 | 0.014 | 0.039 | 0.017 | 0.006 | 0.005 | < 0.002 | 0.002 | 99.75 | 74.14 | 1.70 | 6.64 | 49.03 | 46.92 | 41.16 | 16.81 | 97.3 |
| PR-016631-085 | 0.126 | 0.393 | 0.332 | 0.148 | 0.008 | 0.019 | 0.014 | 98.65 | 73.01 | 2.18 | 10.09 | 48.10 | 45.18 | 36.84 | 24.93 | PR-016631-120 | 0.034 | 0.230 | 0.019 | 0.117 | 0.006 | 0.005 | 0.010 | 99.41 | 73.24 | 2.05 | 9.42 | 48.29 | 45.53 | 37.67 | 23.33 | 89.4 |
| PR-016631-086 | 0.086 | 0.312 | 0.234 | 0.118 | 0.007 | 0.014 | 0.016 | 98.94 | 73.43 | 1.94 | 9.19 | 48.49 | 45.82 | 38.11 | 22.69 | PR-016631-121 | 0.025 | 0.181 | 0.017 | 0.090 | 0.006 | 0.003 | 0.008 | 99.50 | 73.36 | 1.85 | 8.40 | 48.20 | 45.72 | 38.64 | 20.93 | 97.4 |
| PR-016631-087 | 0.060 | 0.235 | 0.117 | 0.093 | 0.007 | 0.010 | 0.011 | 99.25 | 74.34 | 1.95 | 9.18 | 49.97 | 47.24 | 39.37 | 22.45 | PR-016631-122 | 0.020 | 0.124 | 0.016 | 0.055 | 0.005 | 0.002 | 0.006 | 99.61 | 74.55 | 1.79 | 8.00 | 50.02 | 47.57 | 40.63 | 19.75 | 93.8 |
| PR-016631-088 | 0.046 | 0.159 | 0.074 | 0.054 | 0.006 | 0.006 | 0.008 | 99.46 | 73.60 | 1.62 | 8.24 | 48.45 | 46.08 | 39.09 | 20.32 | PR-016631-123 | 0.019 | 0.096 | 0.015 | 0.038 | 0.005 | 0.005 | 0.006 | 99.64 | 72.77 | 1.60 | 7.59 | 47.00 | 44.81 | 38.47 | 19.06 | 91.3 |
| PR-016631-089 | 0.027 | 0.077 | 0.055 | 0.020 | 0.006 | 0.004 | 0.006 | 99.63 | 69.85 | 2.12 | 7.13 | 42.71 | 40.53 | 34.95 | 19.16 | PR-016631-124 | 0.012 | 0.046 | 0.018 | 0.008 | 0.005 | 0.002 | 0.005 | 99.74 | 70.14 | 2.58 | 7.60 | 43.41 | 40.94 | 34.98 | 20.62 | 66.6 |
| PR-016631-090 | 0.024 | 0.074 | 0.053 | 0.016 | 0.006 | 0.003 | 0.006 | 99.65 | 69.96 | 2.75 | 7.90 | 43.27 | 40.69 | 34.52 | 21.51 | PR-016631-125 | 0.016 | 0.056 | 0.026 | 0.012 | 0.005 | 0.002 | 0.005 | 99.71 | 70.61 | 1.93 | 6.64 | 43.68 | 41.63 | 36.31 | 17.72 | 72.5 |
| PR-016631-091 | 0.022 | 0.073 | 0.050 | 0.013 | 0.006 | 0.003 | 0.006 | 99.65 | 69.84 | 2.64 | 7.84 | 43.04 | 40.53 | 34.42 | 21.29 | PR-016631-126 | 0.013 | 0.623 | 0.022 | 0.207 | 0.043 | 0.002 | 0.196 | 98.69 | 69.90 | 2.56 | 7.54 | 43.04 | 40.61 | 34.72 | 20.52 | 62.2 |
| PR-016632-079 | 0.043 | 0.194 | 0.036 | 0.077 | 0.007 | 0.006 | 0.012 | 99.45 | 71.76 | 2.10 | 10.70 | 46.21 | 43.31 | 34.75 | 26.48 | PR-016632-114 | 0.025 | 0.134 | 0.018 | 0.052 | 0.006 | 0.002 | 0.007 | 99.59 | 71.96 | 1.96 | 9.76 | 46.29 | 43.59 | 35.71 | 24.29 | 93.1 |
| PR-016632-080 | 0.042 | 0.253 | 0.043 | 0.110 | 0.008 | 0.007 | 0.010 | 99.34 | 71.55 | 2.18 | 12.48 | 46.23 | 43.00 | 33.19 | 30.32 | PR-016632-115 | 0.028 | 0.220 | 0.018 | 0.113 | 0.007 | 0.005 | 0.011 | 99.42 | 70.83 | 2.09 | 11.50 | 44.91 | 41.94 | 33.00 | 28.42 | 90.1 |
| PR-016632-081 | 0.039 | 0.276 | 0.048 | 0.127 | 0.008 | 0.006 | 0.013 | 99.30 | 71.70 | 2.03 | 11.17 | 46.17 | 43.21 | 34.33 | 27.41 | PR-016632-116 | 0.029 | 0.183 | 0.019 | 0.080 | 0.007 | 0.003 | 0.009 | 99.50 | 71.24 | 1.98 | 10.44 | 45.32 | 42.54 | 34.28 | 25.95 | 79.5 |
| PR-016632-082 | 0.074 | 0.492 | 0.100 | 0.258 | 0.009 | 0.010 | 0.021 | 98.82 | 72.74 | 1.87 | 8.34 | 47.22 | 44.77 | 37.84 | 20.97 | PR-016632-117 | 0.028 | 0.361 | 0.023 | 0.205 | 0.007 | 0.006 | 0.017 | 99.17 | 72.55 | 1.88 | 7.89 | 46.84 | 44.49 | 37.95 | 20.02 | 86.8 |
| PR-016632-083 | 0.166 | 0.577 | 0.262 | 0.279 | 0.011 | 0.017 | 0.024 | 98.42 | 72.54 | 1.94 | 8.08 | 46.89 | 44.47 | 37.78 | 20.50 | PR-016632-118 | 0.027 | 0.365 | 0.024 | 0.204 | 0.008 | 0.006 | 0.016 | 99.17 | 72.88 | 1.92 | 7.68 | 47.33 | 44.98 | 38.55 | 19.54 | 86.9 |
| PR-016632-084 | 0.085 | 0.393 | 0.218 | 0.170 | 0.008 | 0.012 | 0.016 | 98.87 | 72.96 | 1.92 | 7.52 | 47.42 | 45.10 | 38.78 | 19.18 | PR-016632-119 | 0.023 | 0.302 | 0.021 | 0.166 | 0.007 | 0.006 | 0.015 | 99.28 | 72.85 | 1.97 | 7.23 | 47.23 | 44.94 | 38.87 | 18.61 | 81.8 |
| PR-016632-085 | 0.077 | 0.425 | 0.225 | 0.198 | 0.008 | 0.014 | 0.018 | 98.80 | 72.99 | 1.99 | 7.57 | 47.52 | 45.15 | 38.79 | 19.35 | PR-016632-120 | 0.024 | 0.311 | 0.021 | 0.173 | 0.007 | 0.006 | 0.014 | 99.26 | 73.52 | 1.92 | 7.03 | 48.23 | 45.96 | 39.97 | 17.99 | 91.3 |
| PR-016632-086 | 0.055 | 0.346 | 0.162 | 0.158 | 0.008 | 0.012 | 0.016 | 99.02 | 73.39 | 1.96 | 7.19 | 48.07 | 45.77 | 39.65 | 18.42 | PR-016632-121 | 0.022 | 0.291 | 0.023 | 0.162 | 0.007 | 0.004 | 0.013 | 99.30 | 73.69 | 1.89 | 6.34 | 48.35 | 46.22 | 40.77 | 16.42 | 95.9 |
| PR-016632-087 | 0.047 | 0.275 | 0.150 | 0.111 | 0.008 | 0.011 | 0.017 | 99.14 | 73.94 | 1.89 | 6.73 | 48.83 | 46.61 | 40.81 | 17.23 | PR-016632-122 | 0.028 | 0.209 | 0.018 | 0.108 | 0.007 | 0.003 | 0.011 | 99.44 | 74.58 | 1.84 | 6.24 | 49.73 | 47.61 | 42.13 | 15.99 | 97.5 |
| PR-016632-088 | 0.031 | 0.183 | 0.086 | 0.071 | 0.007 | 0.005 | 0.009 | 99.41 | 70.59 | 2.26 | 7.44 | 43.93 | 41.60 | 35.69 | 19.84 | PR-016632-123 | 0.016 | 0.136 | 0.017 | 0.065 | 0.006 | 0.004 | 0.008 | 99.58 | 70.38 | 2.12 | 6.69 | 43.43 | 41.30 | 35.98 | 18.06 | 84.7 |
| PR-016632-089 | 0.019 | 0.091 | 0.047 | 0.031 | 0.006 | 0.003 | 0.005 | 99.62 | 69.91 | 2.16 | 6.60 | 42.73 | 40.63 | 35.44 | 17.99 | PR-016632-124 | 0.012 | 0.075 | 0.018 | 0.027 | 0.006 | < 0.002 | 0.005 | 99.69 | 70.05 | 1.98 | 5.92 | 42.73 | 40.82 | 36.12 | 16.23 | 83.4 |
| PR-016632-090 | 0.018 | 0.083 | 0.046 | 0.022 | 0.006 | 0.003 | 0.006 | 99.64 | 70.93 | 2.24 | 7.00 | 44.34 | 42.08 | 36.46 | 18.77 | PR-016632-125 | 0.012 | 0.074 | 0.019 | 0.025 | 0.006 | < 0.002 | 0.007 | 99.69 | 71.40 | 2.12 | 6.43 | 44.90 | 42.77 | 37.53 | 17.26 | 83.1 |
| PR-016633-078 | 0.080 | 0.303 | 0.042 | 0.138 | 0.008 | 0.007 | 0.014 | 99.22 | 68.96 | 3.53 | 17.44 | 43.62 | 39.29 | 26.86 | 42.66 | PR-016633-113 | 0.052 | 0.231 | 0.017 | 0.119 | 0.007 | 0.004 | 0.011 | 99.38 | 70.07 | 2.93 | 15.61 | 44.76 | 40.84 | 29.27 | 37.95 | 90.4 |
| PR-016633-079 | 0.078 | 0.272 | 0.042 | 0.123 | 0.008 | 0.007 | 0.013 | 99.28 | 69.42 | 3.53 | 17.94 | 44.39 | 39.93 | 27.05 | 43.43 | PR-016633-114 | 0.058 | 0.237 | 0.017 | 0.117 | 0.007 | 0.004 | 0.010 | 99.37 | 69.40 | 3.21 | 16.56 | 44.01 | 39.90 | 27.89 | 40.41 | 92.9 |
| PR-016633-080 | 0.180 | 0.453 | 0.397 | 0.189 | 0.009 | 0.018 | 0.018 | 98.48 | 69.44 | 3.19 | 16.23 | 44.03 | 39.96 | 28.15 | 39.72 | PR-016633-115 | 0.025 | 0.110 | 0.021 | 0.026 | 0.015 | 0.007 | 0.018 | 99.61 | 69.73 | 2.91 | 15.14 | 44.18 | 40.37 | 29.19 | 37.13 | 93.2 |
| PR-016633-081 | 0.166 | 0.433 | 0.357 | 0.174 | 0.010 | 0.020 | 0.018 | 98.58 | 69.83 | 3.02 | 15.95 | 44.51 | 40.51 | 28.78 | 38.83 | PR-016633-116 | 0.024 | 0.106 | 0.021 | 0.024 | 0.015 | 0.007 | 0.019 | 99.62 | 70.50 | 2.76 | 14.82 | 45.23 | 41.46 | 30.29 | 36.03 | 95.2 |
| PR-016633-082 | 0.134 | 0.423 | 0.255 | 0.170 | 0.009 | 0.019 | 0.018 | 98.71 | 71.18 | 2.90 | 15.03 | 46.37 | 42.45 | 30.95 | 36.34 | PR-016633-117 | 0.029 | 0.117 | 0.021 | 0.029 | 0.015 | 0.007 | 0.019 | 99.59 | 71.60 | 2.50 | 13.40 | 46.59 | 43.06 | 32.59 | 32.52 | 95.6 |
| PR-016633-083 | 0.111 | 0.311 | 0.215 | 0.114 | 0.008 | 0.016 | 0.016 | 98.91 | 71.30 | 2.52 | 14.62 | 46.34 | 42.63 | 31.38 | 35.11 | PR-016633-118 | 0.044 | 0.183 | 0.016 | 0.093 | 0.007 | 0.005 | 0.010 | 99.47 | 72.38 | 2.21 | 13.42 | 47.70 | 44.23 | 33.55 | 32.00 | 95.2 |
| PR-016633-084 | 0.124 | 0.236 | 0.087 | 0.091 | 0.007 | 0.007 | 0.013 | 99.23 | 71.90 | 3.04 | 15.64 | 47.66 | 43.51 | 31.39 | 37.41 | PR-016633-119 | 0.038 | 0.139 | 0.014 | 0.070 | 0.006 | 0.004 | 0.010 | 99.55 | 72.77 | 2.38 | 14.26 | 48.52 | 44.81 | 33.42 | 33.71 | 96.0 |
| PR-016633-085 | 0.076 | 0.100 | 0.047 | 0.032 | 0.006 | 0.004 | 0.007 | 99.55 | 71.00 | 2.43 | 12.02 | 45.41 | 42.19 | 32.85 | 29.79 | PR-016633-120 | 0.025 | 0.061 | 0.014 | 0.021 | 0.005 | 0.002 | 0.004 | 99.70 | 71.67 | 1.86 | 10.13 | 45.87 | 43.17 | 35.06 | 25.06 | 94.1 |
| PR-016633-086 | 0.036 | 0.069 | 0.035 | 0.015 | 0.006 | 0.005 | 0.005 | 99.66 | 70.81 | 1.67 | 7.95 | 44.10 | 41.91 | 35.58 | 20.34 | PR-016633-121 | 0.017 | 0.048 | 0.015 | 0.012 | 0.005 | 0.004 | 0.005 | 99.73 | 71.66 | 1.51 | 6.44 | 45.04 | 43.15 | 37.87 | 16.63 | 95.6 |
| PR-016633-087 | 0.032 | 0.081 | 0.046 | 0.019 | 0.006 | 0.003 | 0.003 | 99.64 | 71.74 | 1.54 | 6.68 | 45.22 | 43.28 | 37.80 | 17.19 | PR-016633-122 | 0.015 | 0.050 | 0.017 | 0.009 | 0.006 | 0.002 | 0.004 | 99.73 | 72.42 | 1.48 | 5.35 | 45.98 | 44.29 | 39.78 | 14.03 | 95.0 |
| PR-016634-081 | 0.166 | 0.454 | 0.469 | 0.182 | 0.009 | 0.024 | 0.018 | 98.40 | 72.55 | 1.92 | 9.87 | 47.22 | 44.49 | 36.41 | 24.33 | PR-016634-116 | 0.036 | 0.341 | 0.024 | 0.180 | 0.007 | 0.007 | 0.013 | 99.21 | 73.14 | 1.85 | 9.08 | 47.97 | 45.37 | 37.80 | 22.44 | 91.6 |
| PR-016634-082 | 0.151 | 0.446 | 0.423 | 0.171 | 0.009 | 0.021 | 0.019 | 98.49 | 72.32 | 1.86 | 9.23 | 46.71 | 44.13 | 36.59 | 22.95 | PR-016634-117 | 0.035 | 0.322 | 0.023 | 0.168 | 0.007 | 0.006 | 0.013 | 99.25 | 73.28 | 1.81 | 9.09 | 48.17 | 45.59 | 37.98 | 22.38 | 93.1 |
| PR-016634-083 | 0.088 | 0.381 | 0.234 | 0.156 | 0.008 | 0.017 | 0.016 | 98.86 | 73.13 | 1.76 | 8.51 | 47.82 | 45.37 | 38.25 | 21.12 | PR-016634-118 | 0.032 | 0.300 | 0.023 | 0.154 | 0.007 | 0.005 | 0.012 | 99.29 | 73.52 | 1.73 | 8.73 | 48.46 | 45.96 | 38.59 | 21.49 | 87.3 |
| PR-016634-084 | 0.076 | 0.341 | 0.201 | 0.138 | 0.007 | 0.014 | 0.014 | 98.95 | 73.42 | 1.80 | 8.54 | 48.30 | 45.81 | 38.62 | 21.15 | PR-016634-119 | 0.025 | 0.222 | 0.018 | 0.112 | 0.006 | 0.004 | 0.010 | 99.43 | 74.10 | 1.72 | 8.07 | 49.25 | 46.85 | 39.93 | 19.93 | 93.5 |
| PR-016634-085 | 0.033 | 0.139 | 0.079 | 0.044 | 0.006 | 0.006 | 0.008 | 99.49 | 70.84 | 2.10 | 7.23 | 44.19 | 41.95 | 36.16 | 19.16 | PR-016634-120 | 0.019 | 0.183 | 0.019 | 0.105 | 0.006 | 0.002 | 0.009 | 99.48 | 71.98 | 1.90 | 6.89 | 45.79 | 43.64 | 37.96 | 17.97 | 86.2 |
| PR-016634-086 | 0.034 | 0.134 | 0.084 | 0.042 | 0.007 | 0.006 | 0.008 | 99.49 | 70.20 | 2.30 | 7.38 | 43.35 | 41.04 | 35.22 | 19.84 | PR-016634-121 | 0.016 | 0.087 | 0.018 | 0.032 | 0.006 | 0.002 | 0.005 | 99.66 | 71.40 | 2.10 | 7.15 | 45.02 | 42.77 | 36.97 | 18.86 | 71.7 |
| PR-016634-087 | 0.028 | 0.108 | 0.061 | 0.031 | 0.007 | 0.007 | 0.007 | 99.57 | 68.51 | 2.79 | 8.37 | 41.26 | 38.67 | 32.39 | 22.96 | PR-016634-122 | 0.023 | 0.086 | 0.019 | 0.034 | 0.006 | 0.002 | 0.005 | 99.66 | 69.83 | 2.55 | 8.03 | 43.01 | 40.50 | 34.26 | 21.63 | 72.5 |
| PR-016634-088 | 0.019 | 0.063 | 0.037 | 0.013 | 0.006 | 0.002 | 0.005 | 99.68 | 67.29 | 3.17 | 9.33 | 39.83 | 37.02 | 30.27 | 25.85 | PR-016634-123 | 0.019 | 0.054 | 0.018 | 0.015 | 0.006 | < 0.002 | 0.005 | 99.71 | 68.11 | 2.95 | 8.78 | 40.81 | 38.12 | 31.61 | 24.15 | 68.3 |
| PR-016634-089 | 0.015 | 0.058 | 0.028 | 0.008 | 0.005 | 0.004 | 0.004 | 99.71 | 69.48 | 2.70 | 7.94 | 42.55 | 40.01 | 33.89 | 21.67 | PR-016634-124 | 0.012 | 0.050 | 0.017 | 0.013 | 0.005 | < 0.002 | 0.004 | 99.73 | 70.72 | 2.40 | 7.11 | 44.12 | 41.78 | 36.10 | 19.20 | 68.3 |
| PR-016635-078 | 0.085 | 0.296 | 0.154 | 0.114 | 0.007 | 0.009 | 0.012 | 99.11 | 71.19 | 2.56 | 12.52 | 45.83 | 42.46 | 32.72 | 30.90 | PR-016635-113 | 0.037 | 0.192 | 0.017 | 0.097 | 0.006 | 0.004 | 0.009 | 99.46 | 71.94 | 2.41 | 11.39 | 46.75 | 43.57 | 34.47 | 28.18 | 94.6 |
| PR-016635-079 | 0.047 | 0.161 | 0.081 | 0.056 | 0.006 | 0.008 | 0.008 | 99.45 | 70.59 | 2.08 | 8.98 | 44.13 | 41.60 | 34.53 | 23.08 | PR-016635-114 | 0.022 | 0.109 | 0.015 | 0.048 | 0.006 | 0.002 | 0.005 | 99.62 | 70.76 | 1.90 | 7.66 | 44.06 | 41.84 | 35.73 | 19.94 | 90.7 |
| PR-016635-080 | 0.031 | 0.096 | 0.038 | 0.030 | 0.005 | 0.005 | 0.008 | 99.62 | 69.37 | 2.09 | 8.37 | 42.22 | 39.86 | 33.45 | 22.03 | PR-016635-115 | 0.021 | 0.092 | 0.017 | 0.038 | 0.006 | 0.002 | 0.007 | 99.65 | 70.17 | 1.90 | 7.38 | 43.15 | 41.00 | 35.19 | 19.44 | 87.6 |
| PR-016635-081 | 0.026 | 0.075 | 0.038 | 0.015 | 0.006 | 0.005 | 0.007 | 99.66 | 70.03 | 2.34 | 8.58 | 43.32 | 40.79 | 34.11 | 22.59 | PR-016635-116 | 0.016 | 0.056 | 0.018 | 0.013 | 0.006 | 0.002 | 0.003 | 99.72 | 70.46 | 2.14 | 7.85 | 43.75 | 41.41 | 35.20 | 20.66 | 83.8 |

Figure 12: Part 2 of $MAMODtest$ in Site-C sand quarry.

# Appendix-d

Videos of the experiments were recorded by a time-lapse camera installed on the Southern shore and by a few smartphone cameras of people present in the field. In this appendix, screenshots collections from the recordings of the time-lapse camera are presented to show evidences of the observations made from the shore.

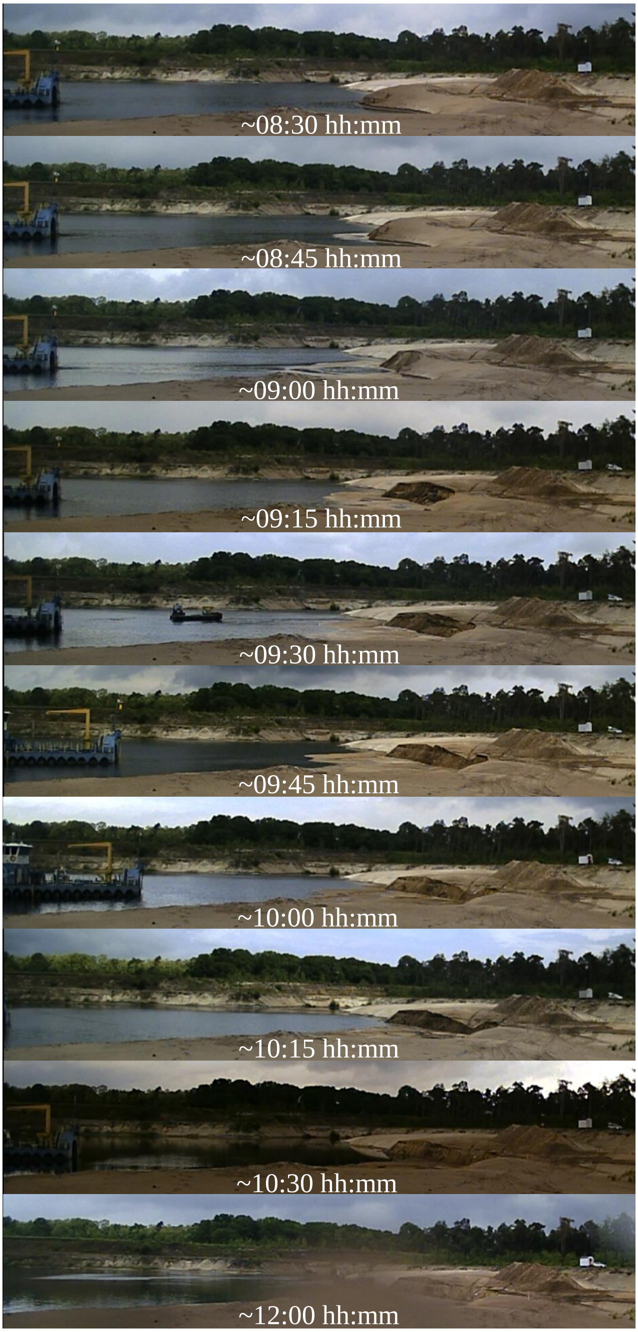

Figure 13: Selection of screenshots from the first RBF in Site-B as observed from the time-lapse camera.

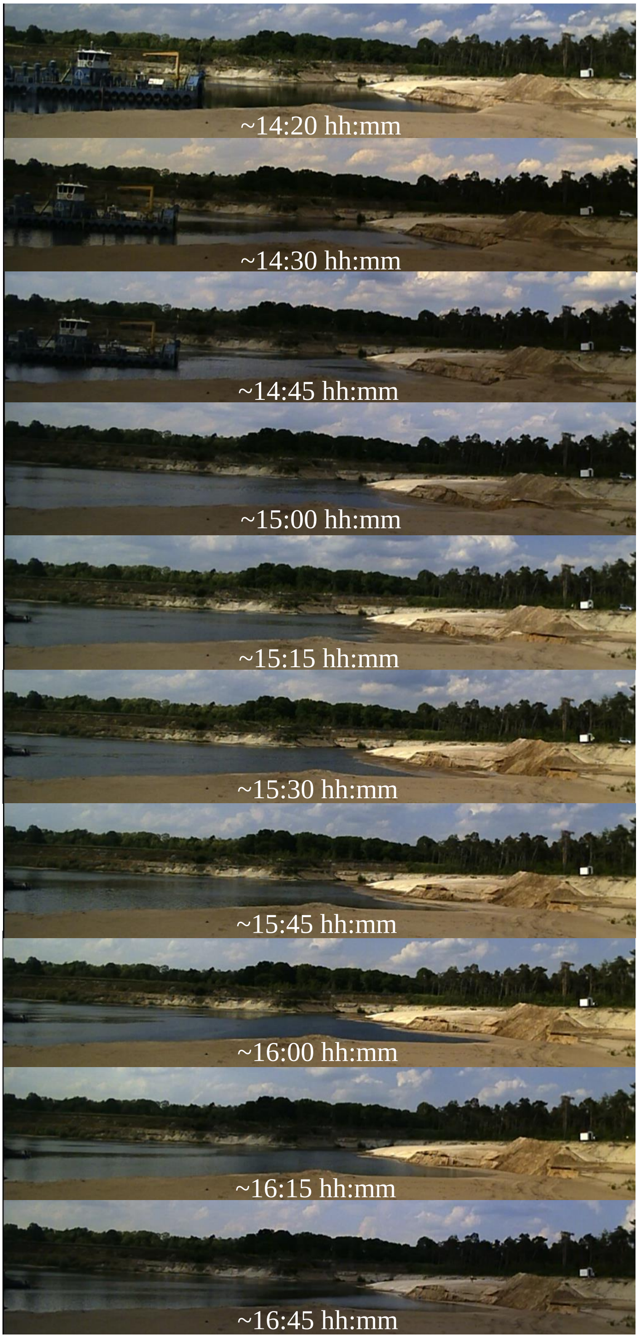

Figure 14: Selection of screenshots from the second RBF in Site-B as observed from the time-lapse camera.

# Curriculum Vitæ

## **Marco BOLOGNIN**

05-04-1987 Born in Cesena, Italy.

## Education

| | |
|---|---|
| 2006–2009 | Bachelor in Mechanical Engineering (unfinished),<br>La Sapienza University, Rome, Italy |
| 2009–2012 | Bachelor in Civil Engineering<br>Transport Infrastructures direction,<br>University of RomaTre, Rome, Italy |
| 2013–2015 | Master of Science in Civil Engineering<br>Structural Engineering direction,<br>University of Bologna, Bologna, Italy |
| 2016–2020 | PhD. in Civil Engineering<br>Delft University of Technology, Delft, The Netherlands<br>*Dissertation:* Material Point Method for underwater sand flow-slides analysis<br>*Promoters:* Prof. dr. S.N Jonkman, Prof. dr. M.A.Hicks, Prof. dr. P.J. Vardon |
| in 2020 | Postdoc in Enviromental Fluid Mechanics<br>Hydraulic Engineering,<br>Delft University of Technology, Delft, The Netherlands |

## Professional

| | |
|---|---|
| 2021-2023 | Geotechnical Consultant<br>DIANA FEA b.v.,<br>Delft, The Netherlands |
| 2023-2025 | Geotechnical Consultant<br>NLyse Consultants b.v.,<br>Delft, The Netherlands |

# List of Publications

9. Meda et al. No. 116. Fibre reinforced sprayed concrete in tunnels and underground spaces - Technical report (67 pages, ISBN 978-2-88394-194-6, April 2025).

8. P.J. Vardon, G. Remmerswaal, **M. Bolognin**, M.A. Hicks. (Abstract) *Application of boundary conditions in MPM, MAFELAP 2019 mini-symposium: The Mathematics of Hybrid Particle Mesh Methods, London, United Kingdom*.

7. G.Remmerswaal, **M.Bolognin**, P.J.Vardon, M.A.Hicks, A.Rohe. (Abstract) *Implementation of non-trivial boundary conditions in MPM for Geotechnical applications*, 2nd International Conference on the Material Point Method for Modelling Soil-Water-Structure Interaction, MPM2019, Cambridge, United Kingdom.

6. X. Zhao, **M. Bolognin**, D. Liang, A. Rohe, P.J. Vardon. (Journal paper) *Development of in/outflow boundary conditions for MPM simulation of uniform and non-uniform open channel flows*, Computer and Fluids, (2019), 179, 27-33.

5. B.Z. Coelho, A. Rohe, A. Aboufirass, J. Nuttall, **M. Bolognin**. (Conference paper) *Assessment of dike safety within the framework of large deformation analysis with the material point method, NUMGE2018, Porto, Portugal*.

4. **M. Bolognin**, A. Rohe, P.J. Vardon, M.A. Hicks, S.N. Jonkman. (Poster) *Real Scale Test design of a sand by MPM slope (in)stability analysis*, ALERT Poster session 2017, Aussois, France.

3. **M. Bolognin**, A. Rohe, P.J. Vardon, M.A. Hicks, S.N. Jonkman. (Abstract and speaker) *Real Scale Test design of a sand by MPM slope (in)stability analysis*, ALERT Workshop 2017, Aussois, France.

2. **M. Bolognin**, A. Rohe, P.J. Vardon, M.A. Hicks, S.N. Jonkman. (Poster) *MPM validation for underwater flow-slide simulations*, Winter school "Multi scale approaches and multiphysics couplings in fluid and solid mechanics", Grenoble 16–20th of January 2017, France.

1. **M. Bolognin**, M. Martinelli, K.J. Bakker, S.N. Jonkman. (Journal paper) *Validation of material point method for soil fluidisation analysis*, Journal of Hydrodynamics, (2017), 29(3) 431-437.

Abstract: This dissertation validates the Material Point Method (MPM) for simulating underwater flow slides and slope stability. Through a combination of numerical benchmarks, coupled multi-phase modeling, and field experiments, the study demonstrates that MPM can accurately capture failure initiation, large deformations, and post-failure behavior. The results highlight MPM’s advantages over conventional methods in modeling transient hydro-mechanical processes, supporting its application for improved analysis and design of flood defense systems.

Author bio: Marco Bolognin is a structural engineer with expertise in numerical modeling, soil mechanics, and advanced simulation methods. They are passionate about innovative computational techniques, to better understand complex soil–water interactions, large-deformations, and complex engineering structural challenges. With experience in integrating experimental data and numerical analysis, their research contributes to improving the reliability and safety assessment of civil structures.